CONTROLLING LIGHT-MATTER INTERACTIONS IN QD PHOTONIC SOURCES VIA OPTICAL GAIN AND LOSS

A Dissertation
Presented to
The Academic Faculty

by

Chun Hao Lin

In Partial Fulfillment
Of the Requirements for the Degree
Doctor of Philosophy in the
School of Materials Science and Engineering

Georgia Institute of Technology
August 2018

CONTROLLING LIGHT-MATTER INTERACTIONS IN QD PHOTONIC SOURCES VIA OPTICAL GAIN AND LOSS

Dissertation committee:

Dr. Vladimir V. Tsukruk, Advisor
School of Materials Science and Engineering
Georgia Institute of Technology

Dr. Zhiqun Lin
School of Materials Science and Engineering
Georgia Institute of Technology

Dr. Dong Qin
School of Materials Science and Engineering
Georgia Institute of Technology

Dr. Wenshan Cai
School of Electrical and Computer Engineering,
School of Materials Science and Engineering
Georgia Institute of Technology

Dr. Eric Vogel
School of Materials Science and Engineering
Georgia Institute of Technology

Date of Final Approval: **June 13, 2018**

Dedicated to my friends and family for their support, in particular my parents and my wife who have always given me freedom to chase my dream.

ACKNOWLEDGEMENTS

I would like to thank my advisor, Prof. V. V. Tsukruk, for his constant support and guidance in the past five years. Starting from the beginning, he encouraged me to develop strong problem solving skills, to critically analyze experimental results on my own, and to sharpen up my technical writing. I also appreciate his patience to teach me how to correct my attitude toward my project when I made mistake in the past five years. Prof. Tsukruk has developed a research group with the atmosphere to encourage lab members to work and collaborate with each other. This gains me experiences not only in research but also how to be a team player in a project. I also want to thank my PhD dissertation committee members, Prof. Z. Lin, Prof. W. Cai, Prof. E. Vogel and Prof. D. Qin for their recommendations and direction.

I also want to thank our main collaborators from Georgia Institute of Technology and University of UTAH. These include Dr. J. Jung and Y.J. Yoon from Prof. Lin's group in Georgia Institute of Technology for the synthesis of different types of colloidal quantum dots. In addition, Dr. E. Lafalce and Q. Zeng from Prof. V. Vardeny's group in University of UTAH provided many good suggestions and measurement assistance. Further thanks go to my collaborators on the Synthetic Photonics Multidisciplinary University Research Initiative (MURI) for their suggestions on the design of parity-time symmetry systems. These collaborators include Dr. G. Liang/Dr. T. Ramathasan/Prof. E. Thomas (Rice University) and Prof. T. Kottos (Wesleyan University).

Finally, I want to thank all the SEMA group members who provided technical assistance and discussion, in particular Dr. S. Malak, Dr. P.A. Ledin, Dr. C. Ye, M. Smith, S. Zhang, S. Yu. I also greatly appreciate my lovely wife, Yin Chi's support which help me finish this dissertation.

TABLE OF CONTENTS

ACKNOWLEDGEMENTS…….. iv
LIST OF TABLES…….…….... xi
LIST OF EQUATIONS……..…..…xiii
LIST OF FIGURES……..…..... xiv
SUMMARY……..……..... xxxiii

1 INTRODUCTION……1

1.1 Quantum dots as gain and loss medium……...…….. 2

1.1.1 Introduction to quantum dots…….…..... 2

1.1.1.1 Cd-based QDs

1.1.1.2 Lead halide perovskite QDs

1.1.2 Fundamental exciton dynamics……..….. 8

1.1.2.1 Quantum confined effect

1.1.2.2 Exciton relaxation and Auger recombination

1.2 QD assembly for photonic systems…..……...…….16

1.2.1 Optical gain systems……..…….……..18

1.2.1.1 Built up of stimulated emission in QD assembly

1.2.1.2 Estimation of optical gain values

1.2.2 Fabrication techniques of QD based films and structures……..…… 20

1.2.2.1 Deposition techniques of QD planar films

1.2.2.2 Physical patterning of QD patterns

1.2.2.3 Photopattenring of QD microscale arrays

1.2.3 QD based photonic cavities……...……..28

1.2.3.1 Coating structure

1.2.3.2 Self-assembled QD-polymer composite structure

1.2.3.3 Inkjet-printed structure

1.2.3.4 Lithographically patterned structure

1.2.4 Parity-time symmetric photonic systems……..41

1.3 Summary of critical issues and motivation…….…… 46

1.4 References (Chapter 1)…… 49

2 RESEARCH GOALS, TECHNICAL OBJECTIVES, AND DISSERTATION OVERVIEW……..…..…56

2.1 Research goals……..…56
2.2 Technical objectives……..……57
2.3 Organization and composition of dissertation……..……60

3 EXPERIMENTAL TECHNIQUES AND MATERIALS…… 64

3.1 Quantum dots for lasing……..… 64
3.1.1 Chemicals and materials……..……64
3.1.2 Synthesis of CdSe/$Cd_{1-x}Zn_xSe_{1-y}S_y$ core/graded shell QDs……64
3.1.3 Ligand exchange process…… 65
3.1.4 Synthesis of $CsPbBr_3$ perovskite QDs……...…… 66
3.2 Film deposition & patterning methods……..……...…..66
3.2.1 Preparation of QD films……..…..… 66
3.2.2 Patterning of Cd-based QD microdisk lasers……..…….… 67
3.2.3 Orthogonal lithography patterning process……... 68
3.3 Fourier transform infrared spectroscopy (FTIR)…… 69
3.4 Thermal gravimetric analysis (TGA)……..……..…69
3.5 Nuclear magnetic resonance (NMR)……..……..…… 70
3.6 SEM / EDX / TEM……...70
3.7 Atomic force microscopy (AFM)…… 71
3.8 Optical microscopies (bright field, dark field, photoluminescence)……71
3.9 Spectroscopic ellipsometry……..…… 71
3.10 UV-vis and fluorescence spectroscopy……..72
3.11 Photoluminescence stability measurement……..……..72
3.12 Hyperspectral scanning and imaging……..... 73
3.13 Quantum yield (QY) determination……...……...73
3.14 Optical gain and loss measurements…..……...74
3.15 Finite-difference time-domain (FDTD) modeling…….. 75
3.16 Confocal micro-photoluminescence measurement……..……75
3.17 Femtosecond-transient absorption…… 76
3.18 Collaborative efforts…….. 77
3.19 References (Chapter 3)……..……..77

4 CRAFTING CORE/GRADED SHELL/SHELL QUANTUM DOTS WITH SUPPRESSED RE-ABSORPTION AND TUNABLE STOKES SHIFT..... 78

4.1 Introduction……78
4.2 Experimental details……...81
4.3 Results and discussion……83
4.3.1 Synthesis of QDs with different core/shell design…….....83
4.3.2 Spectroscopic analysis……86
4.3.3 Suppressed Auger recombination…….. 91
4.4 Conclusions……..……..92
4.5 Chapter acknowledgements……..…..93
4.6 References (Chapter 4)……..……93

5 ENHANCEMENT OF OPTICAL GAIN CHARACTERISTICS OF QUANTUM DOT FILMS BY ORGANIC LIGAND SHELL……..……95

5.1 Introduction……..……95
5.2 Experimental details……..……96
5.3 Results and discussion……..……..... 98
5.3.1 Quantum dot characteristics……..…..…98
5.3.2 QD film uniformity & morphology……..... 99
5.3.3 Ligand characteristics & QD-loading (volume fraction)…….102
5.3.4 Optical gain threshold, magnitude, & stability…….103
5.3.5 Photostability of the QD films……..... 111
5.3.6 Optical loss……... 112
5.3.7 Ligand selection…….…… 113
5.4 Conclusions……..……115
5.5 Chapter acknowledgements……..……116
5.6 References (Chapter 5)…….……116

6 CORE/ALLOYED-SHELL QUANTUM DOT ROBUST SOLID FILMS WITH HIGH OPTICAL GAINS……..……120

6.1 Introduction…….. 120
6.2 Experimental details……122
6.3 Results and discussion…….. 124
6.3.1 Choice of bifunctional crosslinker……. 124
6.3.2 Film fabrication and properties……..... 125

6.3.3 Optical gain studies of DIAH-tethered QD films…… 128
6.3.4 PL stability study of QD film with different ligands…… 134
6.4 Conclusions……..……135
6.5 Chapter acknowledgements…….. 137
6.6 References (Chapter 6)…….…….. 137

7 LARGE-SCALE ROBUST QUANTUM DOT MICRODISK LASERS WITH CONTROLLED CAVITY MODES……... 140

7.1 Introduction……..…… 140
7.2 Experimental details……142
7.3 Results and discussion……..…… 144
7.3.1 Fabrication of disk arrays……..144
7.3.2 Characterization of disk morphology…….…….. 146
7.3.3 Optical properties and lasing behavior…… 148
7.4 Conclusions……...156
7.5 Chapter acknowledgements…….157
7.6 References (Chapter 7)…….157

8 LARGE-AREA LASING AND MULTICOLOR PEROVSKITE QUANTUM DOT ARRAYS……..……..…… 160

8.1 Introduction…….. 160
8.2 Experimental Details……...162
8.3 Results and discussion……..… 164
8.3.1. Fabrication of CsPbBr3 micropatterns……...…….…… 164
8.3.2. Optical gains of CsPbBr3 QD film……..…..… 167
8.3.3. Optical properties and lasing behavior of microdisks…… 169
8.3.4. Dual color pixel arrays…… 172
8.4 Conclusions……175
8.5 Chapter acknowledgements……..… 177
8.6 References (Chapter 8)…….……177

9 SPECTRAL AND DIRECTIONAL PROPERTIES OF NOTCHED AND ELLIPTICAL QUANTUM-DOT MICROLASERS…..……..…….. 181

9.1 Introduction……..…… 181
9.2 Experimental Details……...……183
9.3 Results and discussion……..… 184
9.3.1 Spectral properties of notched microdisk lasers…… 184
9.3.2 Spectral properties of elliptical microdisk lasers…… 186
9.3.3 Directional emission of elliptical microdisk lasers…….. 190
9.4 Conclusions……..….192
9.5 Chapter acknowledgements……..…194
9.6 References (Chapter 9)…….……..…194

10 COALESCENCE OF PARASITIC MODES AT AN EXCEPTIONAL POINT IN COUPLED MICRODISK LASERS……196

10.1 Introduction……..……... 196
10.2 Experimental Details……...……198
10.3 Results and discussion……..…… 200
10.3.1 Lasing properties of single disks……..…… 200
10.3.2 Lasing properties of coupled-disk pairs……... 202
10.3.3 Spatial gain variation…….. 206
10.3.4 Intra-cavity mode coalescence…… 208
10.4 Conclusions……..……211
10.5 Chapter acknowledgements……..……212
10.6 References (Chapter 10)…….……..…… 212

11 GENERAL CONCLUSIONS AND BROADER IMPACT……..…… 215

11.1 General conclusions and discussion……215
11.2 Significance and broader impact……..…… 220
11.3 General acknowledgements……..……226
11.4 Dissemination of work…… 227
11.4.1 Publications……..…… 227
11.4.2 Presentations……..……228
11.5 References (Chapter 11)……229

APPENDICES

Appendix A (Chapter 5 supporting data)……..……..230
Appendix B (Chapter 6 supporting data)……..……..248
Appendix C (Chapter 7 supporting data)……..……..261
Appendix D (Chapter 8 supporting data)……..……..269
Appendix E (Chapter 10 supporting data)…….……..…….. 274

VITA……281

LIST OF TABLES

Table 4.1: The optical properties of conventional CdSe/ZnS QDs and CdSe/$Cd_{1-x}Zn_xSe_{1-y}S_y$/ZnS QDs.....87

Table A.1: Table of the optical properties of the QDs before and after the ligand exchange process. A reduction in quantum yield typically occurs after ligand exchange. The reduction in QY is likely due to a decrease in the passivation of surface bonds that can occur when oleic acid is removed and replaced with the amine ligands. The absorbance and emission profiles are similar before and after the ligand exchange procedure.....230

Table A.2: Table of the predicted stimulated emission lifetime of the ligand-QD films based on the measured refractive index and optical gain values of the QD films. The predicated stimulated emission lifetime was calculated using Eq A.2.....231

Table A.3: Table of the QD-loading (%) of the QD films, the QD volume fraction (%) of the QD solutions (determined by ellipsometry and TGA, respectively), and the thermodynamic properties of each ligand.....232

Table B.1: Thermodynamic properties and refractive index of ligands used in this study. Large differences in thermodynamic properties between BA and DIAH leads to a plausible different behavior when they are capped on the QD surface. BA has a free-state melting point (-49 ℃) significantly lower than room temperature, likely causing BA to be in a fluid-like state at room temperature even when bound on the QD surface. Furthermore, BA has a high vapor pressure (68 mmHg at 20℃) which indicates that BA experiences desorption upon exposure to air. On the other hand, DIAH has a much higher melting point (26-29℃) and lower vapor pressure (<1 mmHg at 25℃) than BA, yielding a more solid, physically stable QD film under ambient conditions.....248

Table B.2: The refractive indices of QD films. The QD-loading was calculated using the effective medium Bruggeman model.....248

Table B.3: The FTIR results showing the ratios of peak areas for different vibrational modes. Both ratios of asymmetric and symmetric (CH_3/CH_2) peak areas decreased dramatically

during the crosslinking process, indicating that a substantial amount of butylamine was replaced with 1,7 diaminoheptane…….249

Table B.4: The optical properties of the OA and BA capped QDs that are dispersed in chloroform……..249

LIST OF EQUATIONS

Equation 1.1: Radius dependent band gap energy of a QD using the approximation of particle-in-a-sphere model……..…….10

Equation 1.2: Equation of built up time of stimulated emission that include several variables, where "τ_{SE}" is the stimulated emission build up time, "c" is the speed of light, "G" is the gain value, "nr" is the effective refractive index, "V_{dot}" is the volume of QD, "ξ" is the QD packing fraction, and "σ_g" is the gain cross-section……..19

Equation 1.3: Equation of resonant modes inside the WGM photonic cavity, where m is the angular mode number, λ is the wavelength of the light and L is the circumference of the microcavity and n_{eff} is the effective refractive index of the medium……30

Equation 10.1: Equation of coupled differential equations considering the modal distribution of the coupled pair……204

Equation 10.2: Equation of eigenvalues that are derived from Equation 10.1……..205

Equation 10.3: Equation of Hamiltonian that describes the eigenvalue problem……..209

Equation A.1: Equation outlining the various factors that influence the optical gain magnitude in QD films……..246

Equation A.2: Equation outlining the various factors that influences the stimulated emission lifetime in QD films. ……..246

LIST OF FIGURES

Figure 1.1: (a) TEM images of QDs consist of different materials. QDs can be synthesized to have simple (core) or complex core/shell architectures. (b) Schematic of a core/multishell QD (top). Schematics of different energy level alignments: type-I (bottom left), quasi type-II (bottom center), and type-II (bottom right) core/shell QDs.……3

Figure 1.2: (a) On-time histograms of Qdot655ITK (reference QDs) (left) and g-NQD CdSe/19CdS (right). Insets show the PL time traces of individual Qdot655ITK and g-NQD CdSe/19CdS, respectively. (b) PL time trace (middle) and on- and off-time histogram (right) of a single CdSe–CdS core–shell QD (left) with a CdSe core radius of 2.2 nm and a shell thickness of 2.4 nm. (c) Photoluminescence time trace (middle) and on-time histogram (left) of a single SQW QD (left) with a CdS core radius of 1.3 nm, a CdSe shell thickness of 0.9 nm and a CdS shell thickness of 5.2 nm..……5

Figure 1.3: (a) PL spectrum of MAPbBr3 QD solution. Inset shows MAPbBr3 QD solution under UV lamp. (b) Image of CsPbX3 QD solutions under UV lamp (top). PL spectra of QD solutions with different composition (bottom). (c) Absorption and PL spectra of FAPbBr3 QDs (left). PL spectra of FAPbBr3 QDs of different size (right)…..……7

Figure 1.4: ((a) Schematic outlining the anion exchange process of CsPbX3 QDs using different routes and precursors. (b) PL evolution of CsPbCl3 and CsPbI3 QDs by using different precursors including OLAM-X, ODA-X, TBA-Cl and PbX2 (from top to bottom)……..……..…8

Figure 1.5: (a) Schematic showing how the quantum confinement effect change the bandgap compared with bulk material (b) Tuning of absorption and emission peak position via size variation of CdSe QDs……..……9

Figure 1.6: (a)Jablonski Energy diagram describing different radiative and non-radiative pathways (b) Multiple exciton generation process (c) Electronic transitions that lead to generation of single exciton and biexciton……..11

Figure 1.7: (a) Schematic showing the relaxation of translational momentum conservation makes Auger recombination efficient in QDs (bottom) while the Auger recombination is less efficient in bulk material (b) Volume scaling law of Auger recombination lifetime of CdSe QDs (left) and different materials (right) (c) Transient absorption spectra for (left) traditional CdSe/ZnS QD and (right) CdSe/CdS giant QD……...13

Figure 1.8: (a) PL (solid) and absorption (dashed) spectra of CdSe/CdS (C/S) (black) and CdSe/alloyed shell/CdS QD film. (b) Biexciton dynamics measured from single CdSe/CdS (C/S) (black) and CdSe/alloyed shell/CdS QDs. (c) Radial distributions of electron and hole charge densities in type-II CdS/ZnSe QD. (d) Schematic showing the competition between stimulated emission and absorption where X-X coulomb interaction determines the transient stark shift ($\Delta_S=\Delta_{XX}$)……...14

Figure 1.9: (a) Schematic showing the state-filling, band-edge states and quasi-Fermi level splitting of CdSe QD under hydrostatic and biaxial. (b) Synthetic steps of selective-facet epitaxy growth. (c) Schematic of layered structure of PC-DFB cavity laser (left). Normalized integrated emission intensity versus pumping power (right). Inset shows the spectrum above threshold. ……....16

Figure 1.10: (a) Schematic showing the set up of VSL method (b) lasing threshold behavior of QDs with different color (red, green, blue) (c) emission spectra at different pumping fluences……20

Figure 1.11: Schematic of fabrication process (top) and QD patterns (bottom) by using (a) electrohydrodynamic printing (b) PDMS transfer printing (c) electron beam lithography……23

Figure 1.12: Schematic outlining the proposed physical evolution of each type of QD (CdSe core, CdSe/ZnS core/shell, or CdSe/$Cd_{1-x}Zn_xSe_{1-y}S_y$ core/graded shell) under light exposure in air over a period of 45 minutes (organic ligand not shown for clarity)……..…...24

Figure 1.13: Examination of the photoluminescence stability of QD-PMMA films with different types of QD design (CdSe core, CdSe/ZnS core/shell, or CdSe/$Cd_{1-x}Zn_xSe_{1-y}S_y$ core/graded shell). (a) 3D and (b) 2D representation of PL intensity and (c) spectral peak position under continuous light exposure (blue light: 450-490nm, 24-28mW). The ribbons represent a standard deviation range for the emission evolution of the QDs in darkness…..25

Figure 1.14: (a) Schematic of the general photopatterning process to fabricate negative and positive photopatterns. Photluminescence images of (b) an unpatterned green QD-polymer film, (c) a negative photopattern, and (d) a positive photopattern……...27

Figure 1.15: (a) Photoluminescence image of a multicolor photopattern in a QD-polymer film composed of red and green QDs. Hyperspectral scans of the (b) red and green channels, (c) red channel, and (d) green channel……28

Figure 1.16: Four common types of photonic cavity depending on confinement mechanism (a) Fabry–Perot microcavities (b) whispering gallery mode microcavities (c) distributed feedback (DFB) microcavities. (d) photonic crystal defect microcavities……...29

Figure 1.17: (a) Microsphere. (b) Microring. (c) Microdisk. (d) Microtoroid. (e) Optical fiber. (f) Microcapillary. (g) Microbottle. (h) Microbubble. (i) Hemisphere……31

Figure 1.18: (a) Optical microscopy image of fabricated silica microsphere with a diameter of ~30 μm. Scale bar is 30 μm. (b) Evolution of laser emission near the lasing threshold. (c) Lasing spectra of silica microsphere coated with CdSe/CdS nanorods pumped under an infrared laser with varying power……..32

Figure 1.19: (a) Fluorescence image of 20 μm silica microspheres coated with CdSe/CdZnS titania composite film. Insets show 30 μm silica microspheres coated with blue (top) and red (bottom) CdSe/CdZnS titania composite film. Scale bar of insets are 15 μm. (b) Fluorescence images of 20 μm silica microspheres coated with CdS/ZnS silica composite film under white (top left) and UV (top right) light illumination, respectively. Lasing spectra under different pumping fluences (bottom)……33

Figure 1.20: Normalized integrated emission intensity versus different pump fluences (left). Schematic showing the microcapillary tube integrated with QDs that demonstrates WG mode……34

Figure 1.21: (a) Schematic showing the fabrication process of self-assembled hemispheres by using a cylindrical tip coated with a hydrophobic layer. (b) Lasing spectra of a hemisphere microlaser coated with QDs under different pulse energy. Left inset shows the PL intensity versus the pulse energy where a non-linear behavior was observed. Right inset shows a single self-assembled hemisphere coated with QDs that is on top of a DBR substrate. (c)

optical microscopy image of the actual self-assembled hemisphere coated with QDs. (d) PL image of self-assembled hemisphere coated with QDs above lasing threshold……..35

Figure 1.22: (a) Schematic showing how the QD-PMMA microbubble was formed during the bubbling process Lasing spectra of microbubbles mixed with red (b) and green (c) QDs under different pulse energies. Right insets show the PL intensity versus the pulse energy. Left insets show the PL image of the corresponding red and green QD-PMMA microbubbles……37

Figure 1.23: (a) Schematic illustrating how ink-jet printing can be used to fabricate quasitoroid microlasers from self-assembled CdZnS/ZnS QDs on top of a DBR substrate. (b) Optical microscopy image of arrays of fabricated quasitoroid structures. (c) SEM image of single quasitoroid structure. (d) Zoom-in SEM image of the rim form the quasitoroid structure……..……..38

Figure 1.24: (a) Schematic showing the fabrication process of the SiN/QD/SiN microdisk laser. (b) Optical microscopy image of an array of SiN/QD/SiN microdisks. (top). SEM image of a SiN/QD/SiN microdisk and waveguide (middle). Falsed-color SEM image of cross section of microdisk and waveguide (bottom). (c) Lasing spectra of SiN/QD/SiN microdisk lasers under different pumping fluences where P_{th} is the pumping threshold. Insets show the PL images of SiN/QD/SiN microdisk lasers pumped under pulsed laser. (d) Integrated PL intensity versus pump fluence where a non-linear behavior was observed. Inset shows the relationship of **i**ntegrated PL intensity versus pump fluence at different wavelengths……40

Figure 1.25: Schematic showing representative example (coupled waveguides) obeying parity-time symmetry where Re[n] and Im[n] are the real and imaginary parts of the refractive index variation n……..42

Figure 1.26: (a) Lasing spectra of single mciroring (top), coupled microrings that are both pumped (middle), coupled microrings (bottom) with only one being pumped. (b) Diagram of coupled optical PT resonators(top), lasing spectra showing the PT induced revival of Raman lasing with increasing losses (bottom)……43

Figure 1.27: Transverse intensity distribution at the point of closest proximity between two cavities……..44

Figure 1.28: (a) Schematics illustrating CPA laser, where the gain/loss modulation is introduced by placing periodic loss structures on gain waveguide. The periodicity is designed to be half of the effective wavelength of guided light (left). The spectra of output coefficient Θ demonstrating amplification peak of 15 dB while the anti-lasing mode induced absorption down to -15 dB at around 1556nm……...45

Figure 2.1. Research tasks at different hierarchical levels that are investigated and developed to understand fundamental light-matter interactions at each level of QD photonic sources from individual and assembled nanostructures to individual and coupled optical QD cavities.……..……..58

Figure 4.1: The energy level alignment for (a) CdSe/ZnS QDs, and (b) CdSe/$Cd_{1-x}Zn_xSe_{1-y}S_y$/ZnS QDs.……84

Figure 4.2: TEM images of (a) plain CdSe QDs as core (green-emitting; *D* = 2.3 nm), (b) CdSe/$Cd_{1-x}Zn_xSe_{1-y}S_y$ QDs (*D* = 4.4 nm), (c) CdSe/$Cd_{1-x}Zn_xSe_{1-y}S_y$/ZnS QDs (*D* = 6.0 nm), and (d) CdSe/$Cd_{1-x}Zn_xSe_{1-y}S_y$/ZnS QDs (*D* = 8.4 nm). All chemical composition gradient QDs were synthesized using 2.3-nm green-emitting CdSe QDs as seeds at 250 °C……..85

Figure 4.3: The absorption and emission spectra of (a) CdSe/ZnS QDs and (b) CdSe/$Cd_{1-x}Zn_xSe_{1-y}S_y$/ZnS QDs, in which the diameter of originally green-emitting CdSe QD core, *D* is 2.3 nm. All CdSe/ZnS, CdSe/$Cd_{1-x}Zn_xSe_{1-y}S_y$, and CdSe/$Cd_{1-x}Zn_xSe_{1-y}S_y$/ZnS QDs were grown from green-emitting CdSe QD at 250 °C.……87

Figure 4.4: Absorption and photoluminescence spectra of green-, orange-, and red-emitting CdSe/$Cd_{1-x}Zn_xSe_{1-y}S_y$/ZnS QDs synthesized by employing green-emitting CdSe QD (*D* = 2.3 nm), green-emitting CdSe QD (*D* = 2.5 nm), and red-emitting CdSe QD (*D* = 4.1 nm) as seeds.……89

Figure 4.5: High-resolution TEM images of (a) green-, (b) orange-, and (c) red-emitting CdSe/$Cd_{1-x}Zn_xSe_{1-y}S_y$/ZnS QDs prepared by capitalizing on green-emitting CdSe QD (*D* = 2.3 nm), green-emitting CdSe QD (*D* = 2.5 nm), and red-emitting CdSe QD (*D* = 4.1 nm) as seeds. The scale bar in inset is 10 nm……90

Figure 4.6: Dynamics of photobleaching of red-emitting CdSe core QDs (*D* = 4.1 nm), red-emitting CdSe/$Cd_{1-x}Zn_xSe_{1-y}S_y$/ZnS QDs (*D* = 8.1 nm), orange-emitting CdSe/$Cd_{1-x}Zn_xSe_{1-y}S_y$/ZnS QDs (*D* = 8.5 nm), and green-emitting CdSe/$Cd_{1-x}Zn_xSe_{1-y}S_y$/ZnS QDs (*D* = 8.4 nm)……91

Figure 5.1: The QDs show broadband absorption and narrowband emission (a). Ligands of different size (b) were used to stabilize the QDs in order to control the spacing between adjacent QDs when deposited into film (c). The QD-QD spacing dictates the maximum QD-packing density……99

Figure 5.2: AFM surface morphology (column 1), 3D topography projection (column 2), topographical cross-section (column 3), and phase (column 4) for (a) oleic acid, (b) hexadecylamine, (c) octylamine, and (d) butylamine capped QD films. Z-scale is 20 nm for the oleic-QD film scan and 10 nm for all others. Phase scale is 20° for the oleic-QD film scan and 10° for all others……100

Figure 5.3: Four ligands of different size were used to examine how QD-packing is affected by ligand size. (a) HR-TEM micrographs of drop-cast QD solutions and (b) ellipsometry characterization of spin-cast QD films show that reducing the size of the ligand increases the QD-loading (packing density) of QDs in films. Scale bar is 20 nm for all TEM micrographs……..….103

Figure 5.4: ASE in the QD films is identified by multiple characteristics of QD emission as the QD film is pumped with different excitation powers. (a) Emission intensity (log-log, scaled for clarity) showing threshold behavior, and (b) full-width at half-maximum (FWHM) of the emission peak showing spectral narrowing……..104

Figure 5.5: The optical characteristics of the QD films were determined using the variable strip length (VSL) method. (a) Emission of an OctA-QD film (log-intensity) at various pump strip lengths. The emergence of ASE is indicated by narrowing of the emission peak. (b) Emission intensity versus pump length for various QD-ligands (curves were off-set for clarity). The intensity data was fit to determine the gain value (I_{pump} = 200 uJ/cm^2)…….107

Figure 5.6: The magnitude and stability of optical gain depends on the type of QD-ligand pairing. (a) Optical gain versus QD-packing density. QD films with higher QD-packing exhibit higher optical gains. (b) Stability of ASE over a 30 minute period……...108

Figure 5.7: (a) Typical emission spectra from the variable attenuation length method for a HDA-QD film (log intensity). (b) Optical loss fitting for the HDA-QD, OctA-QD, and BA-QD films shows an exponential decrease with collection length. (c) Optical loss for different QD-ligand films……113

Figure 6.1: (a) Crosslinked QD solid film fabrication: the as-synthesized oleic acid (OA)-capped CdSe/$Cd_{1-x}Zn_xSe_{1-y}S_y$ core/alloyed-shell QDs (i) undergo the solution-phase ligand exchange by adding butylamine (BA) in the QD solution (ii); after the solution-phase ligand exchange, the concentrated BA-capped QD solution is cast to form a close-packed QD film, which is subsequently soaked in a 0.1 M methanol solution of 1,7 diaminoheptane (DIAH) to perform the solid-state ligand exchange. The crosslinked QDs are tethered with DIAH ligand and shows tight packing (HRTEM scale bar is 10 nm) (iii). (b) Absorbance (solid) and emission (dashed) spectra of as-synthesized OA-capped QD solution (black line), BA-capped QD film (blue line) and DIAH-tethered QD film (red line). The baselines (green solid lines) of BA-capped QD film and DIAH-tethered QD film are offset for clarity. (c) Molecular models and chemical formulas of the organic ligands used in this study: oleic acid (OA); butylamine (BA), and 1,7 diaminoheptane (DIAH)……..126

Figure 6.2: AFM scans of height (a), phase (b), and (c) height cross-section along the line in (a) for the DIAH-tethered QD film. The height scale is 10 nm and the phase scale is 80 degrees. Fluorescence imaging shows uniform emission over large areas (d) while bright field (e) and dark field (f) optical micrographs show uniform morphology with minimal physical defects. All scale bars are 30 μm. ……128

Figure 6.3: The optical characteristics of the DIAH-tethered QD film under pulsed excitation (440 nm, 5 ns pulse): (a) emission spectra from the DIAH-tethered QD film under different pumping energy density show the ASE and spectral narrowing (inset); (b) emission vs fluence behavior with a ASE threshold of ~60 μJ/cm^2; (c) the VSL measurement shows an exponential increase in ASE intensity with longer pump strip lengths (pumped fluence of 500 μJ/cm^2). Fitting the VSL curve yields a net gain value of 650 cm^{-1}. (d) ASE stability tests of DIAH-tethered QD films pumped with 500 μJ/cm^2 over 45 minutes of excitation. (e) CW PL stability tests of the DIAH-tethered QD film, BA-capped QD film, and OA-capped QD film

under ambient conditions. (f) Comparison of gain values observed in this study and in recent literature. ……130

Figure 7.1: Schematic outlining the hybrid top-down/bottom-up approach using a pattern-assisted LbL assembly of QDs that used to fabricate the QD microdisks. ……145

Figure 7.2: Left: Optical micrograph of a substrate under UV illumination with an array of microdisks (diameter of 52.1 μm). Right: bright field image of a microdisk array at higher magnification. ……146

Figure 7.3: Bright field (a) and PL (b) imaging of QD microdisks with diameters of 10.6, 26.0, 41.6 and 52.1 μm. (c) Bright field image (left panel) and PL image (right panel) of a 3x3 disk array (52.1 μm in diameter). (d) SEM of a microdisk (inset: side wall). ……...147

Figure 7.4: From left to right: AFM topographical images (top-view), 3D projection, and height cross-section profiles of QD microdisks with diameters of (a) 10.6 μm, (b) 26.0 μm, (c) 41.6 μm, and (d) 52.1 μm, respectively. ……...148

Figure 7.5: (a) 2D (b) 3D representations of lasing spectra of QD microdisk (diameter of 26.0 μm) under varying pump fluence (F_{th} is ~29 μJ/cm^2). Baselines of the 2D lasing spectra are offset for clarity. ……149

Figure 7.6: (a) PL emission vs excitation fluence of a QD microdisk. The threshold pump fluence, F_{th} is determined from the interception of the linear and superlinear behaviors. (b) PL emission images of the QD microdisk (diameter of 26.0 μm) below (left) and above (right) lasing threshold. The scale bar is 5 μm for both images. ……..150

Figure 7.7: Lasing spectra of QD microdisks with diameter of 10.6 μm (red), 26.0 μm (orange), 41.6 μm (green) and 52.1 μm (blue). Δλ is the average mode spacing between the observed longitudinal cavity modes. ……151

Figure 7.8: (a) Mode spacing of cavity modes as a function of reciprocal optical path length. (b) Microdisk quality factor as a function of disk diameter. ……...152

Figure 7.9: Power Fourier transform of lasing spectra from micodisks with diameters of (a) 10.6 μm, (b) 26.0 μm, (c) 41.6 μm, (d) 52.1 μm ($\Delta l = n\pi D$). ……..153

Figure 8.1: (a) Absorbance and fluorescent emission of $CsPbBr_3$ QDs in hexane. (b) Schematic of solvent constraint of $CsPbBr_3$ QDs……165

Figure 8.2: Schematic that outlines orthogonal lithography approach for fabricating $CsPbBr_3$ QD patterns via the insertion of fluorinated polymer layer and standard photolithography..166

Figure 8.3: (a) Left panel: Optical micrograph of a substrate under UV illumination with arrays of different QD patterns. Right panel: fluorescent images of QD arrays of different patterns at the corresponding positions. All scale bars are 200 μm. Bright field (b) and fluorescent (c) images of different individual elements. ……..167

Figure 8.4: (a) Emission intensity vs excitation fluence response of CsPbBr3 QD film with ASE threshold as noted. (b) Emission spectra of QD film at various stripe lengths. (c) The optical gain spectra and (d) fitted optical gain values at 534 nm for as-prepared $CsPbBr_3$ QD film at various pump fluences. (e) The optical gain spectra and (f) optical gain values at 534 nm of $CsPbBr_3$ QD film after immersion into fluorinated stripper for an hour at various fluences. ……168

Figure 8.5: (a) Bright field (top) and fluorescent (bottom) images of QD microdisks with diameters of 11.7, 21.8, 26.7, 31.8, 41.6 and 52.2 μm. All scale bars are 5 μm (b) From left to right: AFM topographical image (top-view), height profiles, and 3D image of QD microdisk with diameter of 31.8 μm. ……...170

Figure 8.6: (a) Emission intensity vs. excitation fluence measured from a $CsPbBr_3$ QD microdisk. The threshold intensity, F_{th} is determined from the interception of the linear and superlinear responses. Inset: PL images of QDs microdisk (D = 26.7 μm) below (left) and above (right) lasing threshold. The scale bar is 10 μm for both images. (b) Lasing spectra of QD microdisks with D = 11.7 μm, 21.8 μm, 26.7 μm, 31.8 μm, 41.6 μm and 52.2 μm, respectively. Δλ is the average 'mode spacing' of the observed longitudinal cavity modes.170

Figure 8.7 (a) The mode spacing, $\Delta\lambda$ of the WG modes in QD micridisk lasers with various diameter, *D* vs. the reciprocal geometrical path length, $1/\pi D$. The group index, n is calculated from the relation: $\Delta\lambda = \lambda^2/n\pi D$. (b) The plot of mode number versus the disk size……...171

Figure 8.8: Schematic that outlines the orthogonal lithography approach that is used multiple times for fabricating dual-color patterns of QDs. ……173

Figure 8.9: (a) Fluorescent image of an array of $CsPbBr_3$ microdisks. (b) Fluorescent image of the binary array of $CsPbBr_3$ QDs (green) and $CdSe/Cd_{1-x}Zn_xSe_{1-y}S_y$ QDs (red) microdisks and corresponding high-resolution fluorescent image (c). (d) Spatial distribution of PL intensity for ~11.7 μm individual green and red QD microdisks. (e) Fluorescent image shows the preliminary result of RGB arrays of red, green and blue QD patterns using our approach. ……...175

Figure 9.1: Emission spectrum from a microdisk laser with uniform circumferential edge (a) and one with unintended defects that result from the fabrication process (b). The inset in each figure shows the florescent image obtained at the same intensity at which the spectrum was measured. ……184

Figure 9.2: Emission spectrum from a microdisk laser with an intentional 'notch' defect of circumferential width, w = 0.5μm and radial depth, d = 2μm (a), and another one with dimensions of w = 2μm and d = 2μm (b). The inset in each figure shows the florescent image obtained at the same intensity at which the spectrum was measured. ……...185

Figure 9.3: Total emissive power measured as a function of the azimuthal angle for the microdisk of Fig. 3a (a), for the microdisk of Fig 3b (b), and for that of Fig 4b (c). (d) Spectra recorded from microdisk shown in (c) at the angular positions of 60° and 240° as indicated. ……...186

Figure 9.4: (a) Spectral of ellipse microdisk with aspect ratio of 0.68. (b) The mode splitting wavelength of each peaks. ……187

Figure 9.5: (a) Laser emission spectrum from an elliptical micro-cavity with the ratio of short axis to long axis, ρ=0.8. The inset shows the fluorescent image of the laser measured above threshold. (b) Power Fast Fourier Transform (FFT) of a resonator with ρ = 1 (red) compared

to that of the spectrum shown in (a) (blue). (c) The ratio of the first to the second harmonic of the FFT for different elliptical microcavities with different values of ρ. (d) The extracted primary optical path length from resonators of different ρ. The various symbols represent different microcavities measured for each value of ρ. The line through the data points is the expected path length based on the perimeter of each ellipse taking a constant n_{eff} = 2…...188

Figure 9.6: (a) Simulation of the EM field in several elliptical micro-cavities with (a) ρ=0.80, (b) ρ=0.68, and (c) ρ=0.92. ……190

Figure 9.7: (a) Collection-angle dependence of the laser emission with fluorescent image at the center for an elliptical cavity with (a) ρ=0.8 and (b) ρ=0.68. ……...190

Figure 9.8: (a) Collection-angle dependence of the laser emission from a pair of elliptical cavities (ρ=0.68) with H-type coupling and fluorescent image to the right. (b) Same as in (a) but the two ellipses have J-type coupling. ……...192

Figure 10.1: (a) Emission from a microdisk pumped at various intensities: 16μJ/cm^2 (black), 29μJ/cm^2 (red), 66μJ/cm^2 (blue), 116μJ/cm^2 (green). Inset shows the FFT of the 116μJ/cm^2 ploted vs. the optical path length $n_{eff}\pi D$ where n_{eff}=1.85 is the effective mode index and $D = 25\mu m$. (b) Collection-angle dependence of the spectrally integrated emissive power in the plane of the disk with fluorescent image at the center. (c) Emission spectrum from a different microdisk of the same diameter pumped at 116μJ/cm^2. The shaded regions indicate Lorentzian fits to the data. (d) Collection-angle dependence of the spectrally integrated emissive power in the plane of the disk in with fluorescent image at the center. The peaks in the data are positioned diametrically from the visible bright spots seen image. ……201

Figure 10.2: (a-c) Emission from a coupled microdisk pair pumped at various intensities where the pair is placed at different locations in the pump beam spot, such that only the left or right disk is pumped (a,c) or the pair is pumped evenly (b), as illustrated schematically. (d-f) Emission spectra from three different microdisk pairs at 116μJ/cm^2. In each figure the spectrum from the left (red), right (green) and center (blue) pump configurations is shown. ……203

Figure 10.3: (a) Emission spectra from a coupled microdisk pair as the pair is shifted through different locations relative to the pump beam spot, as illustrated schematically to the

left of each spectrum. The corresponding fluorescent images are shown to the right of each spectrum. (b) False-color contour plot of the emission intensity vs emission wavelength and the relative distance between the center of the pair to the center of the beam spot, ΔD_p…207

Figure 10.4: (a) E False-color contour plot of the emission intensity vs emission wavelength and ΔD_p. (b) Magnified view of the region inside the box in (a). (c) Peak positions, λ_c, vs ΔD_p for the region in (b), showing the mode coalescence. ……...208

Figure 10.5: Calculated difference in eigenvalues from their uncoupled values of modes 1,2, of disk A and mode 3 of disk B vs. the gain differential between disk A and B Δg_{AB} for parameters comparable to the experiment and (b) for general values of the intradisk mode coupling κ, and inter-disk coupling γ_{13} and γ_{13}, in the limit $\gamma_{13} \ll \gamma_{23}$. ……...210

Figure A.1: NMR was used to evaluate the effect of washing the ODE/oleic acid capped QDs before the ligand exchange. (a) NMR of oleic acid. (b) NMR of oleic acid capped QDs at different points during the washing process. Examination of the 4.7-6 ppm regions shows (c) that the ODE peaks disappear and that the peak near 5.35 ppm assigned to vinylic hydrogens broadens, indicating removal of excess free oleic acid. (d) Close-up of the 2.5-0 ppm region shows broadening of the 1.6, 2.0, and 2.3 ppm peaks after successive washing. ……233

Figure A.2: NMR was used to evaluate the efficiency of the ligand exchange. (a) NMR of butylamine (the ligand that will be displacing oleic acid on the QD surface). (b) NMR of butylamine and of QDs that underwent a ligand exchange from oleic acid to butylamine. The BA peak at 2.8 ppm (hydrogen peak) shifts to 3.2 ppm which is likely due to interaction with QD surface. (c) Comparison of NMR from different points in the washing process and ligand exchange process. ……..234

Figure A.3: Bright field (column 1), dark field (column 2), and fluorescence (column 3) images of (a) oleic acid, (b) hexadecylamine, (c) octylamine, and (d) butylamine capped QD films. Imaging shows that the films exhibit similar uniform morphology and fluorescence emission as well as some scattering due to surface defects. All scale bars are 30 um……235

Figure A.4: Plot of the predicted free volume of each QD ligand and the corresponding maximum theoretical FCC QD-packing density (assuming diameter of 8 nm). Reducing the

size of the ligand leads to a larger maximum FCC packing for the QDs in the film (and vice versa). ……236

Figure A.5: Examination of the QD fraction in solutions and how it compares to QD films. (a) Thermogravimetric analysis (TGA) of QD solutions. (b) The difference in QD volume fraction between QD films and the QD solutions. The (c) vapor pressure and (d) boiling point of each ligand. Note, the vapor pressure of oleic acid and hexadecylamine area very low at room temperature (< 1 mmHg) and therefore were approximated to have a zero value…..237

Figure A.6: ASE threshold plots and fitting for different QD-ligand combinations. The threshold value of the QD film is determined by linear fitting of the shallow and steep pump fluence versus emission curve. The pump fluence value at the intersection of the linear fit from the two regions is the threshold fluence. Examples of threshold determination are shown for (a) oleic acid-QD, (b) HDA-QD, (c) OctA-QD, and (d) BA-QD films……..239

Figure A.7: ASE threshold plots for different QD-ligand combinations from multiple spots. The threshold behavior of the QD films was determined by examining how the pump fluence affects the emission intensity. A transition from a shallow slope to a steep slope indicates an ASE threshold. The threshold behavior for each type of QD film was verified over multiple trials. Examples of threshold examination are shown for (a) oleic acid-QD, (b) HDA-QD, (c) OctA-QD, and (d) BA-QD films. ……240

Figure A.8: Peak position of the maximum emission peak versus pump strip length. The presence of ASE is supported by examining a number of parameters including a shift of the ASE peak with respect to the PL peak. Typically the ASE peak red-shifts compared to the PL peak due to reabsorption of the emitted light by the film. All the QD films with amine functionalization in this study exhibited a red-shift of approximately 10-15 nm compared to the PL peak, while the oleic-QD film show a red-shift of only 4 nm, indicating a smaller amount of reabsorption during light propagation. ……...241

Figure A.9: Data of the emission intensity versus pump strip length from the variable stripe length (VSL) method for various QD-ligand combinations. The optical gain of the QD films was determined by fitting data from the VSL method with an exponential function. The gain value for each type of QD film was determined by averaging over multiple trials. Examples of VSL data and fitting are shown for (a) HDA-QD, (b) OctA-QD, and (c) BA-QD films……242

Figure A.10: (a) Plot of the confinement factor (Ex, TE 0% mode) at 635 nm for films of different thickness and different refractive index. The relative confinement factor of each film compared to (b) the HDA-QD film and compared to (c) the oleic-QD film. The confinement factor is higher (for a given film thickness) for films with a higher refractive index. The grey shaded areas represent typical QD film thicknesses in this study.. ……..243

Figure A.11: Plot of the critical thickness for the primary waveguiding mode for QD films with different refractive index on a CYTOP film (refractive index of 1.34). The critical thickness indicates the minimum thickness a film requires in order to support at least one waveguide mode. The function used to calculate the critical film thickness (t_c) assumes that the top layer is air. Each film has a thickness that allows for only one waveguide mode……..244

Figure A.12: Plots of optical loss data and fitting for various QD-ligand combinations. The optical loss of the QD films was examined by altering the distance the emission travels through the QD film before reaching the edge of the film. The optical loss value is determined by fitting the data with an exponential decay function. The loss value for each type of QD film was determined by averaging over multiple trials. Examples of loss data and fitting are shown for (a) oleic acid-QD, (b) HDA-QD, (c) OctA-QD, and (d) BA-QD films….245

Figure B.1: The crosslinking process provides chemical resistance to both polar (methanol) and nonpolar solvent (toluene/heptane). (a) QD films capped with commonly used ligands such as oleic acid and butylamine would be dissolved after washing with toluene three times (a). The sample shown here is the QD film capped with oleic acid. (b) Crosslinked QD films maintain their photoluminescence after multiple washes with toluene and methanol……...250

Figure B.2: High-resolution transmission electron microscopy (HR-TEM) images of QDs that are capped with (a) oleic acid, (b) butylamine, and (c) 1,7 diaminoheptane. All scale bars are 10 nm. ……251

Figure B.3: AFM and optical microscopy images (500nm x 500nm) of the BA-capped QD film: AFM scans of (a) height, (b) phase, and (c) height cross-section for the BA-capped capped QD film. Fluorescence imaging shows uniform emission of large areas (d), while bright field (e) and dark field (f) optical micrographs show uniform morphology with minimal

physical defects. All scale bars are 30μm. Large area AFM images (10μm x 10μm) of the DIAH-tethered and BA-capped QD film: AFM scans of (g) height, (h) phase for the DIAH-tethered QD film and (i) height, (j) phase for the BA-capped QD film. ……252

Figure B.4: DSC of the DIAH crosslinked QD films with a glass transition near 97°C (inset). ……253

Figure B.5: (a) FTIR spectra from 2500 cm^{-1} to 3500 cm^{-1} for crosslinked DIAH QD film (red line) and BA capped QD film (black line). The C-H stretching band (blue frame) shows the decreased CH_3 asymmetric and symmetric stretching peaks during the solid-exchange ligand exchange process while the N-H stretching band (green frame) remains similar. (b) Magnification of the N-H stretching band region. The assigned peaks are symmetric N-H stretching at 3324 cm^{-1} and shoulder band at 3133 cm^{-1}, respectively. (c) Magnification of the C-H stretching band. The assigned peaks are asymmetric and symmetric CH_3 stretching peaks at 2958 cm^{-1} and 2873 cm^{-1}, asymmetric and symmetric CH_2 stretching peaks at 2925 cm^{-1} and 2854 cm^{-1} and C-C-H peak at 2898 cm^{-1}, respectively. ……..254

Figure B.6: Transient absorption dynamic at 630 nm for a CdSe/Cd1-xZnxSe1-ySy QD film. The positive sign of the signal indicates that this feature is due to photo-bleaching (PB) of the ground state absorption. The dynamics are adequately described by a bi-exponential fitting, with two distinct lifetimes of 36 ps and 3.5 ns. The amplitudes associated with these decay times are 0.2 and 0.8 respectively. The complex decay mechanisms possibly include surface trapping, Auger recombination, and radiative recombination as well as possible overlap with the PB due to biexcitons. The data indicates that a substantial fraction of the exciton population survives on the time scale of several ns. For QD's of this size, 36 ps is much shorter than expected for Auger decay and is possibly related to other processes…255

Figure B.7: Optical gain measurements of the crosslinked QD films from the VSL method. An average gain value for the DIAH crosslinked QD films was obtained by examining multiple spots over multiple substrates. Typically, these values exhibited similar net gain values (a). The presence of optical gain was also confirmed from observing threshold behavior in input power-output power plots. These data were also collected from multiple spots over multiple substrates, and also exhibited consistent values (b). Spectral narrowing of the VSL data is a further indication of optical gain (c) The PL spectra of figure 2a that show the transition from spontaneous emission to ASE with increasing pumping fluence. The

PL intensity is presented in log scale (d). Thickness dependent confinement factor at 640nm of DIAH- and OA- QD films calculated by using lumerical mode solutions (e)……...256

Figure B8. Emission spectra of BA capped QD films under different excitation strip lengths (a). All spectra are pumped at 440 nm with 5-ns pulse (pumped under 500 μJ/cm^2). The ASE intensity exhibits an exponential increase with longer excitation strip lengths for certain lengths, which indicates the presence of optical gain. The net gain values are fitted with an average net gain of 510±110 cm^{-1} for the BA-capped QD films (b). The presence of optical gain is also supported by threshold behavior in input power-output power plots (average of 50 ±3 μJ/cm^2) (c) spectral narrowing of the emission peak as the pump strip length is increased (d). ……257

Figure B.9: An example of the experimental data and the fitting from an optical loss measurement for the low loss DIAH-tethered QD films. ……258

Figure B.10: PL stability tests of DIAH-crosslinked and BA-capped QD films stored in a desiccator under vacuum. The PL intensity of the DIAH-tethered QD film (black) remains stable over 16 days while that of the BA-capped QD film (red) decreased to 60%.....259

Figure C.1: (a) Optical absorbance (solid) and photoluminescence (dashed) spectra of the oleic acid capped QDs in solution. (b) TEM micrograph of oleic acid-capped core/graded-shell CdSe/$Cd_{1-x}Zn_xSe_{1-y}S_y$ QDs. …….. 261

Figure C.2: Film thickness as a function of the number of deposited QD layers during the LbL assembly..……..262

Figure C.3: Bright field optical images of fabricated QD microdisks (diameter of ~25 μm) using the same batch of butylamine capped QDs with (left) and without (right) the crosslinking process. Cracks and non-circular circumference form during sonication in the non-crosslinking case (right). ……263

Figure C.4: (a) PL image of an array of microdisks with diameter of 10.6 μm (b) SEM image of an array of microdisks with diameter of 26.0 μm. ……..264

Figure C.5: Lasing spectra with mode splitting in microdisk with diameter of (a) 10.6 μm, (b) 26.0 μm, (c) 41.6 μm, and (d) 52.1 μm. ……265

Figure C.6: Quality factor of the longitudinal cavity modes from lasing spectra (mode splitting) of microdisks with diameter of (a) 10.6 μm, (b) 26.0 μm, (c) 41.6 μm, and (d) 52.1 μm. (e) quality factor of lasing spectra with mode splitting as a function of disk diameter…….266

Figure C.7: Quality factor of the longitudinal cavity modes from microdisks with diameter of (a) 10.6 μm, (b) 26.0 μm, (c) 41.6 μm, and (d) 52.1 μm. ……...267

Figure C.8: Schematic of the confocal photoluminescence measurement apparatus……. 268

Figure D.1: TEM micrograph of oleic acid-capped $CsPbBr_3$ QDs……269

Figure D.2: Bright field (b) and fluorescence (c) images of different individual patterns…..270

Figure D.3: (a) Emission spectra of $CsPbBr_3$ QD film under different pump fluences showing ASE and spectral narrowing. (b) Optical gain value of $CsPbBr_3$ QD film fitted by using variable stripe length method. ……271

Figure D.4: Emission spectra of (a) $CsPbBr_3$ QD disk pattern; (b) $CdSe/Cd_{1-x}Zn_xSe_{1-y}S_y$ QD disk pattern by integrating the PL emission of an 2 μmx2 μm region within green and red microdisks using hyperspectral system. ……...272

Figure D.5: Emission spectrum of blue $CdSe/Cd_{1-x}Zn_xSe_{1-y}S_y$ QDs dispersed in hexane.. 273

Figure E.1: TEM micrograph of oleic acid-capped $CdSe/Cd_{1-x}Zn_xSe_{1-y}S_y$ QDs…… 274

Figure E.2: (a) bright field (b) dark field and (c) photoluminescence microscopic imaging of microdisk with diameter of 25 μm. (d) AFM topographical image (top-view) and (e) 3D projection of microdisk with defects formed near circumference. ……275

Figure E.3: (a) bright field (b) dark field and (c) photoluminescence microscopic imaging of coupled microdisk with disk diameter of 25 μm. (d), (e), (f) SEM images of 3 sets of coupled microdisks. ……276

Figure E.4: shows three representative examples of the behaviors of individual microdisks. In (a) the spectrum shows a single mode progression, while the fluorescent and bright field microscope images show a relatively uniform circumference. In (b) and (c) mode splitting is observed in the spectrum and the fluorescent and bright field microscope images show defects along circumference. Not the relative blue shift of the mode envelope between (a), and (b) and (c). ……277

Figure E.5: As an important control experiment, we perform the spatial gain variation measurement on an isolated 25μm diameter disk. Here the behavior is largely different from that of the disk pair due to absence of coupling to another disk. As the disk enters the beam spot, threshold is achieved first at the longest wavelength modes. Then, as it moves completely into the beam spot the shorter wavelength modes are observed and grow more quickly in intensity than the long wavelength modes. This behavior is expected because of the large material loss at shorter wavelength. Thus, when the disk is only partially pumped, the unexcited region contributes much more loss at short wavelength than at long wavelength. There is then a 25μm plateau in emission intensity as the disk moves through the spot but is entirely pumped. The negligible variation in the measured spectrum in this region is a testament to the negligible effects of pump inhomogeneity with the beam spot. We can thus safely conclude that the onset of the long wavelength modes as well as the self-termination of short wavelength modes from the evenly pumped pair are entirely due to the mutual coupling between them and influence of gain/loss contrast between them, and not a property of isolated disks or due to experimental error……..278

Figure E.6: (a) shows the eigenfrequencies $\omega_1^{(A)}$ (blue), $\omega_2^{(A)}$ (red), and $\omega_3^{(B)}$ (green), vs. the gain differential Δg_{AB} for different values of γ_{23} with κ fixed. As γ_{23} increases the point of coalescence of intra-cavity modes $\omega_1^{(A)}$ and $\omega_2^{(A)}$ moves to larger (negative) values of Δg_{AB}. In (b) a similar behavior occurs for varying values of κ with γ_{23} fixed, however, the coalescence point moves to lower magnitude of Δg_{AB} as κ increases. Empirically, we find that this coalescence occurs at the point $\Delta g_{AB} = (\gamma_{23})^2/2\kappa$. This signals the cross-over from the strong intra-cavity coupling regime to the intermediate coupling regime. In (a), the subsequent bifurcation of inter-cavity modes $\omega_1^{(A)}$ and $\omega_3^{(B)}$ occurs closer to $\Delta g_{AB} = 0$. The bifurcation point scales with γ_{23} as $\Delta g_{AB} = 2\gamma_{23}$. Meanwhile, in (b) we see the bifurcation

point is seen to be insensitive to κ. Hence, in this region the inter-cavity coupling dominates and effectively reduces the problem to that of two coupled modes……..279

Figure E.7: both γ_{23} and κ are held constant while the value of γ_{12} is increased from zero. It is clear that as γ_{12} increases the coalescence is transformed into and avoided crossing. In the high γ_{23} limit the minimum splitting $\Delta\omega$ that is achieved is ≈ γ_{12}. Thus when γ_{12} = 0 a true exceptional point is obtained. It is also clear from this figure that the points of coalescence and bifurication are independent of γ_{12}…….280

SUMMARY

In this work, quantum dots are used as the optically active nanostructures due to their tunable emission/absorption properties and high photostability. In addition, they are solution-processable via the unique combination of organic ligands and inorganic cores, leading to improved material processing. Generally, the goal of this research is to control light-matter interactions in three levels of hierarchical QD photonic systems: individual and assembled nanostructures, individual and coupled cavities. Specifically, controlled optical properties of individual nanostructures such as emission/absorption band position and photoluminescence intensity were investigated via the selection of materials and dimensions. In addition, spatial arrangements of assembled nanostructures were examined to see the effect on the degree of light amplification/attenuation and real refractive index which are important variables for the design of novel photonic systems that obey parity-time symmetry. Finally, manipulation of optical activity of photonic cavities including cavity resonance, emission output and mode splitting will be investigated by altering localized gain/loss contrast and arrangement of engineered defects.

To summarize, this research work provides a scientific framework which demonstrates a comprehensive solution when designing the photonic system that requires the control of light-matter interactions including emission, gain and optical mode characteristics. Major themes present in this work include:

1. Examine, measure and investigate the quantum confinement of excitons in individual nanostructures and the coupling behavior within assembled nanostructures (large scale arrangement), aiming to control the optical and lasing properties of these nanostructures;

2. Develop microfabrication methods to control spatial distribution of QD based photonic cavities to control light-matter interactions in these microscale structures, aiming to utilize these controlled interactions to design novel photonic systems;

3. Develop approaches to tailor the deformation of boundary and gain/loss contrast of cavities to discover new optical phenomena for designing novel photonic systems.

Specifically, core/shell and ligand engineering were adopted to develop high quality assembled quantum dot solids with superior lasing properties such as tunable gain/loss values, low lasing thresholds and stable lasing output. Microscale and nanoscale deposition and microfabrication techniques were used to further arrange quantum dots into photonic cavities. In addition, physical and non-physical method are proposed to manipulate the optical gain/loss values in localized region to achieve the exceptional point. The design and fabrication principles in this work will help guide the development of miniaturized photonic system with highly tunable optical properties, tunable mode activity and other optical phenomena such as parity-time symmetry.

CHAPTER 1

INTRODUCTION

The pursuit of miniaturized and advanced photonic systems with precisely tailored gain/loss, scattering, reflectivity/transmission, emission directionality and cavity mode activity has encouraged the development of novel structure designs and new materials that can provide unprecedented functionality and wide tunability. In the past, inorganic and organic semiconducting materials have been used widely to fabricate photonic structures. Inorganic materials that provide superior lasing performance are typically grown by using molecular beam epitaxy (MBE) and metal-organic chemical vapor deposition (MOCVD).[1,2] For these inorganic materials, similar lattice constant of material and substrate is required to epitaxially grow the material, restricting the accessible type of substrates and materials. Furthermore, these fabrication approaches often require complicated processes and expensive equipment which increase the cost significantly.

In contrast, the organic system has no such limitations since polymers and organic dyes are solution-processable under ambient condition. However, these organic dyes suffer from the photobleaching effect where the photoluminescence (PL) intensity of dyes decrease dramatically under intense optical pumping.[3] Clearly, new material should be proposed and identified to resolve the issues encountered in the abovementioned systems. Among intensive efforts, nanomaterials, especially quantum dots (QDs), have attracted great attention because they can be both solution-processable and photostable, showing their ability to be utilized in the design of practical and reliable photonic systems Furthermore, unlike conventional bulk materials these tiny particles exhibit optical properties that can be tuned by simply changing their size, shape and capping ligands due to quantum confinement of excitons in these nanoscale particles. Combining with

various deposition and microfabrication techniques, QD based photonic systems can be fabricated that become a promising candidate over conventional inorganic and organic photonic systems to advance the future development of photonic devices with their highly tunable and stable optical properties. In the chapter below, we will discuss QDs in different aspects including synthesis of materials, fundamental physics of QDs as the optically active media and microfabrication techniques which have been used in the past to fabricate QD assemblies. These discussions can be important basis for us to identify and select suitable materials and fabrication methods while investigate unprecedented optical phenomena that can be observed through the novel design of photonic structures with controlled gain/loss contrast, coupling strength and engineered defects.

1.1 Quantum dots as gain and loss medium

1.1.1 Introduction to quantum dots

QDs are nanoscale semiconducting particles which typicall have sizes less than ~10nm. These zero-dimensional nanostructures can be made of different semiconducting materials including binary composition such as CdSe, CdS, CdTe, PbS, PbSe, InP and ternary compostion such as $CsPbX_3$ (X=Cl, Br, I) (**Figure 1.1a**).[4,5] In the past, semiconducting QDs have been synthesized via a variety of physical and chemical processes.[6,7] Here, we focused on the low-energy-input chemical colloidal synthesis, hot-injection method, to prepare semiconducting colloidal particles.[8] These colloidal particles will be referred to as QDs that are composed of crystalline inorganic cores coated with shell of organic molecules. The hot injection method generally involves the pyrolysis of organometallic precursors by injecting these precursors into hot coordinating solvent such as trioctylphosphine oxide, TOPO.

The subsequent thermally decomposed precursors lead to the formation of monomers and nuclei that eventually grow into large particles. In contrast to QDs that are grown by physical processes, these colloidally-synthesized QDs are solution-processable since they are coated with an organic ligand shell preventing particles from agglomeration in organic solvents. Furthermore, thanks to efforts that have been made to refine the synthesis procedure, promising properties like near-unity quantum yield and extremely low size dispersity of less than 10% had also been achieved.[9,10]

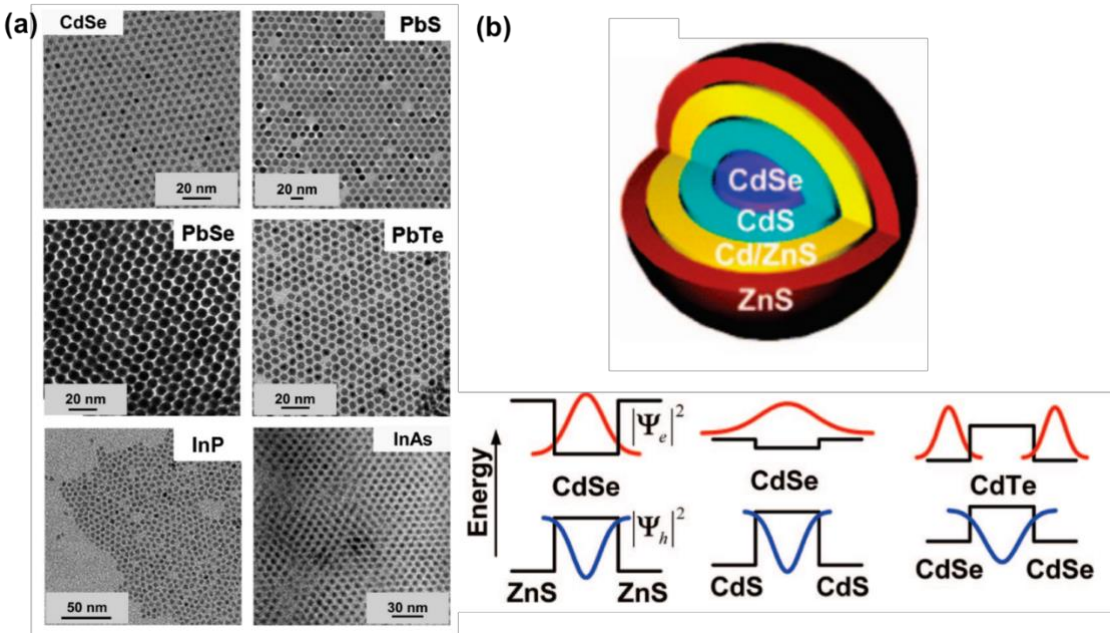

Figure 1.1 (a) TEM images of QDs consist of different materials. QDs can be synthesized to have simple (core) or complex core/shell architectures. (b) Schematic of a core/multishell QD (top). Schematics of different energy level alignments: type-I (bottom left), quasi type-II (bottom center), and type-II (bottom right) core/shell QDs. **(Images adapted from Ref 4)**

In addition to synthesis procedure of core QDs, those of more complex layered structures such as core/shell and core/shell/shell have also been well-established. Depending on the localization of electron and hole wave functions within core/shell structures, energy level alignments of QDs can fall into three categories: Type-I, Type-II

and quasi Type II (**Figure 1.1b**).[4] Different configurations of QDs that are designed via core/shell engineering indeed provide suitable optical emitters/ absorbers to wide applications because the overlap between electron and hole wave functions can affect the exciton relaxation pathway significantly. For instance, the type-I energy-level alignment confines both electron and hole wave functions in core. This increases the radiative recombination rate and prevent these carriers away from the surface trap states, making type-I QD a good optical emitter due to the improved quantum yield. improvement of photoluminescence quantum yield (PLQY).

1.1.1.1 Cd-based QDs

The synthetic chemistry of QDs aims to provide the flexibility to tailor the electronic states and optical properties of QDs via the growth of core and shell. The synthetic strategies can be used to reduce non-radiative pathways and control the energy transfer between neighboring QDs significantly. To improve the performance of photonic system, high PLQY of individual nanostructure is a key parameter since it affects the efficiency to convert absorbed photons to photons emitting at longer wavelength. Generally, the growth of inorganic ZnS shell can help passivate the surface of CdSe core and reduce the non-radiative pathways. However, the relative large lattice mismatch of ~12% between ZnS and CdSe resulted in the formation of strain-induced defects.[11] A more popular core/shell system to date is CdSe/CdS QDs, possessing better emission properties and smaller lattice mismatch of 4% in comparison to CdSe/ZnS QDs.[12]

The fluorescence intermittency, known as blinking, is a dynamic process where the PL of single QD randomly switches between neutral ("ON") and charged ("OFF") states.[13] This process is detrimental to limit the photostability of devices in different applications such as single photon sources.[14,15,16] Hence, numerous efforts have been made to suppress

this phenomenon since this phenomenon was discovered.[14] One of the method is to coat the cdse core with a giant shell of CdS (19 monolayers) by using successive ion layer absorption and reaction (SILAR) method. [17] PL blinking was suppressed significantly where more than 20% of the giant QDs are nonblinking with a ON time fraction of >0.99 (**Figure 1.2a**).

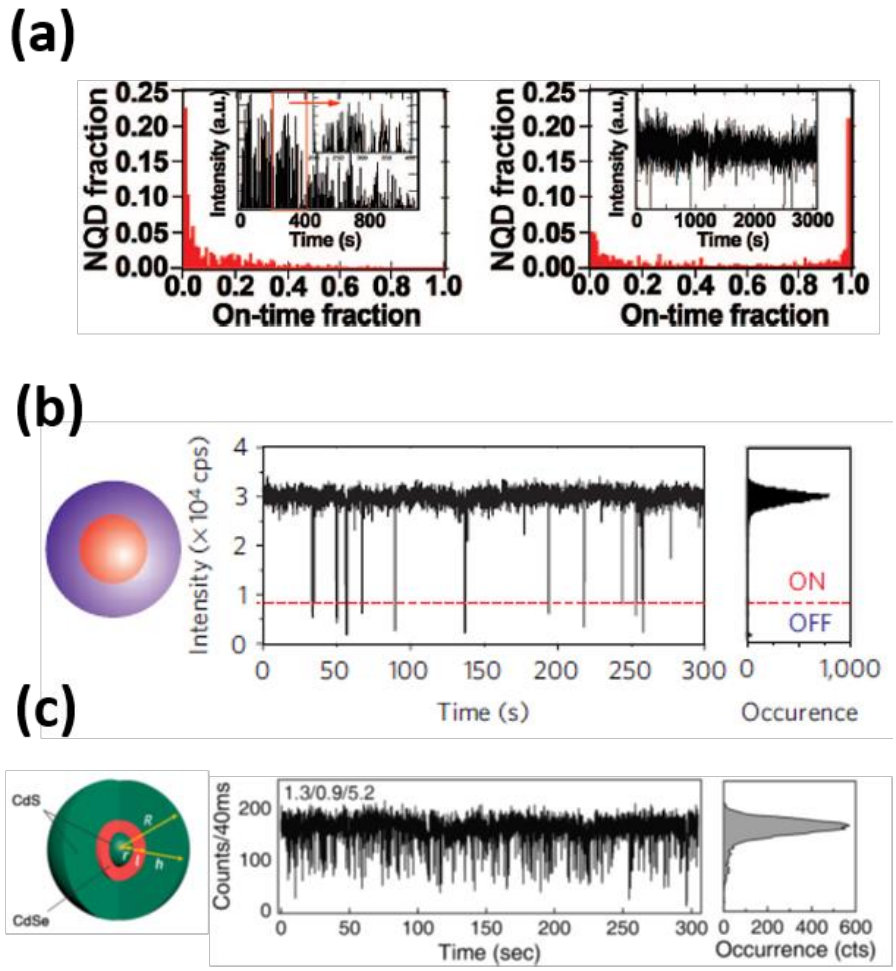

Figure 1.2 (a) On-time histograms of Qdot655ITK (reference QDs) (left) and g-NQD CdSe/19CdS (right). Insets show the PL time traces of individual Qdot655ITK and g-NQD CdSe/19CdS, respectively. (b) PL time trace (middle) and on- and off-time histogram (right) of a single CdSe–CdS core–shell QD (left) with a CdSe core radius of 2.2 nm and a shell thickness of 2.4 nm. (c) Photoluminescence time trace (middle) and on-time histogram (left) of a single SQW QD (left) with a CdS core radius of 1.3 nm, a CdSe shell thickness of 0.9 nm and a CdS shell thickness of 5.2 nm. **(Images adapted from Ref 13,17,18)**

In contrast, Bawendi group developed a synthetic approach that utilized octanethiol and cadmium oleate as precursors to support the slow growth rate of CdS shell.[13] The PL blinking of synthesized CdSe/CdS QDs with only a relatively thin shell was highly suppressed (~94% average ON time fractions) (**Figure 1.2b**). Among recent attempts, Bae group proposed to synthesize thick-shell QDs with unique seed/spherical quantum well/shell (SQW) geometry.[18] In SQW QDs, thin emissive layer of CdSe remained coherently strained and therefore inhibited the formation of misfit defects. The resulting QDs exhibited a near-unity PLQY while the blinking was significantly suppressed with a ON time fraction of > 0.9 (**Figure 1.2c**).

1.1.1.2 Lead halide perovskite QDs

Lead halide perovskite QDs have recently emerged as promising nanomaterials due to their attractive optical and electronic properties, which can potentially enhance the performance of photonic systems. Depending on whether the monovalent cation of lead halide perovskite QDs is organic or inorganic, they are classified as organic-inorganic perovskite QDs ($MAPbX_3$ and $FAPbX_3$) and all-inorganic perovskite QDs ($CsPbX_3$) where MA stands for methylammonium, FA stands for formamidinium and X is the monovalent halide anion (Cl, Br and I) (**Figure 1.3**).[19,20,21,22,23] Synthesis of $MAPbX_3$ QDs has mostly relied on two ways: solvent-induced and ligand-assisted reprecipitation [19,24,25,26] while $CsPbX_3$ and $FAPbX_3$ QDs are typically synthesized by using hot-injection method.[21,22,23,27]

Among these materials, $CsPbX_3$ QDs has attracted great attention since Kovalenko group demonstrated the first synthetic route in 2015.[21] This is because $CsPbX_3$ QDs showed relatively higher photostablity against the environment in comparison to the

$MAPbX_3$ QDs. In addition, the emission wavelength of $CsPbX_3$ QDs can be easily tuned over the entire visible region while maintain high PLQY as high as 90% and FWHM of 12-42nm, leading to wide color gamut covering up to 140% of the NTSC color standard (**Figure 1.3b**).[21] Unlike Cd-based QDs that require core/shell engineering to improve the PLQY of QDs, lead halide perovskite QDs can preserve high PLQY without the passivation of inorganic shell, excluding the delicate process of shell growth.

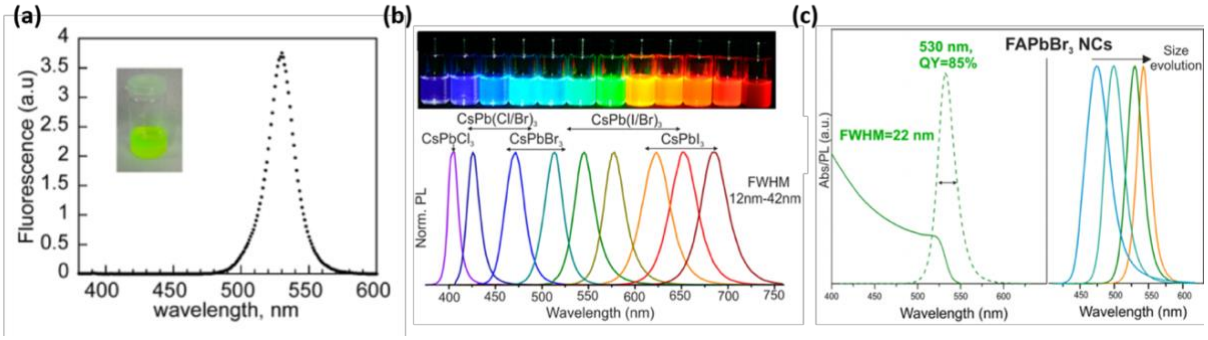

Figure 1.3 (a) PL spectrum of $MAPbBr_3$ QD solution. Inset shows $MAPbBr_3$ QD solution under UV lamp. (b) Image of $CsPbX_3$ QD solutions under UV lamp (top). PL spectra of QD solutions with different composition (bottom). (c) Absorption and PL spectra of $FAPbBr_3$ QDs (left). PL spectra of $FAPbBr_3$ QDs of different size (right). **(Images adapted from Ref 19,21,27)**

Furthermore, emission and absorption of lead halide perovskite QDs can not only be tuned by changing size of QD but also by tuning the composition via anion exchange.[28] This anion exchange can generally occur within seconds, leading to facile and precise control of their composition and hence the optical properties of lead halide perovskite QDs. Manna group reported an anion exchange process to tune the emission wavelength of $CsPbX_3$ over the entire visible spectrum by adding excess lead halide salts such as oleylammonium chloride/iodide as halide sources into QD solutions, facilitating the replacement of Br^- with Cl^- or I^- (**Figure 1.4a and b**).[29]

In addition, anion exchange in solid and gas phase is also possible as reported by Yang and Manna group, providing the flexibility to use different processing condition to tailor optical properties of lead halide perovskite QDs while preserving their shape and morphology.[30,31]

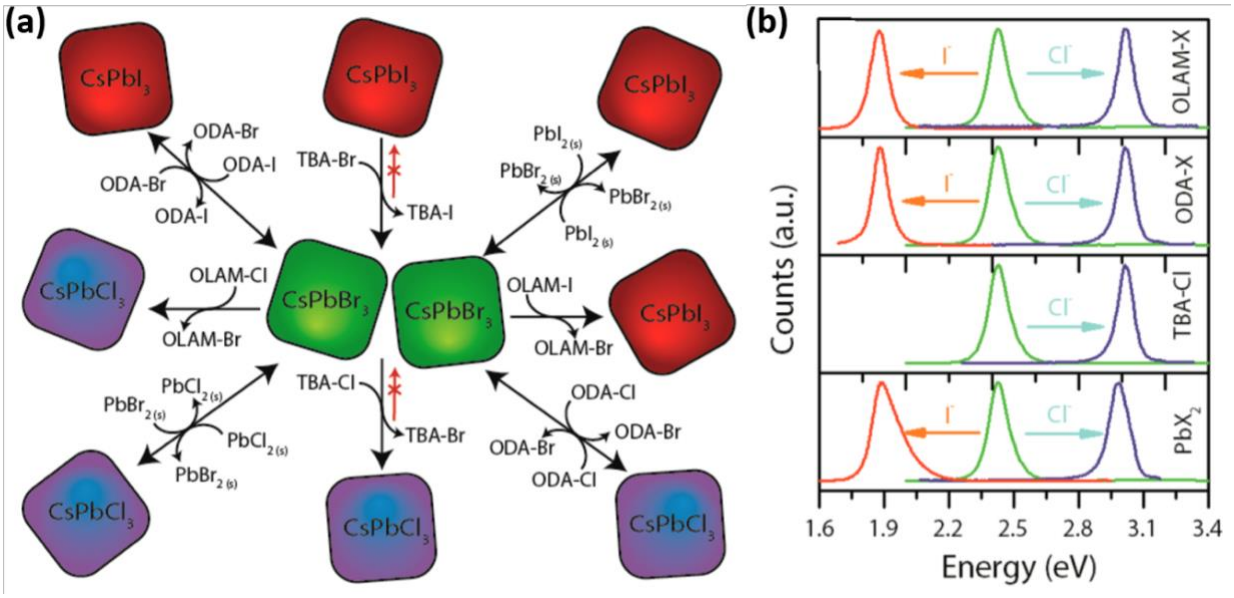

Figure 1.4 (a) Schematic outlining the anion exchange process of $CsPbX_3$ QDs using different routes and precursors. (b) PL evolution of $CsPbCl_3$ and $CsPbI_3$ QDs by using different precursors including OLAM-X, ODA-X, TBA-Cl and PbX_2 (from top to bottom). **(Images adapted from Ref 29)**

1.1.2 Fundamental exciton dynamics

1.1.2.1 Quantum confined effect

The flexibility of tuning QD emission/absorption profile comes from the quantum confined effect, where excitons generated in QD feel the presense of boundary in three-dimensional space due to exceptionally small QD size (**Figure 1.5**). To describe the quantum confined effect within QD clearly, several points need to be explained and

considered. The first thing needs to be explained is the term “exciton”. Exciton is an electrically neutral quasiparticle that emerges upon the abosorption of electromagnetic radiation (or to say photon).[32] It forms when materials abosrb photons which subsequently excite the electron from valenced band to conduction band, leading to the formation of an electron-hole pair that are bound to each other via the electrostatic coulomb interaction. The relaxation of excition via radiative route can remit photon and therefore is a essential process that is required in any light-emitting applications such as light-emitting diodes or lasers. This process would be discussed in more detail later)

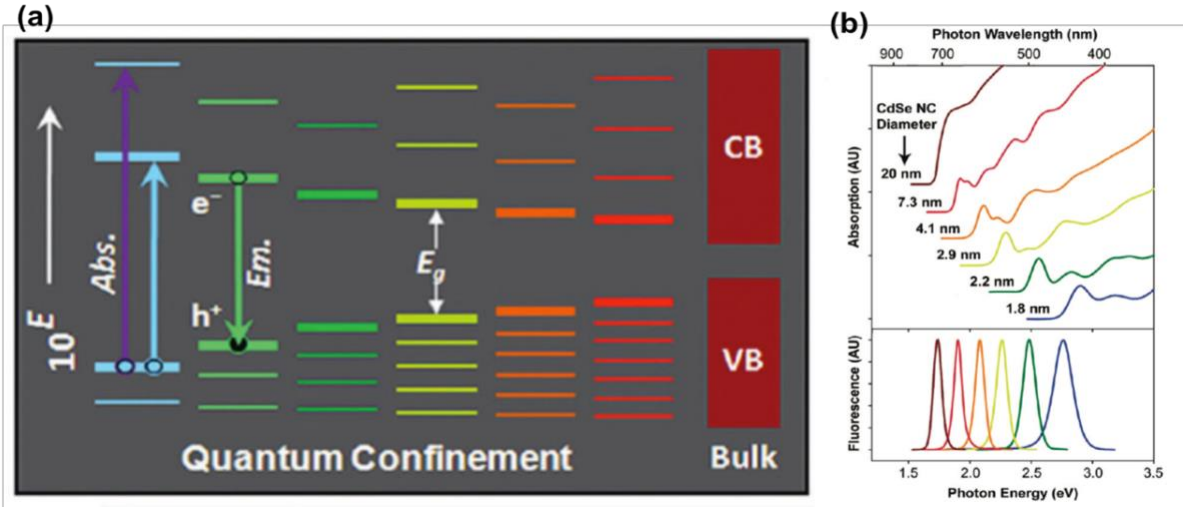

Figure 1.5 (a) Schematic showing how the quantum confinement effect change the bandgap compared with bulk material (b) Tuning of absorption and emission peak position via size variation of CdSe QDs **(Images adapted from Ref 35 and 36)**

Second, excitons are said to be hydrogenic (hydrogen-like) particles since they are two-particle system with a negative charge electron and a postive charge hole attracted to each other. However, exciton in different materials has its own radius, known as exciton Bohr radius.[33] The exciton Bohr radius in different material is generally much larger than

hydrogen atom and depends on the dielectric constat of the material and effective masses of excited electron and hole.

Thrid, as the dimension of material approaches the length scale of exciton Bohr radius, exciton starts to feel the presense of boundaries in three-deimensoal space and even be squeezed. In this regime, electronic states of material change from continous energy bands to discrete energy levels. This phonomenon is also known as the quatnum confined effect, resulting in the atomic-like optical properties in QDs.

This distnict feature can be understood by using the particle-in-a-sphere model, where the QD (particle) wave function is confined in a spherical particle of radius R with an infinitely high potential barrier. When radius become comparable or smaller than exciton Bohr radius, only some specific energy levels are still available, leading to the formation of discrete energy levels instead of continous energy bands.[34] **Equation 1.1** shows that as the radius becomes smaller, the bandgap of QD gradually increases from the unconfined band gap of bulk material E_g (bulk), where m_r is the reduced electron-hole mass and R is the radius of QD. **Figure 1.5** shows clearly bulk CdSe possesses continuous conduction and valence bands with a fixed and smallest band gap while CdSe QD has dicrete energy levels with tunable band gap that depends on size.[35,36]

Equation 1.1: Radius dependent band gap energy of a QD using the approximation of particle-in-a-sphere model. **(Equation from Ref 34)**

$$E_g(QD) = E_g(bulk) + \frac{\pi^2 \hbar^2}{2 m_r R^2}$$

$$m_r = \frac{1}{\left(\frac{1}{m_e} + \frac{1}{m_h}\right)}$$

1.1.2.2 Exciton relaxation and Auger recombination

Exciton dynamics of QDs can be important research topic since it can help researchers to understand how these excitions relax to the groud state via different pathways. Generally, the relaxation of excitons follows the Jablonski diagram developed for more traditional fluorescent dyes (**Figure 1.6a**) except that triplet states (phosphorescence) only exist in some type of QDs such as Mn^{2+} doped QDs and carbon QDs.[37] In QDs, radiative relaxation of single exciton (X) to the ground state is mainly via the band edge recombination which subsequently emit photons. Typically, QDs have stokes shift of 10-20nm (that is, the difference between first absorption peak and emission maxima) while full width half maximum (FWHM) can be 10-40nm depending on the composition and shape of QDs Interestingly, quantum dots can not only support generation of single excitions but also the formation of biexcitons (XX) and higher order multi-excitions (MX).

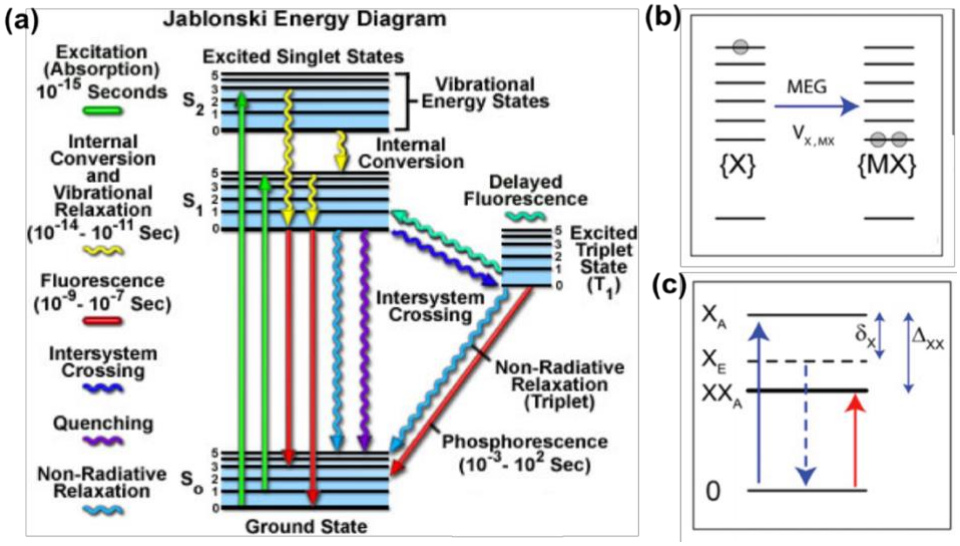

Figure 1.6 (a)Jablonski Energy diagram describing different radiative and non-radiative pathways (b) Multiple exciton generation process (c) Electronic transitions that lead to generation of single exciton and biexciton. **(Reproduced from Ref 37,38)**

The understanding of biexciton and multi-excition dynamics can be significant because optical phonomenon such as light amplification that requires population inversion generally occurs in these regime. Biexciton and multiexciton can form in two ways. The first way is the multiple excition genereation (MEG), where a high-energy single exciton can transform into multiple low-energy excitons (**Figure 1.6b**).[38] Unlike MEG process, when multiple single excitons generated upon intensive excitation, they are forced to interact with each other due to the strong confinement within QDs, leading to the formation of new quasi-particles that consist of multiple electron-hole pairs.[38]

As mentioned, the dominant channel of single exciton dynamics in the well-passivated QDs is the intrinsic radiative recombination that is on the time scale of nanosecond. The situation is quiet different in the case of biexciton and multi-exciton recmobination which initiate a severe non-radiative pathway, known as Auger recombination.[39] In this proces, energy generated during exciton relaxation is not converted into photons. Instead, it tends to excite the third charged carrier (electron or hole) to a higher energy levels. Auger recombination process fundamentally requires the conservation of energy and translational momentum. As a result, it is a temperature-assisted process in bulk materials whose rate can be expressed as $r_A \propto \exp(-\gamma_A E_g/k_B T)$, where γ_A is a constant dependent on the material and E_g is the bandgap of the material. The equation indicates that Auger recomnination becomes more efficient with increasing temperature. This can be understood by considering the fact that higher temperature can provide more translational momentum required in Auger recombination process.

In the QD regime, the Auger recombination is in fact even more efficient due to the discrete energy levels which relax the translational momentum conservation (**Figure 1.7a**). Clearly, understanding the relationship between QD size and Auger recombination lifetime is desired. Generally, an universal linear scaling law of Auger

recombination lifetime was found for almost all types of QDs, which is also known as "volume scaling law" (**Figure 1.7b**).[39] The ultrafast Auger recombination lifetime typically ranging from 10-100ps severly impeded the development of colloidal quantum dot lasers since this ultrafast non-radiative pathyway can easily destroy population inversion within QDs by disintegrating the multi-excitons into single excitons in a non-radiative way.

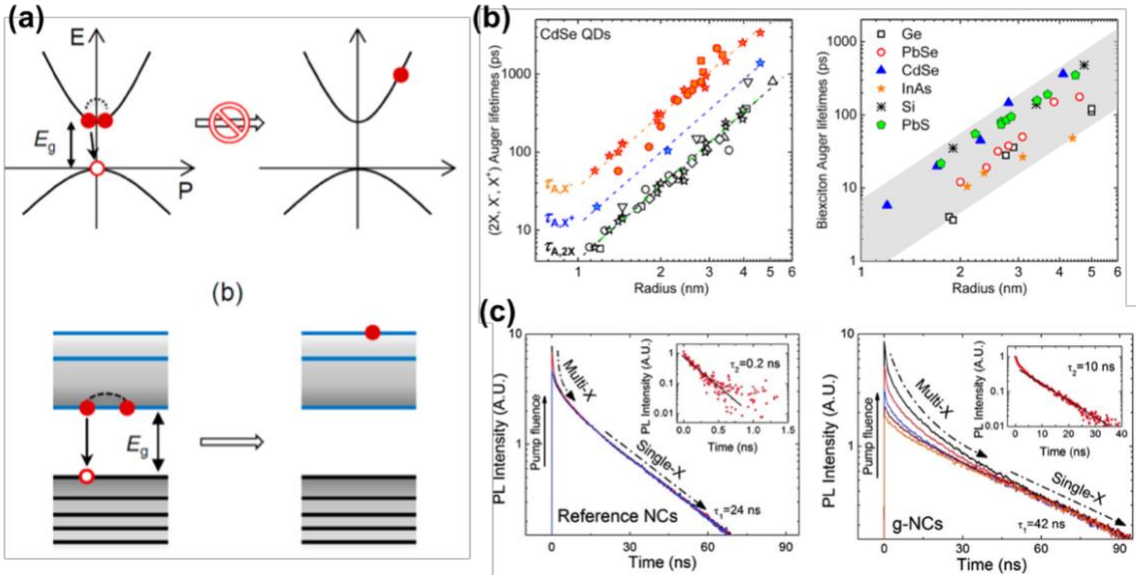

Figure 1.7 (a) Schematic showing the relaxation of translational momentum conservation makes Auger recombination efficient in QDs (bottom) while the Auger recombination is less efficient in bulk material (b) Volume scaling law of Auger recombination lifetime of CdSe QDs (left) and different materials (right) (c) Transient absorption spectra for (left) traditional CdSe/ZnS QD and (right) CdSe/CdS giant QD. (**Reprint from Ref 39,41**)

Generally, several core/shell designs have been used to suppress or circumvent the Auger recombination to achieve low lasing threshold. Alloying the core/shell interface to smoothen the confinement potential was found to lengthen the Auger lifetime significantly due to the reduced strength of the intraband transition that is involved in Auger recombination. Klimov group reported the insertion of an alloyed $CdSe_xS_{1-x}$ shell between CdSe core and CdS shell can further extend the Auger lifetime from less than

700ps to 1.8ns (Figure **1.8a**).[40] These QDs with alloyed shells all feature strongly suppressed Auger recombination originated from the softened confinement potential.

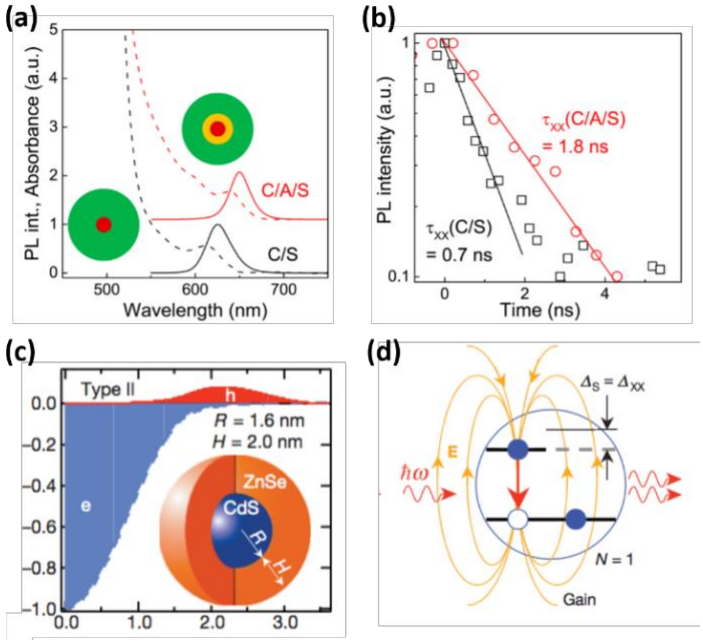

Figure 1.8 (a) PL (solid) and absorption (dashed) spectra of CdSe/CdS (C/S) (black) and CdSe/alloyed shell/CdS QD film. (b) Biexciton dynamics measured from single CdSe/CdS (C/S) (black) and CdSe/alloyed shell/CdS QDs. (c) Radial distributions of electron and hole charge densities in type-II CdS/ZnSe QD. (d) Schematic showing the competition between stimulated emission and absorption where X-X coulomb interaction determines the transient stark shift (Δ_S=Δ_{XX}). **(Images adapted from Ref 40,42)**

Reducing the overlap of wave function between electrons and holes by engineering the core/shell structure is another effective method to suppress the Auger decay. Typical example is the giant CdSe/CdS QDs where an energy-level alignment of quasi-type II formed. In this configuration, wave function of electrons is delocalized over the entire structure while that of holes is still confined in core. The reduced overlap of wavefunction was found to suppress the auger recombination significantly where a prolonged biexcition lifetime of 10 ns was obtained in giant CdSe/CdS QDs (**Figure 1.7c**).[41] This

value is 50 times longer than the reference sample of CdSe/ZnS QDs, indicating strongly suppressed Auger recombination within giant CdSe/CdS QDs. Importantly, a large bandwidth of optical gain spectra (>500meV) was observed, suggesting the participation of multi-excitons of very high order is possible in giant CdSe/CdS QDs. Finally, QDs with a type-II heterostructure such as CdS/ZnSe QDs can be used to circumvent Auger recombination.[42] The spatially separated electrons and holes resulted in a giant transient Stark shift of the absorption spectrum, enabling the single exciton gain with no multi-exciton Auger recombination involved in the light amplification process (**Figure 1.8b**).

In addition to numerous efforts to suppress auger recombination, it is noteworthy that a promising synthesis method to improve optical gain performance was recently proposed by Sargent group to decrease the valance-band-edge degeneracy by utilizing biaxial strain that has proved successful in more conventional system of epitaxial quantum well.[43] The biaxial strain can cause additional splitting and concentrate holes into lowest-energy levels, lowering the overall gain threshold (**Figure 1.9a**). The synthetic strategy is to introduce the built-in biaxial strain into QDs via facet-selective epitaxy where trioctylphosphine sulfide (TOPS) enabled the growth of CdS shell on $(000\bar{1})$ and $\{10\bar{1}0\}$ facets while oleylamine blocked the shell growth on (0001) facet, resulting in high degree of facet selectivity (**Figure 1.9b, left**).[44] QDs with unpassivated (0001) facet were subsequently coated with a uniform second CdS shell by using octanethiol, leading to enhancement of PLQY from 25% to 90% (**Figure 1.9b, right**).

The synthesized biaxially strained QDs indeed showed progressive splitting of first absorbance peak while the single-dot emission linewidth (36±3 meV) is lower than that of single nanoplatelet due to the spreading exciton fine structure. A very low continuous-wave lasing threshold of around 6.4-8.4 kW cm^{-2} was achieved in the film of biaxially strained QDs deposited on photonic crystal distributed feedback (PC-DFB) cavity

(**Figure 1.9c**). It is noteworthy that this value is 3-4 times lower than that of the hydrostatically strained CQDs in the same PC-DFB cavity, demonstrating the synthetic approach to manipulate strain within QDs is promising and should be explored extensively in the future.

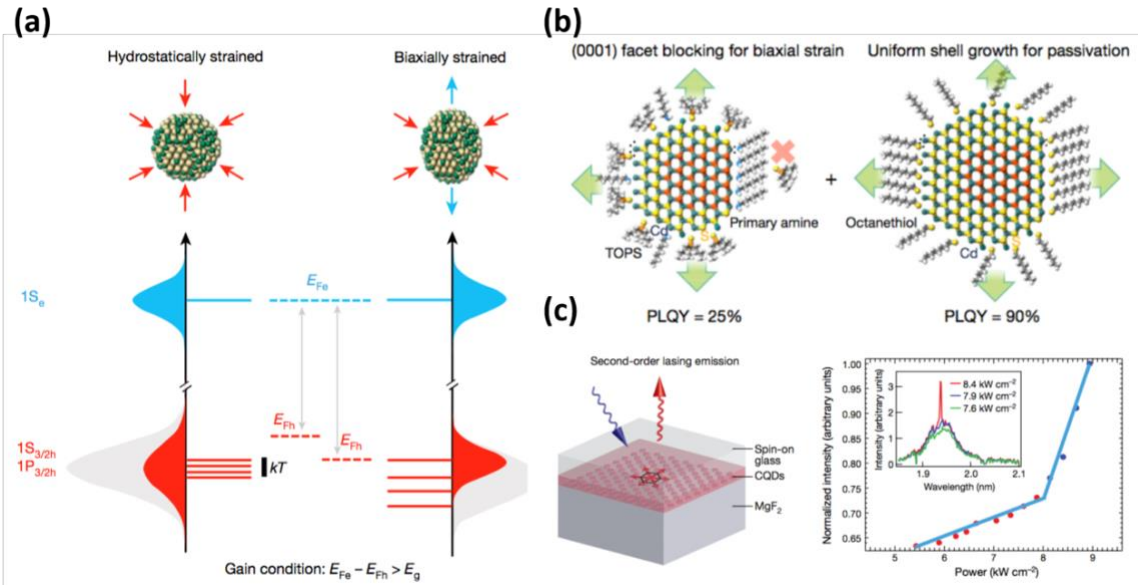

Figure 1.9 (a) Schematic showing the state-filling, band-edge states and quasi-Fermi level splitting of CdSe QD under hydrostatic and biaxial. (b) Synthetic steps of selective-facet epitaxy growth. (c) Schematic of layered structure of PC-DFB cavity laser (left). Normalized integrated emission intensity versus pumping power (right). Inset shows the spectrum above threshold. **(Images adapted from Ref 44)**

1.2 QD assembly for photonic systems

With the advent of self-assembled epitaxially grown QDs that demonstrates superior lasing properties such as high optical gains and ultra-low lasing thresholds, colloidal QDs have been considered an ideal candidate for next-generation optical gains system. Unlike the epitaxially grown counterpart that may suffer from lattice mismatch of film on the substrate, these colloidal QDs can be deposited onto any desired substrate since

they are solution-processable. In addition, colloidal QDs are also advantageous over traditional organic dyes as gain medium for two reasons. First, optical pumping to traditional organic dyes causes dramatic decrease in photoluminescence intensity, which is also known as photobleaching. In contrast, colloidal QDs have been proven to give stable lasing output under intensive pumping.

Second, emission/first absorption peak position of QDs can be easily tuned from blue to IR region, which provides the flexibility to the design of photonic systems that require the operation in specific emission bands. For example, peak position of Cd-based QDs can be tuned from 400 nm to 800 nm, while for Pb based QDs it can be tuned from 700 nm to more than 2000 nm.[45] This shows a wide emission/absorption range can be covered by using only two types of materials. In contrast, organic dyes with infrared emission of 1-2 μm are difficult to achieve and rarely reported in literature. These facts have strongly encouraged researchers to develop colloidal QDs as promising gain/loss medium for the fabrication of next-generation advanced photonic elements.

1.2.1 Optical gain systems

Optical gain describes the light amplification process occurring in semiconductor lasers, which is attributed to the stimulated emission associated with the recombination of electrons and holes. Different form the spontaneous emission, stimulated emission occurs when more electrons are in higher excited energy states, also known as population inversion. To achieve population inversion, more than 50% electrons in the excited states needs to be excited upon the absorption of electromagnetic radiation (intensive optical pumping). When population inversion occurs, rate of stimulated emission starts to exceed that of absorption. This leads to the net amplification of light intensity, known as net gain value that is usually expressed in cm^{-1}.

With various deposition methods, different types of media can be used as optically active layers to amplify the light intensity. Generally, inorganic semiconducting media such as InGaAsP demonstrate superior optical gain values on the order of 10^3 cm^{-1}.[46] However, this type of material needs to be grown on specific substrate due to requirement of lattice match. In addition, they are brittle and can be difficult to be flexible. On the other hand, the organic media such as organic dyes and conjugated polymers are highly flexible with optical gain values on the order of 10^1-10^2 cm^{-1}.[47] Nevertheless, these organic gain media are prone to photobleaching effect, restricting the possibility to be an ideal candidate for the design of novel photonic structures. This motivates us to develop QDs as optical active medium here since they have potential to be flexible while maintaining high gain values and stable lasing intensity.

1.2.1.1 Built up of stimulated emission in QD films

The built up of stimulated emission in QD films was a challenging task in the early development stage of high performance QD lasing system since lasing action was difficult to achieve from these QD films. Initially, this was thought to be associated with the high density of trap states on the QD surface. Later, it was found that the extremely fast auger recombination is the dominant non-radiative channel which ruins the population inversion on the time scale of 10-100 ps.[34] In order to beat auger recombination, a fs or at least several ps laser is required. This is still not enough for QDs to achieve stimulated emission because eventually not the rate of the pumping source but rate of stimulated emission within QD films needs to be shorter than that of auger recombination. The stimulated emission built up time depends on many variables such as QD volume, effective refractive index of film, gain cross-section and QD packing fraction of film (**Equation 1.2**). By putting real values of the above-mentioned equation, it was found that the QD volume fraction of film should be at least larger than 0.002. In

practical, stimulated emission (optical gain) were typically achieved in film with QD packing fraction above 0.02-0.05.[48] This limitation indicates that the QD packing can be important parameter to be investigated to achieve optimal gain performance.

Equation 1.2 Equation of built up time of stimulated emission that include several variables, where "τ_{SE}" is the stimulated emission build up time, "c" is the speed of light, "G" is the gain value, "nr" is the effective refractive index, "V_{dot}" is the volume of QD, "ξ" is the QD packing fraction, and "σ_g" is the gain cross-section. (**Equation obtained from Ref 48)**

$$\tau_{SE} = \frac{n_r}{cG} = \frac{n_r V_{dot}}{c\sigma_g \xi}$$

1.2.1.2 Estimation of optical gain values

The ability to develop stable, high-performance optical gain media with tunable emission from the visible to infrared spectral regions promises new opportunities in flexible lasing devices. Optical gain value exhibited by these materials is widely recognized as an important 'figure of merit' to consider when developing new photonic systems that demonstrate parity-time (PT) symmetry, which require a sensitive balance between optical gain and loss. Net gain value describes the degree of light amplification when light propagate through a specific gain medium. Net gain value is commonly estimated by the variable stripe length (VSL) method (**Figure 1.10a**).[49,50] Generally, QD film is pumped by a pulsed laser, where the pump light is focused into a stripe whose length can be varied. When the pumping power gradually increases, optical gain within QD film begins to compete with the optical loss (absorption). Above the threshold point, where the optical gain exceeds loss value, the light intensity starts to grow exponentially as

stripe length increases. The relationship between stripe length and exponential increase in light intensity can be fitted by Malko model to estimate the net gain value.[51] In the past, optical gain ranging from blue to infrared has been obtained in a variety of CQDs. The typical net gain value of these CQDs ranges from 60-200cm^{-1}.[49,51,52] Most studies in the area of QD gain medium have focused on the sophisticated engineering of the core/shell structure in order to suppress the Auger recombination rate (AR). To date, little attention has been paid to how modification of the ligand can affect gain performance and PL stability of the QD films. Clearly, how these molecular characteristics can affect gain values should be investigated systematically.

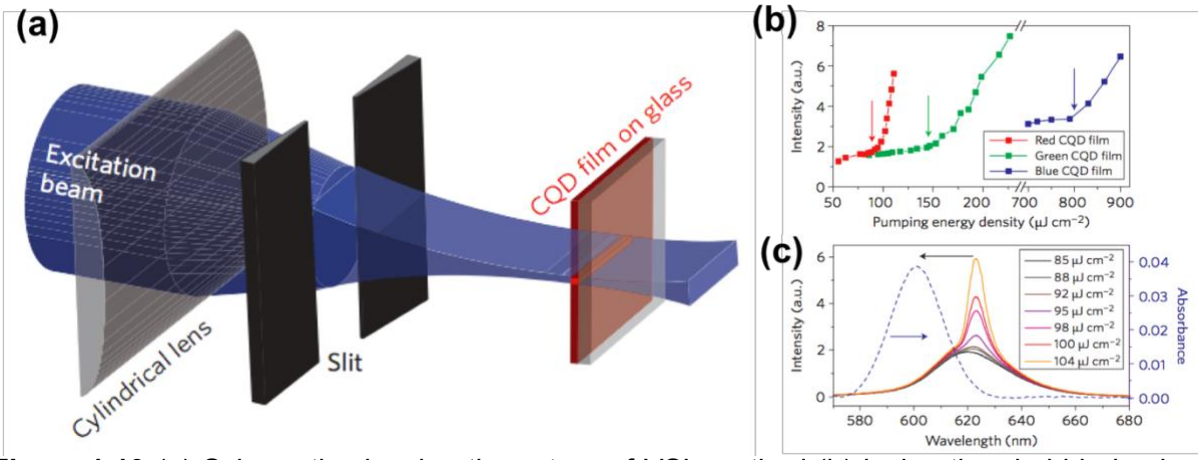

Figure 1.10 (a) Schematic showing the set up of VSL method (b) lasing threshold behavior of QDs with different color (red, green, blue) (c) emission spectra at different pumping fluences. (**Reprint from Ref 49**)

1.2.2 Fabrication techniques of QD based films and structures

1.2.2.1 Deposition techniques of QD planar films

To integrate tiny QDs into solid-state forms, different deposition methods have been developed in the past. Four types of deposition method were typically used to fabricate

these quantum dot solids. The first method is traditional and relies on the solvent drying such as spin-casting, drop casting and spray coating. The second method is the electrophoretic deposition which is accomplished by suspending two conductive electrodes in the QD solutions with an applied voltage. The electric field between electrodes drives QDs to be deposited on the substrates. The main advantage of this method is the efficient use of the starting QD solution.[53]

The third method is the Langmuir-Blodgett and Langmuir-Schaefer methods, where QDs are deposited via the emersion of substrate from the water interface with suspended QDs. Monolayer of QDs can be adsorbed homogeneously with each emersion step so that the thickness of film can be precisely controlled.[54]

The last method is the layer-by-layer (LbL) method. In this method, QD films deposited via spin coating or drop casting are modified by ligand exchange and no longer soluble to original solvents, enabling the repeatable deposition of QD films.[55] By using these different deposition methods, film properties can be controlled precisely including film thickness, emission/absorption bands, electrical conductivity and dot-to-dot arrangement.

1.2.2.2 Physical patterning of QD patterns

In addition to the deposition of QD films, patterning of localized QD assembly can be exceptional important to develop novel photonic structures and practical optoelectronic devices that require micro- or nanoscale features.

Generally, three types of techniques have been developed over the past decade. The first technique is the ink-jet or more advanced electrohydrodynamic printing. Ink-jet printing relies on the thermal/acoustic formation and ejection of liquid droplets via nozzle apertures.[56] Typically, highest resolution by using this technique is ~20-30 μm which

can be useful in some specific applications that only require modest-resolution. To further increase the resolution of this type of technique, electrohydrodynamic printing appears to be promising because it utilizes electric field instead of the thermal/acoustic energy to help shrink the size of the droplet down to several hundred nanometers. Thus, through the optimization of printing process, features down to submicron length scale can be fabricated (**Figure 1.11a**).

Another popular patterning technique is based on the well-developed soft lithography. Via the use of polydimethylsiloxane (PDMS) stamp, different patterning method such as transfer printing, capillary force lithography, μContact printing and solvent-assisted μContact molding can be used to fabricate multi-color and high-resolution features.[57,58,59,60] For example, PDMS stamps were used to transfer specific QD patterns onto substrate by direct printing. The manipulation of interfacial energy between QD/PDMS and QD/substrate enables the successful transfer of QDs. Multi-color features whose length scale are only few microns can be printed onto substrate easily. This is especially desired for LED applications that require high pixel per inch to fabricate high quality displays. Another example is the capillary force lithography, where a PDMS stamp is placed on a small amount of QD solution drop casted onto the substrate. Upon contact with the stamp, the QD solution filled in the patterned trenches via the capillary force. After drying, high resolution submicron patterns such as pillars or gratings can be obtained (**Figure 1.11b**).

The last technique is based on the electron beam lithography (EBL), where specialized photoresist reacts to electron beam exposures. The exposed/unexposed area can be subsequently removed during the development process. This creates polymer templates with trenches in specific locations.[61] The QD solution is typically casted onto the templates to back-fill the trenches. After lifting off the photoresist, well-defined QD

patterns down to nanoscale can be fabricated. This technique has been used to characterize unexplored electrical or optical properties of QD patterns whose dimensions shrink to nanoscale regime (**Figure 1.11c**).

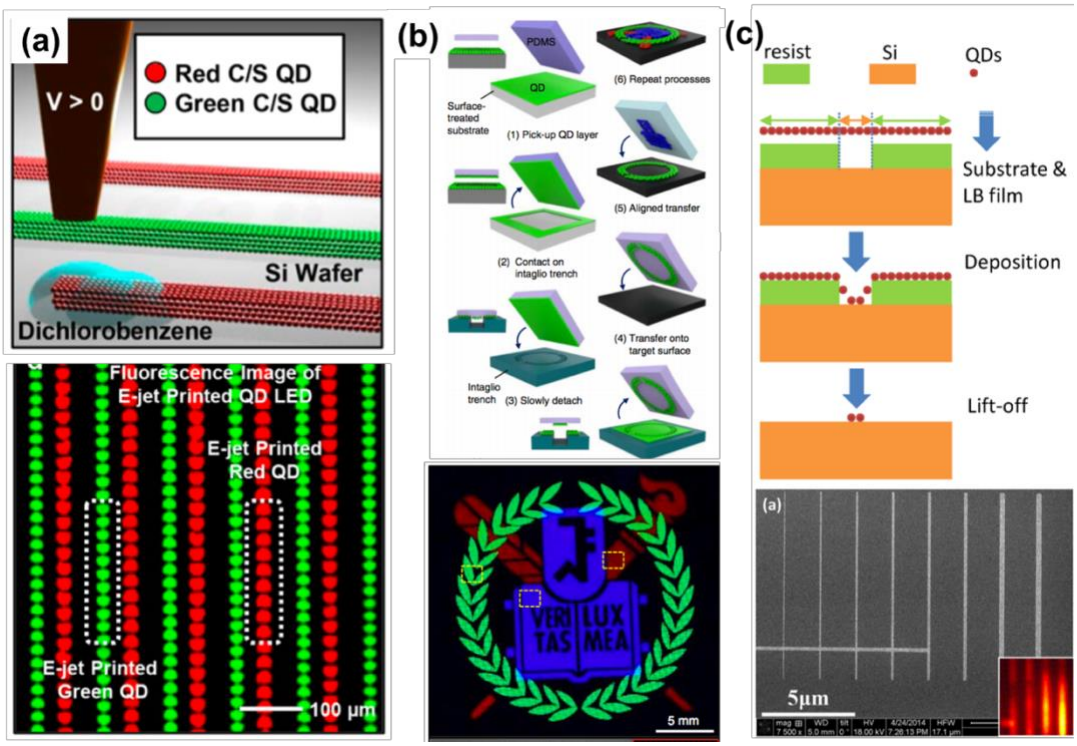

Figure 1.11 Schematic of fabrication process (top) and QD patterns (bottom) by using (a) electrohydrodynamic printing (b) PDMS transfer printing (c) electron beam lithography. (**Reprint from Ref 56,57,61**)

1.2.2.3 Photopatterning of QD microscale arrays

Photopatterns are fundamentally different from physical patterns fabricated using lithographic approaches because emissive photopatterns result from targeted intrinsic modification of the QD emission (essentially doping QDs with light), not from the addition, removal, or rearrangement of material. Therefore, emissive photopatterns have no modulated physical topography. We have previously developed QDs as

optically tunable emitters whose emission intensity can be controlled via light exposure. The unique decay-to-recovery phenomena of photoluminescence (PL) of Cd-based core-shell quantum dots in polymer film matrices were investigated in terms of different composition profile including CdSe core, CdSe/ZnS core/shell with sharp interface and CdSe/$Cd_{1-x}Zn_xSe_{1-y}S_y$ core/graded shell.[62]

As shown in **Figure 1.12**, photooxidation and degradation of CdSe and or ZnS is proposed to be the reason for both the irreversible blue-shift of PL peak, and the decay of PL intensity. The recovery of the PL intensity under light exposure is due to light mediated H_2O adsorption/desorption on the exposed core surface of CdSe as ZnS shell is corroded by oxidation.

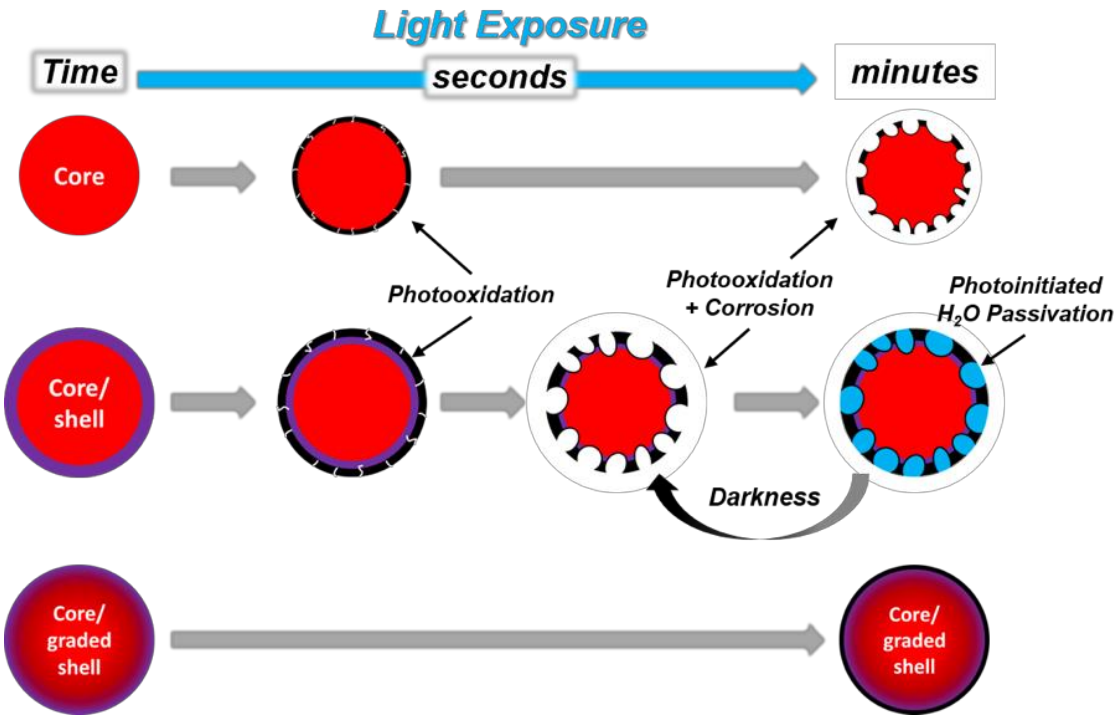

Figure 1.12. Schematic outlining the proposed physical evolution of each type of QD (CdSe core, CdSe/ZnS core/shell, or CdSe/$Cd_{1-x}Zn_xSe_{1-y}S_y$ core/graded shell) under light exposure in air over a period of 45 minutes (organic ligand not shown for clarity). (**Reprint from Ref 62**)

Therefore, in the case of core/shell CdSe/ZnS quantum dots, a fast decay and slow recovery of PL intensity, as well as irreversible blue shift under continuous light exposure are shown in **Figure 1.13**. While only irreversible decay and blue shift are observed in pure CdSe core quantum dots. As for the core/graded shell with thick shell, both intensity and peak position of PL are quite stable as the core is isolated from the environment.

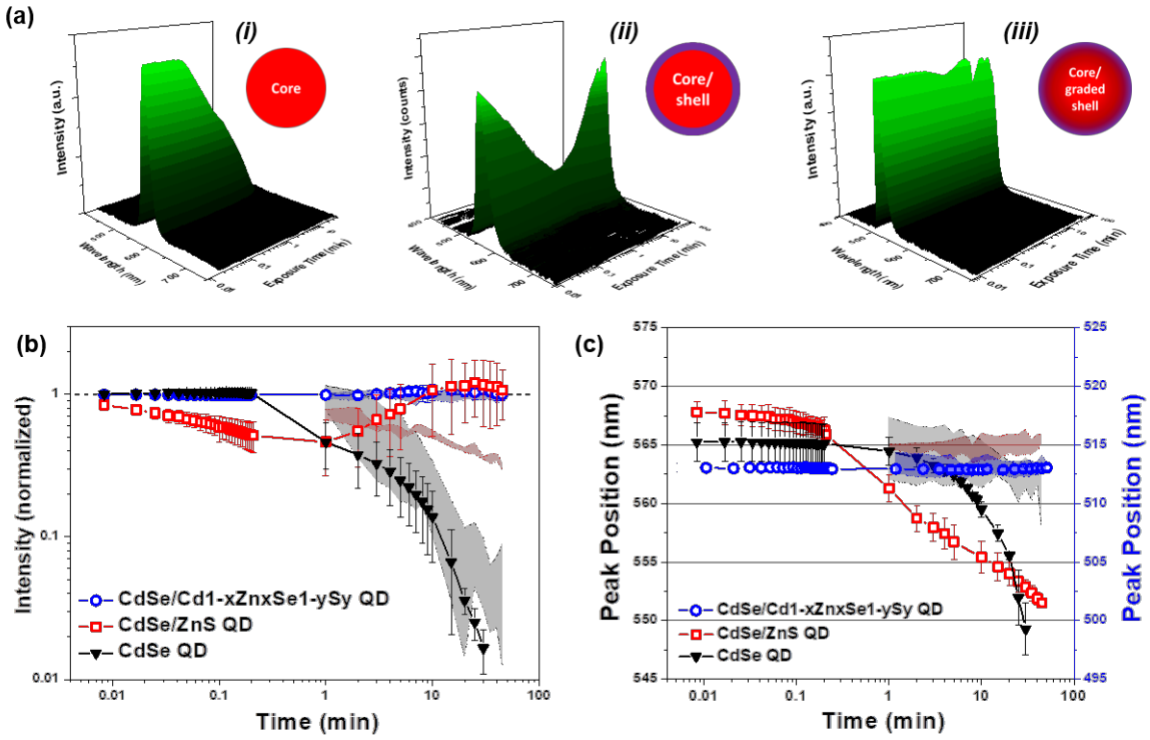

Figure 1.13. Examination of the photoluminescence stability of QD-PMMA films with different types of QD design (CdSe core, CdSe/ZnS core/shell, or CdSe/$Cd_{1-x}Zn_xSe_{1-y}S_y$ core/graded shell). (a) 3D and (b) 2D representation of PL intensity and (c) spectral peak position under continuous light exposure (blue light: 450-490nm, 24-28mW). The ribbons represent a standard deviation range for the emission evolution of the QDs in darkness. (**Reprint from Ref 62**)

Photopatterning strategy was developed that allow for the fabrication of either negative (darkened regions) or positive (brightened regions) photopatterns (**Figure 1.14a**).[63] These negative and positive strategies utilize a specific core/shell QD that exhibits decay-to-recovery of its PL intensity upon light exposure. We demonstrated pre-determined formations of positive and negative contrast emissive patterns for single color in QD-polymer composite films can be achieved depending on the light development (exposure) time t_{Devel}. The negative photopatterning approach yields a photopattern where the regions of the QD-polymer film exposed to the development light have a lower PL intensity than the regions protected by the photomask.

A negative photopattern is fabricated by developing the film for a time (t_{Devel}) shorter than the QD time-to-minimum intensity period (i.e. $t_{devel} < \tau_{decay}$) since the exposed QDs are still within the decay phase of their PL evolution (**Figure 1.14a**). On the other hand, the positive photopatterning approach yields a photopattern where the regions of the film exposed to the development light have a higher PL intensity than the regions protected by the photomask. A positive photopattern forms if the pattern development time is longer than the decay period (i.e. $\tau_{decay} < t_{devel}$) since the exposed regions enter the recovery phase of their PL evolution (**Figure 1.14a**).

This is the first time a single type of quantum dot has been used to fabricate photopatterns of negative and positive contrast (**Figure 1.14b, c and d**). These new approaches not only expand the number and type of photopatterns that can be created on QD-polymer films, they significantly improve characteristics like resolution, feature density, throughput, uniformity, contrast, and color complexity.

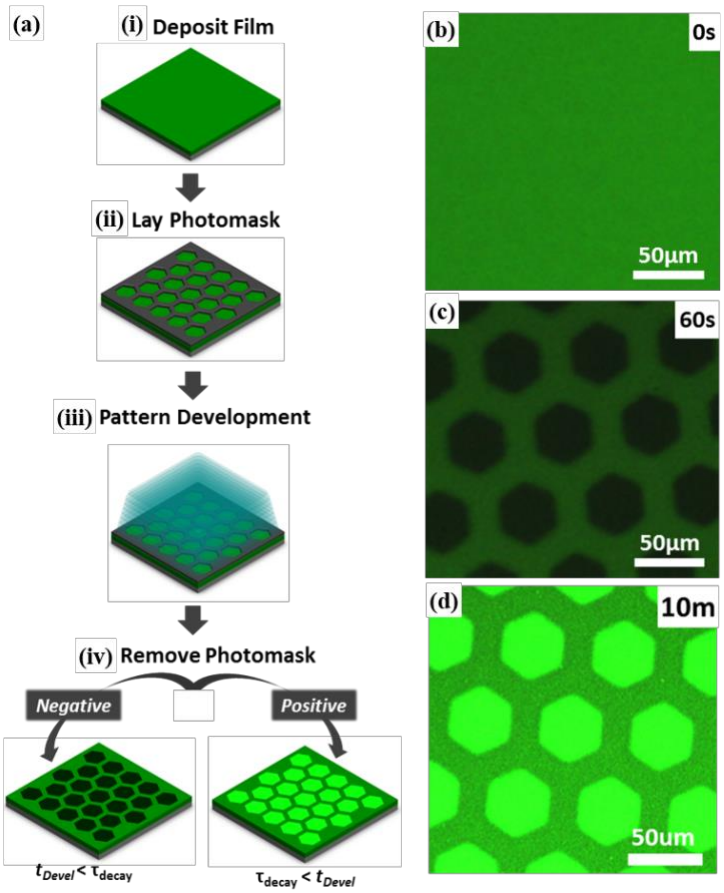

Figure 1.14 (a) Schematic of the general photopatterning process to fabricate negative and positive photopatterns. Photluminescence images of (b) an unpatterned green QD-polymer film, (c) a negative photopattern, and (d) a positive photopattern. (**Reprint from Ref 63**)

Besides the QD photopatterns of single color, QD-polymer films composed of a mixture of quantum dots with different color emission were fabricated and exposed to specific light wavelengths to develop multicolor photopatterns (**Figure 1.15a**).[64] By judicious consideration and implementation of the development wavelength, specific QD colors within the film could be selectively or collectively modified (**Figure 1.15b, c and d**). For example, the red QD color can be selectively enhanced, or both the red and green QD colors can be collectively enhanced. The resulting multicolor photopatterns are the first in the field of QD photopatterns, and these strategies make it possible to fabricate

multicolor photopatterns with highly predictable control. These collective and selective exposure strategies are easy to implement, applicable to a large variety of QD systems, yield complex multipeak emission profiles, and represent a significant departure from previous single-component photopatterning studies. In addition, these spectral tuning strategies are compatible with the previously outlined photopatterning approaches and therefore do not compromise on pattern resolution, uniformity, or throughput.

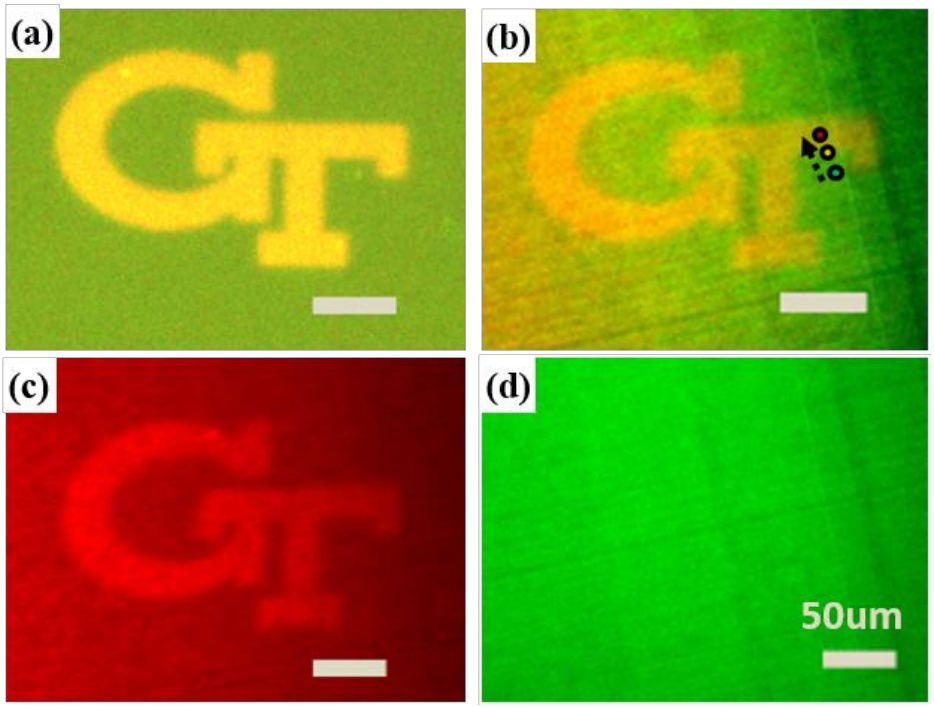

Figure 1.15 (a) Photoluminescence image of a multicolor photopattern in a QD-polymer film composed of red and green QDs. Hyperspectral scans of the (b) red and green channels, (c) red channel, and (d) green channel. (**Reprint from Ref 64**)

1.2.3 QD based photonic cavities

Current research has focused on the miniaturization of semiconductor lasers that can lead to smaller, cheaper, and more sensitive high performance on-chip photonic cavities, including a variety of micro and nanoscale lasers of different geometries.[65,66,67] These miniaturized photonic cavities can be tailored to manipulate the resonant optical modes

within the cavity via total internal reflection or light oscillation between reflective end facets. To fabricate micro- or nanoscale laser, the basic component is the photonic cavity that can confine light within gain medium to enhance the light amplification. In general, there are four common types of photonic cavity depending on the confinement mechanism: Fabry–Perot microcavities, whispering gallery mode (WGM) microcavities, distributed feedback (DFB) microcavities, and photonic crystal defect microcavities (**Figure 1.16**).[68]

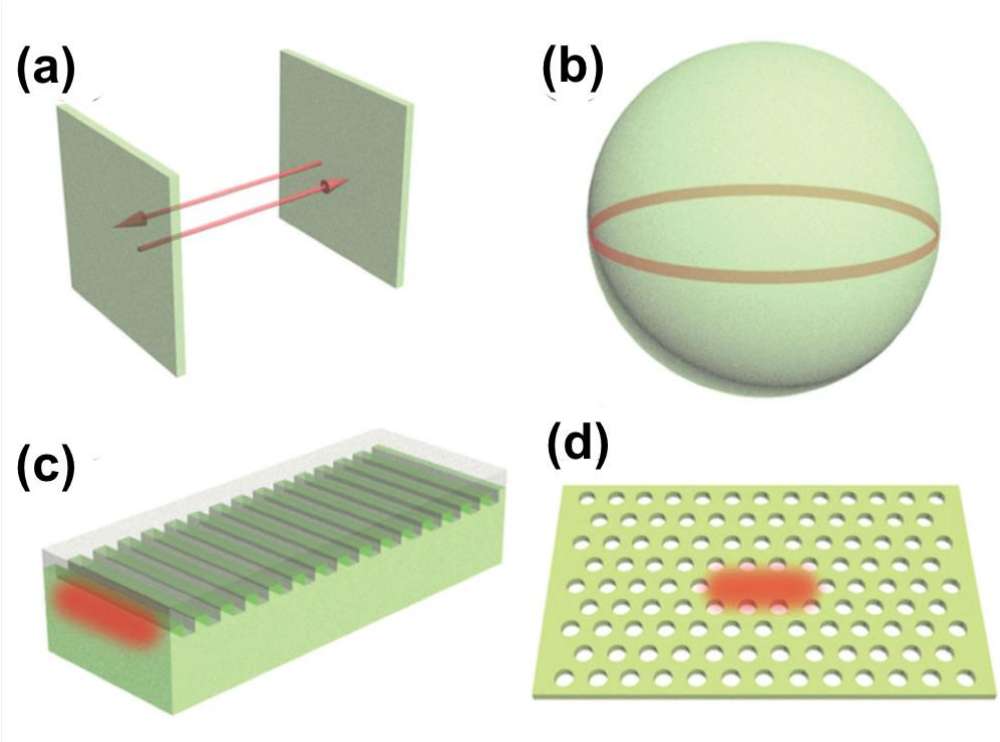

Figure 1.16 Four common types of photonic cavity depending on confinement mechanism (a) Fabry–Perot microcavities (b) whispering gallery mode microcavities (c) distributed feedback (DFB) microcavities. (d) photonic crystal defect microcavities. (**Reprint from Ref 68**)

Among all these different types of cavities, WGM microcavities have been attracted great attentions due to their high quality factor (that is how well cavity can store energy inside the cavity) and low mode volume which can enhance the light-matter interaction

inside the cavity significantly. In addition, multiple cavities can be coupled via the evanescent field resulting from total internal reflection near the boundary. The coupling between WGM cavities can be powerful tool to design novel photonic structure sine the energy transfer between cavities can be tuned via the control of coupling strength. In this research, we will focus on the fabrication of WGM cavities due to their promising properties to enhance light-matter interactions.

To sustain the WGM, different structures have been proposed including microspheres, microrings, microdisks, microtoroids, optical fibers, microcapillaries, microbottles, microbubbles, and hemispheres (**Figure 1.17**). These structures have been utilized in wide applications such as chemical and bio-sensors, single mode lasing and add-drop filters. The utilization of these WGM cavities relies on the monitoring of the resonant mode activity. To briefly quantify the resonant modes inside the WGM, one can assume a 2D circular WGM cavities, where light is confined via the total internal reflection. When self-interference occurs after light propagates for one round trip, specific resonant modes would be enhanced and can be expressed as **Equation 1.3.**

Equation 1.3 Equation of resonant modes inside the WGM photonic cavity, where m is the angular mode number, λ is the wavelength of the light and L is the circumference of the microcavity and n_{eff} is the effective refractive index of the medium. (**Equation obtained from Ref 68)**

$$m\lambda = Ln_{eff}$$

These enhanced resonant modes are known as WGM and are highly sensitive to the change in geometry of the cavity, refractive index perturbation of environment and coupling between cavities. Hence, the fundamental understanding of mode activity inside the QD based photonic cavity can be important in order to further design advanced photonic systems such as the PT symmetric microcavities.

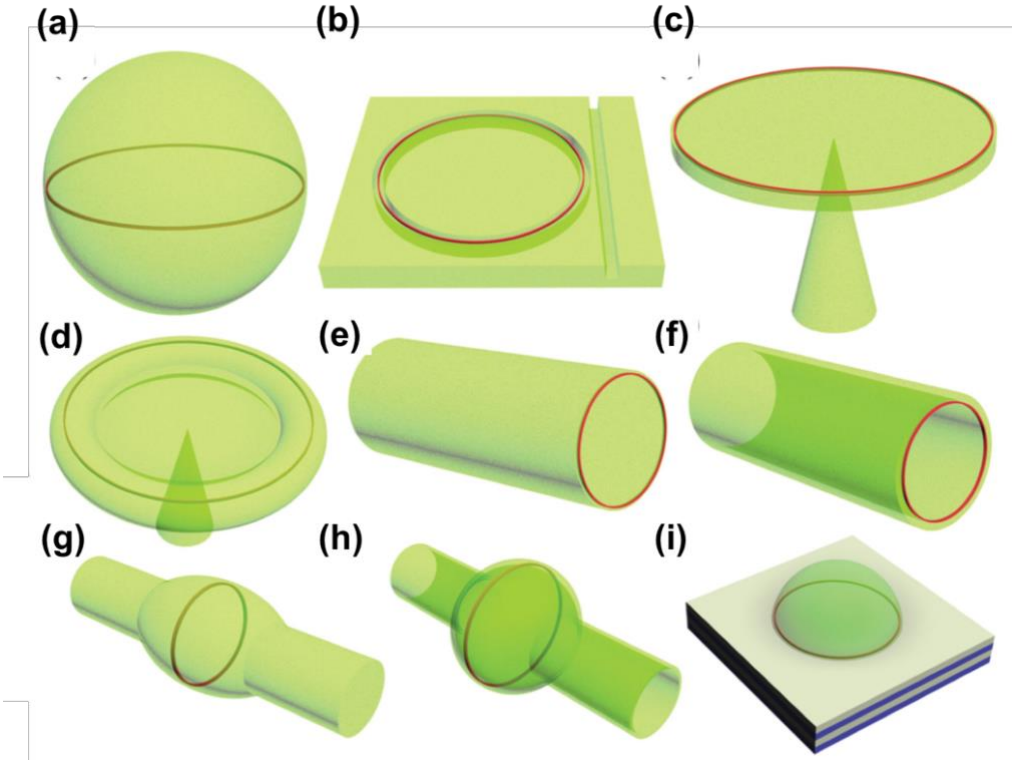

Figure 1.17 (a) Microsphere. (b) Microring. (c) Microdisk. (d) Microtoroid. (e) Optical fiber. (f) Microcapillary. (g) Microbottle. (h) Microbubble. (i) Hemisphere. (**Reprint from Ref 68**)

1.2.3.1 Coating structure

Coating passive microcavity with solution-processed QDs as active gain medium has been the most popular method in the field to demonstrate laser action and resonant cavity mode activity due to its simplicity in terms of processing. This method utilizes the excellent optical properties of passive microcavity such as ultra-high quality factor with

value up to 10^8 and low mode volume while circumventing the issue of phase separation that may be induced when mixing QDs into the matrix of microcavity.

We discuss below different configurations of passive microcavity coated with QDs that have been reported in literatures. The first example is the silica microsphere that is fabricated by using laser thermal processing.[69] The microsphere was produced by thermally melting one end of the fibre tapers at temperature above 1000 °C with a CO_2 laser beam. During melting process, melted silica glass would be thermally reflowed into spherical shape due to the surface tension, enabling the fabrication of silica microsphere with highly uniform surface and measured quality factor higher than 10^8 (**Figure 1.18a**).

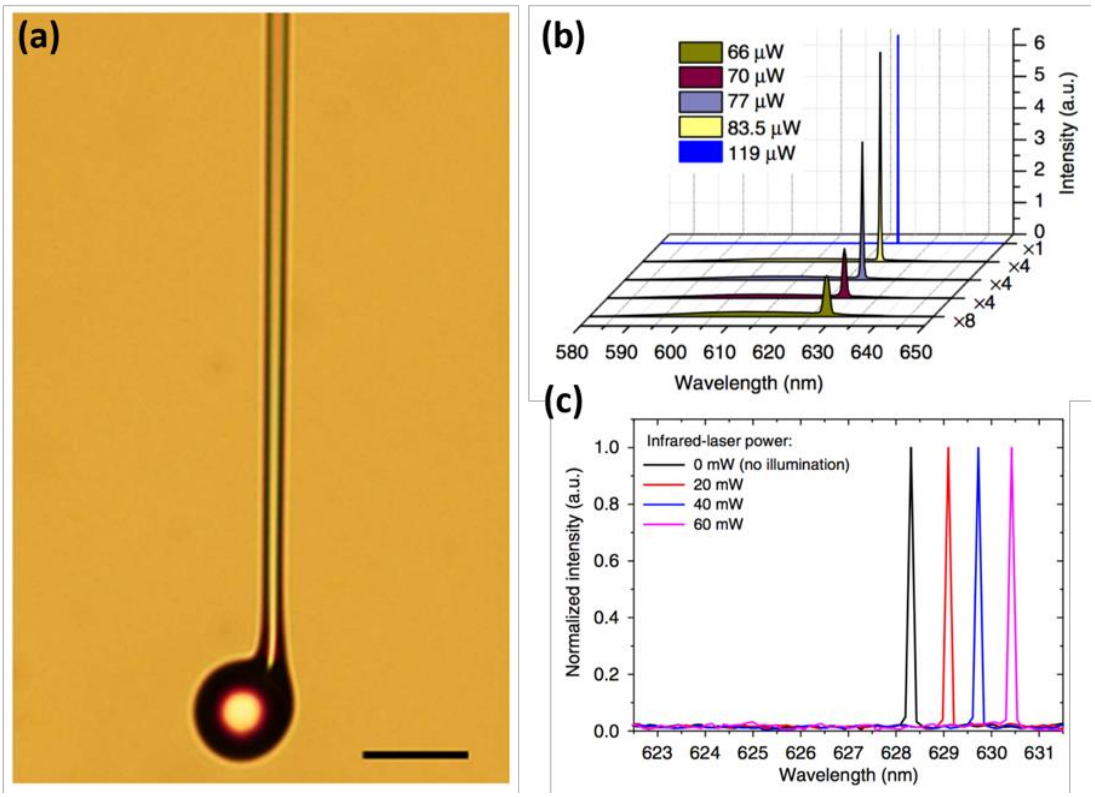

Figure 1.18 (a) Optical microscopy image of fabricated silica microsphere with a diameter of ~30 μm. Scale bar is 30 μm. (b) Evolution of laser emission near the lasing threshold. (c) Lasing spectra of silica microsphere coated with CdSe/CdS nanorods pumped under an infrared laser with varying power. **(Images adapted from Ref 69)**

The coating of CdSe/CdS nanorods was then deposited by immersing into nanorod solution in toluene. The final structure exhibited a quality factor of ~10^4 which is lower than the uncoated microsphere due to the introduced surface roughness and scattering loss caused by QD gain medium. In addition, a single mode laser was realized by selecting the sufficiently small microsphere that can provide a free spectral range wider than the gain spectrum of QDs (**Figure 1.18b**). The laser emission of the single mode laser was easily tuned by pumping the silica microsphere under an infrared laser of 3.5 μm pulse with varying power, leading to the heat-induced increase in size of microsphere and therefore the corresponding resonant cavity mode (**Figure 1.18c**).

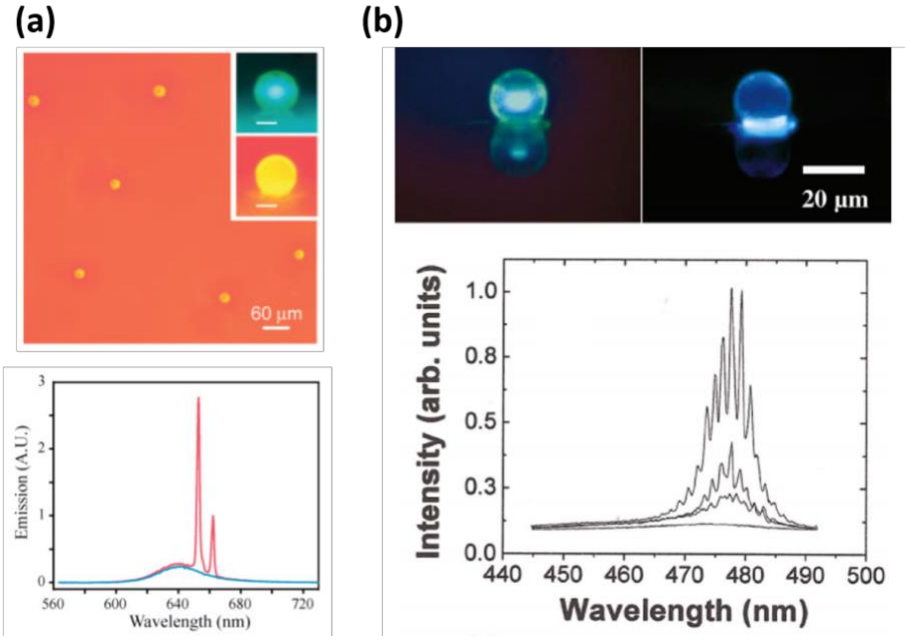

Figure 1.19 (a) Fluorescence image of 20 μm silica microspheres coated with CdSe/CdZnS titania composite film. Insets show 30 μm silica microspheres coated with blue (top) and red (bottom) CdSe/CdZnS titania composite film. Scale bar of insets are 15 μm. (b) Fluorescence images of 20 μm silica microspheres coated with CdS/ZnS silica composite film under white (top left) and UV (top right) light illumination, respectively. Lasing spectra under different pumping fluences (bottom). **(Images adapted from Ref 72,73)**

In addition to the microsphere produced by laser thermal processing, monodisperse colloidal silica microsphere can also be synthesized by using the well-known Stöber process. These commercially available silica microspheres have been used frequently as the initial demonstration of WGM resonators and lasing action. Typically, silica microspheres suspended in water or ethanol were drop casted onto substrate. These randomly distributed silica microspheres were then conformally coated with different types of QD gain medium including PbS QDs, $CsPbBr_3$ QDs, CdS/ZnS silica and CdSe/CdZnS titania composites (**Figure 1.19)**.[70,71,72,73] The uniformly coated surface led to quality factor of up to 3800 and can serve as a facile platform to exploit the promising lasing properties of QDs.

Besides spherical cavities, commercially available microcapillary tubes have also been widely adopted since QDs solution can be readily filled into inner hollow region, forming a QD coating on the inner wall of tube which acts as WGM cavity to demonstrate lasing action (**Figure 1.20**).[74,75,76]

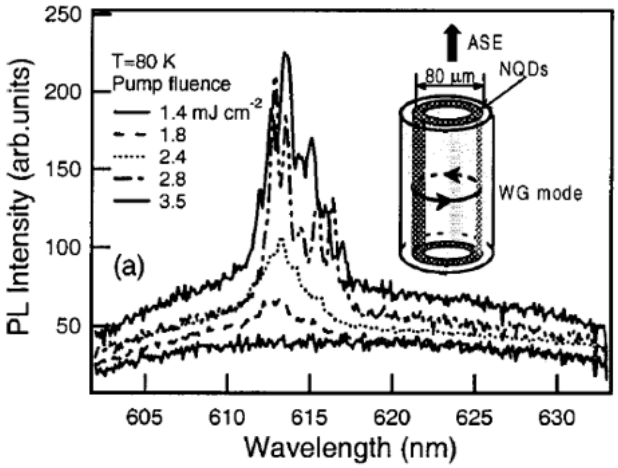

Figure 1.20 Normalized integrated emission intensity versus different pump fluences (left). Schematic showing the microcapillary tube integrated with QDs that demonstrates WG mode. **(Images adapted from Ref 51)**

All solution-processed self-assembled hemisphere is another promising configuration that can be fabricated on the substrate in a more cost-effective way. The generation of these micro-hemispheres relied on the hydrophobic effect of surface modification which cause the viscous epoxy resin solution to self-assemble on the tip surface (**Figure 1.21a**).[77,78] A small amount of resin solution was spread on the surface of cylindrical tip that is coated with 1H,1H,2H,2H-perfluorooc-tyltriethoxysilane as hydrophobic layer. After several minutes, a line of individual droplets was formed and transferred by lowering the tip with these droplets onto a distributed Bragg reflector (DBR) substrate coated with same hydrophobic layer, resulting in a line of hemispheres on the DBR substrate with size typically ranging from 5-120 μm.

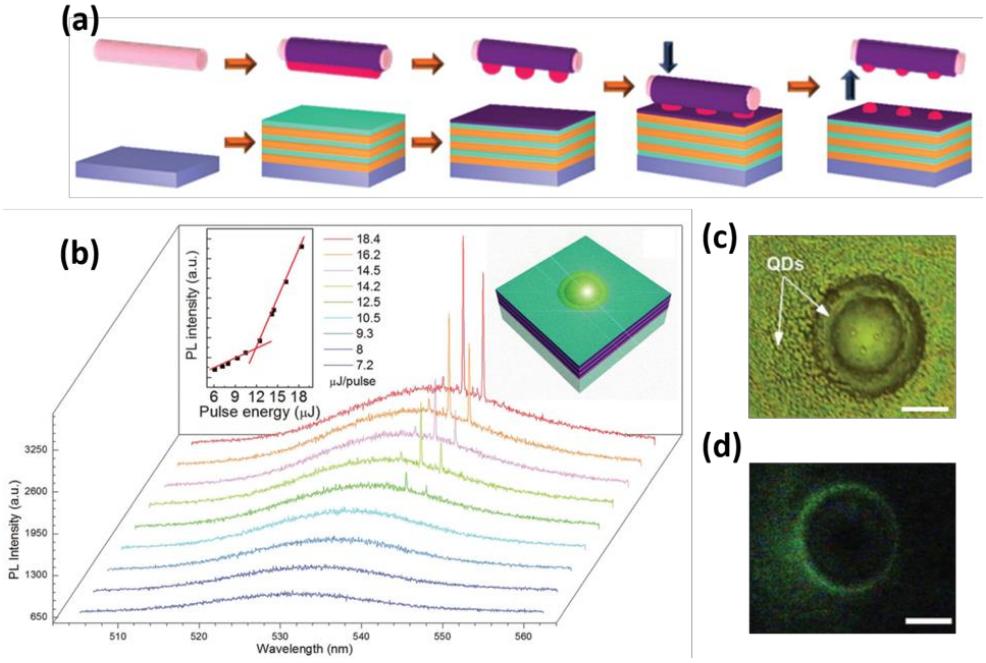

Figure 1.21 (a) Schematic showing the fabrication process of self-assembled hemispheres by using a cylindrical tip coated with a hydrophobic layer. (b) Lasing spectra of a hemisphere microlaser coated with QDs under different pulse energy. Left inset shows the PL intensity versus the pulse energy where a non-linear behavior was observed. Right inset shows a single self-assembled hemisphere coated with QDs that is on top of a DBR substrate. (c) optical microscopy image of the actual self-assembled hemisphere coated with QDs. (d) PL image of self-assembled hemisphere coated with QDs above lasing threshold. **(Images adapted from Ref 68,77)**

After drying for several days, the final solid-state hemispheres were fabricated. These hemispheres were subsequently coated by immersing them into $Cd_{1-x}Zn_xSe_{1-y}S_y$/ZnS QD solutions, resulting in a quality factor of ca. 3500 and a low threshold of 10.5 mJ/cm^2 under quasi-continuous wave pumping (**Figure 1.21b, c and d**).[77]

1.2.3.2 Self-assembled QD-polymer composite structure

Self-assembled polymer-based WGM microcavity has attracted great attention due to the ease of fabrication and low cost while maintaining high performance. Importantly, unlike inorganic sol-gel titania or silica, QDs with commonly used organic ligands can be facilely doped into these polymer matrices without complicated ligand exchange process to improve the compatibility. Sun group recently proposed a bubbling method to generate QD-polymer microbubbles.[79] PMMA was selected as the polymer matrix due to its high optical transparency, chemical inertness and mechanical flexibility. By varying the concentration of CdZnS/ZnS QDs that were mixed in PMMA solution, microbubbles with different sizes can be formed at the contact line (**Figure 1.22a**). It is noteworthy that the concentration (25-45%) of QD-PMMA solution used to fabricate microbubbles is much higher than those (<~10%) applied in other applications such as solar concentrators, light-emitting diodes and active waveguides. The high concentration of QDs can help shorten the time to build up stimulated emission and therefore achieve lasing action more efficiently.

The origin of the bubbling was attributed to the synergetic effects of both QDs and PMMA. The evaporating QD droplet was found to form microbubbles at the contact line while PMMA with mechanical flexibility stabilized the structure of microbubbles when the

contact line of the droplet moved over it and dried. The final QD-PMMA microbubbles achieved a quality factor of ~2500 and a low threshold of ~10.8 μJ (**Figure 1.22b and c**). A water-vapor sensor based on the QD-PMMA microbubbles was also demonstrated where the lasing peak positions were sensitive to the loading of water vapor and revealed a clear blue-shift. This showed the ability of microbubbles to serve as an efficient platform to sense the perturbation of refractive index induced by water vapor.

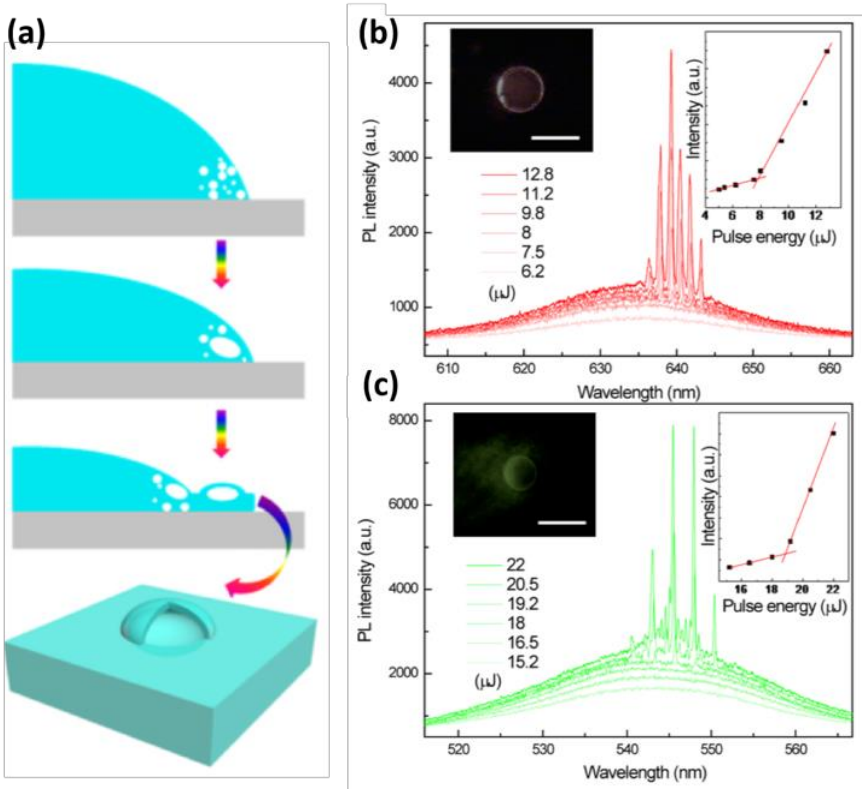

Figure 1.22 (a) Schematic showing how the QD-PMMA microbubble was formed during the bubbling process Lasing spectra of microbubbles mixed with red (b) and green (c) QDs under different pulse energies. Right insets show the PL intensity versus the pulse energy. Left insets show the PL image of the corresponding red and green QD-PMMA microbubbles. **(Images adapted from Ref 79)**

1.2.3.3 Inkjet-printed structure

Solution-processed self-assembled QD-polymer microcavity can be a promising structure due to the ease of fabrication and high performance. However, the location of

these microbubbles can not be controlled precisely during the random bubbling process. To further support the development of advanced photonic circuits, it is important to develop microfabrication techniques that are able to integrate these self-assembled optical components into desired positions. One of the facile technique that can enable controllable spatial distribution of these structures is solution-processed ink-jet printing. As mentioned in section 1.2.2.2, ink-jet printing is a one-step fabrication method with low material usage. More importantly, it can enable the fabrication of large-area arrays into locations that are assigned by microplotter system. Quasitoroid microlasers from self-assembled CdZnS/ZnS QDs were fabricated by ink-jet printing where QD solution with concentration of ~5mg/mL was loaded into print head nozzle (**Figure 1.23a and b**).[80]

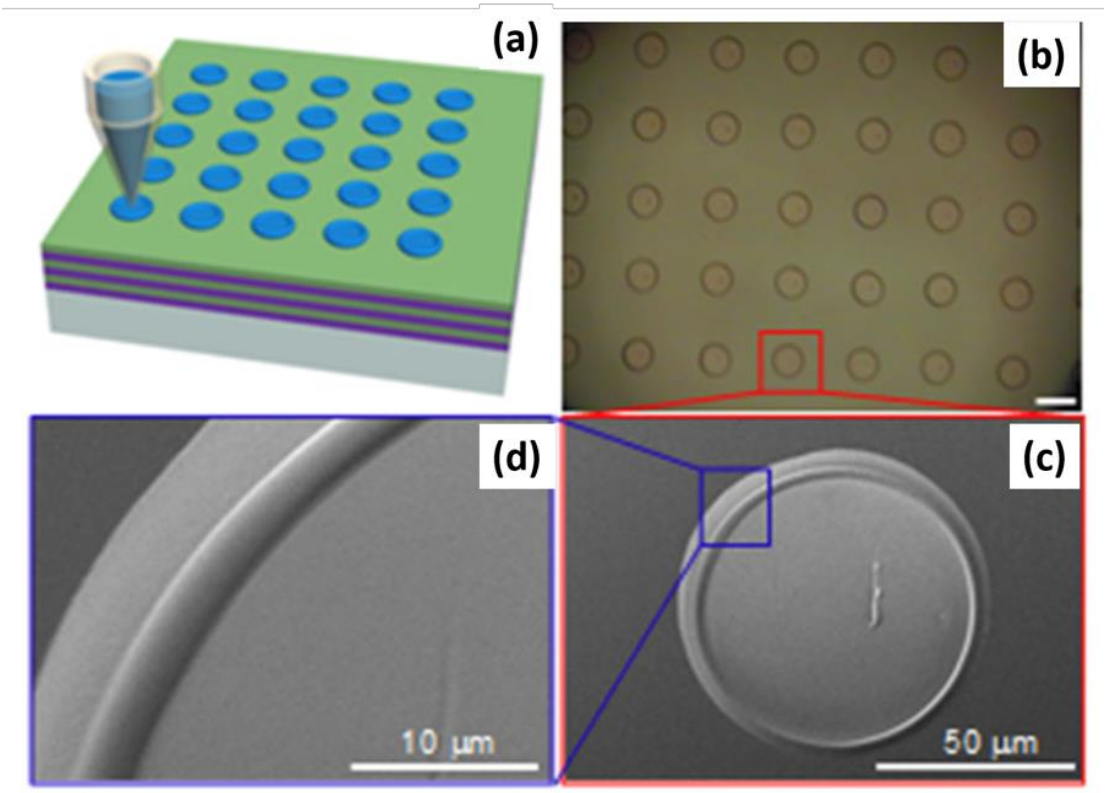

Figure 1.23 (a) Schematic illustrating how ink-jet printing can be used to fabricate quasitoroid microlasers from self-assembled CdZnS/ZnS QDs on top of a DBR substrate. (b) Optical microscopy image of arrays of fabricated quasitoroid structures. (c) SEM image of single quasitoroid structure. (d) Zoom-in SEM image of the rim form the quasitoroid structure. **(Images adapted from Ref 80)**

After drying, a ring wall appeared near the boundary due to the coffee-stain effect, suggesting the formation of a quasitoroid structure (**Figure 1.23c and d**). This quasitoroid structure can be a more favorable optical microcavity in comparison to disk with flat surface due to the better light confinement. Arrays of quasitoroid microlasers in assigned locations were successfully fabricated and possessed a high quality factor of ~2500, a value that is comparable to the abovementioned self-assembled QD-PMMA microbubbles.

1.2.3.4 Lithographically patterned structure

Although ink-jet printing is able to assign the location of QD microlasers, size of these self-assembled microcavities can not be controlled precisely due to the moderate resolution of ink-jet printing that is around 20-30 μm. Moreover, control of cavity geometry is also difficult for ink-jet printing due to the radially drying process that typically leads to patterns of circular shape. Cavity geometry is an important factor for the design of advanced optical microcavity since it can influence the mode activity and emission output significantly. For example, highly directional laser action has been demonstrated in elliptical microdisks with the addition of small notches, where light waves are scattered by the notch toward a preferential direction.[81] To precisely control these properties, microfabrication methods with the ability to modify size and geometry of QD based microcavity should be developed.

Researchers have attempted to fabricate QD based microcavities by using lithography process such as photolithography and EBL since it can provide very high resolution down to subwavelength scale.[82,83] Importantly, it can predefine the size and shape of microcavity precisely by creating a resist template of specific pattern and subsequent

filling or etching. Among recent examples, an attempt was made to fabricate microdisks of QDs sandwiched between silicon nitride (SiN) layers using a top-down approach with the assistance of photolithography (**Figure 1.24a**). The high transparency of SiN from blue to near-infrared region promises its use in low-loss photonic integrated circuits. To fabricate on-chip QD/SiN microcavity, a top-down CMOS-like process was adopted to preserve the optical properties of QDs and performance of microcavity in terms of quality factor. During the deposition of a tri-layer stack (SiN/QD/SiN), the spin-casted QD layer of 55 nm was sandwiched between high density SiN layers of 100nm deposited by using plasma enhanced chemical vapor deposition at 270 °C (**Figure 1.24b**).

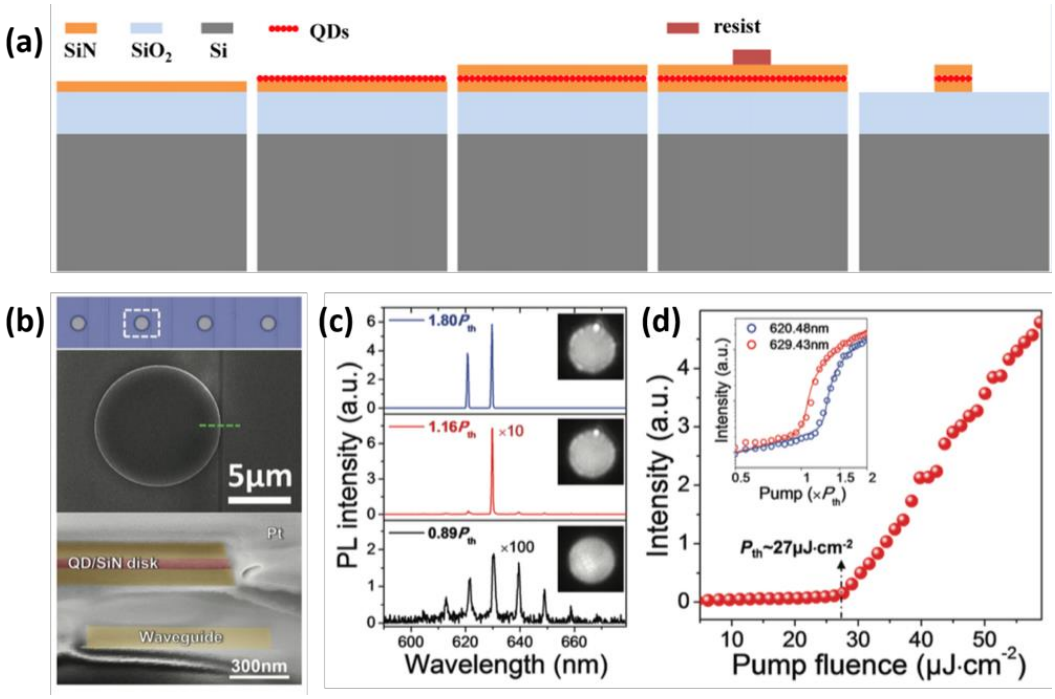

Figure 1.24 (a) Schematic showing the fabrication process of the SiN/QD/SiN microdisk laser. (b) Optical microscopy image of an array of SiN/QD/SiN microdisks. (top). SEM image of a SiN/QD/SiN microdisk and waveguide (middle). Falsed-color SEM image of cross section of microdisk and waveguide (bottom). (c) Lasing spectra of SiN/QD/SiN microdisk lasers under different pumping fluences where P_{th} is the pumping threshold. Insets show the PL images of SiN/QD/SiN microdisk lasers pumped under pulsed laser. (d) Integrated PL intensity versus pump fluence where a non-linear behavior was observed. Inset shows the relationship of integrated PL intensity versus pump fluence at different wavelengths. **(Images adapted from Ref 82,84)**

The resist template created using photolithography acted as a mask for the subsequent anisotropic reactive ion etching process to etch away the underlying SiN/QD/SiN layers. In this top-down approach, selection of gas species played an important role to obtain smooth side walls with a continuous surface. This is because the difference in material density between these three layers can results in different horizontal etching rate and hence sidewalls with a step-like profile. The combination of CF_4 and H_2 was found to give the best result in comparison to CF_4/O_2 or CF_4 due to the formation of a protective polymer layer in the presence of H_2 which enhanced the anisotropic etching in vertical direction.[84] This led to smoother sidewalls and therefore high quality factor of up to 5700 as well as very low lasing threshold of 27 $\mu J/cm^2$ (**Figure 1.24c and d)**.

1.2.4 Parity-time symmetric photonic systems

Optical gain within cavity leads to the light amplification while optical loss causes the attenuation of light. One may think intuitively that only optical gain can be beneficial to the development of advanced photonic lasers. In fact, a proposed theory, PT symmetry, suggests that optical loss can be also good in some cases to achieve unprecedented optical phenomena. PT symmetry describes systems that satisfy some requirements on the complex refractive index (**Figure 1.25**). The first requirement is to have the same real part "n" of the complex refractive index be an even function which can be expressed as "$n(x, \lambda) = n(-x, \lambda)$". The second requirement is the imaginary part "k" be an odd function which can be expressed as "$k(x, \lambda) = -k(-x, \lambda)$".[85] The imaginary part k is directly related to the amplification/absorption properties of the material. This indicates that in order to be an odd function k needs to be positive (absorption-loss) and negative (amplification-gain) in localized and symmetric regions.[86]

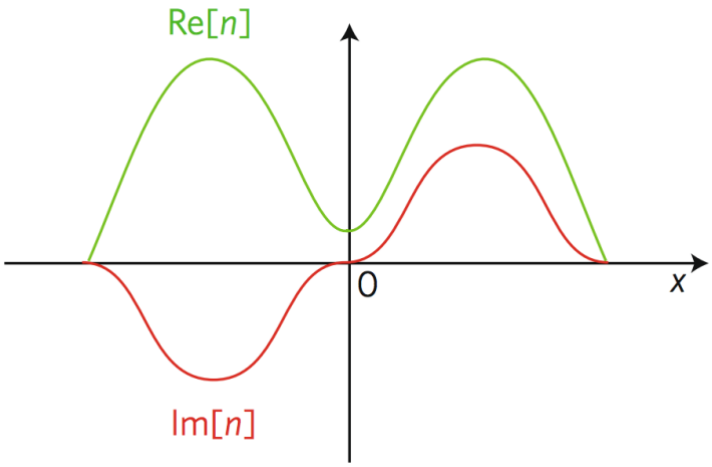

Figure 1.25 Schematic showing representative example (coupled waveguides) obeying parity-time symmetry where Re[n] and Im[n] are the real and imaginary parts of the refractive index variation n. **(Images adapted from Ref 85)**

As mentioned before, photonic cavities can provide valuable platforms to manipulate the optical modes and emission output within individual cavity. More importantly, photonic cavities may enable the development of novel photonic structures that judiciously utilize the evanescent field extending hundreds of nanometers from the cavity boundary to control mode activity and light transport. To achieve PT symmetry, it is common to place two photonic cavities in proximity so that they are coupled via the extending evanescent field. The modulation of gain/ loss values (γ) is typically accomplished by the optical pumping on localized regions. The control of gain and loss values within cavity can be important since the gain/loss contrast must match with the coupling strength (κ) between two cavities to achieve the exceptional point ($\gamma=\kappa$).[87]

QDs can be an ideal candidate since the gain and loss value can be potentially tuned by the change of optical or film properties such as emission/absorption position and QD packing fraction. In addition, the real part of complex refractive index can be easily

tuned in QD films by changing the ratio between organic ligands and inorganic cores. The tunable optical properties of QDs can accommodate all possible requirements that needs to be satisfied when designing novel PT structures. Recently, some impressive photonic structures of PT symmetry have exhibited intriguing optical phenomena including single-mode microring lasers, ultra-sensitive sensors, loss-induced Raman lasing and unidirectional invisibility.[87,88,89,90] For example, individual microring laser typically demonstrates multimode activity. By coupling with another lossy microring, only a specific mode can lase beyond the exceptional point while other modes are suppressed since they are under PT unbroken phase (**Figure 1.26a**).[87]

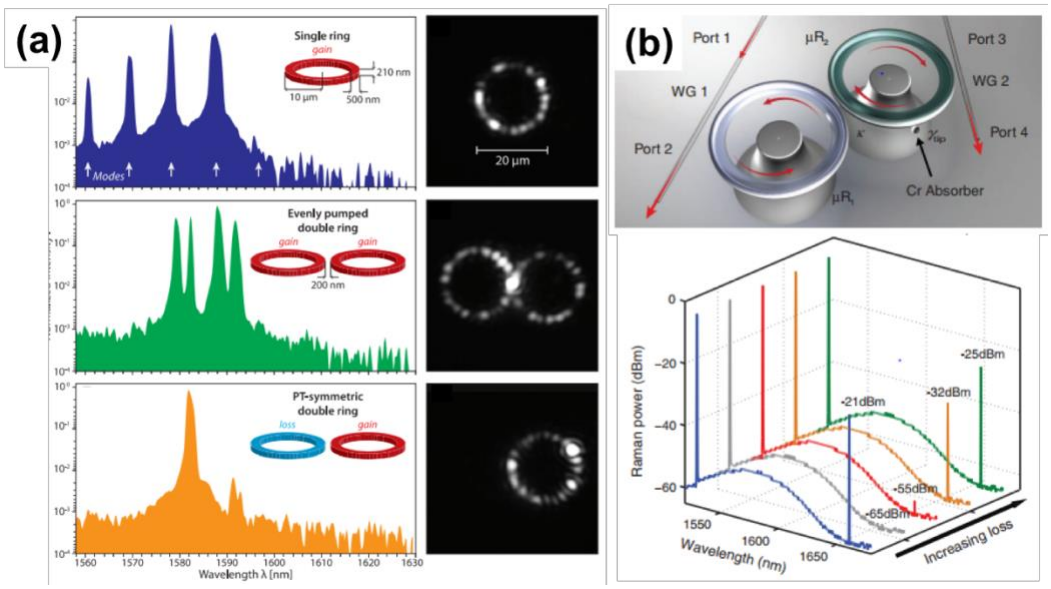

Figure 1.26 (a) Lasing spectra of single mciroring (top), coupled microrings that are both pumped (middle), coupled microrings (bottom) with only one being pumped. (b) Diagram of coupled optical PT resonators(top), lasing spectra showing the PT induced revival of Raman lasing with increasing losses (bottom). (**Reprint from Ref 87,89**)

Another work also demonstrates counterintuitive optical phenomenon due to PT symmetry. Generally, addition of optical loss to the microresonator typically suppress

the lasing intensity. However, it was found that optical loss can actually induce the revival of lasing within the PT symmetric microresonators (**Figure 1.26b**).[89] Abovementioned works clearly demonstrates unique optical phenomena can be achieved by carefully designed photonic structures with PT symmetry. Importantly, these unique properties may further support the development of future information processors, ultra-sensitive sensors and coherent perfect absorber and laser.

Furthermore, modulation of localized gain/loss values within cavities can also alter the optical activity significantly. This modulation can be important in PT systems since the gain/loss contrast needs to be matched with the coupling strength to achieve the exceptional point ($\gamma=\kappa$). When any pair of modes is below the exceptional point ($\gamma<\kappa$), it remains in the state of neutral oscillations (**Figure 1.27a**). (PT unbroken phase), where modes distribute equally in gain and loss region. Once the PT phase is broken ($\gamma>\kappa$), a conjugate pair of amplifying and decaying modes emerges (**Figure 1.27b**). By adjusting the pumping threshold, it is possible to select a specific pair of mode to undergo PT broken phase while others remain neutral.[91]

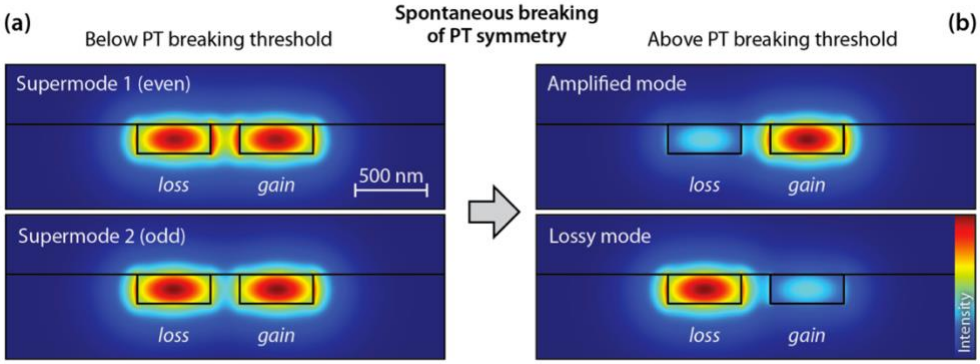

Figure 1.27 Transverse intensity distribution at the point of closest proximity between two cavities. (**Reprint from Ref 91**)

In addition, previous works have demonstrated intriguing phenomena can be achieved by altering the localized gain/loss values of photonic cavities. For example, a theoretical

work shows single mode and directional output can be achieved simultaneously in the individual microdisks if the gain/loss distribution within the cavity is stripe-like configuration.[92] Furthermore, laser and anti-laser can be achieved in single cavity by modulation of gain/loss distribution of single waveguide into periodic lattices (**Figure 1.28a**).[93] When it comes to the coupled photonic cavities, an experimental work has demonstrated the coupling induced mode splitting can be tuned via the modulation of gain/loss contrast within coupled cavities (**Figure 1.28b**).[91] These works indeed show that the modulation of gain and loss opens up a new avenue to tailor the optical activity of photonic structures significantly.

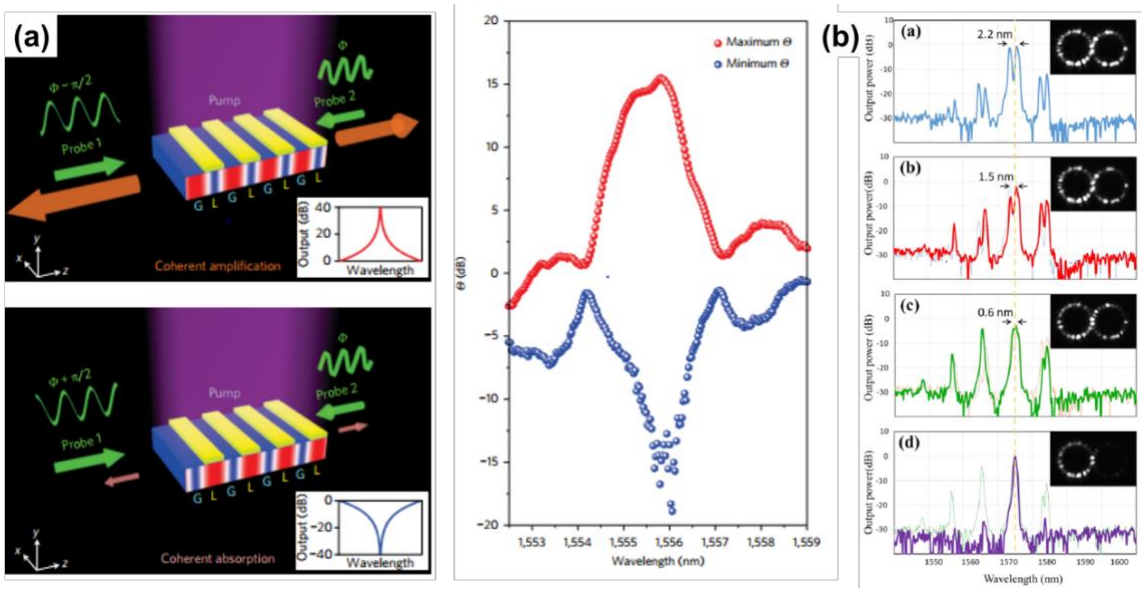

Figure 1.28 (a) Schematics illustrating CPA laser, where the gain/loss modulation is introduced by placing periodic loss structures on gain waveguide. The periodicity is designed to be half of the effective wavelength of guided light (left). The spectra of output coefficient Θ demonstrating amplification peak of 15 dB while the anti-lasing mode induced absorption down to -15 dB at around 1556nm. (**Reprint from Ref 88,93**)

1.3 Summary of critical issues and motivation

In summary, the current inorganic and organic systems have their own disadvantages such as restrictions on selection of materials/substrates and low photostability. In contrast, colloidal QDs consist of inorganic core and organic ligand shell can be advantageous over current systems since they can be dispersed in common organic solvents while their optical properties are stable and tunable. Indeed, a great amount of work has been done in the past to study the lasing phenomena of photonic nanostructures with different confinement conditions. However, extensive studies on how these photonic nanostructures can be affected by various system design including individual and assembled nanostructures, individual and coupled local assemblies (cavities) have been left unexplored.

For example, to improve the gain performance of QDs, most studies have focused on the sophisticated engineering of the core/shell structure in order to suppress the Auger recombination rate (AR).[42,49] To date, little attention has been paid to how modification of the ligand can affect gain performance and PL stability of the QD films.[94,95] This is in striking contrast to other fields where ligand engineering has attracted great attention since it can significantly improve device performance.[96,97,98,99] Moreover, some studies have shown that ligand engineering can be utilized to impart mechanical strength using bifunctional crosslinkers to form crosslinked and mechanically robust QD solids.[100,101] These studies all suggest that the ligand replacement can be an effective method to be explored to improve both the gain performance and the mechanical strength of the QD materials. However, the enhancement of these properties via the proper selection of ligands has not been realized to date.

Furthermore, a variety of QD cavities have been fabricated to date. However, these cavities in most cases are made by filling QDs into or coating QDs onto microcapillary tubes and silica microspheres. Although cavity modes were observed in these QD photonic structures, it is difficult to integrate these types of structures into on-chip photonic circuits, on flexible substrates, or over large-scale areas. In addition, current QD patterning techniques are lack of either scalability (EBL) or resolution (ink-jet printing). Among recent examples, lithographically patterned structure such as SiN/QD/SiN mcirodisk laser was a notable development. However, this approach requires careful selection and optimization of etching gas mixtures as well as a relatively expensive chemical vapor deposition system to deposit SiN layers. In addition, the high processing temperature for the deposition of SiN significantly reduced the photoluminescence intensity to 20% of the original intensity.[82] Clearly, fabrication methods that can precisely control dimensions of photonic cavity without deteriorating the photoluminescence of QDs should be developed in this work. Thus, the patterning technique should be up-scalable while preserving high resolution since PT symmetric systems requires the coupling between cavities and the fine modulation of localized regions to create gain/loss lattices.

Finally, QDs with flexible selection of structures, compositions and materials are very promising candidates for PT symmetric systems because the real refractive index, optical gain and emission position can be tuned while preserving their high quantum yield. In other words, the photoluminescence intensity of QD is not significantly quenched when tuning other optical properties. This make the design and modification of the PT symmetric systems that require modulation of magnitude of the n, k

components much easier. Overall, QD can provide flexibility in both material processing and optical properties to satisfy almost any requirements of PT symmetric that cannot be achieved in other systems facilely.

1.4 References (Chapter 1)

1 G. K. Kuang, I. C. Hernandez, M. McElhinney, L. Zeng, B. Caliva, R. Walker, *J. Cryst. Growth* **2004**, 268, 8.

2 O. Féron, M. Sugiyama, W. Asawamethapant, N. Futakuchi, Y. Feurprier, Y. Nakano, Y. Shimogaki, *Appl. Surf. Sci.* **2000**, 159-160, 318.

3 D. Beer, J. Weber, *Opt. Commun.* **1972**, 5, 307.

4 D. V. Talapin, J.-S. Lee, M. V. Kovalenko, E. V. Shevchenko, *Chem. Rev.* **2010**, 110, 389.

5 J. Pan, S. P. Sarmah, B. Murali, I. Dursun, W. Peng, M. R. Parida, J. Liu, L. Sinatra, N. Alyami, C. Zhao, E. Alarousu, T. K. Ng, B. S. Ooi, O. M. Bakr, O. F. Mohammed, *J. Phys. Chem. Lett* **2015**, 6, 5027.

6 G. Medeiros-Ribeiro, *physica status solidi (b)* **2002**, 230, 443.

7 J. Hu, T. W. Odom, C. M. Lieber, *Acc. Chem. Res.* **1999**, 32, 435.

8 W. W. Yu, X. Peng, *Angew. Chem. Int. Ed.* **2002**, 41, 2368.

9 A. B. Greytak, P. M. Allen, W. Liu, J. Zhao, E. R. Young, Z. Popovic, B. J. Walker, D. G. Nocera, M. G. Bawendi, *Chem. Sci.* **2012**, 3, 2028.

10 R. E. Bailey, A. M. Smith, S. Nie, *Physica E: Low-dimensional Systems and Nanostructures* **2004**, 25, 1.

11 B. O. Dabbousi, J. Rodriguez-Viejo, F. V. Mikulec, J. R. Heine, H. Mattoussi, R. Ober, K. F. Jensen, M. G. Bawendi, *J. Phys. Chem. B* **1997**, 101, 9463.

12 D. V. Talapin, R. Koeppe, S. Götzinger, A. Kornowski, J. M. Lupton, A. L. Rogach, O. Benson, J. Feldmann, H. Weller, *Nano Lett.* **2003**, 3, 1677.

13 O. Chen, J. Zhao, V. P. Chauhan, J. Cui, C. Wong, D. K. Harris, H. Wei, H.-S. Han, D. Fukumura, R. K. Jain, M. G. Bawendi, *Nat. Mater.* **2013**, 12, 445.

14 M. Nirmal, B. O. Dabbousi, M. G. Bawendi, J. J. Macklin, J. K. Trautman, T. D. Harris, L. E. Brus, *Nature* **1996**, 383, 802.

15 P. Frantsuzov, M. Kuno, B. Jankó, R. A. Marcus, *Nature Physics* **2008**, 4, 519.

16 M. Kuno, D. P. Fromm, A. Gallagher, D. J. Nesbitt, O. I. Micic, A. J. Nozik, *Nano Lett.* **2001**, 1, 557.

17 Y. Chen, J. Vela, H. Htoon, J. L. Casson, D. J. Werder, D. A. Bussian, V. I. Klimov, J. A. Hollingsworth, *J. Am. Chem. Soc.* **2008**, 130, 5026.

18 B. G. Jeong, Y.-S. Park, J. H. Chang, I. Cho, J. K. Kim, H. Kim, K. Char, J. Cho, V. I. Klimov, P. Park, D. C. Lee, W. K. Bae, *ACS Nano* **2016**, 10, 9297.

19 L. C. Schmidt, A. Pertegás, S. González-Carrero, O. Malinkiewicz, S. Agouram, G. Mínguez Espallargas, H. J. Bolink, R. E. Galian, J. Pérez-Prieto, *J. Am. Chem. Soc.* **2014**, 136, 850.

20 H. Huang, S. Susha Andrei, V. Kershaw Stephen, F. Hung Tak, L. Rogach Andrey, *Advanced Science* **2015**, 2, 15001

21 L. Protesescu, S. Yakunin, M. I. Bodnarchuk, F. Krieg, R. Caputo, C. H. Hendon, R. X. Yang, A. Walsh, M. V. Kovalenko, *Nano Lett.* **2015**, 15, 3692.

22 E. Yassitepe, Z. Yang, O. Voznyy, Y. Kim, G. Walters, A. Castañeda Juan, P. Kanjanaboos, M. Yuan, X. Gong, F. Fan, J. Pan, S. Hoogland, R. Comin, M. Bakr Osman, A. Padilha Lazaro, F. Nogueira Ana, H. Sargent Edward, *Adv. Funct. Mater.* **2016**, 26, 8757.

23 L. Protesescu, S. Yakunin, S. Kumar, J. Bär, F. Bertolotti, N. Masciocchi, A. Guagliardi, M. Grotevent, I. Shorubalko, M. I. Bodnarchuk, C.-J. Shih, M. V. Kovalenko, *ACS Nano* **2017**, 11, 3119.

24 S. Gonzalez-Carrero, R. E. Galian, J. Perez-Prieto, *J. Mater. Chem. A* **2015**, 3, 9187.

25 F. Zhang, H. Zhong, C. Chen, X.-g. Wu, X. Hu, H. Huang, J. Han, B. Zou, Y. Dong, *ACS Nano* **2015**, 9, 4533.

26 B. Luo, Y.-C. Pu, Y. Yang, S. A. Lindley, G. Abdelmageed, H. Ashry, Y. Li, X. Li, J. Z. Zhang, *J. Phys. Chem. C* **2015**, 119, 26672.

27 L. Protesescu, S. Yakunin, M. I. Bodnarchuk, F. Bertolotti, N. Masciocchi, A. Guagliardi, M. V. Kovalenko, *J. Am. Chem. Soc.* **2016**, 138, 14202.

28 G. Nedelcu, L. Protesescu, S. Yakunin, M. I. Bodnarchuk, M. J. Grotevent, M. V. Kovalenko, *Nano Lett.* **2015**, 15, 5635.

29 Q. A. Akkerman, V. D'Innocenzo, S. Accornero, A. Scarpellini, A. Petrozza, M. Prato, L. Manna, *J. Am. Chem. Soc.* **2015**, 137, 10276.

30 A. B. Wong, M. Lai, S. W. Eaton, Y. Yu, E. Lin, L. Dou, A. Fu, P. Yang, *Nano Lett.* **2015**, 15, 5519.

31 F. Palazon, Q. A. Akkerman, M. Prato, L. Manna, *ACS Nano* **2016**, 10, 1224.

32 P.T. Yu, M. Cardona, Fundamentals of semiconductors, physics and materials properties, 4th ed. Springer **2010**, chapter 7 emission spectroscopies.

33 S.T. Thornton, A. Rex, Modern physics for scientists and engineers, 3rd ed. Thomson Brooks/Colse **2006**, chapter 6: quantum mechanics.

34 V. I. Klimov, in *Annu. Rev. Phys. Chem.*, Vol. 58, 2007, 635.

35 K. D. Wegner, N. Hildebrandt, *Chem. Soc. Rev.* **2015**, 44, 4792.

36 A. M. Smith, S. Nie, *Acc. Chem. Res.* **2010**, 43, 190.

37 B. Herman, V.E. Frohlich, J.R. Lakowicz, D.B. Murphy, K.R. Spring, M.W. Davidson, Fluorescence microscopy: Basic concepts in fluorescence microscopy. National High Magnetic Field Laboratory, Florida State University, 2013.

38 P. Kambhampati, *J. Phys. Chem. Lett* **2012**, 3, 1182.

39 J. M. Pietryga, Y.-S. Park, J. Lim, A. F. Fidler, W. K. Bae, S. Brovelli, V. I. Klimov, *Chem. Rev.* **2016**, 116, 10513.

40 Y.-S. Park, W. K. Bae, T. Baker, J. Lim, V. I. Klimov, *Nano Lett.* **2015**, 15, 7319.

41 F. García-Santamaría, Y. Chen, J. Vela, R. D. Schaller, J. A. Hollingsworth, V. I. Klimov, *Nano Lett.* **2009**, 9, 3482.

42 V. I. Klimov, S. A. Ivanov, J. Nanda, M. Achermann, I. Bezel, J. A. McGuire, A. Piryatinski, *Nature* **2007**, 447, 441.

43 E. Yablonovitch, E. Kane, *J. Lightwave Technol.* **1986**, 4, 504.

44 F. Fan, O. Voznyy, R. P. Sabatini, K. T. Bicanic, M. M. Adachi, J. R. McBride, K. R. Reid, Y.-S. Park, X. Li, A. Jain, R. Quintero-Bermudez, M. Saravanapavanantham, M. Liu, M. Korkusinski, P. Hawrylak, V. I. Klimov, S. J. Rosenthal, S. Hoogland, E. H. Sargent, *Nature* **2017**, 544, 75.

45 N. Gaponik, G. Hickey Stephen, D. Dorfs, L. Rogach Andrey, A. Eychmüller, *Small* **2010**, 6, 1364.

46 M. T. Hill, M. C. Gather, *Nat. Photonics* **2014**, 8, 908.

47 A. Costela, O. García, L. Cerdán, I. García-Moreno, R. Sastre, *Opt. Express* **2008**, 16, 7023.

48 V. I. Klimov, A. A. Mikhailovsky, S. Xu, A. Malko, J. A. Hollingsworth, C. A. Leatherdale, H. J. Eisler, M. G. Bawendi, *Science* **2000**, 290, 314.

49 C. Dang, J. Lee, C. Breen, J. S. Steckel, S. Coe-Sullivan, A. Nurmikko, *Nat. Nanotech.* **2012**, 7, 335.

50 K. L. Shaklee, R. F. Leheny, *Appl. Phys. Lett.* **1971**, 18, 475.

51 A. V. Malko, A. A. Mikhailovsky, M. A. Petruska, J. A. Hollingsworth, H. Htoon, M. G. Bawendi, V. I. Klimov, *Appl. Phys. Lett.* **2002**, 81, 1303.

52 F. Todescato, I. Fortunati, S. Gardin, E. Garbin, E. Collini, R. Bozio, J. J. Jasieniak, G. Della Giustina, G. Brusatin, S. Toffanin, R. Signorini, *Adv. Funct. Mater.* **2012**, 22, 337.

53 W. Song Katherine, R. Costi, V. Bulović, *Adv. Mater.* **2012**, 25, 1420.

54 A. Gole, N. R. Jana, S. T. Selvan, J. Y. Ying, *Langmuir* **2008**, 24, 8181.

55 G. I. Koleilat, L. Levina, H. Shukla, S. H. Myrskog, S. Hinds, A. G. Pattantyus-Abraham, E. H. Sargent, *ACS Nano* **2008**, 2, 833.

56 B. H. Kim, M. S. Onses, J. B. Lim, S. Nam, N. Oh, H. Kim, K. J. Yu, J. W. Lee, J.-H. Kim, S.-K. Kang, C. H. Lee, J. Lee, J. H. Shin, N. H. Kim, C. Leal, M. Shim, J. A. Rogers, *Nano Lett.* **2015**, 15, 969.

57 M. K. Choi, J. Yang, K. Kang, D. C. Kim, C. Choi, C. Park, S. J. Kim, S. I. Chae, T.-H. Kim, J. H. Kim, T. Hyeon, D.-H. Kim, *Nat. Comm.* **2015**, 6, 7149.

58 K. Y. Suh, H. H. Lee, *Adv. Funct. Mater.* **2002**, 12, 405.

59 L. Kim, P. O. Anikeeva, S. A. Coe-Sullivan, J. S. Steckel, M. G. Bawendi, V. Bulović, *Nano Lett.* **2008**, 8, 4513.

60 A. Rizzo, M. Mazzeo, M. Palumbo, G. Lerario, S. D'Amone, R. Cingolani, G. Gigli, *Adv. Mater.* **2008**, 20, 1886.

61 W. Xie, R. Gomes, T. Aubert, S. Bisschop, Y. Zhu, Z. Hens, E. Brainis, D. Van Thourhout, *Nano Lett.* **2015**, 15, 7481.

62 S. T. Malak, Y. J. Yoon, M. J. Smith, C. H. Lin, J. Jung, Z. Lin, V. V. Tsukruk, *ACS Photonics* **2017**, 4, 1691.

63 S. T. Malak, M. J. Smith, Y. J. Yoon, C. H. Lin, J. Jung, Z. Lin, V. V. Tsukruk, *Adv. Opt. Mater.* **2017**, 5, 1600509.

64 S. T. Malak, J. Jung, Y. J. Yoon, M. J. Smith, C. H. Lin, Z. Lin, V. V. Tsukruk, *Adv. Opt. Mater.* **2016**, 4, 608.

65 Q. J. Wang, C. Yan, N. Yu, J. Unterhinninghofen, J. Wiersig, C. Pflügl, L. Diehl, T. Edamura, M. Yamanishi, H. Kan, F. Capasso, *Proc. Natl. Acad. Sci. USA* **2010**, 107, 22407.

66 S. W. Eaton, A. Fu, A. B. Wong, C.-Z. Ning, P. Yang, *Nature Reviews Materials* **2016**, 1, 16028.

67 Z. Xu, Q. Liao, X. Wang, H. Fu, *Adv. Opt. Mater.* **2014**, 2, 1160.

68 S. Yang, Y. Wang, H. Sun, *Adv. Opt. Mater.* **2015**, 3, 1136.

69 C. Grivas, C. Li, P. Andreakou, P. Wang, M. Ding, G. Brambilla, L. Manna, P. Lagoudakis, *Nat. Comm.* **2013**, 4, 2376.

70 S. Hoogland, V. Sukhovatkin, I. Howard, S. Cauchi, L. Levina, E. H. Sargent, *Opt. Express* **2006**, 14, 3273.

71 S. Yakunin, L. Protesescu, F. Krieg, M. I. Bodnarchuk, G. Nedelcu, M. Humer, G. De Luca, M. Fiebig, W. Heiss, M. V. Kovalenko, *Nat. Comm.* **2015**, 6, 8056.

72 Y. Chan, J. S. Steckel, P. T. Snee, J. M. Caruge, J. M. Hodgkiss, D. G. Nocera, M. G. Bawendi, *Appl. Phys. Lett.* **2005**, 86, 073102.

73 P. T. Snee, Y. Chan, D. G. Nocera, M. G. Bawendi, *Adv. Mater.* **2005**, 17, 1131.

74 Y. Wang, X. Li, J. Song, L. Xiao, H. Zeng, H. Sun, *Adv. Mater.* **2015**, 27, 7101.

75 Y. Xu, Q. Chen, C. Zhang, R. Wang, H. Wu, X. Zhang, G. Xing, W. W. Yu, X. Wang, Y. Zhang, M. Xiao, *J. Am. Chem. Soc.* **2016**, 138, 3761.

76 M. A. Petruska, A. V. Malko, P. M. Voyles, V. I. Klimov, *Adv. Mater.* **2003**, 15, 610.

77 Y. Wang, S. Yang, H. Yang, H. Sun, *Adv. Opt. Mater.* **2015**, 3, 652.

78 D. Ta Van, R. Chen, D. Sun Han, *Adv. Mater.* **2012**, 24, OP60.

79 Y. Wang, V. D. Ta, K. S. Leck, B. H. I. Tan, Z. Wang, T. He, C.-D. Ohl, H. V. Demir, H. Sun, *Nano Lett.* **2017**, 17, 2640.

80 Y. Wang, E. Fong Kah, S. Yang, Van D. Ta, Y. Gao, Z. Wang, V. Nalla, V. Demir Hilmi, H. Sun, *Laser Photonics Rev.* **2015**, 9, 507.

81 Q. J. Wang, C. Yan, N. Yu, J. Unterhinninghofen, J. Wiersig, C. Pflügl, L. Diehl, T. Edamura, M. Yamanishi, H. Kan, F. Capasso, *Proc. Natl. Acad. Sci. USA* **2010**, 107, 22407.

82 W. Xie, T. Stöferle, G. Rainò, T. Aubert, S. Bisschop, Y. Zhu, F. Mahrt Rainer, P. Geiregat, E. Brainis, Z. Hens, D. Van Thourhout, *Adv. Mater.* **2017**, 29, 1604866.

83 B. le Feber, F. Prins, E. De Leo, F. T. Rabouw, D. J. Norris, *Nano Lett.* **2018**, 18, 1028.

84 W. Xie, Y. Zhu, T. Aubert, S. Verstuyft, Z. Hens, D. Van Thourhout, *Opt. Express* **2015**, 23, 12152.

85 L. Feng, R. El-Ganainy, L. Ge, Nat. Photonics 2017, 11, 752.

86 R. El-Ganainy, K. G. Makris, D. N. Christodoulides, Z. H. Musslimani, *Opt. Lett.* **2007**, 32, 2632.

87 H. Hodaei, M.-A. Miri, M. Heinrich, D. N. Christodoulides, M. Khajavikhan, *Science* **2014**, 346, 975.

88 J. Ren, H. Hodaei, G. Harari, A. U. Hassan, W. Chow, M. Soltani, D. Christodoulides, M. Khajavikhan, *Opt. Lett.* **2017**, 42, 1556.

89 B. Peng, Ş. K. Özdemir, S. Rotter, H. Yilmaz, M. Liertzer, F. Monifi, C. M. Bender, F. Nori, L. Yang, *Science* **2014**, 346, 328.

90 Z. Lin, H. Ramezani, T. Eichelkraut, T. Kottos, H. Cao, D. N. Christodoulides, *Phys. Rev. Lett.* **2011**, 106, 213901.

91 H. Hodaei, M. A. Miri, A. U. Hassan, W. E. Hayenga, M. Heinrich, D. N. Christodoulides, M. Khajavikhan, *Opt. Lett.* **2015**, 40, 4955.

92 Q. Song, J. Li, W. Sun, N. Zhang, S. Liu, M. Li, S. Xiao, *Opt. Express* **2015**, 23, 24257.

93 Z. J. Wong, Y.-L. Xu, J. Kim, K. O'Brien, Y. Wang, L. Feng, X. Zhang, *Nat. Photonics* **2016**, 10, 796.

94 S. Hoogland, V. Sukhovatkin, I. Howard, S. Cauchi, L. Levina, E. H. Sargent, *Opt. Express* **2006**, 14, 3273.

95 V. Sukhovatkin, S. Musikhin, I. Gorelikov, S. Cauchi, L. Bakueva, E. Kumacheva, E. H. Sargent, *Opt. Lett.* **2005**, 30, 171.

96 G. I. Koleilat, L. Levina, H. Shukla, S. H. Myrskog, S. Hinds, A. G. Pattantyus-Abraham, E. H. Sargent, *ACS Nano* **2008**, 2, 833.

97 J. M. Luther, M. Law, Q. Song, C. L. Perkins, M. C. Beard, A. J. Nozik, *ACS Nano* **2008**, 2, 271.

98 N. Zhao, T. P. Osedach, L.-Y. Chang, S. M. Geyer, D. Wanger, M. T. Binda, A. C. Arango, M. G. Bawendi, V. Bulovic, *ACS Nano* **2010**, 4, 3743.

99 M. H. Zarghami, Y. Liu, M. Gibbs, E. Gebremichael, C. Webster, M. Law, *ACS Nano* **2010**, 4, 2475.

100 B. Kowalczyk, M. Apodaca Mario, H. Nakanishi, K. Smoukov Stoyan, A. Grzybowski Bartosz, *Small* **2009**, 5, 1970.

101 H. Schlicke, D. Battista, S. Kunze, C. J. Schröter, M. Eich, T. Vossmeyer, *ACS Appl. Mater. Interfaces* **2015**, 7, 15123.

CHAPTER 2

RESEARCH GOALS, TECHNICAL OBJECTIVES, AND DISSERTATION OVERVIEW

2.1 Research goals

The primary goal of this research is to understand and control fundamental light-matter interactions in three hierarchical levels of hybrid organic and inorganic photonic systems: individual and assembled nanostructures, individual and coupled cavities. We aim to utilize quantum confined nanostructures as the optically active components to build up robust and stable planar films and photonic structures with highly tunable optical properties such as refractive index, broad-band absorption and emission. Furthermore, methods will be proposed to control fundamental lasing properties of planar films and photonic structures including optical gain value, lasing threshold, stable lasing output, mode activity and emission output direction. Understanding the abovementioned properties can be significant in the design of advanced photonic system that is proper for PT symmetry, where control of refractive index and gain/loss values is required to achieve PT symmetry. These PT symmetric photonic systems can exhibit unique properties like asymmetric energy transfer, unidirectional light propagation, and single mode lasing, loss-less unidirectional reflection, further supporting the development of synthetic photonic systems enabling control of light propagation, mode manipulation and light intensity modulation.

In addition to the investigation of the fundamental optical and lasing properties, promising and reliable methods are used to fabricate large scale and robust optical cavities with controllable spatial distribution including dimensions, locations and geometries. Furthermore, another focus is placed on the fabrication of coupled optical

cavities with modulated gain/loss values and geometries that is desired to facilitate the energy transfer between these assemblies. These microfabrication techniques can be useful in wide applications particularly in light-emitting diodes, lasers and photodetectors that may require high resolution arrays in large area.

2.2 Technical objectives

As discussed above, the main research goal in this work is to understand the light-matter interactions in different hierarchical levels from individual nanostructures to different large-scale arrangement of nanostructure assemblies. To fully investigate all the possible optical properties that can be manipulated, this research can be presented into three tasks (**Figure 2.1**).

Task 1 *concentrates on the investigation and tuning of optical properties and gain performance of individual and assembled nanostructures by adopting core/shell and ligand engineering. Emphasis is placed on how the quantum yield of individual QDs can be maximized via the shell passivation and how the arrangement of assembled nanostructures can affect the refractive index, optical gain/loss values and photostability.*

Task 2 *concentrates on the promising microfabrication techniques that help fabricate individual assemblies with controllable lasing properties such as mode activity and directional lasing output. Specifically, up-scalable microfabrication method is proposed to fabricate individual assemblies with controllable dimensions and geometry that can be important to alter the fundamental light-matter interactions of the structure.*

Task 3 *concentrates on high resolution fabrication method that is used to fabricate coupled cavities with controllable coupling strength, enabling the control of energy transfer between coupled assemblies.* In addition, *non-physical method is developed to manipulate the gain/loss values in localized regions. Furthermore, we also investigate how the manipulation of gain/loss values may lead to intriguing optical phenomena which have not been observed in the past.*

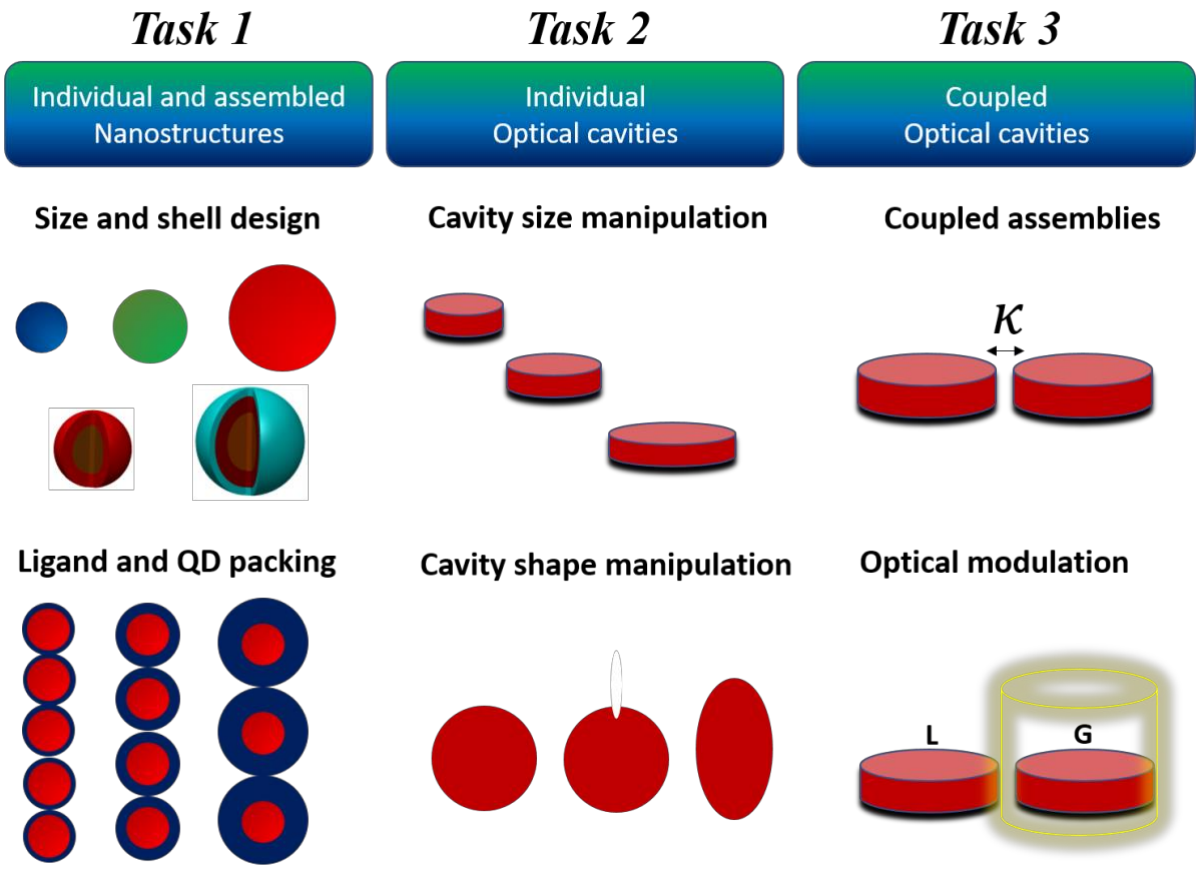

Figure 2.1 Research tasks at different hierarchical levels that are investigated and developed to understand fundamental light-matter interactions at each level of QD photonic sources from individual and assembled nanostructures to individual and coupled optical QD cavities.

These above-mentioned tasks will be broken down into specific objectives below.

Task 1: Individual and assembled nanostructures

- Measure and control optical properties of QD including emission/absorption peak position and quantum yield of core and core-graded shell QDs of different sizes, before and after ligand exchange procedures to determine how the properties of QDs can be manipulated.
- Adopt suitable core/shell structures to synthesize QD materials with well-passivated surface, high quantum yield and suppressed auger recombination while establish measurement procedures to characterize these optical properties correctly.
- Systematically investigate how the replacement of ligand via ligand exchange process affect the QD loading, refractive index, optical gain/loss values and surface roughness of films.
- Create criteria for the selection of ligands to identify appropriate ligand component for the improvement of QD gain performance such as low lasing threshold, high optical gain, low optical loss and stable lasing output.

Task 2: Individual optical cavities

- Develop microfabrication technique that allows for the fabrication of QD based cavities with controllable dimensions and lasing properties combined with long-term photostability.
- Establish characterization methods to examine the lasing properties of fabricated assemblies including quality factor, lasing threshold, cavity mode activity and effective refractive index.

- Investigate how the geometry of the cavities including circle and ellipsoid can affect the mode activity and lasing output direction of photonic structures.
- Investigate how the size of engineered defects can affect the mode activity and lasing output direction of photonic structures.

Task 3: Coupled optical cavities

- Develop reliable fabrication method that allows for coupling between coupled photonic structures.
- Develop methods that can manipulate gain and loss values in localized regions to achieve the balance between gain/loss contrast and coupling strength (exceptional point).
- Study how the manipulation of gain/loss contrast can affect light-matter interactions like light propagation, coupling, intensity, and emission direction with the aim to establish guiding principles for the development of devices that exhibit novel phenomena.

2.3 Organization and composition of dissertation

Chapter 1 provides a comprehensive review of literature which involves QDs. Synthesis routes including core/shell engineering as well as the fundamental exciton dynamics of QDs are discussed. Different aspects of QD assembly including optical gain systems, deposition, patterning and microfabrication techniques are also detailed. The overview of the PT symmetric photonic system is provided lastly.

Chapter 2 outlines the research goals and technical objectives of this dissertation. Brief descriptions of the organization and each chapters of this dissertation are also provided.

Chapter 3 outlines all different experimental techniques used in this dissertation including materials, synthesis of QDs, ligand exchange process, film deposition, microfabrication of QD patterns FDTD modeling, and various characterization methods.

Chapter 4 outlines a robust preparative strategy to craft a set of CdSe/$Cd_{1-x}Zn_xSe_{1-y}S_y$ core/graded shell QDs and CdSe/$Cd_{1-x}Zn_xSe_{1-y}S_y$/ZnS core/graded shell/shell QDs with suppressed re-absorption and reduced Auger recombination, larger quantum yield, and tunable Stokes shift. The as-synthesized CdSe/$Cd_{1-x}Zn_xSe_{1-y}S_y$ and CdSe/$Cd_{1-x}Zn_xSe_{1-y}S_y$/ZnS QDs exhibited unique optical properties as a direct consequence of the delocalization of electron wave function over the entire QD. Furthermore, the deposition of thicker outermost ZnS shell resulted in the progressive red-shift of emission peak and the effective suppression of the first absorption peak from innermost CdSe QD core, thereby leading to suppressed re-absorption of CdSe core and tunable Stoke shift in CdSe/$Cd_{1-x}Zn_xSe_{1-y}S_y$/ZnS QDs.

Chapter 5 examines how the molecular dimensions and chemical functionality of the organic ligands of QDs can be explored for the improvement of film properties including QD loading, refractive index and optical gain values.

Chapter 6 reports a method that utilizes bifunctional crosslinkers to impart mechanical robustness to QD films while preserving high optical gain. These tethered QD solid films display very high net optical gain as high as 650 cm^{-1} combined with low pump excitation gain threshold of 44 $\mu J/cm^2$. In addition, the functionalization of the QDs using short-

chain bifunctional crosslinkers provides stable passivation of the QDs which imparts excellent mechanical robustness and chemical resistance to solvents.

Chapter 7 report the facile on-chip fabrication of $CdSe/Cd_{1-x}Zn_xSe_{1-y}S_y$ quantum dots microdisk lasers and their large-area arrays via a pattern-assisted layer-by-layer assembly process. This approach combines the versatility of colloidal semiconducting nanoparticles (bright emission, solubility, and high stability) with the spatial precision of optical lithography to create robust large-area optical lasing arrays.

Chapter 8 reports a high-resolution and high throughput orthogonal lithography approach for patterning of all inorganic perovskite $CsPbX_3$ (X= Cl, Br, I) quantum dots. The reported method utilizes the combination of fluorinated polymer and solvent to provide the orthogonality to the $CsPbX_3$ QD during the lift-off process.

Chapter 9 outlines the study of notched and elliptical microdisk lasers. The spectral and directional properties of notched and elliptical microdisk lasers were investigated by characterizing the laser emission spectra under optical pumping and angular dependent laser emission measurements.

Chapter 10 studies the effect of gain/loss modulation in evanescently coupled microdisks of solution-processed quantum dots. Varying the gain differential between such disks by optical modulation leads to coalescence of parasitic intra-cavity modes that result from material inhomogeneity.

Chapter 11 summarizes the general results and conclusions discussed in chapter 4-10. In addition, the scientific significance in the field and the impact to the future development of potential applications are also provided.

CHAPTER 3

EXPERIMENTAL TECHNIQUES AND MATERIALS

3.1 Quantum dots for lasing

3.1.1 Chemicals and materials

Cadmium oxide, tri-n-octylphosphine (TOP, 90%), ethyl lactate and selenium powder, were obtained from Sigma Aldrich. 1-tetradecylphosphonic acid (TDPA, 98%), tri-n-octylphosphine oxide (TOPO, 90%), diethylzinc (15 weight% in hexane), cesium acetate (99.9%), lead acetate trihydrate (99.995%) and tetra-n-octylammonium bromide (TOABr) (98+%) were obtained from Alfa Aesar. 1-octadecene (ODE, 90%), hexadecylamine (HDA, 90%), butylamine (BA, 98%), oleic acid (OA, 97%), and bis(trimethylsilyl) sulfide (95%) were obtained from TCI. 1,7 diaminoheptane (DIAH, 98%) and ethyl lactate was obtained from Sigma Aldrich. Hexane, acetone, toluene (ACS reagent grade) and heptane were obtained from BDH Chemicals. CYTOP was obtained from AGC Chemicals. NR 71-3000p photoresist was purchased from Futurrex. OSCoR SL 1 (fluorinated polymer), thinning solvent 700 and Orthogonal Stripper 700 (fluorinated stripper) were purchased from Orthogonal, Inc. All chemicals were used as received.

3.1.2 Synthesis of $CdSe/Cd_{1-x}Zn_xSe_{1-y}S_y$ core/graded shell QDs

Chemical composition gradient $CdSe/Cd_{1-x}Zn_xSe_{1-y}S_y$ core/graded-shell QDs were synthesized by modifying reported methods and provided by collaborators (Prof. Lin's group, School of Materials Science and Engineering, Georgia Institute of Technology).[1] Briefly, 0.2 mmol of CdO, 4 mmol of $Zn(acetate)_2$, 5 ml of oleic acid, and 15 ml of 1-octadecene (ODE) were placed in a three-neck flask and degassed at 150°C for 1 hr. The reaction was heated to 300°C under Ar. At the elevated temperature (300°C),

1 mmol of Se and 4 mmol of S in 2 ml of TOP were rapidly injected into the reaction vessel. The reaction was allowed to proceed at 300°C for 10 minutes, and then the heating mantle was removed to stop reaction. 5 ml of hexane was added to the solution once the temperature reached 70°C.

3.1.3 Ligand exchange process

The oleic acid-capped CdSe/$Cd_{1-x}Zn_xSe_{1-y}S_y$ QDs were centrifuged with acetone three times to remove excess oleic acid and ODE. Subsequently, purified oleic acid-capped CdSe/$Cd_{1-x}Zn_xSe_{1-y}S_y$ QDs were re-dispersed in hexane and an excess amount of hexadecylamine, octylamine, butylamine was added to perform the solution-phase ligand exchange. The ligand exchange reaction was allowed to proceed at 45℃ for 1 day. The solution was then precipitated using methanol and re-dispersed in a mixture of hexane and an excess ligand amount. This procedure was repeated for three times.[7]

The solid-state exchange is performed by soaking the prepared butylamine-capped QD films in a 0.1 M methanol solution of 1,7 diaminoheptane for 1 hour. After soaking, the films are washed with methanol 3 times to remove any excess 1,7 diaminoheptane. It was observed that the QD loading did not significantly change during the networking step (53% to 49%), which may be due to the similar length of two BA ligands and the length of one DIAH ligand if the ligands are fully extended between adjacent QD surfaces.[7]

3.1.4 Synthesis of $CsPbBr_3$ QDs

$CsPbBr_3$ QDs were synthesized by modifying the reported method.[2] 1 mmol of cesium acetate, 2 mmol of lead acetate trihydrate, 5 ml of ODE, and 2 ml of OA is added into a three neck flask. The solution is vacuum dried at 100°C for 30 minutes and then changed to argon atmosphere at 75°C. 2 mmol of TOABr is dissolved in anhydrous toluene and oleic acid. The TOABr solution is injected into the three-neck flask. After 10 seconds, the heating mantle is removed and cooled in a water bath. The as-prepared $CsPbBr_3$ QD solution was purified by adding acetone at a ratio of 1:2 (toluene:acetone) and subsequently centrifuged at 10000 rpm for 30 min. This washing step was performed twice. The supernatant was discarded and the purified $CsPbBr_3$ QDs were redispersed in heptane (2 ml). The QD solution was centrifuged at 8000 rpm for 10 min to remove any possible aggregates in solution and the remaining supernatant was used as the final $CsPbBr_3$ QD solution.

3.2 Film deposition & patterning methods

3.2.1 Preparation of QD films

QD films are fabricated by spin-coating a QD heptane solution of ~60 mg/mL at 1000 rpm for 1 minute. The film thickness ranged from 150-250 nm in order to support only the first waveguide mode. The QD films were deposited on CYTOP (AGC Chemicals) coating, which has a sufficiently low refractive index (n_{650} = 1.34) to provide light confinement and waveguiding within the QD film. The CYTOP was exposed to air or Ar plasma for 5 seconds in order to improve the wetting of CYTOP by QDs. Silicon, with a 290-295 nm thick SiO_2 surface layer, was used as a substrate since its large extinction coefficient attenuates much of the light that leaks into the substrate. The

attenuation of light that leaks from the QD film into the Si substrate ensures that the light detected at the edge is the light that has propagated through the QD film. The substrate was cleaved to obtain sharper, cleaner edges to improve the intensity of the output light and ensure that the area of the film exposed to the pump light was uniform over the length of the pump strip length.

3.2.2 Patterning of Cd-based QD microdisk lasers

The patterning process used for fabricating QD microdisks includes several stages. First, a low refractive index layer of CYTOP (n = 1.34) was deposited on the Si wafer (n = 3.44) in order to provide light confinement within the QD cavities. A short oxygen plasma etch (5 seconds) was performed to improve the wettability of the CYTOP surface for the deposition of the negative photoresist (NR 71-3000p). Ethyl lactate was added to the negative resist NR71-3000p solution to dilute it to one third of the original concentration provided by the company. The diluted resist was spun cast on the silicon substrate (3000 rpm for 1 minute). The cast film was subsequently soft baked at 165℃ for 5 minutes and exposed to 365 nm with a dosage of 123mW. The exposed film was then post-baked at 100℃ for 5 minutes and developed by soaking in RD6 developer for 5 sec. After the development, the film was rinsed with water and dried by blowing with air. The QD microdisks were fabricated by spin casting butylamine-capped QD solution (in heptane) of ~3-6 mg/mL at 1000 rpm for 1 minute onto the polymer pattern. The cast layer was subsequently immersed in 0.1M diaminoheptane solution in methanol for 1 minute and rinsed with methanol 2 times while spinning at 3000 rpm for 1 minute. The above process was repeated multiple times to achieve the desired thickness. The

polymer pattern was subsequently removed by soaking in acetone while sonicating for 3-10 seconds.

3.2.3 Orthogonal lithography patterning process

The patterning process used for fabricating QD patterns includes several stages. First, thinning solvent 700 was added to the OSCoR SL 1 resist solution to dilute it to half of the original concentration provided by the company. The diluted resist was spun cast on the silicon substrate to form a 400nm thick film (2000 rpm for 1 min). The cast film was baked at 100℃ for 1 min to remove the residual solvent. Short oxygen plasma etching (5 sec) was performed to improve the wettability of the OSCoR SL 1 film surface for the deposition of the negative photoresist (NR 71-3000 p). Ethyl lactate was added to the negative resist NR71-3000p solution to dilute it to one third of the original concentration provided by the company. The diluted resist was spun cast on top of OSCoR SL 1 film surface (3000 rpm for 1 minute). The cast film was subsequently soft baked at 100℃ for 5 minutes and exposed to 365 nm with a dosage of 123mW. The exposed film was then post-baked at 100℃ for 5 minutes and developed by soaking in RD6 developer for 5 sec.

After the development, the film was rinsed with water and dried by blowing with air. Plasma etching (300W) with fixed gas flow at 45 sccm (O_2) and 5 sccm (Ar) was performed for 60 seconds in order to etch the underlying OSCoR SL 1 resist. $CsPbBr_3$ QD solution was spun cast (1000rpm for 1 minute) on the patterned templates. The sample was subsequently immersed into Orthogonal Stripper 700 for an hour to dissolve the OSCoR SL 1 resist and lift off the photoresist along with the attached $CsPbBr_3$ QD

assemblies. To fabricate QD microdisk arrays, a low refractive index layer of CYTOP (n = 1.34, 1.5μm thick) was deposited on the Si wafer (n = 3.44) prior to the deposition of OSCoR SL 1 resist, in order to provide light confinement within the QD cavities.

3.3 Fourier transform infrared spectroscopy (FTIR)

ATR-FTIR measurements of crosslinked and non-crosslinked QD films were conducted using a Bruker FTIR spectrometer Vertex 70 equipped with a narrow-band mercury cadmium telluride detector in accordance with a procedure described previously.[3] Non-crosslinked QD films were deposited on the silica crystal by spin coating 30 μL of a butylamine (BA)-capped QD heptane solution at 1000 rpm for 1 minute. After the measurement of non-crosslinked QD films, the as-deposited film was soaked in a 0.1 M methanol solution of 1,7 diaminoheptane (DIAH) to perform the solid-state ligand exchange. FTIR spectra were collected in the range of 4000-900 cm^{-1} with a resolution 1 cm^{-1}. An accumulation of 10 scans was analyzed to confirm the successful chemical transformation.

3.4 Thermal gravimetric analysis (TGA)

The mass fraction of the QDs in solution was determined by analyzing the amount of mass present versus temperature using a thermal gravimetric analysis (TGA) instrument (TA Instruments TGA Q50) with a 100 uL open platinum pan. Samples were analyzed by first equilibrating at 30°C followed by ramping of the temperature to 600°C using a 10°C/min temperature profile under a constant flow of nitrogen. Volume fractions of the organic and inorganic components were calculated using the bulk density of each

component. TGA measurements were typically made by Marcus Smith (Prof. Vladimir Tsukruk's group, Georgia Institute of Technology).

3.5 Nuclear magnetic resonance (NMR)

Nuclear magnetic resonance was used to examine how effectively the new QD ligand displaced the original QD ligand by examining changes in peak intensity, shifts in peak position, and the emergence of new peaks. Measurements were made using a Varian Mercury 400 NMR instrument with samples in deuterated chloroform. All NMR measurements were performed by our collaborators (Dr. Jaehan Jung in Prof. Lin's research group, Georgia Institute of Technology).

3.6 SEM / TEM

SEM characterization was performed on a Hitachi S-3400N SEM with a back scattered electron detector with an accelerating voltage in the range of 5-10 kV.

The interparticle distance and size of CdSe/$Cd_{1-x}Zn_xSe_{1-y}S_y$ QDs was studied using a high-resolution transmission electron microscope (Tecnai F30). An accelerating voltage of 300 keV was used. TEM samples were prepared by diluting the original QD solution of ~6 mg/mL 30 times. 5-10 µL of the diluted solution was then drop-cast on the TEM grid and allowed to dry completely. The DIAH-tethered QD sample was prepared by making the BA-capped QD sample and then subsequently performing the crosslinking process for 1 hour.

3.7 Atomic force microscopy (AFM)

Atomic force microscopy (AFM) images were collected using an Icon microscope (Bruker) in tapping mode according to usual procedure.[4] MikroMasch pyramidal silicon tips were used with a height of 15 μm and a cantilever length of 150 μm. Scan sizes ranging from 1 μm to 60 μm (on a side) with a scan rate in the range of 0.3-0.8 Hz.

3.8 Optical microscopies (bright field, dark field, photoluminescence)

Dark field, bright field, and photoluminescence images were collected using a CytoViva hyperspectral system with a Dagexcel-M Digital Firewire camera (cooled) installed on optical microscope (Olympus bx51) and a 50x. PL imaging was performed using photoluminescence excitation from a blue bandpass filter (450-490 nm) with a dichroic mirror that reflects optical wavelengths below 495 nm, and with a longpass emission filter that passes optical wavelengths above 500 nm. The light source is a quartz halogen lamp with an aluminum reflector providing a wavelength range of 420−850 nm and a power of 150 W of unpolarized light. All filters and dichroic mirror are from Chroma Technology Corp. The light source was a quartz halogen lamp with an aluminum reflector providing an emission range of 420-850 nm and a maximum power of 150 Watts.

3.9 Spectroscopic ellipsometry

The QD films were examined using a spectroscopic ellipsometer from Woollam (model M2000) with a wavelength range of 245-1000 nm and a rotating compensator configuration. Film thickness was determined by applying a cauchy model to the transparent region of the optical spectrum. The refractive index at 650 nm (also in the

transparent region) was estimated using the cauchy model. QD-loading (volume fraction) was determined by applying the effective medium approximation Bruggeman model to the refractive index at 650 nm to fit for the volume fraction of QDs in the film (with thickness treated as a constant). The refractive index of CdSe/$Cd_{1-x}Zn_xSe_{1-y}S_y$ QD was approximated using the refractive index of bulk CdSe (n_{bulk} = 2.4), and the refractive index value of the ligand at 650 nm was adjusted according to the ligand content.[5]

3.10 UV-vis and fluorescence spectroscopy

UV-vis extinction spectra of QD solutions (quartz cuvette) from 350-900 nm (1 nm intervals) were collected using a Shimadzu UV-vis-2450 spectrometer with D2 and tungsten lamps offering a wavelength range of 300-1100 nm. The QD extinction spectra were corrected against the pure solvent background and the same quartz cuvette. Photoluminescence spectra of QD solutions were collected using a Shimadzu RF-5301PC spectrofluorophotometer with the excitation wavelength of 525 nm.

3.11 Photoluminescence stability measurement

PL from QD films were collected from hyperspectral datacubes. Hyperspectral datacubes were collected using a CytoViva hyperspectral imaging system utilizing a diffraction grating spectrophotometer with a spectral range of 400-1000 nm and a spectral resolution of 2.8 nm. A 10x objective (NA: 0.30) was used to scan the surface with scans of 50 lines with an automated stage (10 nm step size scan resolution). A 0.1 second exposure time (per line) was used. Hyperspectral scans were performed using the blue bandpass filter (450-490 nm) excitation setup. The light source was the quartz halogen lamp with an aluminum reflector. Spectra were collected and averaged

from hundreds of points on the sample. The lamp power was set to 1 mW for all measurements.

Hyperspectral images were collected using a CytoViva Hyperspectral imaging system utilizing a diffraction grating spectrophotometer with a spectral range of 420-1000 nm and a spectral resolution of 2.8 nm.

3.12 Hyperspectral scanning and imaging

For scanning the QD arrays of circle patterns, a 50x dark field objective (NA: 0.90) in reflectance mode was used to scan the surface with scans of 1392 x 100 lines with an automated stage with a 10 nm step size scan resolution. A 0.5-1 second exposure time (per line) was used when using non-polarized light. The light source is a Quartz halogen lamp with an aluminum reflector providing a wavelength range of 420-850 nm and a power of 150 Watts.

3.13 Quantum yield (QY) estimation

Quantum yields of QDs dispersed in hexane and chloroform are determined by the relative quantum yield method.[6] Standard samples, rhodamine 101 (QY = 91.5%), dissolved in ethanol was used to determine QDs emitting at red regions while rhodamine 6G (QY = 95%) dissolved in ethanol was used to determine QDs emitting at green regions. UV−vis extinction spectra of QD solutions (quartz cuvette) from 350 to 900 nm (1 nm intervals) were collected using a Shimadzu UV− vis-2450 spectrometer with D2 and tungsten lamps offering a wavelength range of 300−1100 nm. The QD extinction spectra were corrected against the pure solvent background and the same quartz cuvette. Photoluminescence spectra of QD solutions were collected using a Shimadzu

fluorescent RF- 5301PC spectrofluorophotometer with the excitation wavelengths of 525 nm for red emitting QDs while 480nm was used for green emitting QDs. All the extinction values of solutions are diluted to be less than 0.1 before measurement in order to avoid the reabsorption effect.

3.14 Optical gain and loss measurements

Measurements are done by collaborator, Prof. Valy Vardeny group in the University of UTAH. The third harmonic (355 nm) of a Spectra Physics Quanta-Ray INDI-series Pulsed Nd:YAG laser (pulse width of 5-8 ns, repetition rate of 10 Hz) was used directly as a seed for a GWU-Lasertechnik basiScan Beta-Barium Borate Optical Parametric Oscillator, producing tunable pulses of 440 with a 25 mJ maximum pulse power (pulse width of 3-7 ns). For the variable stripe length (VSL) gain measurements, the excitation beam was shaped into a stripe of 125 μm width using a cylindrical lens (15 cm focus length), and the stripe length was controlled by a pair of blades mounted on mechanically controlled stages that provided an adjustable slit. Only the central 10 % of the beam was used to minimize pump inhomogeneity due the Gaussian intensity profile. The pump beam intensity, I_{pump}, was varied by means of a pair of polarizers. One end of the stripe excitation was placed on the cleaved edge of the film while the length of the excitation stripe was progressively increased.[7]

The emission from the edge was collected with a 1 mm diameter fiber and recorded using a commercial spectrometer (Ocean Optics USB4000; resolution 2 nm). Gain values were extracted according to the model proposed by Malko et al.[8] Loss measurements were conducted in the same experimental geometry. In this case, the length of the excitation stripe was held constant, while the distance of the stripe from the

edge of the film, d, was varied by simultaneously varying the position of both blades. As the emission propagates towards the collecting fiber, it experiences attenuation by scattering and reabsorption from the unexcited region of the film. The decay of the collected emission signal with increasing distance from the edge was fit to an exponential $I(d) = I(0) \exp(-\alpha d)$ to extract the loss coefficient α.

3.15 Finite-difference time-domain (FDTD) modeling

Confinement factor was calculated using Lumerical Mode Solutions. The model was based on the real QD system, with a stack of 5 layers: Si (3 μm)/ SiO2(292 nm)/ CYTOP(1.5 μm)/ QD(varied thickness)/ air(5 μm). The power confined in the QD layer was integrated by using the option of power and intensity integration.

3.16 Confocal micro-photoluminescence measurement

Measurements are done by collaborator, Prof. Valy Vardeny group in the University of UTAH. A Passat LTD. Compiler diode-pumped solid-state laser delivering 7ps pulses at 532nm with 100Hz repetition rate was used to pump the samples. A pair of polarizers was used to control the pump fluence, I_p, while an iris was used to control the beam spot size. The pump is directed through a 40x (NA = 0.65) microscope objective using a dichroic mirror and focused on the sample. The emission is collected through the same objective, transmitted through the dichroic mirror and focused onto a 0.5mm diameter optical fiber coupled to a 1/2m spectrometer and CCD array (resolution = 0.29nm) or collimated and projected onto a camera lens for fluorescence imaging. An additional long pass filter is used to further attenuate the reflected pump beam.

3.17 Femtosecond-transient absorption

Pump-probe transient absorption spectroscopy was measured by Yaxin Zhai in University of UTAH using a homemade Ti:sapphire laser oscillator operating at a 1 kHz repetition rate at 800 nm of 150 fs pulse duration. The laser beam was split into two beams. One beam was subsequently frequency doubled to 400 nm with pulse energy of 10 μJ using a $BaBO_2$ nonlinear crystal and used to pump the sample, while the other was used to generate a white light supercontinuum with an energy range of 1.15 eV to 2.7 eV to serve as the probe beam. The pump and probe beams were carefully adjusted to obtain a complete spatial overlap. The transmission of the probe beam, T, is measured by a photodiode after dispersion by a monochromator in the absence of the pump and at various time delays after the pump arrives at the sample, yielding the normalized pump-induced change in transmission, $\Delta T(\lambda, t)/T$.[7]

3.18 Collaborative efforts

A great amount of the work described in this thesis was done in collaboration with Professor Z. Lin's research group in Georgia Institute of Technology and Professor Vardeny's research group in University of Utah. Synthesis of QDs were all done and obtained from Professor Z. Lin's research group. The gain measurement, transient absorption and confocal micro-photoluminescence measurement were done by Professor Vardeny's research group (University of Utah).

3.19 References (Chapter 3)

1 W. K. Bae, K. Char, H. Hur, S. Lee, *Chem. Mater.* **2008**, 20, 531.

2 E. Yassitepe, Z. Yang, O. Voznyy, Y. Kim, G. Walters, A. Castañeda Juan, P. Kanjanaboos, M. Yuan, X. Gong, F. Fan, J. Pan, S. Hoogland, R. Comin, M. Bakr Osman, A. Padilha Lazaro, F. Nogueira Ana, H. Sargent Edward, *Adv. Funct. Mater.* **2016**, 26, 8757.

3 N. Mirsaleh-Kohan, V. Iberi, P. D. Simmons, N. W. Bigelow, A. Vaschillo, M. M. Rowland, M. D. Best, S. J. Pennycook, D. J. Masiello, B. S. Guiton, J. P. Camden, *Journal of Physical Chemistry Letters* **2012**, 3, 2303.

4 M. E. McConney, S. Singamaneni, V. V. Tsukruk, *Polymer Reviews* **2010**, 50, 235.

5 Sigma-Aldrich. Butylamine, 1,7 diaminoheptane, & oleic acid.

6 C. Wurth, M. Grabolle, J. Pauli, M. Spieles, U. Resch-Genger, *Nature Protocols* **2013**, 8, 1535.

7 C. H. Lin, E. Lafalce, J. Jung, M. J. Smith, S. T. Malak, S. Aryal, Y. J. Yoon, Y. Zhai, Z. Lin, Z. V. Vardeny, V. V. Tsukruk, *ACS Photonics* **2016**, 3, 647.

8 A. V. Malko, A. A. Mikhailovsky, M. A. Petruska, J. A. Hollingsworth, H. Htoon, M. G. Bawendi, V. I. Klimov, *Appl. Phys. Lett.* **2002**, 81, 1303.

CHAPTER 4

CRAFTING CORE/GRADED SHELL/SHELL QUANTUM DOTS WITH SUPPRESSED RE-ABSORPTION AND TUNABLE STOKES SHIFT

4.1 Introduction

Semiconductor quantum dots (QDs) possess size-dependent optical and electronic properties due to their quantum confinement effect. This opens up opportunities for revolutionary advances in solar cells,[1,2,3,4,5] lasers,[6] solar concentrators,[7] light emitting diodes,[8,9] optical amplifiers,[10] and bioimaging.[11] The solution processability of QDs enabled by the capping of organic ligands renders the easy incorporation of colloidal QDs in polymer matrix and expands the possibilities for development of scalable and low-cost manufacturing techniques. Among various types of QDs, CdSe QD is one of most appealing and widely studied inorganic semiconductors due to its optimum bandgap corresponding to emission in the visible region. Moreover, their emission wavelength can be readily tuned by varying the size of CdSe QD.[12,13,14,15,16,17,18,19] However, the utilization of CdSe QD in optoelectronic devices is hindered due to the unstable optical properties resulting from the surface dangling bonds which act as nonradiative recombination sites. To this end, surface passivation by organic ligands is employed to reduce surface dangling bonds in CdSe QD, thereby leading to enhanced luminescence efficiency and improved photo and colloidal stability.[20] However, the difficulty in passivating the entire surface (i.e., anionic and cationic sites) with organic ligands still causes chemical degradation or photo-oxidation of QDs.[21] In this context, inorganic surface passivation has been proven to be effective in completely covering the

surface of QD, yielding core/shell architecture. For CdSe QD, its surfaces are often passivated with either ZnS or CdS to establish *Type I* energy alignment system, where the bandgap of CdSe lies within the band gap of shell material.

It is worth noting that to realize the utility of CdSe QDs as lasing media, it is of key importance to reduce ultrafast optical gain decay induced by Auger recombination, in which the electron-hole recombination energy is transferred to a third particle such as an electron or a hole that is re-excited to a higher-energy state.[10] The Auger recombination rate depends heavily on the size of CdSe nanocrystals.[8] It has been demonstrated that the implementation of larger CdSe QDs and CdSe QDs with graded shell architecture can reduce Auger recombination rate.[22] In this context, giant CdSe/CdS core/shell QDs (denoted CdSe/CdS g-QDs in which small CdSe core was passivated by large CdS shell) synthesized by the successive ion layer adsorption and reaction of monolayers (SILAR) method exhibited the reduced surface trapping and Auger recombination.[12,22] Moreover, they displayed the pronounced red-shift of emission peak, which is the indicative of the extension of CdSe core wave function into the CdS shell region, that is, the increase of effective size of core.[22] Interestingly, the first absorption peak of CdSe/CdS g-QDs is relatively suppressed as well due to the absorption primarily from thick CdS shell as the bandgap of CdS is larger than that of CdSe. However, achieving the re-absorption-suppressed CdSe/CdS g-QDs with emission position over the entire visible region is limited due to the large bandgap of CdS (e.g., 2.42 eV; corresponding to an onset of absorption at 512 nm) compared to CdSe. In addition, g-QDs are typically prepared by SILAR method, which requires time-consuming multi-steps to epitaxially deposit the desired shell material. Clearly, it is highly desirable to develop alternative simple yet robust synthetic routes to g-QDs.

Here, we report a viable strategy to craft highly luminescent CdSe/$Cd_{1-x}Zn_xSe_{1-y}S_y$/ZnS core/graded shell/shell QDs with suppressed re-absorption, reduced Auger recombination, and tunable Stokes shift. The plain CdSe QDs with desired emission were first synthesized and used as seeds. $Cd_{1-x}Zn_xSe_{1-y}S_y$ shell possessing chemical composition gradient toward the radial direction was then grown on the CdSe QD surface, forming CdSe/$Cd_{1-x}Zn_xSe_{1-y}S_y$ QDs. Notably, the graded $Cd_{1-x}Zn_xSe_{1-y}S_y$ shell was simply achieved by a *one-pot* synthesis via capitalizing on the chemical reactivity difference between cadmium oleate and zinc oleate precursors.[23] Subsequently, ZnS shell was further passivated on the surface of CdSe/$Cd_{1-x}Zn_xSe_{1-y}S_y$ QD via secondary injection of S precursors, yielding CdSe/$Cd_{1-x}Zn_xSe_{1-y}S_y$/ZnS core/graded shell/shell QDs. The size and shape of QDs was examined by high-resolution TEM. The absorption and photoluminescence studies of CdSe/$Cd_{1-x}Zn_xSe_{1-y}S_y$/ZnS QDs revealed the dependence of emission peak position on the ZnS shell thickness. These chemical composition gradient QDs possess the outstanding photo-stability as a result of the alleviated lattice strain between CdSe and ZnS due to the judicious incorporation of $Cd_{1-x}Zn_xSe_{1-y}S_y$ graded shell. Moreover, the Stokes shift (i.e., the difference between absorption and emission maxima) of these QDs with the graded shell architecture can be readily engineered by simply further tailoring the thickness of outermost ZnS shell (i.e., red-shift with the increased ZnS shell thickness), which cannot be observed in conventional CdSe/ZnS QDs owing to their large energy level mismatch.[24] It is also notable that CdSe/$Cd_{1-x}Zn_xSe_{1-y}S_y$/ZnS QDs are advantageous over giant CdSe/CdS QDs as the larger bandgap of ZnS than CdS offers a high degree of tunability in selecting the emission position in visible region due to the suppression of re-absorption of QDs. In comparison to plain CdSe QDs, all CdSe/$Cd_{1-x}Zn_xSe_{1-y}S_y$/ZnS QDs with different emission positions exhibited the extended lifetime, signifying the reduced Auger

recombination rate as a direct consequence of electron wave function delocalization over the entire QD.

4.2 Experimental details

Preparation of green-emitting CdSe QDs with a diameter of 2.3 nm and 2.5 nm: TDPA-capped CdSe QDs were synthesized by following a reported method.[25] A mixture of CdO (51 mg), TDPA (223 mg), and TOPO (3.777g) was degassed in a three neck flask for 1 hr at 120 °C. The temperature was then increased to 320 °C under Ar. Subsequently, 1M Se/TOP injection solution was prepared in a glovebox. After the solution turned clear and colorless, the temperature was set to 300 °C and 1ml of injection solution was then introduced to initiate the nucleation and growth. The heating mantle was removed to stop reaction after CdSe QDs were allowed to grow at 300 °C for 10 sec and 15 sec to reach the diameter of 2.3 nm and 2.5 nm, respectively. 5 ml of hexane was added when the solution was cooled to 60 °C. The resulting TDPA-capped CdSe QDs were precipitated with methanol twice and then re-dispersed in chloroform.

Preparation of red emitting CdSe QDs with a diameter of 4.1 nm**:** high quality OA-capped red-emitting CdSe QDs were prepared by slightly modifying a reported method.[8] A mixture of CdO (1 mmol), OA (4 mmol), ODE (15 ml) were degassed in a three-neck flask for 1 hr at 120°C. After that, the temperature was increased to 280 °C under Ar, where the solution turned transparent. 0.5 ml of 1 M Se/TOP solution prepared in a glovebox was injected to initiate the nucleation and growth. The heating mantle was removed to stop reaction after 5 min. Once temperature reached 60 °C, 5 ml of hexane was added. The resulting OA-capped CdSe QDs were precipitated with methanol twice and then re-dispersed in desired solvent.

***Preparation of conventional CdSe/ZnS core/shell QDs*:** CdSe/ZnS core/shell QDs were synthesized by following a reported method. [26] Diethylzinc ($ZnEt_2$) and hexamethyldisilathiane ($(TMS)_2S$) were used as Zn and S sources, respectively. First, 0.2 μ mol of TDPA-capped CdSe QDs (i.e., green-emitting CdSe QDs as described above) were introduced as seed in 2g of HDA and 1g of TOPO, and degassed at 120 °C for 1 hr. After that, the temperature was elevated to 220 °C. 0.05 ml $ZnEt_2$ and 0.15 ml of $(TMS)_2S$ dissolved in 1ml of TOP were then injected dropwise. The heating mantle was removed to stop reaction after 60 min.

***Preparation of graded CdSe/$Cd_{1-x}Zn_xSe_{1-y}S_y$/ZnS core/shell QDs*:** 10 ml of as-prepared Cd-oleate and Zn-oleate in ODE described above was placed in a 50ml three neck flask. The temperature was then increased to 250°C under Ar. Subsequently, the injection solution containing 0.1 mmol of Se and 4 mmol of S in 2 ml of TOP was prepared in a glove box. After the solution turned transparent, the temperature was set to 250°C. 0.2 μmol plain CdSe QDs (i.e., two green-emitting QDs (D = 2.3 nm and 2.5 nm, respectively) and one red-emitting QDs (D = 4.1 nm) as described above) were then introduced, and the as-prepared injection solution was added dropwise (forming CdSe/$Cd_{1-x}Zn_xSe_{1-y}S_y$ QDs). In order to further passivate CdSe/$Cd_{1-x}Zn_xSe_{1-y}S_y$ QDs with ZnS shell (forming CdSe/$Cd_{1-x}Zn_xSe_{1-y}S_y$/ZnS QDs), 0.5 M S/TOP solution was added (as Zn precursors were previously added in excess, the addition of Zn was not needed at this stage). The heating mantle was removed to stop reaction after 90 min. Once temperature reached 60 °C, 5 ml of hexane was added as solvent to prevent the solidification. The resulting CdSe/$Cd_{1-x}Zn_xSe_{1-y}S_y$/ZnS QDs were precipitated with acetone twice and then re-dispersed in desired solvent.

Characterizations: The morphology of as-prepared CdSe QDs, CdSe/ZnS QDs, CdSe/$Cd_{1-x}Zn_xSe_{1-y}S_y$ QDs and CdSe/$Cd_{1-x}Zn_xSe_{1-y}S_y$/ZnS QDs was examined by high-resolution transmission electron microscope (Tecnai F30). Their absorption and emission spectra were recorded using a UV-vis spectrometer (UV-2600, Shimadzu) and a spectrofluorophotometer (RF-5301PC, Shimadzu), respectively. In the transient photomodulation (PM) spectroscopy measurement, the pump pulse excites the sample and the mechanically delayed probe pulse measures the pump-induced changes (ΔT(t)) in the sample transmission (T). We used a Ti : Sapphire oscillator based laser system at high power (energy/pulse ~10 μJ) and low repetition rate (~1 kHz) for the visible spectral range, in which the white light super-continuum was generated for $\hbar\omega$ (probe) ranging from 1.15 to 2.7 eV. The pump excitation was set at $\hbar\omega$=3.1 eV (400nm), which is above the optical gap of the studied QDs here. The PM spectrum may contain photoinduced absorption (PA) bands with ΔT < 0 due to the excited state absorption, and photoinduced bleaching (PB) with ΔT > 0 caused by pump-induced bleaching of the ground state absorption.

4.3 Results and discussion

4.3.1 Synthesis of QDs with different core/shell design

Highly luminescent CdSe/$Cd_{1-x}Zn_xSe_{1-y}S_y$ core/shell QDs were synthesized by passivating the surface of plain CdSe QD core with the graded $Cd_{1-x}Zn_xSe_{1-y}S_y$ shell. The radially graded $Cd_{1-x}Zn_xSe_{1-y}S_y$ shell on CdSe QD surface was formed via a careful control of the ratio of Cd and Zn precursors. A further epitaxial growth of ZnS shell through secondary injection of S precursors (i.e., S/TOP) yielded CdSe/$Cd_{1-x}Zn_xSe_{1-y}S_y$/ZnS core/graded shell/shell QDs. It is worth noting that the graded $Cd_{1-x}Zn_xSe_{1-y}S_y$

shell was achieved by simply exploiting the difference in chemical reactivity of cadmium and zinc precursors (i.e., Cd-oleate and Zn-oleate). Specifically, the weaker binding energy of oleic acid with Cd^{2+} than that with Zn^{2+} resulted in a higher reactivity of Cd-oleate than Zn-oleate during the crystal growth reaction.[23, 27] Consequently, the formation of CdSe and CdS is more favorable than ZnSe and ZnS, yielding $Cd_{1-x}Zn_xSe_{1-y}S_y$ shell with a gradual increase of Zn and S ratio over Cd and Se.[23] It is important to note that the energy level of the resulting CdSe/$Cd_{1-x}Zn_xSe_{1-y}S_y$/ZnS QDs with gradient chemical compositions can be regarded as the graded smooth alignment rather than the sharp interface as in conventional CdSe/ZnS QDs as depicted in **Figure 4.1**.

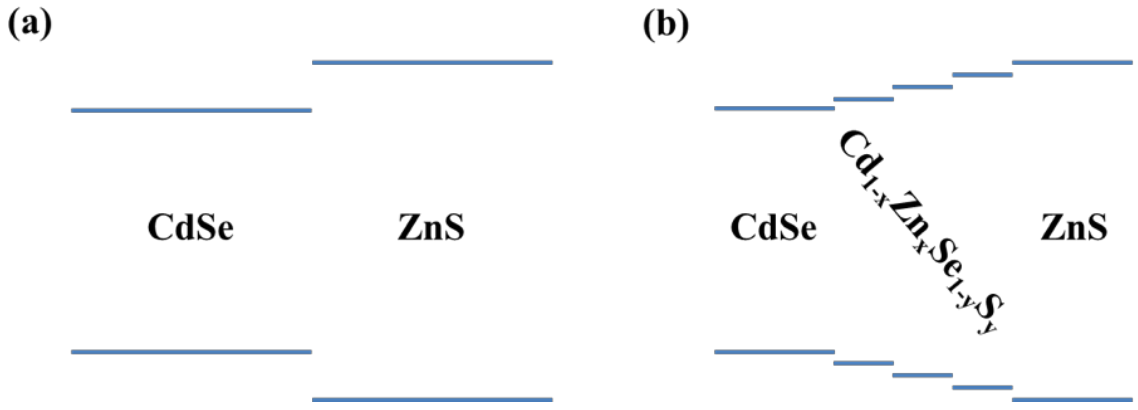

Figure 4.1 The energy level alignment for (a) CdSe/ZnS QDs, and (b) CdSe/$Cd_{1-x}Zn_xSe_{1-y}S_y$/ZnS QDs.

Moreover, the graded shell architecture can effectively reduce the interfacial lattice strain between CdSe and ZnS (i.e., a 12% lattice mismatch between CdSe and ZnS), which would otherwise lead to a dramatic increase in trapping sites with the increase of ZnS shell thickness.[12,2612, 26]

Figure 4.2 shows high-resolution TEM images of chemical composition gradient QDs prepared at 300 °C using 2.3-nm green-emitting CdSe QD as seeds. The diameter of QDs increased from 2.3±0.1 nm for as-prepared CdSe QD core (**Figure 4.2a**) to 4.4±0.2 nm for CdSe/$Cd_{1-x}Zn_xSe_{1-y}S_y$ QDs (**Figure 4.2b**) to 6.0±0.2 nm for CdSe/$Cd_{1-x}Zn_xSe_{1-y}S_y$/ZnS QDs (grown for 30 min), and eventually to 8.4±0.4 nm for CdSe/$Cd_{1-x}Zn_xSe_{1-y}S_y$/ZnS QDs (grown for 90 min) clearly suggesting the success in depositing $Cd_{1-x}Zn_xSe_{1-y}S_y$ graded shell and subsequent ZnS shell. The CdSe/$Cd_{1-x}Zn_xSe_{1-y}S_y$/ZnS QDs also possessed high crystallinity as revealed by TEM (for example, **Figure 4.2d**).

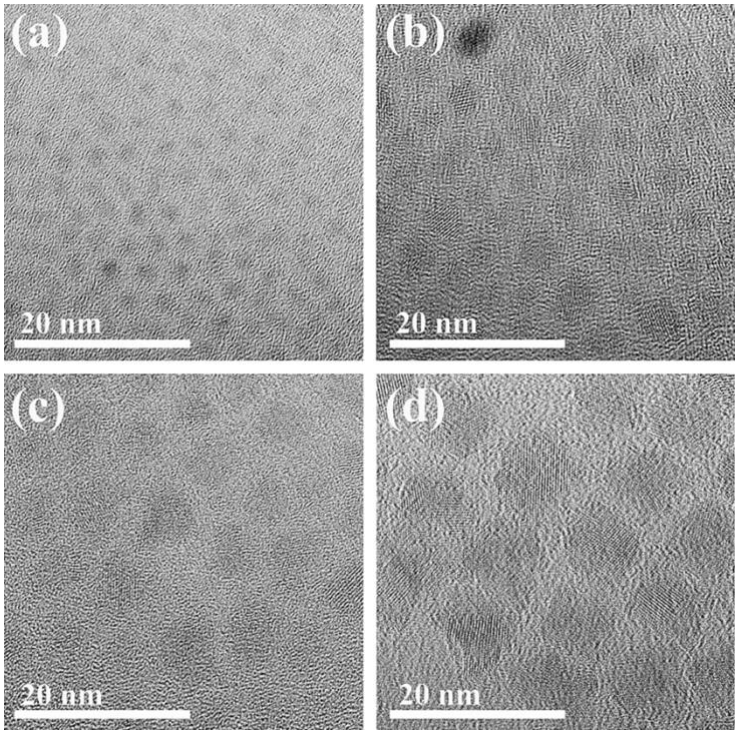

Figure 4.2 TEM images of (a) plain CdSe QDs as core (green-emitting; *D* = 2.3 nm), (b) CdSe/$Cd_{1-x}Zn_xSe_{1-y}S_y$ QDs (*D* = 4.4 nm), (c) CdSe/$Cd_{1-x}Zn_xSe_{1-y}S_y$/ZnS QDs (*D* = 6.0 nm), and (d) CdSe/$Cd_{1-x}Zn_xSe_{1-y}S_y$/ZnS QDs (*D* = 8.4 nm). All chemical composition gradient QDs were synthesized using 2.3-nm green-emitting CdSe QDs as seeds at 250 °C.

Optical properties of as-synthesized CdSe/$Cd_{1-x}Zn_xSe_{1-y}S_y$/ZnS QDs containing the chemical composition gradient shell were investigated by absorption and

photoluminescence spectroscopy measurements. The conventional CdSe/ZnS QDs were also synthesized and used as control.

4.3.2 Spectroscopic analysis

In order to scrutinize the effect of graded shell on the change in absorption (i.e., the first absorption peak) and emission properties (i.e., emission peak) and quantum yield (QY), plain CdSe QDs were passivated with both graded shell (i.e., $Cd_{1-x}Zn_xSe_{1-y}S_y$) and graded shell/shell (i.e., $Cd_{1-x}Zn_xSe_{1-y}S_y$/ZnS), respectively. The absorption and emission spectra of tetradecylphosphonic acid (TDPA)-capped CdSe QDs (D = 2.3 nm; green-emitting) with the first absorption peak at 488 nm, emission peak, λ_{em} at 500 nm, FWHM of emission at 29 nm, and QY of 2.2% are shown in **Figure 4.3a** and **3b (**black curves). We note that TDPA was utilized for the synthesis of CdSe core QDs as it enables the preparation of CdSe QDs with a narrow size distribution.[28] After passivation of CdSe core with $Cd_{1-x}Zn_xSe_{1-y}S_y$ graded shell and ZnS shell, QYs of both QDs enhanced, that is (i.e., from 2.2% for CdSe QD core to 40.0% for CdSe/$Cd_{1-x}Zn_xSe_{1-y}S_y$ QDs (D = 4.4 nm; blue curve in **Figure 4.3b**), and from 2.2% for CdSe QD core to 36.7% for conventional CdSe/ZnS QDs (D = 3.7 nm; blue curve in **Figure 4.3a**), respectively, which was due to the reduction in surface dangling bonds.[26, 29] The FWHM of emission peaks was maintained in both QDs (i.e., 32 nm; **Table 4.1**) as highly monodisperse TDPA-capped CdSe QDs were employed as seeds. The emission peak position of CdSe/$Cd_{1-x}Zn_xSe_{1-y}S_y$ QDs and CdSe/ZnS QDs was shifted from λ_{em} = 499 nm for CdSe QDs to λ_{em} = 515 nm in both cases. This can possibly be attributed to the increase in the size of CdSe core during the reaction due to the existence of residue cadmium and selenium precursors.[26]

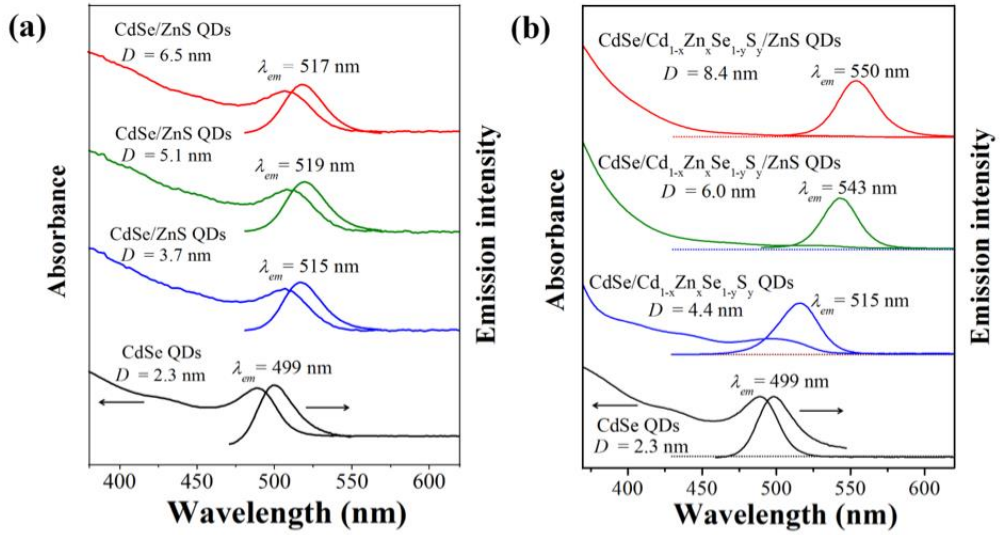

Figure 4.3 The absorption and emission spectra of (a) CdSe/ZnS QDs and (b) CdSe/$Cd_{1-x}Zn_xSe_{1-y}S_y$/ZnS QDs, in which the diameter of originally green-emitting CdSe QD core, *D* is 2.3 nm. All CdSe/ZnS, CdSe/$Cd_{1-x}Zn_xSe_{1-y}S_y$, and CdSe/$Cd_{1-x}Zn_xSe_{1-y}S_y$/ZnS QDs were grown from green-emitting CdSe QD at 250 °C.

	Sample	Diameter (nm)	Quantum Yield (QY)	FWHM (nm)	Emission peak (λ_{em}, nm)
Core	**CdSe**	2.3	2.2 %	29	499
Conventional QDs	**CdSe/ZnS**	3.7	36.7 %	32	515
	CdSe/ZnS	5.1	32.2 %	33	519
	CdSe/ZnS	6.5	27.4 %	36	517
QDs with Graded Shell	**CdSe/$Cd_{1-x}Zn_xSe_{1-y}S_y$**	4.4	40.0 %	32	515
	CdSe/$Cd_{1-x}Zn_xSe_{1-y}S_y$/ZnS	6.0	36.4 %	29	543
	CdSe/$Cd_{1-x}Zn_xSe_{1-y}S_y$/ZnS	8.4	34.2 %	29	550

Table 4.1 The optical properties of conventional CdSe/ZnS QDs and CdSe/$Cd_{1-x}Zn_xSe_{1-y}S_y$/ZnS QDs.

Notably, conventional CdSe/ZnS core/shell QDs without gradient shell, where the emission position stayed same (i.e., approximately λ_{em} = ~ 517 nm; **Figure 4.3a**) regardless of the increase of ZnS shell thickness because of large energy level difference between CdSe and ZnS (**Figure 4.1a**), leading to the electron localization solely in CdSe core (**Figure 4.3a** and **Table 4.1**). Specifically, conventional CdSe/ZnS QDs with different shell thickness were prepared as control by changing the reaction time from 10 min (blue curve, *D* = 3.7 nm; **Figure 4.3a**) to 30 min (green curve, *D* = 5.1 nm; **Figure 4.3a**) to 90 min (red curve, *D* = 6.5 nm; **Figure 4.3a**). Clearly, even for CdSe/ZnS QDs with a *D* of 6.5 nm corresponding to 7 monolayers of ZnS shell (a monolayer of ZnS is 3.1 Å between consecutive planes along the [002] axis in bulk wurtzite ZnS),[26] they did not exhibit a red-shift in emission peak. In stark contrast, the emission peak of chemical composition gradient QDs was further red-shifted (i.e., to λ_{em} = 543 nm for CdSe/$Cd_{1-x}Zn_xSe_{1-y}S_y$/ZnS with *D* = 6.0 nm; green curve in **Figure 4.3b**) and further up to λ_{em} = 550 nm for CdSe/$Cd_{1-x}Zn_xSe_{1-y}S_y$/ZnS with *D* = 8.4 nm; red curve in **Figure 4.3b**) (**Table 4.1**), and quite intriguingly, their first absorption peaks were greatly suppressed.

As evidenced by the TEM measurements (**Figure 4.2c** and **2d**), the increased diameter of QDs suggested the successful passivation of outermost ZnS shell, and thus possibly renders the delocalization of electron wave function into entire CdSe/$Cd_{1-x}Zn_xSe_{1-y}S_y$/ZnS QDs because of the graded energy level alignment (**Figure 4.1b**),[7,22] thereby leading to the emission red-shift. Therefore, compared to conventional CdSe/ZnS QDs, the enhanced Stokes shift in CdSe/$Cd_{1-x}Zn_xSe_{1-y}S_y$/ZnS QDs can be ascribed to the increased effective core size of QDs through a careful energy level engineering, enabling the extension of electron wave function over entire core/grade shell/shell QDs. However, the electron wave function is confined within CdSe core in the case of

conventional CdSe/ZnS QDs. It is also worth noting that the absorption onset of CdSe/$Cd_{1-x}Zn_xSe_{1-y}S_y$/ZnS QDs was found to be around 400 nm, which is indicative of the bandgap of ZnS (**Figure 4.3b**).[30]

As noted above, the advantage of CdSe/$Cd_{1-x}Zn_xSe_{1-y}S_y$/ZnS QDs over CdSe/CdS g-QDs lies in the fact that such chemical composition gradient QDs with emissions across the entire visible region can be crafted due to the larger bandgap of ZnS (i.e., 3.54 eV corresponding to the absorption onset at 350 nm) in comparison to that of CdS (i.e., 2.42 eV corresponding to the absorption onset at 512 nm). However, for CdSe/CdS g-QDs, such full visible-region emission is not possible (for example, blue- and green-emitting cannot be attainable) as the emission at wavelength below 512 nm will be re-absorbed by CdS shell. In contrast, a careful control of thickness and composition in graded shell and outermost ZnS shell may render the ability to form green-emitting CdSe/$Cd_{1-x}Zn_xSe_{1-y}S_y$/ZnS core/grade shell/shell QDs with suppressed re-absorption via imparting the larger Stokes shift as the absorption onset for ZnS shell is below blue wavelength (i.e., 350 nm).

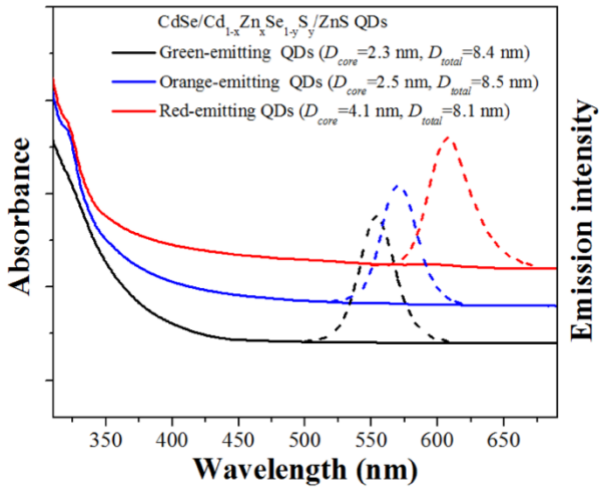

Figure 4.4 Absorption and photoluminescence spectra of green-, orange-, and red-emitting CdSe/$Cd_{1-x}Zn_xSe_{1-y}S_y$/ZnS QDs synthesized by employing green-emitting CdSe QD (*D* = 2.3 nm), green-emitting CdSe QD (*D* = 2.5 nm), and red-emitting CdSe QD (*D* = 4.1 nm) as seeds.

Thus, it is not surprising that CdSe/$Cd_{1-x}Zn_xSe_{1-y}S_y$/ZnS QDs having different emissions with suppressed re-absorption were successfully synthesized by simply employing CdSe core of different size (**Figure 4.4**).

Specifically, plain CdSe QDs of 2.3 nm (green-emitting), 2.5 nm (also green-emitting), and 4.1 nm (red-emitting) in diameter were utilized as seeds to produce green-, orange-, and red-emitting CdSe/$Cd_{1-x}Zn_xSe_{1-y}S_y$/ZnS QDs, respectively (digital images in **Figure 4.5a-c**). The diameters of plain CdSe QD cores were calculated based on their first absorption peak ($\lambda_{1st,\ abs}$ = 499 nm, 520 nm, and 588 nm, respectively)[20] and can be verified by TEM measurements (for example, 2.3-nm CdSe QD as shown in **Figure 4.1a**). The diameters of the resulting green-, orange-, and red-emitting CdSe/$Cd_{1-x}Zn_xSe_{1-y}S_y$/ZnS QDs were 8.4±0.3 nm, 8.5±0.3 nm, and 8.1±0.3 nm, respectively, as measured from TEM analysis (**Figure 4.5d-f**).

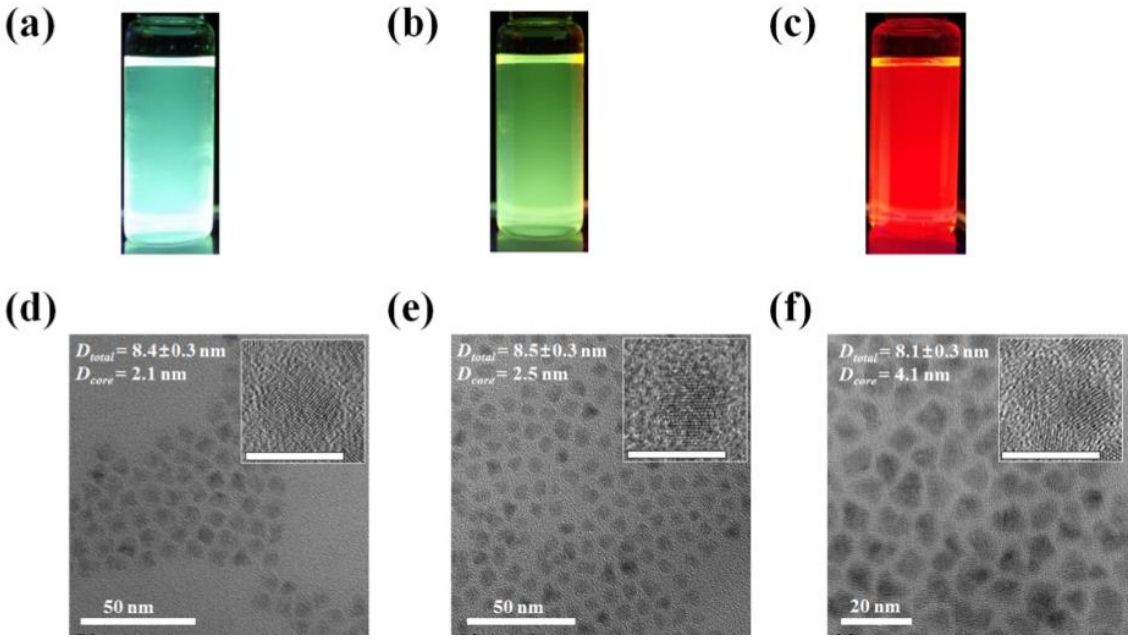

Figure 4.5 High-resolution TEM images of (a) green-, (b) orange-, and (c) red-emitting CdSe/$Cd_{1-x}Zn_xSe_{1-y}S_y$/ZnS QDs prepared by capitalizing on green-emitting CdSe QD (*D* = 2.3 nm), green-emitting CdSe QD (*D* = 2.5 nm), and red-emitting CdSe QD (*D* = 4.1 nm) as seeds. The scale bar in inset is 10 nm.

4.3.3 Suppressed Auger recombination

The transient photomodulation (PM) spectroscopy measurements revealed that compared to plain CdSe QDs, all chemical composition gradient QDs exhibited the reduced Auger recombination rate (**Figure 4.6**). All samples were pumped with 400-nm laser and the range of their first absorption was probed. Clearly, green-, orange-, and red-emitting CdSe/$Cd_{1-x}Zn_xSe_{1-y}S_y$/ZnS QDs presented the extended lifetime compared to that of red-emitting CdSe core QDs (D = 4.1 nm), signifying the reduced Auger recombination rate.[31] In conjunction with pronounced larger Stokes shift, the longer Auger recombination life time strongly supports the electron delocalization over entire CdSe/$Cd_{1-x}Zn_xSe_{1-y}S_y$/ZnS QDs as the Auger recombination rate is proportional to the volume of QDs.[31]

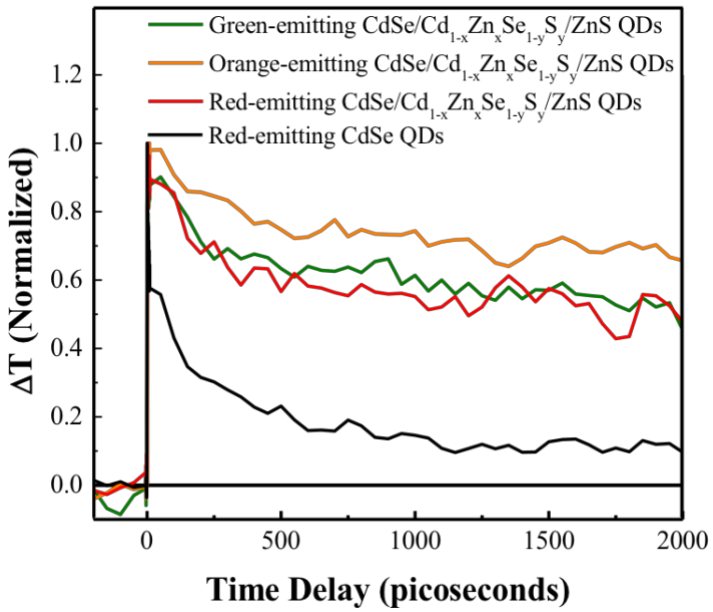

Figure 4.6 Dynamics of photobleaching of red-emitting CdSe core QDs (D = 4.1 nm), red-emitting CdSe/$Cd_{1-x}Zn_xSe_{1-y}S_y$/ZnS QDs (D = 8.1 nm), orange-emitting CdSe/$Cd_{1-x}Zn_xSe_{1-y}S_y$/ZnS QDs (D = 8.5 nm), and green-emitting CdSe/$Cd_{1-x}Zn_xSe_{1-y}S_y$/ZnS QDs (D = 8.4 nm).

4.4 Conclusions

In summary, we developed a robust *one-pot* synthesis strategy to craft chemical composition gradient CdSe/$Cd_{1-x}Zn_xSe_{1-y}S_y$/ZnS QDs by passivating the surface of CdSe QD core with $Cd_{1-x}Zn_xSe_{1-y}S_y$ graded shell, followed by outermost ZnS shell. The resulting CdSe/$Cd_{1-x}Zn_xSe_{1-y}S_y$/ZnS QDs carry intriguing attributes over conventional CdSe/ZnS QDs, including suppressed re-absorption, reduced Auger recombination, and tunable Stokes shift.

4.5 Chapter acknowledgements

Dr. Jaehan Jung and Youngjun Yoon (Prof. Zhiqun Lin's research group, Georgia Institute of Technology): QD synthesis. Dr. Yaxin Zhai (Prof. Valy Vardeny's research group, University of UTAH): the transient photomodulation spectroscopy.

4.6 References (Chapter 4)

1 J. Jung, X. Pang, C. Feng, Z. Lin, *Langmuir* **2013**, 29, 8086.

2 X. Xin, B. Li, J. Jung, Y. J. Yoon, R. Biswas, Z. Lin, *PART. PART. SYST. CHAR.* **2015**, 32, 80.

3 J. Jung, Y. J. Yoon, M. He, Z. Lin, *J. Polym. Sci., Part B: Polym. Phys.* **2014**, 52, 1641.

4 M. He, F. Qiu, Z. Lin, *J. Phys. Chem. Lett.* **2013**, 4, 1788.

5 J. Xu, J. Wang, M. Mitchell, 5P. Mukherjee, M. Jeffries-El, J. W. Petrich, Z. Lin, *J. Am. Chem. Soc.* **2007**, 129, 12828.

6 C. Dang, J. Lee, C. Breen, J. S. Steckel, S. Coe-Sullivan, A. Nurmikko, *Nat. Nanotech.* **2012**, 7, 335.

7 F. Meinardi, A. Colombo, K. A. Velizhanin, R. Simonutti, M. Lorenzon, L. Beverina, R. Viswanatha, V. I. Klimov, S. Brovelli, *Nat. Photon.* **2014**, 8, 392.

8 Q. Sun, Y. A. Wang, L. S. Li, D. Wang, T. Zhu, J. Xu, C. Yang, Y. Li, *Nat. Photon.* **2007**, 1, 717.

9 B. N. Pal, Y. Ghosh, S. Brovelli, R. Laocharoensuk, V. I. Klimov, J. A. Hollingsworth, H. Htoon, *Nano Lett.* **2011**, 12, 331.

10 S. A. Ivanov, J. Nanda, A. Piryatinski, M. Achermann, L. P. Balet, I. V. Bezel, P. O. Anikeeva, S. Tretiak, V. I. Klimov, *J. Phys. Chem. B* **2004**, 108, 10625.

11 Y. Zhang, Y. Li, X.-P. Yan, *Small* **2009**, 5, 185.

12 R. Xie, U. Kolb, J. Li, T. Basché, A. Mews, *J. Am. Chem. Soc.* **2005**, 127, 7480.

13 J. Xu, J. Xia, J. Wang, J. Shinar, Z. Lin, *Appl. Phys. Lett.* **2006**, 89, 133110

14 D. Zimnitsky, C. Jiang, J. Xu, Z. Lin, L. Zhang, V. V. Tsukruk, *Langmuir* **2007**, 23, 10176.

15 D. Zimnitsky, C. Jiang, J. Xu, Z. Lin, V. V. Tsukruk, *Langmuir* **2007**, 23, 4509.

16 J. Xu, J. Xia, Z. Lin, *Angew. Chem. Int. Ed.* **2007**, 46, 1860

17 J. Wang, J. Xu, M. D. Goodman, Y. Chen, M. Cai, J. Shinar, Z. Lin, *J. Mater. Chem.* **2008**, 18, 3270.

18 X. Pang, L. Zhao, W. Han, X. Xin, Z. Lin, *Nat. Nanotech.* **2013**, 8, 426.

19 B. Li, W. Han, B. Jiang, Z. Lin, *ACS Nano* **2014**, 8, 2936.

20 W. W. Yu, L. Qu, W. Guo, X. Peng, *Chem. Mater.* **2003**, 15, 2854

21 H. Zhang, J. Jang, W. Liu, D. V. Talapin, *ACS Nano* **2014**, 8, 7359.

22 Y. Chen, J. Vela, H. Htoon, J. L. Casson, D. J. Werder, D. A. Bussian, V. I. Klimov, J. A. Hollingsworth, *J. Am. Chem. Soc.* **2008**, 130, 5026.

23 W. K. Bae, K. Char, H. Hur, S. Lee, *Chem. Mater.* **2008**, 20, 531.

24 C. She, I. Fedin, D. S. Dolzhnikov, A. Demortière, R. D. Schaller, M. Pelton, D. V. Talapin, *Nano Lett.* **2014**, 14, 2772.

25 Z. A. Peng, X. Peng, *J. Am. Chem. Soc.* **2000**, 123, 183.

26 B. O. Dabbousi, J. Rodriguez-Viejo, F. V. Mikulec, J. R. Heine, H. Mattoussi, R. Ober, K. F. Jensen, M. G. Bawendi, *J. Phys. Chem. B* **1997**, 101, 9463.

27 W. K. Bae, M. K. Nam, K. Char, S. Lee, *Chem. Mater.* **2008**, 20, 5307

28 Z. A. Peng, X. Peng, *J. Am. Chem. Soc.* **2001**, 123, 183.

29 P. Reiss, J. Bleuse, A. Pron, *Nano Lett.* **2002**, 2, 781.

30 D. V. Talapin, A. L. Rogach, A. Kornowski, M. Haase, H. Weller, *Nano Lett.* **2001**, 1, 207.

31 V. I. Klimov, A. A. Mikhailovsky, S. Xu, A. Malko, J. A. Hollingsworth, C. A. Leatherdale, H. J. Eisler, M. G. Bawendi, *Science* **2000**, 290, 314.

CHAPTER 5

ENHANCEMENT OF OPTICAL GAIN CHARACTERISTICS OF QUANTUM DOT FILMS BY ORGANIC LIGAND SHELL

5.1 Introduction

Quantum dots have particular potential in the area of optical gain and lasing systems. For example, gain from the blue to NIR has been demonstrated using many types of QDs, including CdTe,[1] PbS,[2] CdSe,[3,4] CdSe/ZnS,[5] and CdSe/CdS/ZnS.[6] Typical gain values range from 60-200 cm^{-1} depending on the pumping conditions, system design, and type of QD.[1-6] Various feedback mechanisms for lasing have also been demonstrated, including microcapillary resonators,[3, 7] microsphere resonators, [8] distributed feedback resonators, [9] and planar microcavities. [10] These studies clearly demonstrate the potential of quantum dots for optical gain and lasing applications.

To date, the majority of studies have tried to maximize optical gain by minimizing the Auger recombination rate via size, [11] type-I design, [12] type-II design, [13, 14] and QD composition.[1-6] These studies have been complemented by investigations of the formation and relaxation dynamics of the various exciton, biexciton, and multiexciton states in different types of quantum dots (core, core/shell, core/graded shell) using state-resolve pumping/probing. [15, 16, 17, 18] This has resulted in a steady increase in understanding of the structural dynamics of multi-excitons, and led to important discoveries like size-independent occupation thresholds and gain tailoring via excitonic state.[17,19] However, only a few studies have considered how QD packing density and thermodynamic properties of the film affect the optical gain characteristics.[1] This is

surprising since QD packing is a particularly important area of investigation in QD photovoltaics where ligand selection has been used to increase QD packing and therefore charge transport.[20]

In this work, we demonstrate how the optical gain characteristics (threshold, magnitude, and stability) of QD films depend on the type of ligand used to stabilize the QD. These results are examined from the perspective of how the size and thermodynamic properties of the QD ligand affect the physical properties of the film, including QD-loading fraction and refractive index. We show that replacing traditional long chain ligands with shorter ligands can increase QD-loading up to 50% and consequently increase the refractive index up to 1.88 (at 650 nm). These changes profoundly influence the emission light confinement within the film, as well as the optical gain magnitude, with more than a two-fold increase observed between the long and short QD-ligand systems. These property changes have led to exceptionally high net gain values (~500 cm^{-1}) for a Cd-based QD system, as well as excellent optical stability. This research shows a facile approach for tuning the QD gain characteristics that does not require any modification to the QD synthesis process and selection of different QDs.

5.2 Experimental details

QD-ligand film preparation: QD films were fabricated via spin-casting (2000 rpm, 1.5 minutes) a QD solution (heptane or toluene). Film thickness ranged from 150-250 nm in order to support only the first waveguide mode. QD films were deposited on a CYTOP film (1400-1600 nm thick) which has a sufficiently low refractive index (n_{650} = 1.34) to cause light confinement and waveguiding within the QD film.[21] The CYTOP was exposed to air or Ar plasma for 5 seconds in order to improve wetting of the

CYTOP by the QDs. Silicon with a 290-295 nm thick SiO_2 surface layer was used as a substrate to minimize leakage (and attenuation) of light from the QD film. However, the attenuation of light that does leak from the QD film into the Si substrate helps ensure that the light detected at the edge is the light that has propagated through the QD film (and not the substrate). The substrates were cleaved to obtain sharper, cleaner edges which improve the intensity of the output light and to help ensure that the area of the film exposed to the pump light was uniform over the length of the pump strip length.

Optical gain and loss measurements and fitting: The third harmonic (355 nm) of a Spectra Physics Quanta-Ray INDI-series Pulsed Nd:YAG laser (pulse width of 5-8 ns, repetition rate of 10 Hz) was used as a seed for a GWU-Lasertechnik basiScan Beta-Barium Borate Optical Parametric Oscillator, producing a pulse of wavelength 440 nm. This wavelength of 440 nm was used for all ASE threshold, gain, and loss measurements in this study.

Variable stripe length (VSL) gain measurements were performed according to standard procedure.[43] The excitation beam was shaped into a stripe of 125 μm width using a cylindrical lens (15 cm focus length), and the stripe length was controlled by a pair of blades mounted on mechanically controlled stages that provided an adjustable slit. Only the central 10% of the beam was used to minimize pump inhomogeneity due the Gaussian intensity profile. The pump beam intensity, I_{pump}, was varied by means of a pair of polarizers or neutral density filters. One end of the stripe excitation was placed on the cleaved edge of the film while the length of the excitation stripe was progressively increased. The emission from the edge was collected with a 5 mm fiber and recorded using a commercial spectrometer (Ocean Optics USB4000; resolution 2 nm). Gain values were extracted according to the model proposed by Malko et al.,[7] that, in addition

to the exponential gain term, incorporates a linear exciton term to account for photoluminescence. This has been a common approach for fitting QD gain.[1,3,12] Loss measurements were conducted in the same experimental geometry. However, in this case, the length of the excitation stripe was held constant, while the distance of the stripe from the edge of the film, d, was varied by simultaneously varying the position of both blades.[22] As the emission propagates towards the collecting fiber, it experiences attenuation by scattering and re-absorption in the unexcited region of the film. The decay of the collected emission signal with increasing distance, d, from the edge was fit to an exponential law: $I(d) = I(0)\,Exp(-\alpha d)$ to extract the loss coefficient α.

5.3 Results and discussion

5.3.1 Quantum dot characteristics

The quantum dots in this study have a core/graded shell type-I composition ($CdSe/Cd_{1-x}Zn_xSe_{1-y}S_y$), diameter near 8 nm, and exhibit typical broadband absorbance below 614 nm and a Stokes-shifted narrow emission peak near 624 nm (**Figure 5.1a**). All QD films use the same type of quantum dot since the presence (and type) of inorganic passivating shell has been shown to affect exciton dynamics and gain properties.[15,17] The length of the amine-functionalized ligands was varied from 16 (hexadecylamine), 8 (octylamine), to 4 (butylamine) carbon atoms in order to examine how the maximum QD-packing density depends on the ligand length (**Figure 5.1b,c**). Oleic acid was chosen as a standard control primarily for comparative purposes because it is a common QD ligand widely used in the literature. [14,23]

The efficiency of the ligand exchange process is monitored and confirmed via NMR, an example of which is shown in **Figure A.1&2**. The optical properties of the QDs were examined before and after the ligand exchange since the process involves exposure to multiple solvents and washing steps, as well as a change from a carboxylic functional binding group to an amine group. Quantum yield experienced the most notable change (decrease) after the ligand exchange process, with other optical properties remaining nearly unaffected (**Table A.1)**. Decreases in quantum yield are typically attributed to less effective passivation of the QD surface which opens up nonradiative relaxation pathways for exciton recombination.[24,25] However, in this case the variation in QY should not be a critical factor since the stimulated emission lifetime of these QD films (less than 0.1 ns) (**Table A.2**) is much shorter than typical alloyed QD spontaneous recombination lifetimes (<4 ns).[24,25]

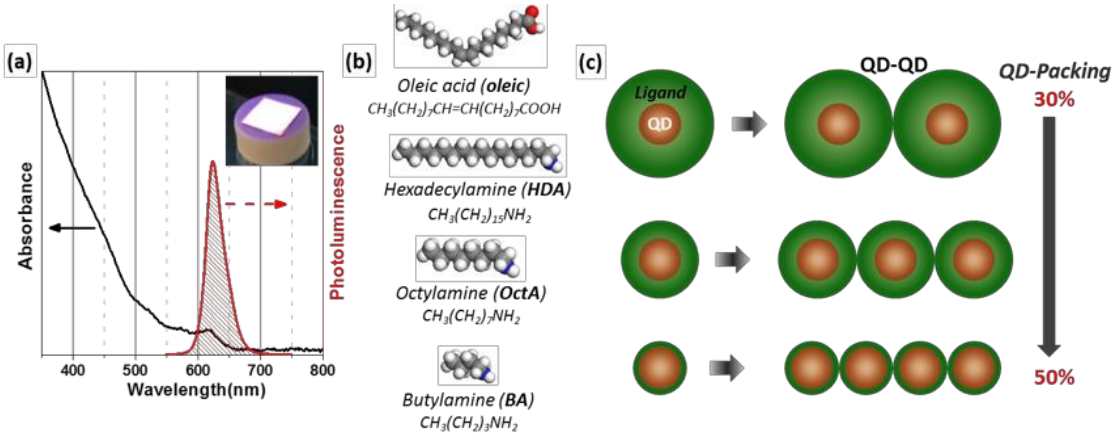

Figure 5.1 The QDs show broadband absorption and narrowband emission (a). Ligands of different size (b) were used to stabilize the QDs in order to control the spacing between adjacent QDs when deposited into film (c). The QD-QD spacing dictates the maximum QD-packing density.

5.3.2 QD film uniformity & morphology

QD films were fabricated via spin-casting, covering the substrates uniformly and having uniform PL emission, as evidenced by bright field, dark field, and photoluminescence

imaging (**Figure A.3**). The QD films were deposited on a fluorinated polymer layer (CYTOP) with a low refractive index to improve light confinement (waveguiding) within the QD film.[21] The CYTOP film was briefly exposed to plasma in order to promote wide-spread wetting by the QD film. AFM topographical and phase images show that the morphology of the QD films depends on the ligand coating the QDs. Films of oleic acid capped QDs (oleic-QD) show the presence of domains with a dense arrangement of QDs (**Figure 5.2a**). The phase image indicates that the QD domains are separated from adjacent QD domains by regions of a different phase which is likely excess oleic acid that was not removed during washing as well as a thick coating of oleic acid from submerged QDs.

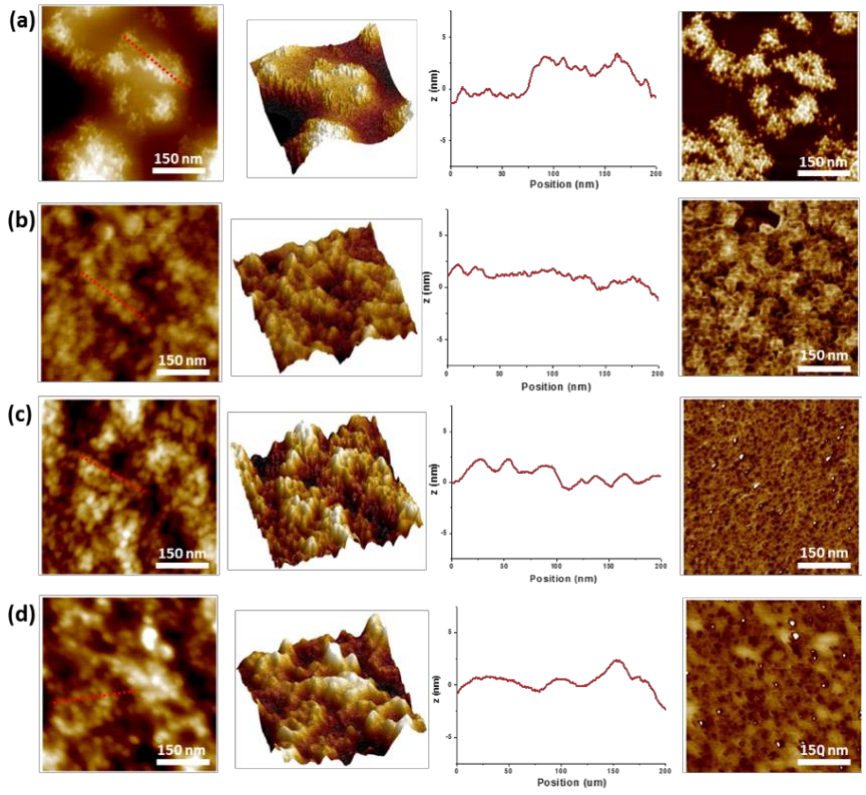

Figure 5.2. AFM surface morphology (column 1), 3D topography projection (column 2), topographical cross-section (column 3), and phase (column 4) for (a) oleic acid, (b) hexadecylamine, (c) octylamine, and (d) butylamine capped QD films. Z-scale is 20 nm for the oleic-QD film scan and 10 nm for all others. Phase scale is 20° for the oleic-QD film scan and 10° for all others.

The QD films of hexadecylamine-capped QDs (HDA-QD), octylamine-capped QDs (OctA-QD), and butylamine-capped QDs (BA-QD) have larger particle-like domains (likely aggregated QDs) that appear to cover the entire surface area (**Figure 5.2b,c,d**). The formation of localized lattice-like regions has been observed previously in oleic acid-QDs films, as well as the transformation to a more chaotic pattern upon replacement with a shorter ligand like butylamine.[20] We attribute the presence of a lattice arrangement in the oleic-QD film and the tighter aggregate arrangement in the BA-QD, OctA-QD, and HDA-QD films to two factors.

First, oleic acid provides exceptional colloidal stability due to its covalent bond with the QD surface and large size, which reduces aggregation of QDs in solution and allows for deposition of individual QDs that can form uniform QD lattice domains during spin-casting. On the other hand, the QD colloidal stability provided by the amine-based ligands (BA, OctA, HDA) is not as effective, which can lead to minor QD aggregation in solution that leads to larger domains in the film state. Second, the volume of oleic acid is greater than all the amine functionalized ligands (discussed later), which leads to greater spacing between QDs in the film state than that provided by the smaller amine-ligands. Greater QD spacing makes it easier for lattice-like QD arrangements to be observed.

Cross-sections of the height scans show a surface with sub-nanometer high bumps, indicating that the QDs are tightly packed with the free ligand filling the areas between adjacent QDs. The R_q roughness spans from approximately 4 nm (500 nm scan area) to 8 nm (10 um scan area) for all samples. In some instances, BA-QD films will appear smooth with no clear indication of QDs if examined very soon after film deposition, which is likely due to the fluid-like nature of butylamine at room temperature (melting point of -

49°C in free state) and its volatility (vapor pressure of 82 mmHg).[26] This fluid nature can compromise the AFM scanning to track surface features.

5.3.3 Ligand characteristics & QD-loading (volume fraction)

The four ligands used in this study each have a different molecular volume in the free-state (oleic acid: 0.320 nm^3, HDA: 0.295 nm^3, OctA: 0.159 nm^3, BA: 0.091 nm^3).[26] Therefore, changing the ligand may change the maximum allowable QD-packing density (volume loading) in QD films, which could impact the magnitude and threshold of optical gain.

The QD-packing density was monitored using a variety of approaches. High-resolution TEM (HR-TEM) of drop-cast QD films shows that the space between QDs decreases as the size of the ligand is decreased, with oleic-QDs having the largest QD spacing and BA-QDs having the smallest (**Figure 5.3a**). In addition, QD content was estimated using ellipsometry .[27] Examination of multiple films for each type of ligand-QD film agrees with the trend observed in HR-TEM, with QD-loading (volume percent) ranging from approximately 30% for oleic-QD films to 50% for the BA-QD films (**Figure 5.3b**). A similar increase in density of QD films has been observed previously upon exchanging oleic acid for butylamine (before film deposition).[28] The observed trend between ligand size and QD-loading follows the theoretical relationship between QD-loading and ligand size, which predicts 40% face-centered-cubic (FCC) loading for oleic-QD and 50% for BA-QD (no unbound ligand is present in the film) (**Figure A.4**).

Finally, TGA of drop-cast QD films shows that the amount of organic material (excess ligand and bound ligand) present in the QD solutions generally decreases for shorter

ligands **(Figure A.5)**, which corroborates the trend seen in HR-TEM and ellipsometry. Differences in the specific QD volume fraction between the spin-cast QD films and drop-cast QD films can be attributed to the difference in deposition methods, as well as the volatility of the ligands (**Figure A.5**).[26,29,30]

QD packing is a critical characteristic since optical gain is proportional to QD volume fraction.[31] For example, an increase of QD packing from 30% to 45% (factor increase of 1.5) is expected to cause a similar 1.5 factor increase in the magnitude of optical gain (**Eq. A.1**). In addition, QD packing affects the film refractive index, which affects the degree of light confinement within the QD film, the number of waveguide modes, and the optical loss due to leakage of light during propagation.[32] A higher film refractive index increases the index contrast with the underlying material (CYTOP) and increases light confinement within the film, a necessary condition for achieving high optical gain.

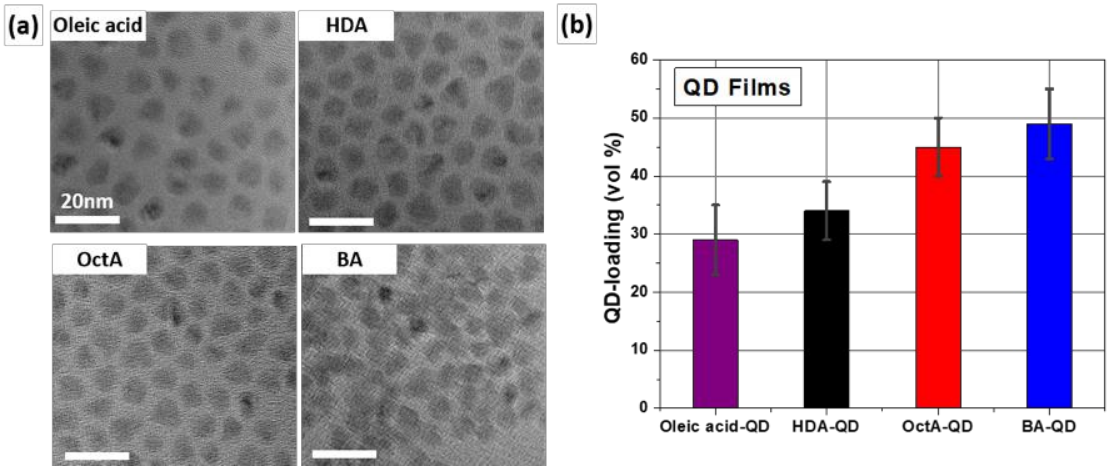

Figure 5.3 Four ligands of different size were used to examine how QD-packing is affected by ligand size. (a) HR-TEM micrographs of drop-cast QD solutions and (b) ellipsometry characterization of spin-cast QD films show that reducing the size of the ligand increases the QD-loading (packing density) of QDs in films. Scale bar is 20 nm for all TEM micrographs.

5.3.4 Optical gain threshold, magnitude, & stability

The existence of ASE is supported by a number of emission characteristics such as the presence of clear threshold behavior in emission intensity versus excitation intensity plots.[12,14,33] At threshold, the emission dependence on the pump excitation intensity transitions from approximately linear at low intensity to super-linear at successively higher pump fluence, as was clearly observed for all QD samples **(Figure 5.4a)** (note both axes are log scale). ASE threshold values were obtained by determining at what fluence this transition occurs (**Figure A.6**). The light-light curves were quite consistent over multiple spots (**Figure A.7**).

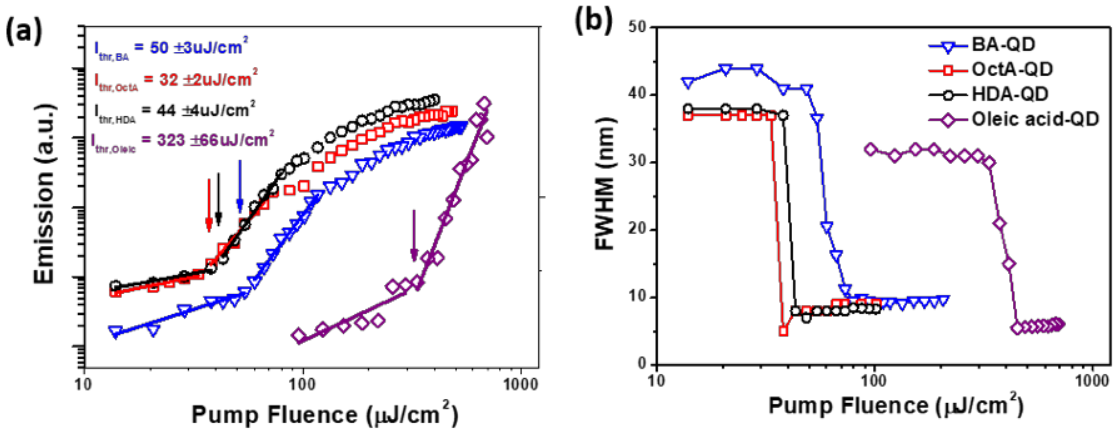

Figure 5.4. ASE in the QD films is identified by multiple characteristics of QD emission as the QD film is pumped with different excitation powers. (a) Emission intensity (log-log, scaled for clarity) showing threshold behavior, and (b) full-width at half-maximum (FWHM) of the emission peak showing spectral narrowing.

The BA-QD, OctA-QD, and HDA-QD films exhibited thresholds of approximately 30-50 uJ/cm^2 which matches many of the lowest QD film thresholds to date,[12] and is 5-10 times lower than the threshold of typical drop-cast QD films using traditional ligands.[14,33] The exceptionally low thresholds are attributed to the uniformity of the QD films and the high QD-packing density, which allow for efficient light generation and propagation. Furthermore, the core/graded shell composition of the QD also plays an important role, with previous studies showing that a graded shell imparts very effective

surface passivation of the core. This passivation decouples the core exciton states from surface trap states, effectively deactivating the non-radiative surface trap relaxation pathway.[15,34]

ASE threshold indicates the point where optical gain and loss are equal, and can depend on a number of factors.[35] In this case, the large differences in threshold are attributed primarily to the nature of the physical and thermal properties of the ligand. All ligands with the alkane structure and amine functionalization (butylamine, octylamine, and hexadecylamine) have similar thresholds, which are also much lower than that shown by the film with the oleic acid ligand (which has an internal double bond and a carboxylic acid terminal group). The internal double bond makes oleic acid waxy at room temperature and therefore highly fluid under optical pumping. This fluidity allows for more QD diffusion, which can lead to QD aggregation that increases optical scattering (optical loss) and modifies the localized refractive index (disrupts light propagation), both of which would delay the onset of ASE (increase the threshold). Furthermore, the waxy nature makes oleic acid QD films highly susceptible to physical damage.

The functional group of the ligand could play a role as well by imparting different degrees of surface passivation to the QD, which has been shown to have an impact on exciton trapping rates and the required average exciton gain threshold.[15,36] Auger recombination (an important obstacle for achieving QD optical gain) has also been shown to depend on factors like charged exciton states that could be influenced by the ligand functional group.[37,38] In addition, non-radiative hole relaxation has been shown to occur through a non-adiabatic ligand-mediated mechanism, which means different ligands could increase or decrease this non-radiative pathway.[39] However, this phenomenon is hindered by the presence of an inorganic shell so it is not likely to be an important factor for the

core/graded shell QDs in this study. Likewise, it has also been shown that the Auger recombination rate can, in certain instances, be relatively independent of surface passivation.[40] So, at this point in time it is unclear how intrinsic exciton dynamics are affected by the ligand choice and its influence on ASE threshold.

Spectral narrowing of the emission peak occurs simultaneously with threshold behavior and is an additional critical indication of the ASE phenomenon.[12,33] The FWHM of PL of all samples was approximately 30-40 nm, but narrowed to around 10 nm once ASE emerged (**Figure 5.4b**), which is common for QD ASE.[12,33] All films show similar spectral narrowing (78 ±3% reduction) compared to their initial PL FWHM. However, the QD film with the oleic acid ligand (carboxylic acid functionality) displayed the narrowest ASE FWHM (6 nm) since it began with the narrowest PL FWHM (32 nm). The QD films with amine functionalized ligands all show similar spectral narrowing to a FWHM of 11 nm (from ≈40 nm). The difference in PL FWHM appears to be correlated with how well the QDs are physically arranged and the chemical functionality of the ligand. As shown previously, the oleic acid-QD film has domains of well-ordered QDs while the amine-QD films (BA-QD, OctA-QD, and HDA-QD) have a less ordered arrangement (**Figure 5.2**). These differences could affect the degree of optical scattering during light propagation (and therefore the broadening of PL FWHM).

In addition, the chemical functionality of the ligand can affect QD surface passivation which affects the emission position, quantum yield, and electronic structure of the QD surface.[41] Additional confirmation of ASE is provided by the 10-15 nm red-shift of the ASE peak compared to the PL peak. This is a common trait of ASE often attributed to interparticle electronic energy transfer and optical re-absorption (**Figure A.8**).[33,42]

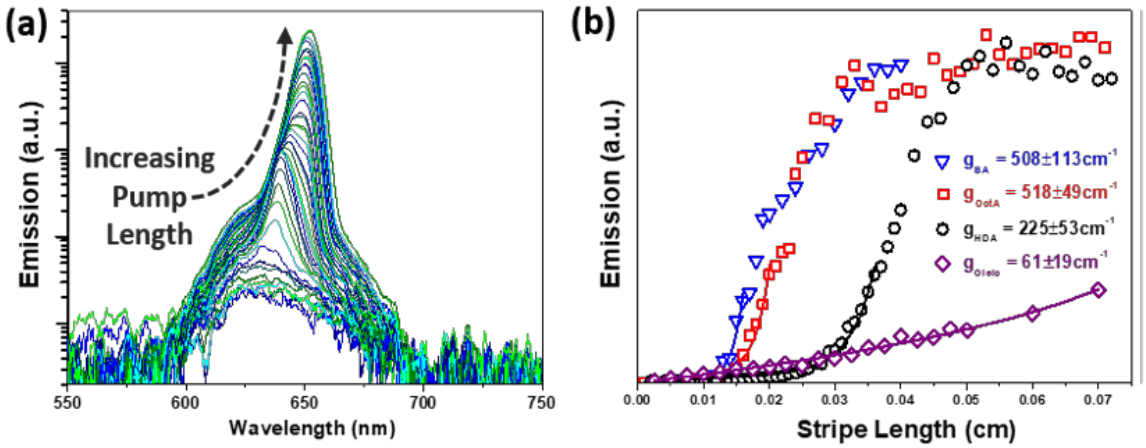

Figure 5.5 The optical characteristics of the QD films were determined using the variable strip length (VSL) method. (a) Emission of an OctA-QD film (log-intensity) at various pump strip lengths. The emergence of ASE is indicated by narrowing of the emission peak. (b) Emission intensity versus pump length for various QD-ligands (curves were off-set for clarity). The intensity data was fit to determine the gain value (I_{pump} = 200 uJ/cm^2).

The direct quantitative measurement of optical gain for each film was obtained using the variable stripe length (VSL) pumping approach, which involves optical excitation of the film using an excitation strip of variable length (**Figure 5.5a,b**).[43] If positive net gain is achieved, the spectrally narrowed ASE peak will emerge as the pump length is increased and the emission will exhibit an exponential increase of intensity as the optical pump strip is lengthened (**Figure 5.5a,b**).[1-3]

Optical gain appears to scale with QD-packing (for the same ligand functional group), with the HDA-QD film displaying modest gain (225 ±53 cm^{-1}) similar to that reported in the literature for Cd-based QD films.[1,33] In contrast, the OctA-QD and BA-QD films exhibit the highest gain (518 ±49 cm^{-1} and 508 ±113 cm^{-1}, respectively) (**Figure 5.6a**). The OctA-QD and BA-QD films have similar gain values because in this case the films had similar QD-loading (50% and 49%, respectively), indicating that QD-loading is

affected by both ligand length and the washing process. Gain values were averaged from multiple spots over a sample (**Figure A.9**).

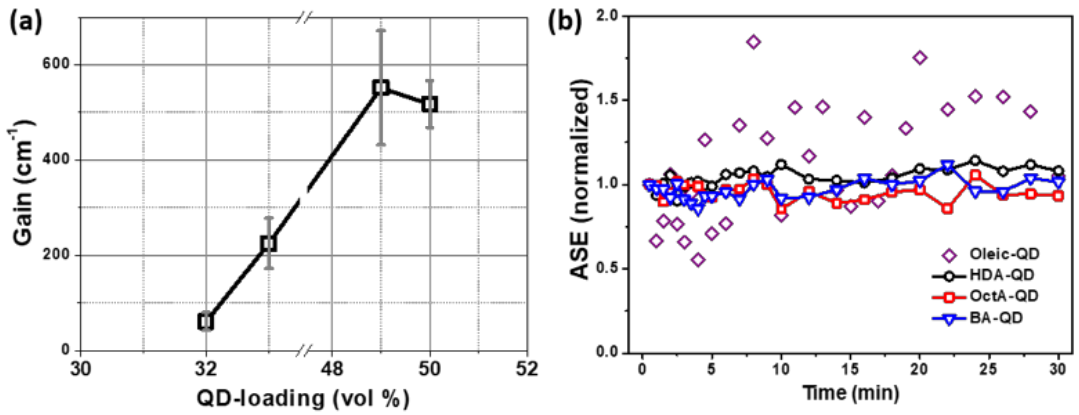

Figure 5.6 The magnitude and stability of optical gain depends on the type of QD-ligand pairing. (a) Optical gain versus QD-packing density. QD films with higher QD-packing exhibit higher optical gains. (b) Stability of ASE over a 30 minute period.

These gain values exceed typical QD gain values (60-200 cm^{-1}) due to the exceptionally high QD-loading,[1-3,5,6] approaching some of the highest values reported.[4] Although, as we suggest, the high optical gain is primarily a result of QD-loading, a number of additional system characteristics play a role. These factors include reduced surface trapping and Auger recombination due to the core/graded shell QD interface,[15] strong light confinement due to the incorporation of a sub-cladding layer with a very low refractive index, and increased absorption of the pump beam caused by the use of a reflective substrate.[27] An oleic acid QD film displayed a low optical gain (61 ±19 cm^{-1}) that was difficult to reliably measure due to its fluctuating ASE but was included as a reference sample since oleic acid is a commonly used QD ligand (discussed below).

The difference in optical gain magnitude between the films with different ligand-QD combinations can be attributed to a number of factors. First, as mentioned above, the

material gain value is expected to depend on the QD packing density (**Eq. A.1**)[31] due to an increase in the density of optically excited QDs that participate in the ASE process as well as an increase in the optical density of the film. An increase of optical gain due to higher QD packing density has been observed experimentally in layer-by-layer systems.[1] For example, the increase of QD packing from the HDA-capped QD film (34%) to the BA-capped QD film (49%) can explain a factor increase of 1.44 for the gain, which accounts for a portion of the differences between these films (factor of 2.3).

Second, gain depends on the degree of light confinement exhibited by the film since efficient light confinement leads to more stimulated emission within the film, as well as lower propagation losses from light leakage into adjacent layers. Light confinement depends primarily on film thickness and refractive index (RI) contrast between the QD film and the surrounding layers, with higher refractive index contrast leading to more efficient light confinement. Refractive index contrast was dictated by the RI of the QD film since the underlying material was always CYTOP (n = 1.34) and the top layer always air. Reducing the molecular dimensions of the ligands increases QD-loading which increases the RI of the film (since QDs have a higher refractive index than the ligand).

For example, the OctA-QD and BA-QD films had the highest refractive index of all the films (1.86±0.05 and 1.88±0.06, respectively) near the propagation wavelength (630-650 nm). On the other hand, the oleic-QD and HDA-QD films had the lowest refractive index (1.72±0.04 and 1.76±0.05, respectively). The resulting degree of light confinement can be quantified by the confinement factor (Γ), which is a measure of the power of the E-field confined to the QD film versus the power of the E-field present within the entire system.[44] Higher confinement factors indicate greater localization of light within the QD

film and an increase of modal gain ($g_{modal} = \Gamma \times g_{material}$).[44] Modeling of the confinement factor for each of the ligand systems for various thicknesses shows that the BA-QD film can exhibit a confinement factor up to 1.7 times that shown by the oleic-QD films and 1.4 times that exhibited by the HDA-QD films for relevant thicknesses (**Figure A.10**). In addition, the refractive index and thickness of the QD film determines the number and type of waveguiding modes, which affects propagation losses and might increase waveguiding efficiency. Therefore, all samples were designed to support only one waveguide mode by ensuring that the film thickness was above the first critical waveguiding thickness ($t_{c,1}$) but below the next highest critical waveguiding thickness ($t_{c,2}$) (**Figure A.11**).[32]

Third, the arrangement of QDs within the film (lattice-like, aggregated, or intermittently spaced) can affect how light propagates through the film, either through the introduction of scattering sites, QD-QD coupling,[42] or transverse localization effects.[45] Optical losses associated with scattering (and re-absorption) are examined later. Fourth, thermal transport (and dissipation) depends on the length of the QD ligand and has been shown to be an important factor in QD gain systems due to thermal mediated Auger recombination.[44,46,48] Finally, the difference in gain value between the oleic-QD and HDA-QD film could be due in part to the chemical functionality of the ligands since these films have similar QD-loading and refractive index. The chemical functionality of the ligand has been shown to affect QD surface passivation, which in turn affects the quantum yield and electronic structure of the QD surface and trapping rates.[36,41] The Auger recombination rate could also play a role, although previous studies have shown the Auger recombination rate is more strongly dependent on other factors like the QD core-shell interface and volume than surface passivation.[39,47] The combination of these factors likely contributes to the difference in optical gain values that can be obtained

from QD films and indicates that the type of ligand on the QD surface can strongly impact optical gain a number of ways.

5.3.5 Photostability of the QD films

The stability of ASE was examined over a period of 30 minutes for each type of QD film (**Figure 5.6b**). The QD films with amine functionalized ligands (HDA-QD, OctA-QD, BA-QD) display very stable ASE, which is an indication of the stable physical and thermal characteristics of the films under pumping. The stability of each ligand-QD combination can be explained by considering the interplay between QD-loading, the thermodynamic properties of the ligands, and the thermal transport/dissipation of the film. In general, stable ASE will arise if QD mobility is minimized since mobility/rearrangement of QDs during optical pumping can lead to the formation of scattering sites (which increase optical loss) in the film, as well as alter the effective refractive index (which can affect light propagation). In addition, ASE will be more stable if heat dissipation is efficient since localized heating of the film can lead to dissociation of the ligands from the QD surface (which results in loss of QD surface passivation), and to more efficient Auger recombination (which also increases intrinsic optical loss).[46]

It is worth noting that the HDA ligand is relatively long so it yields films with relatively low QD-loading (34%) and only moderate thermal conductivity (near 0.25 W/m*k).[48] However, the HDA-QD films show stable ASE, which suggests the solid state of HDA (melting point of 45°C) and its low vapor pressure (≈0 mmHG at 25°C) are the strongest factors.[26] On the other hand, butylamine seems to derive its ASE stability from its high QD packing (49%) and higher thermal conductivity (1.5x higher than oleic-QD),[48] rather than its low melting point (-49°C) or high vapor pressure (8 mmHG at 25°C).[26] In fact, it

is somewhat surprising that BA-QD films exhibit such stable ASE given the volatile nature of butylamine. It is likely that desorption of weakly bound BA occurs very quickly during spin-casting and storage so that by the time gain measurements are conducted there is minimal loosely bound BA to desorb during the optical pumping process. On the other hand, apart from its low vapor pressure (≈0 mmHG at 25°C) oleic acid is a poor choice for imparting optical stability due to the low QD-loading (29%), moderate thermal conductivity (near 0.25 W/m*k),[48] and its relatively low melting point (14°C) due to the double bond in its structure. These characteristics could allow for significant QD mobility and thermal modification of the ligands when the QD films are optically pumped, which manifest in the widely fluctuating ASE. These results show that consideration of the QD ligand is an important factor to consider in terms of optical gain magnitude and stability.

5.3.6 Optical loss

The intrinsic optical loss of the films was also measured to determine whether loss can account for differences in the gain values. Optical loss is determined by measuring the attenuation of ASE over different propagation distances (**Figure 5.7**).[22] Greater attenuation of ASE occurs as the distance travelled by the light to the edge of the sample increases. Attenuation of ASE is clearly evident in the spectra for all films and is shown for the HDA-capped QD film (**Figure 5.7a**). All amine films exhibit an exponential decrease in emission as the collective distance is increased (**Figure 5.7b**), as expected for films that exhibit optical loss. Loss values are averaged from multiple spots (**Figure A.12**).

The optical loss is observed to be proportional to the QD-loading of the film, with the HDA-QD film (lowest QD-loading) exhibiting the lowest loss (60±19 cm^{-1}) and the BA-QD

and OctA-QD films (highest QD-loading) exhibiting the highest loss (82 cm^{-1}) (**Figure 5.7c**). It is difficult to judge the magnitude of these QD loss values since optical loss is often overlooked in gain studies on QD films.

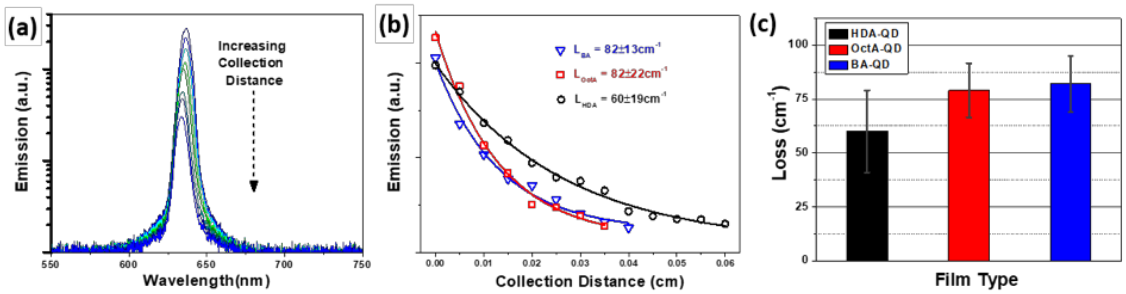

Figure 5.7 (a) Typical emission spectra from the variable attenuation length method for a HDA-QD film (log intensity). (b) Optical loss fitting for the HDA-QD, OctA-QD, and BA-QD films shows an exponential decrease with collection length. (c) Optical loss for different QD-ligand films.

However, these optical loss values are similar (within a factor of 2) to those exhibited by conjugated polymers films.[22] The scaling of loss with QD-loading is not surprising since optical re-absorption (an important component of optical loss) is proportional to QD-loading since the emitted light encounters more QDs (for a given distance) as it propagates through the film. In fact, the predicted loss for the BA-QD and OctA-QD films (scaled against the HDA-QD loss) falls within ±5% of the measured values, well within the measured standard deviations. The unstable nature of ASE for the oleic-QD film made measuring loss unreliable (**Figure 5.6b**). These results suggest that optical loss is not the primary factor underlying the observed trends in gain versus QD-loading since the films with highest optical loss still displayed the highest net optical gain.

5.3.7 Ligand selection

The ideal ligand depends on the relative importance of gain threshold, FWHM, magnitude, and stability, as well as optical loss. Aliphatic amine functionalized ligands

(butylamine, octylamine, hexadecylamine) were shown to provide lower gain threshold than that provided by oleic acid (internal double bond and carboxylic acid functionalization), while the narrowest FWHM of ASE was obtained using oleic acid (presumably due to the well-ordered physical domains). On the other hand, shorter ligands can result in higher QD-loading (which increases the number of optically stimulated QDs) and higher refractive index (which increases the confinement factor), both of which result in proportional increases to optical gain.

Obtaining stable ASE is slightly more complex, but generally requires very tight QD packing, good thermally stability (high melting and boiling points, low vapor pressure), and high thermal transport/dissipation. Unfortunately, these characteristics are not always independent, as seen with short organic ligands that offer high QD packing and large thermal dissipation,[48] but which typically exhibit low melting and boiling points and high volatility (and vice versa).[26] Predicting the relative impact of these factors is difficult. Finally, optical loss scales closely to QD-loading (neglecting losses associated with the presence of physical defects, surface roughness, and waveguiding losses).

Additional considerations when choosing a ligand include the colloidal stability imparted to the QDs in solution. Oleic acid typically provides very good colloidal stability due to its strong covalent bonding to the QD surface (X-type ligand).[49,50] However, amine functionalized ligands (butylamine, octylamine, hexadecylamine) form a coordinate bond to the QD surface (L-type ligand) that leads to reversible adsorption/desorption from the QD surface.[49,50] The desorption of ligands can lead to colloidal instability (aggregation of QDs) which causes scattering sites to form in the QD film during deposition and a lower than expected optical gain. QD instability was observed to be more pronounced for shorter ligands like butylamine than for longer ligands like octylamine or

hexadecylamine. Therefore, the length of time before the colloidal QDs are deposited into films should factor into the choice of ligand.

5.4 Conclusions

This work demonstrates how the molecular dimensions and functionality of the ligand capping the QD affects film morphology, QD-packing density, refractive index, and the resulting optical gain characteristics. Specifically, this work shows that changing the ligand greatly affects the factors that control light propagation in the film (refractive index and refractive index contrast). Furthermore, the ligand affects QD-packing density, which has a direct effect on optical gain. Finally, evidence was provided that the chemical structure and physical and thermal properties of the ligand affect ASE threshold. The combination of these factors resulted in a 2.25 fold increase in optical gain between the lowest and highest QD-packed films (with the same functional group), with the highest QD-packed films exhibiting exceptionally high net gain values (≈500 cm^{-1}). Reductions in ASE threshold and stability were also observed when switching from the commonly used waxy, large ligand oleic acid to the amine-functionalized ligands.

5.5 Chapter acknowledgements

Dr. Jaehan Jung and Youngjun Yoon (Prof. Zhiqun Lin's research group, Georgia Institute of Technology): QD synthesis, TEM and NMR characterization. Dr. Evan Lafalce (Prof. Valy Vardeny's research group, University of UTAH): optical gain and loss measurement. Marcus Smith (Prof. Tsukruk group, Georgia Institute of Technology): TGA measurements and data analysis. Dr. Sidney Malak (Prof. Vladimir Tsukruk's research group, Georgia Institute of Technology): AFM.

5.6 References (Chapter 5)

1 J. Roither, S. Pichler, M.V. Kovalenko, W. Heiss, P. Feychuk, O. Panchuk, J. Allam, B.N. Murdin, *Appl. Phys. Lett.* 2006, **89,** 111120.

2 V. Sukhovatkin, S. Musikhin, I. Gorelikov, S. Cauchi, L. Bakueva, E. Kumacheva, E.H. Sargent, *Opt. Lett.* 2005, **30,** 171.

3 M.A. Petruska, A.V. Malko, P.M. Voyles, V.I. Klimov, *Adv. Mater.* 2003, **15,** 610-613.

4 V.I. Klimov, A.A. Mikhailovsky, S. Xu, A. Malko, J.A. Hollingsworth, C.A. Leatherdale, H.J. Eisler, M.G. Bawendi, *Science* 2000, **290,** 314.

5 Y. Chan, J.S. Steckel, P.T. Snee, J.M. Caruge, J.M. Hodgkiss, D.G. Nocera, M.G. Bawendi, *Appl. Phys. Lett.* 2005, **86,** 073102.

6 J. Jasieniak, I. Fortunati, S. Gardin, R. Signori, R. Bozio, A. Martucci, P. Mulvaney, *Adv. Mater.* 2008, **20,** 69.

7 A.V. Malko, A.A. Mikhailovsky, M.A. Petruska, J.A. Hollingsworth, H. Htoon, M.G. Bawendi, V.I. Klimov *Appl. Phys. Lett.* 2002, **81,** 1303.

8 J. Hare, S. Steiner, F. Orucevic, V. Lefevre-Seguin, Silica microspheres as high-Q microcavities for semiconductor quantum-dot lasers. In *Optoelectronic Integrated Circuits VII*, Eldada, L. A.; Lee, E. H., Eds. 2005, **5729,** 94.

9 V.C. Sundar, H.J. Eisler, T. Deng, Y.T. Chan, E.L. Thomas, M.G. Bawendi, *Adv. Mater.* 2004, **16,** 2137.

10 C.E. Finlayson, D.S. Ginger, N.C. Greenham, *Appl. Phys. Lett.* 2000, **77,** 2500-2502.

11 F. Garcia-Santamaria, Y.F. Chen, J. Vela, R.D. Schaller, J.A. Hollingsworth, V.I. Klimov, *Nano Lett.* 2009, **9,** 3482-3488.

12 C. Dang, J. Lee, C. Breen, J.S. Steckel, S. Coe-Sullivan, A. Nurmikko, *Nat. Nanotech.* 2012, **7,** 335.

13 J. Nanda, S.A. Ivanov, M. Achermann, I. Bezel, A. Piryatinski, V.I. Klimov, *J. Phys. Chem. C* 2007, **111,** 15382.

14 V.I. Klimov, S.A. Ivanov, J. Nanda, M. Achermann, I. Bezel, J.A. McGuire, A. Piryatinski, *Nature* 2007, **447,** 441.

15 B.R. Walsh, J.I. Saari, M.M. Krause, R. Nick, S. Coe-Sullivan, P. Kambhampati, *J. Phys. Chem. C* 2015, **119,** 16383.

16 P. Kambhampati, *Acc. Chem. Res.* 2011, **44,** 1.

17 R.R. Cooney, S.L. Sewall, D.M. Sagar, P. Kambhampati, *J. Chem. Phys.* 2009, **131,** 164706.

18 Kambhampati, *J. Phys. Chem. Lett.* 2012, **3,** 1182.

19 R.R. Cooney, S.L. Sewall, D.M. Sagar, P. Kambhampati, *Phys. Rev. Lett.* 2009, **102,** 127404.

20 C.Y. Kuo, M.S. Su, C.S. Ku, S.M. Wang, H.Y. Lee, K.H. Wei, *J. Mater. Chem.* 2011, **21,** 11605.

21 Bellex International Coportation, Wilmington DE, USA. CYTOP chemical and physical properties. http://www.bellexinternational.com/products/cytop/

22 M.D. McGehee, R. Gupta, S. Veenstra, E.K. Miller, M.A. Diaz-Garcia, A.J. Heeger, *Phys. Rev. B* 1998, **58,** 7035.

23 P. Guyot-Sionnest, B. Wehrenberg, D. Yu, *J. Chem. Phys.* 2005, **123,** 074709.

24 D. Choi, J.Y. Pyo, Y. Kim, D.J. Jang, *J. Mater. Chem. C* 2015, **3,** 3286.

25 P. Maity, T. Debnath, H.N. Ghosh, *J. Phys. Chem. C* 2015, **119,** 10785.

26 Sigma-Aldrich, ChemSpider, and Chemicalize for measured and theoretical thermodynamic data and geometry data for butylamine, octylamine, hexadecylamine, oleic acid, trioctylphosphane oxide, and pyridine.

27C.H. Lin, E. Lafalce, J. Jung, M.J. Smith, S.T. Malak, S. Aryal, Y.J. Yoon, Y. Zhai, Z. Lin, Z.V. Vardeny, V.V. Tsukruk, *ACS Photonics* 2016, **3,** 647.

28 C.Y. Kuo, M.S. Su, C.S. Ku, S.M. Wang, H.Y. Lee, K.H. Wei, *J. Mater. Chem.* 2011, **21,** 11605.

29 B.S. Kim, L. Avila, L.E. Brus, I.P. Herman, *Appl. Phys. Lett.* 2000, **76,** 3715.

30 D.I. Kim, M.A. Islam, L. Avila, I.P. Herman, *J. Phys. Chem. B* 2003, **107,** 6318.

31 S. Hoogland, Optical gain and lasing in colloidal quantum dots, Colloidal Quantum Dot Optoelectronics and Photovoltaics. *Cambridge University Press:* 2013.

32 Robert G. Hunsperger, Integrated Optics, Theory and Technology, Ch.2: Optical Waveguide Modes. *Springer Science and Business Media*, 2009.

33 F. Todescato, I. Fortunati, S. Gardin, E. Garbin, E. Collini, R. Bozio, J.J. Jasieniak, G. Della Giustina, G. Brusatin, S. Toffanin, R. Signorini, *Adv. Funct. Mater.* 2012, **22,** 337.

34 S.L. Sewall, R.R. Cooney, K.E.H. Anderson, E.A. Dias, D.M. Sagar, P. Kambhampati, *J. Chem. Phys.* 2008, **129,** 084701.

35 S. Yang, Y. Wang, H. Sun, *Adv. Opt. Mater.* 2015, **3,** 1136.

36 M. Califano, *ACS Nano* 2015, **9,** 2960

37 Y.-S. Park, W.K. Bae, J.M. Pietryga, V.I. Klimov, *ACS Nano* 2014, **8,** 7288.

38 W.K. Bae, Y.-S. Park, J. Lim, D. Lee, L.A. Padilha, H. McDaniel, I. Robel, C. Lee, J.M. Pietryga, V.I. Klimov, *Nat. Commun.* 2013, **4,** 2661.

39 R.R. Cooney, S.L. Sewall, K.E.H. Anderson, E.A. Dias, P. Kambhampati, *Phys. Rev. Lett.* 2007, **98,** 177403.

40 V.I. Klimov, A.A. Mikhailovsky, D.W. McBranch, C.A. Leatherdale, M.G. Bawendi, *Science* 2000, **287,** 1011.

41 M. Green, *J. Mater. Chem.* 2010, **20,** 5797.

42 C.R. Kagan, C.B. Murray, M.G. Bawendi, *Phys. Rev. B* 1996, **54,** 8633.

43 K.L. Shaklee, R.F. Leheny, *Appl. Phys. Lett.* 1971, **18,** 475.

44 M.M. Adachi, F. Fan, D.P. Sellan, S. Hoogland, O. Voznyy, A.J. Houtepen, K.D. Parrish, P. Kanjanaboos, J.A. Malen, E.H. Sargent, *Nat. Comm.* 2015, **6,** 8694.

45 M. Segev, Y. Silberberg, D.N. Christodoulides, *Nat. Photonics* 2013, **7,** 197.

46 C. Javaux, B. Mahler, B. Dubertret, A. Shabaev, A.V. Rodina, Al. L. Efros; D.R. Yakovlev, R. Liu, M. Bayer, G. Camps, L. Biadala, S. Buil, X. Quelin, J.P. Hermier, *Nat Nano* 2013, **8,** 206.

47 G.E. Cragg, A.L. Efros, *Nano Lett.* 2010, **10,** 313.

48 M. Liu, Y. Ma, R.Y. Wang, *ACS Nano* 2015, **9,** 12079.

49 N.C. Anderson, M.P. Hendricks, J.J. Choi, J.S. Owen, *J. Amer. Chem. Soc.* 2013, **135,** 18536.

50 M.M. Krause, L. Jethi, T.G. Mack, P. Kambhampati, *J. Phys. Chem. Lett.* 2015, **6,** 4292.

CHAPTER 6

CORE/ALLOYED-SHELL QUANTUM DOT ROBUST SOLID FILMS WITH HIGH OPTICAL GAINS

6.1 Introduction

A rich variety of colloidal nanocrystals have been recently synthesized as potential candidates for optical gain media, including Cd- and Pb-based quantum dots (QDs),[1,2,3,4] CdSe nanoplatelets,[5,6,7,8] and $CsPbX_3$ (X = Cl, Br, I) perovskite QDs.[9] Among them, CdSe nanoplatelets have shown one of the highest net gain value of 500-690 cm^{-1} in the green and red spectral range due to their large oscillator strength in comparison to QDs; whereas $CsPbBr_3$ perovskite QD films possess a net gain value of 450 cm^{-1} in the green spectral range. The high net gain value exhibited by these materials is widely recognized as an important 'figure of merit' to consider when developing new photonic systems that demonstrate parity-time symmetry, which require a sensitive balance between optical gain and loss to achieve the breaking point for single-mode lasing,[10,11] double refraction systems,[12] and directional invisibility and reflection.[13,14]

Although net gain values are high in the above-mentioned materials, the colloidal and photoluminescence (PL) stability remain as important issues for the realization of practical photonic structures. In this regard, the PL intensity in the vast majority of studies to date is unstable even under modest external effects such as light illumination, chemical treatments, or mechanical rubbing. For example, the lasing output intensity of CdSe nanoplatelets is reduced to 10%-50% of the original value within one hour under

continuous-wave pumping.[5] Furthermore, the surface of these CdSe structures is highly sensitive to polar solvents, which can lead to an irreversible physical stacking and thus a large reduction of PL intensity due to the efficient energy transfer to defective nanoplatelets.[15] As for the PL stability in $CsPbX_3$ perovskite QDs, it is reported that the PL of $CsPbI_3$ perovskite QDs in the red spectral range gradually vanishes because these materials undergo a structural phase transition from the PL-active cubic to the PL-inactive orthorhombic structure.[9] A recent study also shows an fast (within minutes) photodegradation of $CsPbBr_3$, $CsPbBr_xI_{3-x}$ and $CsPbI_3$ perovskite QDs, exemplifying their highly unstable PL emission.[16]

In stark contrast to these unstable materials, the well-developed Cd-based QDs possess relatively high colloidal stability and stable emission in the visible region,[17] making them promising candidates for the fabrication of stable photonic devices if incorporated in polymer films and coatings.[18] However, the typical net gain value of Cd-based QDs in solid state (mostly, drop-cast films) is relatively low (60-200 cm^{-1}), which is well below those reported in CdSe nanoplatelets and $CsPbBr_3$.[3,19,20] Moreover, the film integrity of QDs capped with monodentate ligands can easily deteriorate during common fabrication processes due to the good solubility of the organic capping ligands in a variety of non-polar solvents.

In this work, we report the crafting of freestanding, mechanically robust, and optically, environmentally, and chemically stable CdSe/$Cd_{1-x}Zn_xSe_{1-y}S_y$ core/alloyed-shell QD films with outstanding net gain values up to 650 cm^{-1}, minimum optical losses around 50 cm^{-1}, and amplified spontaneous emission (ASE) thresholds as low as 44 $\mu J/cm^2$ in the quasi-continuous wave (q-CW) region (ns pulse excitation). These results are achieved by capitalizing on the rationally designed crosslinkable core/alloyed-shell QDs with short bi-

functional ligands. Two consecutive strategies were implemented to achieve stable high gain properties in the resulting film with highly loaded crosslinked QDs. The first strategy involves the maximization of QD-loading density by replacing the long ligand oleic acid (OA) with the shorter ligand butylamine (BA). This ligand replacement greatly increases the QD packing density up to ~50%, which is nearly two-fold higher than that of conventional QD films reported to date, and is in fact closer to the theoretical limit (52% for simple cubic to 74% for face centered cubic for sphere packing without capping ligands).

The second complementary strategy is to further impart mechanical strength, chemical resistance, and optical stability by exposure to a bifunctional crosslinker 1,7 diaminoheptane (DIAH). The bifunctional crosslinker rendered a very stable passivation of the QD surface by connecting (i.e., crosslinking) the adjacent QDs via the strong coordination interaction between CdSe/$Cd_{1-x}Zn_xSe_{1-y}S_y$ core/alloyed shell QDs and the two terminal NH_2 groups of the DIAH linkers. The resulting crosslinked QD materials can be fabricated as mechanically robust large area films of several cm^2 across. Moreover, they can be readily released as a freestanding film and transferred onto different substrates without compromising their structural integrity and while retaining their stable optical activity under mechanical stresses and the harsh chemical environments under which traditional drop-cast films show a fast deterioration. Finally, we demonstrate that our designs are compatible with lithographical patterning techniques for the development of optical lasing arrays.

6.2 Experimental details

***Ligand exchange**:* The oleic acid-capped CdSe/$Cd_{1-x}Zn_xSe_{1-y}S_y$ QDs were centrifuged with acetone three times to remove excess oleic acid and ODE. Subsequently, purified oleic acid-capped CdSe/$Cd_{1-x}Zn_xSe_{1-y}S_y$ QDs were re-dispersed in hexane and an excess amount of butylamine was added to perform the solution-phase ligand exchange. The ligand exchange reaction was allowed to proceed at 45℃ for 1 day. The solution was then precipitated using methanol and re-dispersed in a mixture of hexane and an excess BA amount. This procedure was repeated for three times. Upon ligand replacement, the QD film loading (as determined by refractive index) (**Table S2**) increased from 27% to 53% in the BA-capped QD films, a nearly two-fold increase. This is an extremely high loading of QD considering that the loading of ideal spherical particles without capping ligands ranges from 52% for simple cubic to 74% for face centered cubic arrangements. The choice to use DIAH as the bifunctional crosslinker following ligand exchange can be rationalized as follows. First, the length of a bifunctional crosslinker needs to be carefully chosen so that it can effectively replace the capping ligand BA during the solid-state exchange. In an ideal case, where BAs are fully extended when capping the QD surface, the gaps between QDs is the length of two BA molecules (eight C-C bonds). Thus, an appropriate bifunctional crosslinker should be shorter in order to efficiently fill the gaps between QDs without compromising their close packing.

The solid-state exchange is performed by soaking the prepared butylamine-capped QD films in a 0.1 M methanol solution of 1,7 diaminoheptane for 1 hour. After soaking, the films are washed with methanol 3 times to remove any excess 1,7 diaminoheptane. Notably, after ligand exchange, the film is rendered insoluble in both polar and nonpolar solvents, indicating successful crosslinking treatment by DIAH (**Figure B.1**). It was observed that the QD loading did not significantly change during the networking step

(53% to 49%), which may be due to the similar length of two BA ligands and the length of one DIAH ligand if the ligands are fully extended between adjacent QD surfaces.

***Film preparation**:* QD films were fabricated by spin-coating a QD heptane solution of ~60 mg/mL at 1000 rpm for 1 minute. The film thickness ranged from 150-250 nm in order to support only the first waveguide mode. The QD films were deposited on CYTOP (AGC Chemicals) coating, which has a sufficiently low refractive index (n_{650} = 1.34) to provide light confinement and waveguiding within the QD film. The CYTOP was exposed to air or Ar plasma for 5 seconds in order to improve the wetting of CYTOP by QDs. Silicon, with a 290-295 nm thick SiO_2 surface layer, was used as a substrate since its large extinction coefficient attenuates much of the light that leaks into the substrate. The attenuation of light that leaks from the QD film into the Si substrate ensures that the light detected at the edge is the light that has propagated through the QD film. The substrate was cleaved to obtain sharper, cleaner edges to improve the intensity of the output light and ensure that the area of the film exposed to the pump light was uniform over the length of the pump strip length.

6.3 Results and discussion

6.3.1 Choice of bifunctional crosslinker

The surface of as-synthesized QDs is protected with an organic shell of oleic acid (OA) (**Figure 6.1**). The replacement of the OA ligand with shorter ligands was explored to increase the QD-loading and stabilize QD films. Because thiol functional groups tend to quench the PL intensity [21] we choose amine-terminated ligands as candidates for stabilization and crosslinking of QDs.[22] Finally, excessively volatile ligands with a low

melting point (m_p) and boiling point (b_p) can lead to fast thermal and physical deterioration, which can cause optical quenching due to the loss of surface passivation. Crosslinkers with higher m_p and b_p, as well as a lower vapor pressure, are expected to provide a surface passivation that is resistant to harsh environments and prevents the solid films from fast degradation during fabrication, usage, and storage. Thus, the shorter length of DIAH ligands (7 C-C bonds) and the much higher m_p of 26-29°C and b_p of 223-225°C should provide stable surface passivation under the elevated temperatures present during optical pumping (**Table S1**).[23]

6.3.2 Film fabrication and properties

Figure 6.1a illustrates the material processing steps utilized in this study. First, we synthesized chemical compositional gradient CdSe/$Cd_{1-x}Zn_xSe_{1-y}S_y$ core/alloyed-shell QDs with an average diameter of 8.2 nm by following a published procedure with some modifications.[24] These QD structures have been selected because of their high stability and enhanced quantum yield. In fact, the core/alloyed-shell or alloyed-core/shell QD structure have been reported to effectively increase the Auger recombination lifetime to at least a few hundred ps and even enable single exciton gain.[3,6,37] We then performed the subsequent solution-phase and solid-state ligand exchanges to tether CdSe/$Cd_{1-x}Zn_xSe_{1-y}S_y$ QDs with the DIAH ligand.

High resolution transmission electron microscopy (HR-TEM) confirmed the QD dimensions and allowed for the estimation of interparticle distance of QDs capped with different ligands (**Figure 6.1, B.2**). After the solution-phase ligand exchange from OA to BA, the distance between neighboring QDs decreases significantly from 3.2±0.5 nm for OA-capped QDs to 1.1±0.5 nm for BA-capped QDs.

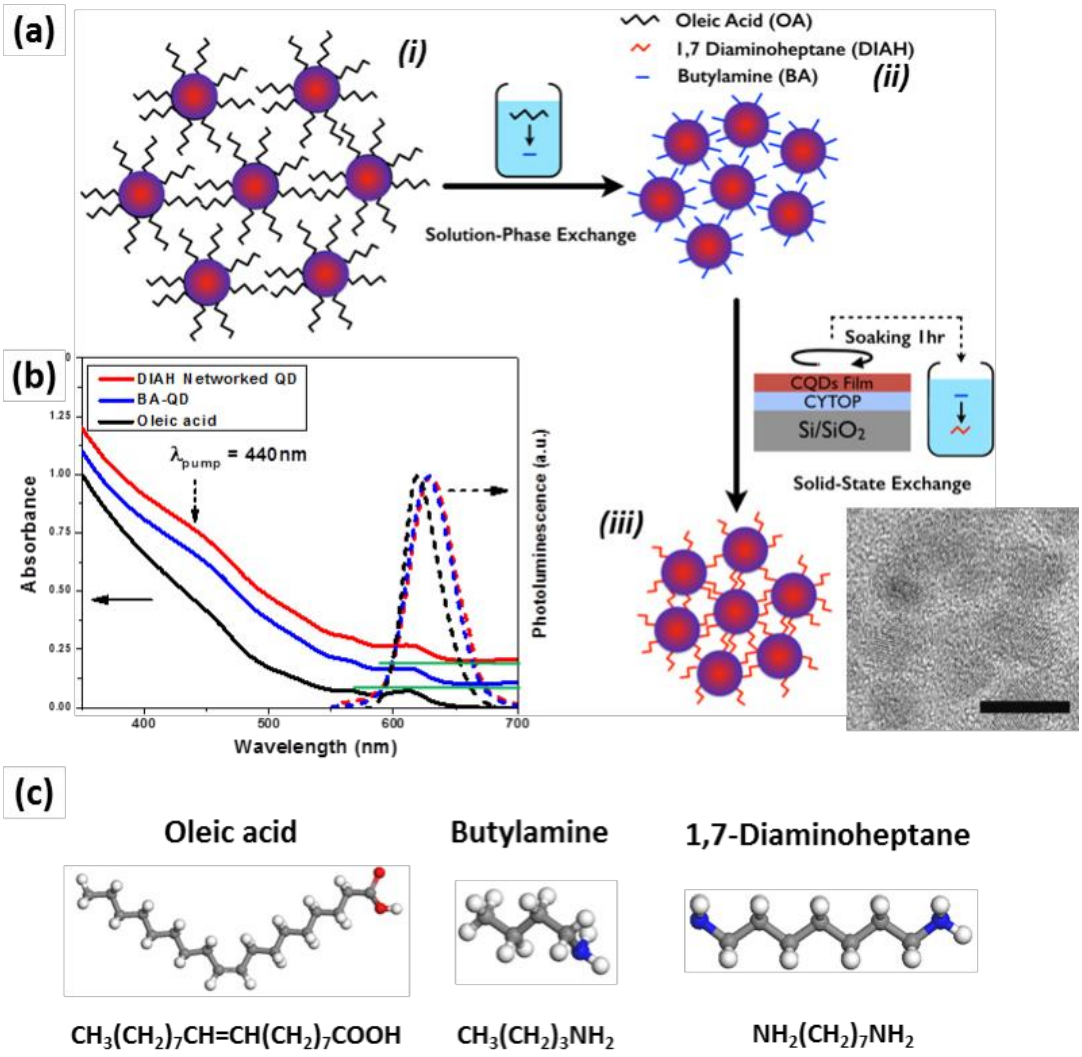

Figure 6.1 (a) Crosslinked QD solid film fabrication: the as-synthesized oleic acid (OA)-capped CdSe/$Cd_{1-x}Zn_xSe_{1-y}S_y$ core/alloyed-shell QDs (i) undergo the solution-phase ligand exchange by adding butylamine (BA) in the QD solution (ii); after the solution-phase ligand exchange, the concentrated BA-capped QD solution is cast to form a close-packed QD film, which is subsequently soaked in a 0.1 M methanol solution of 1,7 diaminoheptane (DIAH) to perform the solid-state ligand exchange. The crosslinked QDs are tethered with DIAH ligand and shows tight packing (HRTEM scale bar is 10 nm) (iii). (b) Absorbance (solid) and emission (dashed) spectra of as-synthesized OA-capped QD solution (black line), BA-capped QD film (blue line) and DIAH-tethered QD film (red line). The baselines (green solid lines) of BA-capped QD film and DIAH-tethered QD film are offset for clarity. (c) Molecular models and chemical formulas of the organic ligands used in this study: oleic acid (OA); butylamine (BA), and 1,7 diaminoheptane (DIAH).

The reduced interparticle distance demonstrates the effective increase in QD loading after exchange with the shorter organic ligand shell. Furthermore, the spacing of the crosslinked films (i.e., DIAH-tethered QDs; 1.2 ±0.4 nm) is similar to that of the BA-capped QD films, confirming that the loading is primarily controlled by the molecular dimensions of organic ligands.[25,26]

The optical properties of QDs (absorption and emission) in solution and solid film state are shown in **Figure 6.1b**. All samples have similar first excitonic absorption peaks near 610 nm, whereas the emission peak shows a red-shift of 9 nm in the condensed solid state (629 nm in solid film vs 620 nm in solution). Such a red-shift indicates higher optical reabsorption and modest coupling interactions between neighboring QDs that can induce enhanced interparticle energy transfer.[27,28] The crosslinking within solid films did not lead to further red-shifting, signifying the absence of excessive QD aggregation. The spin-cast films from BA-capped QDs are uniform, without QD aggregation, and exhibit uniform PL emission. Atomic force microscopy (AFM) revealed that the film possesses a microroughness of 0.6 nm and 3.9 nm over surface areas of 500 nm by 500 nm and 10μm by 10 μm, confirming a uniform material distribution (**Figure B.3a,b,i,j**). The crosslinked DIAH-tethered QD films remain smooth with a microroughness of ~1nm over surface areas of 500 nm by 500nm and 10μm by 10 μm and exhibit a larger phase contrast, which confirms the presence of the limited QD clusters surrounded by an organic matrix (**Figure 6.2 and B.3g,h**).

Differential scanning calorimetry for the DIAH-tethered QD films shows a glass transition near 97°C, and no indication of a melting point which is a characteristic of crosslinked and amorphous polymer films with restricted molecular mobility (**Figure B.4)**. [29] Furthermore, comparative FTIR spectra for all films indicate a clear difference between

BA-capped QD and DIAH-tethered QD films in the spectral range of C-H and N-H stretching mode bands. The large reduction of symmetric and asymmetric CH_3 stretching peaks and the absence of asymmetric N-H stretching peak indicate the crosslinking/coordination of ligands with QD surface **(Figure B.5)**.[30,31]

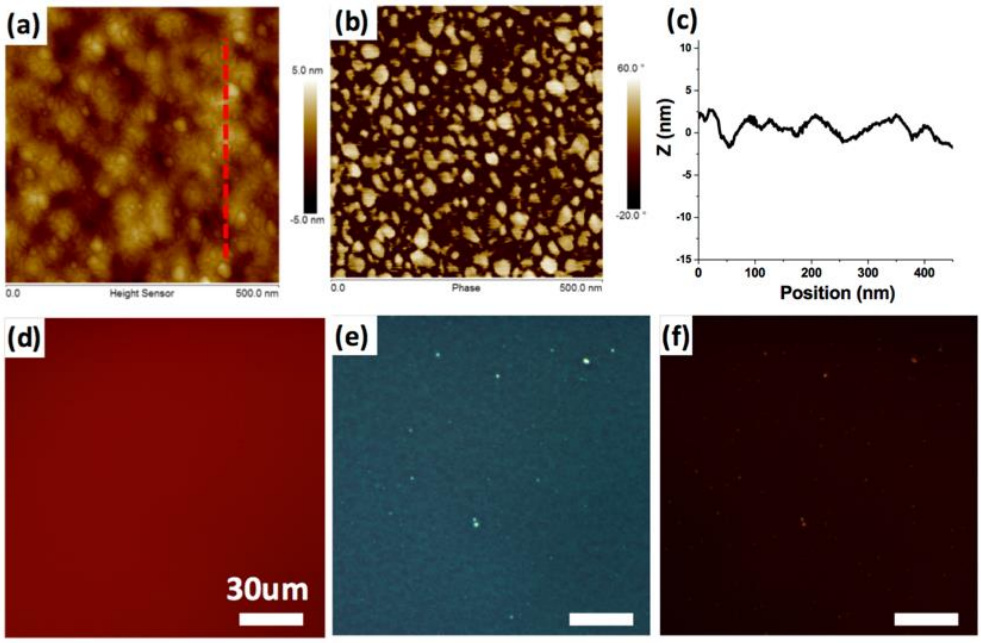

Figure 6.2 AFM scans of height (a), phase (b), and (c) height cross-section along the line in (a) for the DIAH-tethered QD film. The height scale is 10 nm and the phase scale is 80 degrees. Fluorescence imaging shows uniform emission over large areas (d) while bright field (e) and dark field (f) optical micrographs show uniform morphology with minimal physical defects. All scale bars are 30 μm.

6.3.3 Optical gain studies of DIAH-tethered QD films

The optical performance of the DIAH-passivated QD solid films was studied using a standard configuration of the variable stripe length (VSL) method with q-CW nanosecond (ns) pulsed 440 nm laser excitation (see SI).[32] As we observed, amplified spontaneous emission (ASE) from the close-packed QDs films can be clearly detected under q-CW

conditions, which is rarely reported due to efficient Auger recombination rates that typically suppress ASE.[1] In fact, nearly all reported QD net gain values in the literature were measured using ultra-fast femtosecond lasers to overcome the Auger recombination rate.[19] Although the 5 ns pulse duration is much longer than the typical Auger recombination lifetime of 10-300 ps for Cd-based QDs (see below), we were able to observe clear signatures of ASE with increasing pump excitation intensity. The observed phenomena include spectral narrowing, the emergence of a red-shifted dominant emission band, and a clear threshold in the emission intensity vs excitation intensity plot (**Figure 6.3a, b and B.7d)**.

In fact, a significant spectral narrowing was seen as the pump fluence increased with the broad cw PL peak (a FWHM of ~45 nm) collapsing to a narrow ASE peak of ~8 nm FWHM (**inset: Figure 6.3a**). In addition, the ASE peak is positioned at 638 nm, which is red-shifted by ca. 9 nm with respect to the spontaneous PL peak position (~629 nm). The red-shift of ASE peak position may arise from the competition between optical gain from stimulated emission and optical loss from re-absorption in the single-exciton regime,[3] or due to the lower biexciton energies that result from attractive exciton-exciton interactions of type I-like QDs in the biexciton regime.[2] In addition to spectral narrowing and emission red-shifting, a threshold behavior was also observed in the emission intensity vs excitation intensity plots (**Figure 6.3b).** The non-linear behavior is clearly evident from the abrupt increase of output intensity above the certain threshold. The significant spectral narrowing (five-fold) accompanies the exponential increase in emission intensity with the pump length which indicates lasing behavior **(Figures 6.3c, B.7c)**.

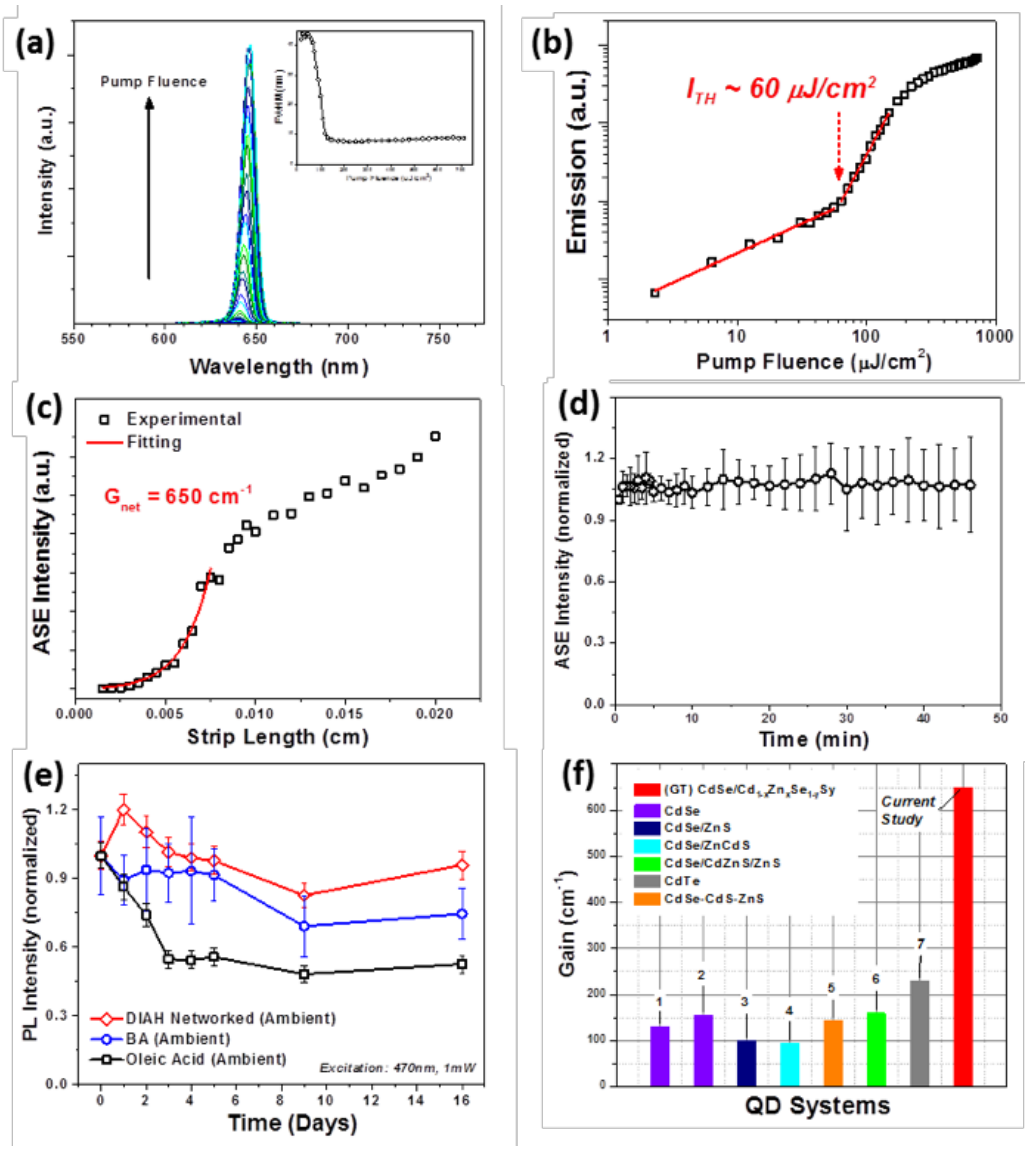

Figure 6.3 The optical characteristics of the DIAH-tethered QD film under pulsed excitation (440 nm, 5 ns pulse): (a) emission spectra from the DIAH-tethered QD film under different pumping energy density show the ASE and spectral narrowing (inset); (b) emission vs fluence behavior with a ASE threshold of ~60 μJ/cm^2; (c) the VSL measurement shows an exponential increase in ASE intensity with longer pump strip lengths (pumped fluence of 500 μJ/cm^2). Fitting the VSL curve yields a net gain value of 650 cm^{-1}. (d) ASE stability tests of DIAH-tethered QD films pumped with 500 μJ/cm^2 over 45 minutes of excitation. (e) CW PL stability tests of the DIAH-tethered QD film, BA-capped QD film, and OA-capped QD film under ambient conditions. (f) Comparison of gain values observed in this study and in recent literature: 1-(Ref. 1), 2-(Ref. 20), 3-(Ref. 1), 4-(Ref. 3), 5-(Ref. 1), 6-(Ref. 19), 7-(Ref. 1).

The DIAH-tethered QD film shows a minimum achievable threshold of approximately 44 μJ/cm^2 (**Figure B.7b**) and an average threshold of 60 ±20 μJ/cm^2 across different films and different spots on the same film. This threshold level is unusually low (an order of magnitude) in comparison to reported thresholds for common QD films such as CdSe/$Zn_{0.5}Cd_{0.5}S$ in the single-exciton regime (at 720 μJ/cm^2), $CsPbBr_3$ perovskite QDs (at 450 μJ/cm^2), and CdSe/CdS nanoplatelets (at 1000 μJ/cm^2) which were also pumped using comparable sub-ns or ns lasers.[3,9]

We suggest that the unusually low ASE threshold of QD films fabricated here is a result of not only the properties of the QD film but also the system design. First, the utilization of large diameter QDs (~8.2 nm) with a large absorption cross section increases the absorption of pump light.[17,36,37] We estimate the absorption cross section of our CdSe/$Cd_{1-x}Zn_xSe_{1-y}S_y$ core/alloyed-shell QDs to be $\sigma \sim 10^{-14}$ cm^2 (based on the absorbance data of our crosslinked QD film), which is much larger than typical values of CdSe QDs that are usually around 10^{-15}-10^{-16} cm^2.[17, 33] Second, highly reflective substrates (silicon, with a 290-295 nm thick SiO_2 surface layer) result in the excitation laser to pass twice through the film. Considering the reflection losses at the air/QD (~7%) and SiO_2/Si interfaces (reflectivity of Si is ~50%).[34] The overall effective pumping fluence is estimated to be 1.4 times (93%x150%) of the input pumping fluence, which leads to a higher absorbed photon density in comparison to films deposited on transparent quartz substrates.[9,36] Finally, lower overall waveguide losses were obtained by introducing strong light confinement within the QD film due to the high index contrast between the QD film (n = 1.9) and the low-index supporting CYTOP layer (n = 1.34) (**Figure 6.1a(iii)**).

Further support for the low gain threshold observed in this system comes from the examination of the average number of excitons per QD, 〈N〉. This value can be calculated by considering the relationship 〈N〉 = f × σ, where f is the pump intensity and σ is the absorption cross-section.[17] This estimation gives 〈N〉 = 2 for a threshold of 84 μJ/cm^2 (this value accounts for the double pass and reflection losses of the excitation laser through the QD film, 1.4 x 60 μJ/cm^2). The average number of excitons per QD calculated here is much higher than that obtained for CdSe/$Zn_{0.5}Cd_{0.5}S$ QDs in the single-exciton regime (〈 N 〉 = 0.86) and $CsPbBr_3$ perovskite QDs (〈 N 〉 = 0.5~0.8).[3,9] This difference can be considered by taking into account the decay of excitons caused by Auger recombination that occurs during the long ns pump pulse duration.[3,9,35] When the 3.5 ns Auger recombination lifetime (measured from our QDs by transient absorption spectroscopy (**Figure B.6**)) is scaled with the 5 ns pulse width used in this study, the average number of excitons per QD is 1.1 ±0.3. This value at ASE threshold is in good agreement with values obtained in other low-threshold Cd-based core/shell QD systems.[17]

Net gain values as high as 650 cm^{-1} were obtained in the crosslinked QD films by fitting the ASE intensity versus the excitation length with the Malko model (under a pump intensity of 500 μJ/cm^2), $I(L) = A_X L + \frac{B_{XX}}{g_{net}}(e^{g_{net}L} - 1)$, where A_X and B_{XX} are constants proportional to spontaneous emission intensity for excitons and biexcitons, L is the stripe length and g_{net} is the net gain value.[20] This gain value is comparable to or higher than those of high gain CdSe nanoplatelets.[6,7,8] An average net gain value of 493 ±106 cm^{-1} was obtained for multiple samples, different batches, and beam locations (**Figure B.7a)**. An average net gain value of 510 ±110 cm^{-1} was found for highly loaded BA-capped QD

films, indicating that DIAH with same functional group and similar length to 2 BA molecules does not change optical properties, surface passivation and packing density much during the solid-state exchange while imparting chemical resistance and physical robustness to the films. In contrast, a much lower net gain value of 60 ±20 $cm^{-}1$ (and higher average ASE threshold of 323 ±66 $\mu J/cm^2$) were obtained from the long-chain OA-capped QD film which is the benchmark for common literature studies. Thus, the average net gain value for both QD films with short ligands (DIAH and BA in this work) is about an order of magnitude higher than that measured under identical conditions for low-density QD films with the long-chain OA ligand, indicating that the loading density, controlled by ligand shells, is critical (**Figure B.8**).

Moreover, we compare current gain values in our study with those measured in literature under different fabrication and pumping conditions (**Figure 6.3f**). The comparison shows a factor of up to three-fold increase in comparison to values reported for a variety of drop-cast Cd-based QD films with different organic ligands (literature reported gains of typically 60-200 cm^{-1}).[36,37] We suggest that the unusually high gain values observed in the QD solid films fabricated here are primarily due to factors discussed below. First, considering the equation of modal gain, $g_{modal} = \Gamma \times g_{material}$,[38] where Γ is the modal confinement factor and $g_{material}$ is the material gain. The much higher QD loading of our films can effectively increase the material gain by two folds. Second, the modal confinement factor can also be an important factor to be considered. The notably thin films (typically 150nm-180nm) we fabricated here and the large difference in refractive index can cause an increasing modal confinement factor (**Figure B.7e**) by around two-fold when compared the DIAH-QD films with the OA-QD films. Third, the passivation of QD surface could also possibly affect the gain value due to the surface trapping. In colloidal quantum dots, two major routes of non-radiative pathway are the surface

trapping and the auger recombination.[1] In the past, the auger recombination was considered to be the dominant factor over surface trapping owing to the fast auger recombination lifetime of 1-100ps. However, due to the much suppressed auger recombination lifetime on the order of ns in our CdSe/$Cd_{1-x}Zn_xSe_{1-y}S_y$ core/alloyed shell quantum dots, we believe the surface trapping related to poor passivation of QD surface may become an important factor to affect gain values. Indeed, our PL stability tests discussed in next section showed that both amine ligand capped QD films (DIAH and BA) have better PL stabilities over the carboxylic acid ligand (OA) capped QD films, indicating amine group provide a more thorough and robust passivation of QD surface compared with the OA ligands. Further study on how different functional groups of ligands can affect the passivation and therefore the optical gain values should be investigated in the future. Also, the much larger net gain value observed here may also be due in part to the high uniformity of the crosslinked QD films, which reduces optical scattering and leads to optical losses being as low as 50 cm^{-1} for some films (usually within the range of 40 cm^{-1} to 200 cm^{-1} for all films tested) (**Figure B.9**).[39]

6.3.4 PL stability study of QD film with different ligands

To further clarify the role of QD crosslinking with short bifunctional ligands, we conducted ASE stability test under continuous optical pumping (**Figure 3d)**. Remarkably, the ASE intensity of DIAH-passivated QD films remains constant during continuous pumping (500 $\mu J/cm^2$) over a period of 45 minutes (>25000 pulses, 10 Hz), indicating an excellent reproducibility over numerous laser shots within ±10%. This high stability is in sharp contrast to cast CdSe films that exhibit a reduction in intensity of up to 50% of the original value within one hour, depending on the pumping intensity of the

CW laser excitation.[5] Unfortunately, ASE stability tests are rarely reported for high performing gain QD materials.[9]

In addition to the ASE stability test, we performed long-term shelf life-time PL stability by repeating PL measurements under identical conditions for samples stored under ambient conditions for an extended time (**Figure 3e**) (see also data for vacuum storage in **Figure B.10**). These tests show that the crosslinked DIAH-tethered QD films display a long-term temporal stability of the PL intensity (within ±5% from the initial values). On the other hand, the PL intensity of non-crosslinked BA-capped QD films and traditional OA-capped QD films (widely reported in the literature) decayed dramatically within the same time period (50%-70% reduction of the original intensity) (**Figure 6.3e**). We suggest that the stronger binding affinity and higher surface coverage of QDs with shorter aliphatic amines provided a more thorough and robust passivation of QD surface compared to the oleic acid ligands. The fast oxidation and diffusion of the conventional unbound ligands promote the generation of defect states on the QD surface that results in PL quenching.[22,40,41,42] Also, volatile aliphatic amines like BA that have a low m_p and b_p and a high vapor pressure can undergo desorption from the QD surface under ambient conditions, which further promotes a reduction of photoluminescence in un-crosslinked short-ligand QD films.

6.4 Conclusions

In summary, mechanically robust, optically stable, and highly loaded crosslinked core/alloyed-shell QD films with net gain values up to 650 cm^{-1} in the q-CW excitation region were successfully crafted by replacing commonly used long-chain organic ligands with short-chain bifunctional ligands with strong affinity to the QD surface. The net gain

values reported here are much higher than those measured for long-chain oleic acid QD films and those reported for drop-cast QD films capped with various conventional organic ligands. The unusually low (an order of magnitude) ASE threshold observed here under ns pulse excitation can be utilized to generate significant optical gains under lower optical powers initiated by near-continuous lasers. The crosslinking of uniformly distributed QDs imparts exceptional mechanical robustness, high chemical resistance, excellent thermal stability, and long-term optical stability, greatly outperforming conventional physically absorbed QD films passivated with traditional ligands.

6.5 Chapter acknowledgements

Dr. Jaehan Jung and Youngjun Yoon (Prof. Zhiqun Lin's research group, Georgia Institute of Technology): QD synthesis. Dr. Evan Lafalce and Yaxin Zhai (Prof. Valy Vardeny's research group, University of UTAH): optical gain and loss measurement and Femtosecond-transient absorption. Dr. Sidney Malak and Marcus Smith (Prof. Vladimir Tsukruk's research group, Georgia Institute of Technology): AFM.

6.6 References (Chapter 6)

1 V. I. Klimov, A. A. Mikhailovsky, S. Xu, A. Malko, J. A. Hollingsworth, C. A. Leatherdale, H. J. Eisler, M. G. Bawendi, *Science* **2000**, 290, 314.

2 V. I. Klimov, S. A. Ivanov, J. Nanda, M. Achermann, I. Bezel, J. A. McGuire, A. Piryatinski, *Nature* **2007**, 447, 441.

3 C. Dang, J. Lee, C. Breen, J. S. Steckel, S. Coe-Sullivan, A. Nurmikko, *Nat. Nanotech.* **2012**, 7, 335.

4 R. D. Schaller, M. A. Petruska, V. I. Klimov, *J. Phys. Chem. B* **2003**, 107, 13765.

5 J. Q. Grim, S. Christodoulou, F. Di Stasio, R. Krahne, R. Cingolani, L. Manna, I. Moreels, *Nat. Nanotech.* **2014**, 9, 891.

6 B. Guzelturk, Y. Kelestemur, M. Olutas, S. Delikanli, H. V. Demir, *ACS Nano* **2014**, 8, 6599.

7 C. She, I. Fedin, D. S. Dolzhnikov, P. D. Dahlberg, G. S. Engel, R. D. Schaller, D. V. Talapin, *ACS Nano* **2015**, 9, 9475.

8 C. She, I. Fedin, D. S. Dolzhnikov, A. Demortière, R. D. Schaller, M. Pelton, D. V. Talapin, *Nano Lett.* **2014**, 14, 2772.

9 S. Yakunin, L. Protesescu, F. Krieg, M. I. Bodnarchuk, G. Nedelcu, M. Humer, G. De Luca, M. Fiebig, W. Heiss, M. V. Kovalenko, *Nature Communications* **2015**, 6, 8056.

10 H. Hodaei, M.-A. Miri, M. Heinrich, D. N. Christodoulides, M. Khajavikhan, *Science* **2014**, 346, 975.

11 L. Feng, Z. J. Wong, R.-M. Ma, Y. Wang, X. Zhang, *Science* **2014**, 346, 972.

12 K. G. Makris, R. El-Ganainy, D. N. Christodoulides, Z. H. Musslimani, *Phys. Rev. Lett.* **2008**, 100, 103904.

13 Z. Lin, H. Ramezani, T. Eichelkraut, T. Kottos, H. Cao, D. N. Christodoulides, *Phys. Rev. Lett.* **2011**, 106, 213901.

14 L. Chang, X. Jiang, S. Hua, C. Yang, J. Wen, L. Jiang, G. Li, G. Wang, M. Xiao, *Nat. Photonics* **2014**, 8, 524.

15 B. Guzelturk, O. Erdem, M. Olutas, Y. Kelestemur, H. V. Demir, *ACS Nano* **2014**, 8, 12524.

16 Y.-S. Park, S. Guo, N. S. Makarov, V. I. Klimov, *ACS Nano* **2015**, 9, 10386.

17 G. Burak, K. Yusuf, G. Kivanc, Y. Aydan, A. M. Zafer, W. Yue, C. Rui, D. Cuong, S. Handong, D. H. Volkan, *Adv. Mater.* **2015**, 27, 2741.

18 M. S. T., J. Jaehan, Y. Y. Jun, S. M. J., L. C. Hao, L. Zhiqun, T. V. V., *Adv. Opt. Mater.* **2016**, 4, 608.

19 T. Francesco, F. Ilaria, G. Samuele, G. Eleonora, C. Elisabetta, B. Renato, J. J. J., D. G. Gioia, B. Giovanna, T. Stefano, S. Raffaella, *Adv. Funct. Mater.* **2012**, 22, 337.

20 A. V. Malko, A. A. Mikhailovsky, M. A. Petruska, J. A. Hollingsworth, H. Htoon, M. G. Bawendi, V. I. Klimov, *Appl. Phys. Lett.* **2002**, 81, 1303.

21 S. F. Wuister, C. de Mello Donegá, A. Meijerink, *J. Phys. Chem. B* **2004**, 108, 17393.

22 D. A. Hines, P. V. Kamat, *ACS Appl. Mater. Interfaces* **2014**, 6, 3041.

23 Sigma-Aldrich. Butylamine, 1,7 diaminoheptane, & oleic acid.

24 W. K. Bae, K. Char, H. Hur, S. Lee, *Chem. Mater.* **2008**, 20, 531.

25 V. Sukhovatkin, S. Musikhin, I. Gorelikov, S. Cauchi, L. Bakueva, E. Kumacheva, E. H. Sargent, *Opt. Lett.* **2005**, 30, 171.

26 F. Xu, L. Gerlein, X. Ma, C. Haughn, M. Doty, S. Cloutier, *Materials* **2015**, 8, 1858.

27 C. R. Kagan, C. B. Murray, M. G. Bawendi, *Physical Review B* **1996**, 54, 8633.

28 V. Wood, M. J. Panzer, J.-M. Caruge, J. E. Halpert, M. G. Bawendi, V. Bulović, *Nano Lett.* **2010**, 10, 24.

29 K. R. Beck, R. Korsmeyer, R. J. Kunz, *J. Chem. Educ.* **1984**, 61, 668

30 G. Socrates, John Wiley & Sons, Ltd.: Chichester, *Infrared and Raman Characteristic Group Frequencies: Tables and Charts*. **2001**; ISBN 0- 471-85298-8.

31 C. P. Marshall, E. J. Javaux, A. H. Knoll, M. R. Walter, *Precambrian Research* **2005**, 138, 208.

32 K. L. Shaklee, R. F. Leheny, *Appl. Phys. Lett.* **1971**, 18, 475.

33 O. Chen, J. Zhao, V. P. Chauhan, J. Cui, C. Wong, D. K. Harris, H. Wei, H.-S. Han, D. Fukumura, R. K. Jain, M. G. Bawendi, *Nat. Mater.* **2013**, 12, 445.

34 M. A. Green, *Sol. Energy Mater. Sol. Cells* **2008**, 92, 1305.

35 Z. E. Lampert, S. E. Lappi, J. M. Papanikolas, C. Lewis Reynolds, *Appl. Phys. Lett.* **2013**, 103, 033303.

36 B. Guzelturk, Y. Kelestemur, M. Z. Akgul, V. K. Sharma, H. V. Demir, *J. Phys. Chem. Lett* **2014**, 5, 2214.

37 Y. Wang, S. Yang, H. Yang, H. Sun, *Adv. Opt. Mater.* **2015**, 3, 652.

38 M. M. Adachi, F. Fan, D. P. Sellan, S. Hoogland, O. Voznyy, A. J. Houtepen, K. D. Parrish, P. Kanjanaboos, J. A. Malen, E. H. Sargent, *Nat. Comm.* **2015**, 6, 8694.

39 M. D. McGehee, R. Gupta, S. Veenstra, E. K. Miller, M. A. Díaz-García, A. J. Heeger, *Phys. Rev. B* **1998**, 58, 7035.

40 J. Y. Rempel, B. L. Trout, M. G. Bawendi, K. F. Jensen, *J. Phys. Chem. B* **2006**, 110, 18007.

41 E. Gómez Daniel , J. van Embden, J. Jasieniak, A. Smith Trevor , P. Mulvaney, *Small* **2006**, 2, 204.

42 T. V. Richter, F. Stelzl, J. Schulz-Gericke, B. Kerscher, U. Wurfel, M. Niggemann, S. Ludwigs, *J. Mater. Chem.* **2010**, 20, 874.

CHAPTER 7

LARGE-SCALE ROBUST QUANTUM DOT MICRODISK LASERS WITH CONTROLLED CAVITY MODES

7.1 Introduction

Compact semiconductor photonic cavities are often fabricated using either top-down[1] or bottom-up [2] approaches. The top-down approach typically involves a lithographic process (e.g., photo or electron beam lithography[24]) to predefine the surface of deposited active semiconductor layers. A patterned photoresist provides protection from an etching process (using appropriate selection of conditions), which subsequently removes the material that is not protected. Depending on the resolution of the photoresist, micro and even nanoscale cavities with well-defined geometry can be reliably fabricated. The ability to control the spatial dimensions of the photonic structures is essential for realizing practical and robust on-chip photonic circuits, and is a primary reason these top-down approaches are utilized. However, these top-down lithography approaches often require complicated microfabrication processes under clean-room conditions and expensive facilities in order to properly etch or deposit the materials.[3]

On the other hand, the bottom-up approach offers facile and low-cost assembly of high quality colloidal photonic cavities directly on the desired substrate via the self-assembly and crystallization process. Colloidal cavities assembled using the bottom-up approach have been shown to possess good lasing performance (quality factors ($\lambda/\delta\lambda$) on the order of 10^3) and low lasing thresholds (down to a few hundred nJ/cm^2).[4] The impressive

lasing characteristics have made them promising candidates for flexible compact semiconductor lasers with low lasing thresholds (~μJ/cm^2)[30] However, at the present time, precise control of the size, shape, and location of these bottom-up colloidal cavities is challenging since the local crystallization and assembly processes depend critically on local temperature gradients, concentration of precursors, and pressure.[5] These obstacles severely hinder the integration of these cavities into practical flexible on-chip photonic circuits that may require optical cavities with specific dimensions and location.

Here we present an efficient hybrid top-down/bottom-up approach via a pattern-assisted layer-by-layer (LbL) assembly process to fabricate large-area on-chip quantum dot microdisk laser arrays.[6,7,8] Utilization of QD nanoparticles along with the pattern-assisted LbL assembly enables the facile and vacuum-free fabrication of robust photonic cavities with predefined size, geometry, and location over a large scale in a simple manner, which is not an easy task for conventional top-down approaches or current bottom-up approaches. Importantly, this patterning approach represents a significant improvement in throughput and can be up-scalable, with fast fabrication of thousands structures per hour which is much higher than previous studies using focused ion beam milling (FIB) and electron beam lithography (EBL) due to the parallel nature of the process. Furthermore, fabricated structures exhibit exceptional uniformity (size variation below 5%) over cm^2 areas, demonstrating the ability to precisely control the dimensions of fabricated structures. In addition, the high chemical resistance and mechanical strength of the microstructures, imparted via chemical crosslinking of functionalized quantum dots, allows them to withstand severe conditions such as sonication and direct exposure to harsh solvents. Furthermore, intense lasing behavior with high quality factors of 1000-2000 were observed, with the number of cavity modes and their mode spacing readily controlled by varying the disk radius. The ability to control the dimension and spatial

distribution of robust and large area cavity arrays, while maintaining high quality factors, may provide a platform for the development of novel PT photonic systems that may exhibit exceptional points for single-mode lasing and directional light propagation.[9,10]

7.2 Experimental details

***Optical characterization**:* UV-vis extinction spectra of QD solutions (quartz cuvette) from 350-900 nm (1 nm intervals) were collected using a Shimadzu UV-vis-2450 spectrometer with D2 and tungsten lamps offering a wavelength range of 300-1100 nm. The QD extinction spectra were corrected against the pure solvent background and the same quartz cuvette. Photoluminescence spectra of QD solutions were collected using a Shimadzu RF-5301PC spectrofluorophotometer with the excitation wavelength of 525 nm.

Photoluminescence (PL) images were collected using a Dagexcel-M Digital Firewire camera. All PL imaging was performed using photoluminescence excitation from a blue bandpass filter (450-490 nm) with a dichroic mirror that reflects optical wavelengths below 495 nm, and with a longpass emission filter that passes optical wavelengths above 500 nm. The light source is a quartz halogen lamp with an aluminum reflector providing a wavelength range of 420−850 nm and a power of 150 W of nonpolarized light.

***Fabrication of QD microdisks**:* The patterning process used for fabricating QD microdisks includes several stages. First, a low refractive index layer of CYTOP (n = 1.34) was deposited on the Si wafer (n = 3.44) in order to provide light confinement within the QD cavities. A short oxygen plasma etch (5 seconds) was performed to

improve the wettability of the CYTOP surface for the deposition of the negative photoresist (NR 71-3000p). Ethyl lactate was added to the negative resist NR71-3000p solution to dilute it to one third of the original concentration provided by the company. The diluted resist was spun cast on the silicon substrate (3000 rpm for 1 minute). The cast film was subsequently soft baked at 165℃ for 5 minutes and exposed to 365 nm with a dosage of 123mW. The exposed film was then post-baked at 100℃ for 5 minutes and developed by soaking in RD6 developer for 5 sec. After the development, the film was rinsed with water and dried by blowing with air. The QD microdisks were fabricated by spin casting butylamine-capped QD solution (in heptane) of ~3-6 mg/mL at 1000 rpm for 1 minute onto the polymer pattern. The cast layer was subsequently immersed in 0.1M diaminoheptane solution in methanol for 1 minute and rinsed with methanol 2 times while spinning at 3000 rpm for 1 minute. The above process was repeated multiple times to achieve the desired thickness. The polymer pattern was subsequently removed by soaking in acetone while sonicating for 3-10 seconds.

Confocal micro PL configuration (**Figure C.8**): A Passat LTD. Compiler diode-pumped solid-state laser delivering 7ps pulses at 532nm with 100Hz repetition rate was used to pump the samples. A pair of polarizers was used to control the pump fluence, I_p, while an iris was used to control the beam spot size. The pump is directed through a 40x (NA = 0.65) microscope objective using a dichroic mirror and focused on the sample. The emission is collected through the same objective, transmitted through the dichroic mirror and focused onto a 0.5mm diameter optical fiber coupled to a 1/2m spectrometer and CCD array (resolution = 0.29nm) or collimated and projected onto a

camera lens for fluorescence imaging. An additional long pass filter is used to further attenuate the reflected pump beam.

7.3 Results and discussion

7.3.1 Fabrication of disk arrays

We adopted a facile one-pot method (with some modification) to synthesize red-emitting core/graded shell CdSe/$Cd_{1-x}Zn_xSe_{1-y}S_y$ QDs with an average diameter of 7.7±0.7 nm. (**Figure C.1**).[11] The graded shell of QDs has been shown to effectively suppress Auger recombination, which is a primary obstacle for achieving optical gain from QDs.[12,13] Moreover, to fabricate mechanically robust QD microstructures, we used a solid state exchange process that tethers neighboring QDs via bifunctional crosslinkers to create highly crosslinked network impart mechanical strength and chemical resistance.[14]

The pattern-assisted LbL assembly used here to fabricate the QD photonic cavities includes several steps. First, circular microholes with a depth of 300 nm were fabricated in a photoresist using a standard photolithography process (**Figure 7.1 a, steps 1-4**).[15] Then, these microholes were subsequently filled with functionalized QDs using a spin-assisted LbL assembly by repeating deposition steps in a controlled sequential manner.[7,16] This deposition process was repeated until the structure achieved the desired thickness within the range of 100-200 nm, as monitored after the completion of fabrication process. The disk thickness grows linearly with the number of deposition cycles, as expected for LbL assembly with an increment of 25-30 nm per layer (**Figure C.2**).[17]

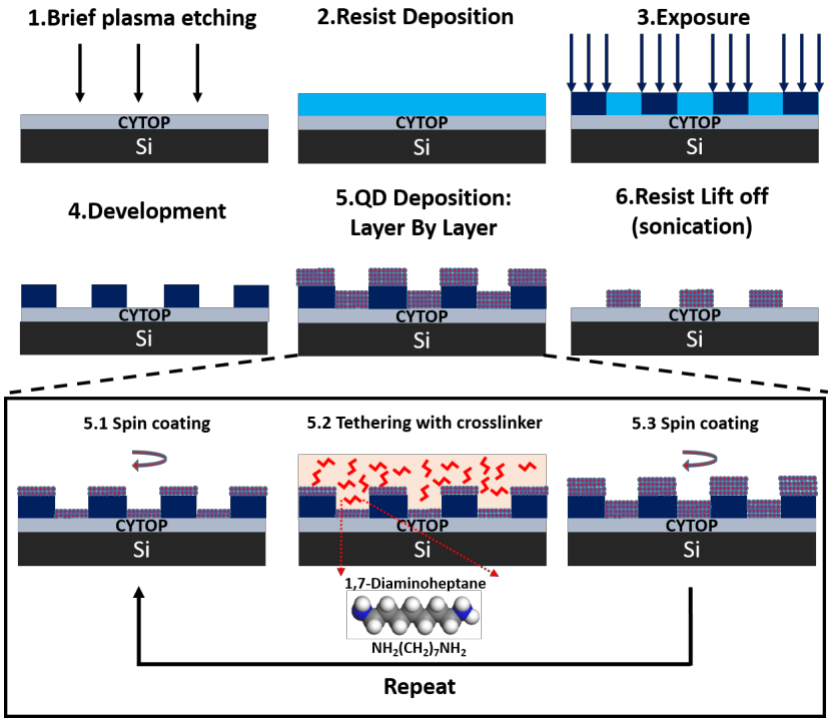

Figure 7.1 Schematic outlining the hybrid top-down/bottom-up approach using a pattern-assisted LbL assembly of QDs that used to fabricate the QD microdisks.

Assembled layers of close-packed QDs within fabricated thin disks were tethered to each other via the solid state ligand exchange process suggested in our previous study (**Figure 7.1a, step 5**).[14] During this process, the capping ligand butylamine was replaced with the bifunctional crosslinker 1,7 diaminoheptane (DIAH) and the neighboring QDs were crosslinked via the strong coordination between QDs and amino end groups of DIAH.[14] Importantly, the DIAH crosslinking process imparts robustness to the QD microdisks, which prevents cracking under sonication during the removal of the photoresist (lift-off process) (**Figure 7.1a, step 6**) and facilitates the mechanical integrity of the structures (**Figure C.3**). It is also worth mentioning that the underlying CYTOP layer acts as potentially important prime layer for fabrication on a variety of substrates due to its low refractive index, mechanical robustness, and chemical resistance to different solvents (polar and non-polar).

With this method, large area organized arrays composed of a few thousand QD microstructures with predefined shape, size, and location can be fabricated in less than an hour (**Figure 7.2, C.4**). Furthermore, because the microdisks are composed of a crosslinked QD network, they are chemically resistant to polar and non-polar solvents.[14] This is a particularly desirable property if the microdisks are exposed to chemically harsh environments during the lift-off process or should operate under variable environment conditions. It is worth noting that the chemical stability of microdisks is in stark contrast to the conventionally fabricated colloidal cavities that are easily dissolvable in polar solvents (e.g., perovskite cavities).[18,19]

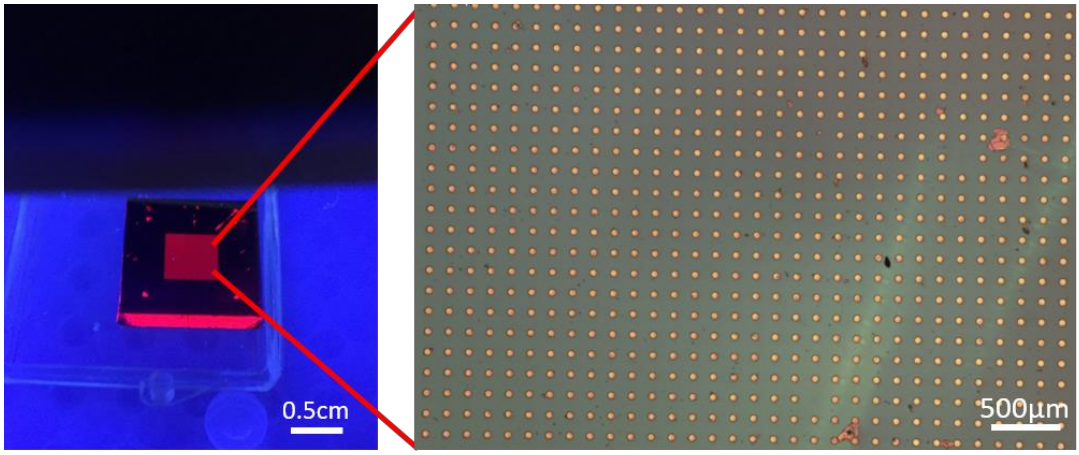

Figure 7.2 Left: Optical micrograph of a substrate under UV illumination with an array of microdisks (diameter of 52.1 µm). Right: bright field image of a microdisk array at higher magnification.

7.3.2 Characterization of disk morphology

Figure 7.3a, b shows a series of fabricated QD microdisks with diameters ranging from 10 to 52 µm. In general, the size and location of the microdisk arrays closely match the original mask patterns (within 5%) (**Figure 7.2, 3c, C.4**). The shape of all fabricated microdisks, which is predefined by the patterned microholes in the photoresist, is almost perfectly circular with minimal density of defects and smooth side walls (**Figure 7.2d**).

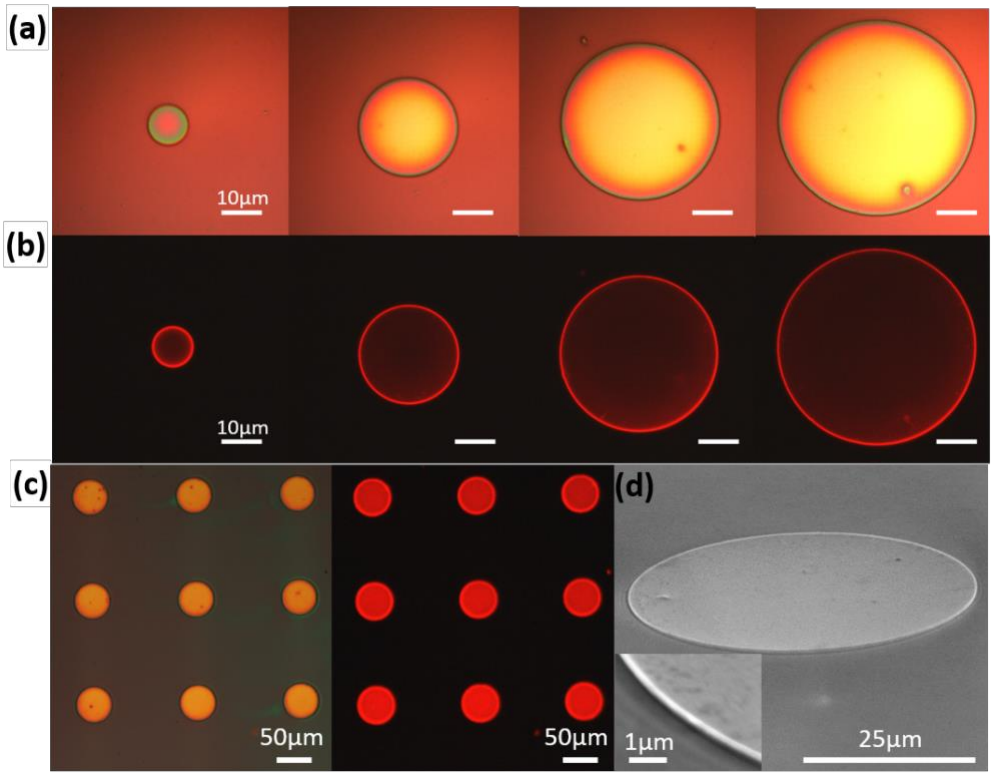

Figure 7.3 Bright field (a) and PL (b) imaging of QD microdisks with diameters of 10.6, 26.0, 41.6 and 52.1 μm. (c) Bright field image (left panel) and PL image (right panel) of a 3x3 disk array (52.1 μm in diameter). (d) SEM of a microdisk (inset: side wall).

The morphology of the fabricated microdisks was further investigated using atomic force microscopy (AFM). It was found that the microdisks actually possess a peculiar nest-like shape with elevated rims, a common feature of a flow- and evaporation-driven assembly of colloidal and polymeric materials, generally known as coffee-ring effect, with fluidic flow under confined spaces (**Figure 7.4**).[20,21,22] This inhomogeneous distribution did not noticeably affect the global disk-like shape since the boundaries of the microholes were well-defined by the photolithography process and the rims compose only a small fraction of the microdisk volume. Generally, the rim height (270-280 nm) is close to the depth of microfabricated holes in the photoresist (~300 nm), while the thickness of the uniform central region of the disk is about half of this value: around 100 nm for larger disks (>26 μm) and around 150 nm for the smallest disk (10.6 μm).

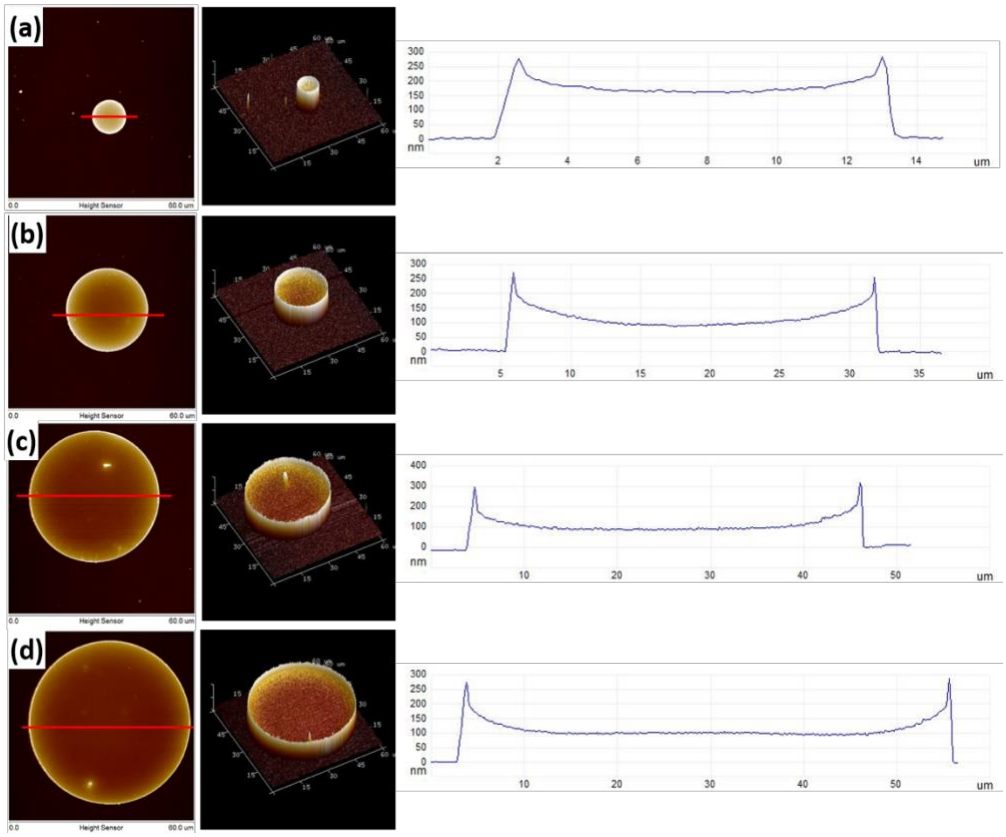

Figure 7.4 From left to right: AFM topographical images (top-view), 3D projection, and height cross-section profiles of QD microdisks with diameters of (a) 10.6 μm, (b) 26.0 μm, (c) 41.6 μm, and (d) 52.1 μm, respectively.

7.3.3 Optical properties and lasing behavior

Optical characterization was performed by pumping the microdisks with a 532 nm, 7 ps pulsed laser in a confocal micro PL set-up. We observed that an increase of pump fluence causes an increase of the optical gain from the QD microdisks, which eventually surpasses the optical loss and leads to consequently the onset of light amplification (amplified spontaneous emission (ASE) threshold) and intense lasing behaviour when inside an optical cavity such as the microdisks. This non-linear behavior leads to the appearance of sharp spectral peaks (due to optical cavity modes) over the broad

spontaneous emission band once threshold is exceeded, confirming the occurrence of lasing action in the fabricated microdisks (**Figure 7.5**).

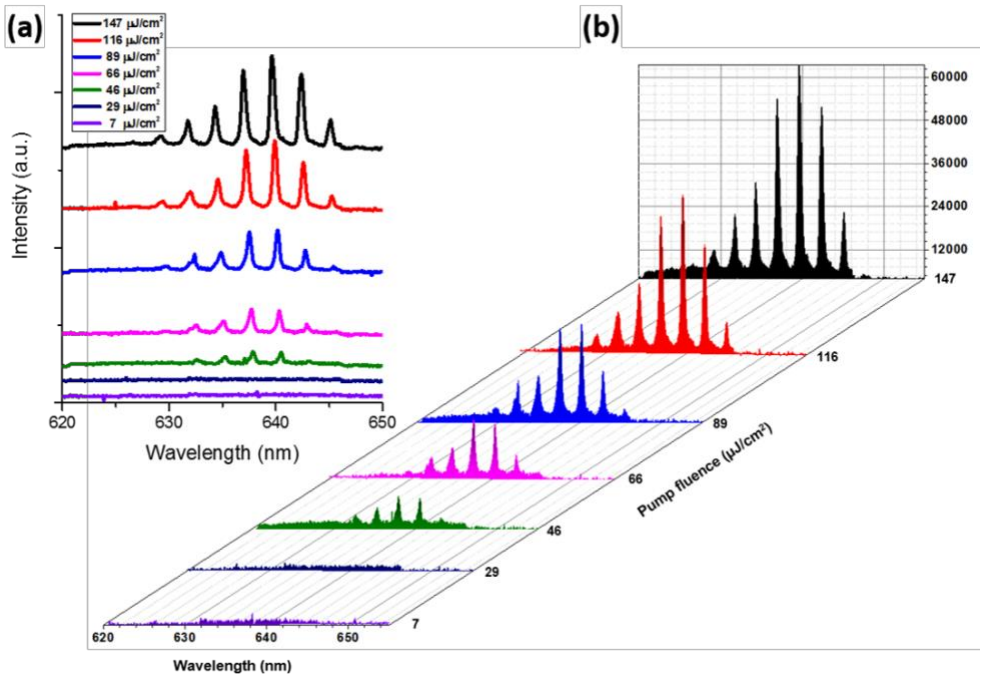

Figure 7.5 (a) 2D (b) 3D representations of lasing spectra of QD microdisk (diameter of 26.0 μm) under varying pump fluence (F_{th} is ~29 μJ/cm^2). Baselines of the 2D lasing spectra are offset for clarity.

This non-linear optical behavior can also be observed in the power-power plot where the microdisk studied (example is shown for 26.0 μm disk) shows an abrupt change from a linear pump dependence to a super-linear pump dependence (on the log-log scale) at the ASE threshold (**Figure 7.6a**).

In general, the ASE thresholds for microdisks of different diameter are found to be on the same order of magnitude (29-90 μJ/cm^2), which are comparable to the best values reported in literatures.[23,30] It is also worth noting that in ~87% of the microdisks the appearance of cavity mode splitting was observed at threshold (**Figure C.5**). Scattering

centers that are responsible for the mode splitting can be clearly seen as bright spots in **Figure 7.6b**.

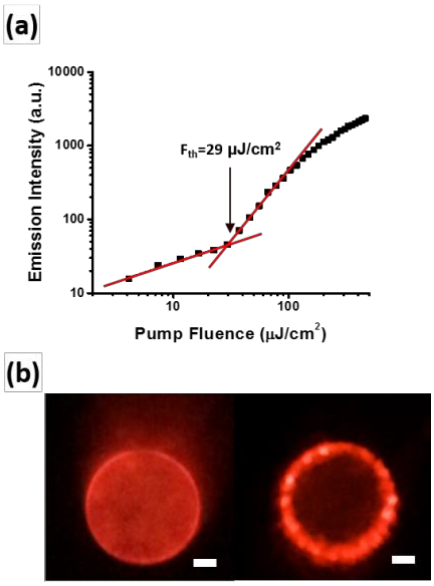

Figure 7.6 (a) PL emission vs excitation fluence of a QD microdisk. The threshold pump fluence, F_{th} is determined from the interception of the linear and superlinear behaviors. (b) PL emission images of the QD microdisk (diameter of 26.0 μm) below (left) and above (right) lasing threshold. The scale bar is 5 μm for both images.

For one of the smaller microdisk, 10.6 μm, we observed mode-splitting at intensities significantly higher than the threshold value. We suggest that the smaller circumference limits the amplification of laser modes and causes the inability of the resonators to sustain high light intensities for lasing. The mode splitting could possibly be related to local heating and annealing near the circumference (namely the rim area) when the pump fluence is highest. The specific mechanisms underlying this behavior are part of an ongoing study.

The cavity mode spacings (Δλ) of QD microdisks with different sizes decrease as the disk diameter increases while at the same time the number of resonant longitudinal cavity modes gradually increases in agreement with theory (see below) (**Figure 7.7**).[24]

Moreover, near-single mode and multimode behavior can be readily controlled by varying the diameter of the fabricated QD microdisk in the relation with the gain spectrum of QDs and Δλ **(Figure 7.7).** Importantly, the much narrower gain spectrum (~30 nm) for QDs compared with those of organic dye molecules (~30-100 nm)[25] can be advantageous to achieve the near-single mode operation over a wider range of disk sizes, providing more flexibility on the structure design. In addition, the readily accessible near-single mode and multimode operation of this system could be extremely useful when trying to accommodate specific needs in a wide range of applications, including optical communication (single mode) and nanoparticle detection (multimode).[26,27]

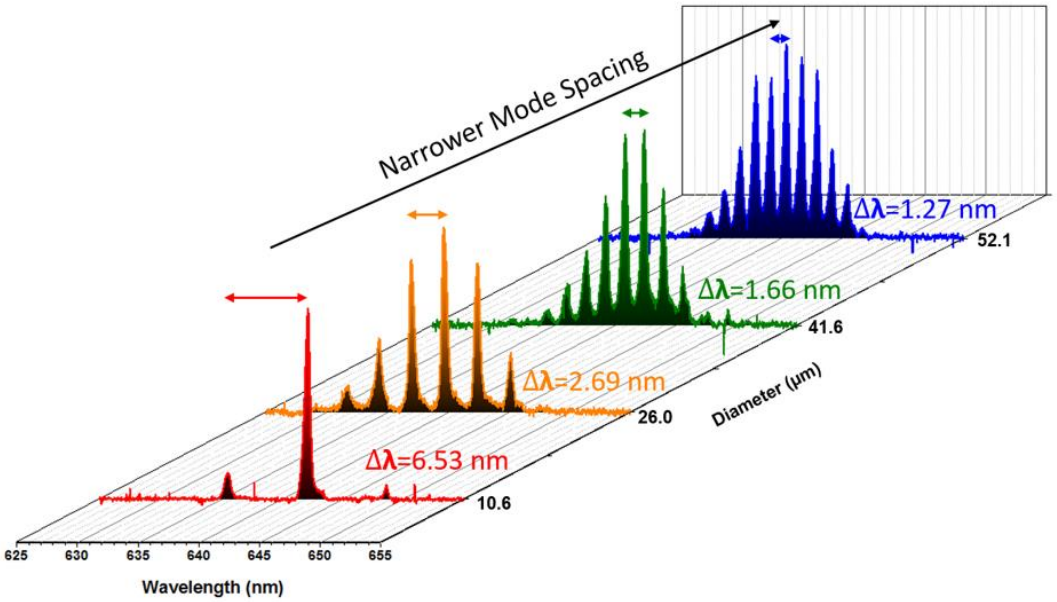

Figure 7.7 Lasing spectra of QD microdisks with diameter of 10.6 μm (red), 26.0 μm (orange), 41.6 μm (green) and 52.1 μm (blue). Δλ is the average mode spacing between the observed longitudinal cavity modes.

The relationship between mode spacing (Δλ) and cavity length (L) can also provide detailed information on the cavity type and the effective refractive index of the microdisks.[24] The behavior of cavity modes can be estimated using the well-known equation, $\Delta\lambda = \lambda^2/2nL$, where λ is the peak wavelength of the cavity mode, n is the

effective refractive index of QDs and 2L is the optical path (round-trip) length.[28] The optical path length 2L in a microdisk cavity is represented by the circumference length, πD, which gives a modified equation of $\Delta\lambda = \lambda^2/n\pi D$.[28] Our study, indeed, confirms a linear relationship between mode spacing (Δλ) and the reciprocal optical path length 1/πD (**Figure 7.8a**). From this relationship, the effective refractive index of microdisks, n, at λ = 642 nm (dominant mode of ~50% microdisks), can be estimated from the slope. The value obtained from this analysis, 1.88 ± 0.02, is in good agreement with the experimental value n = 1.90 measured from the uniform QD film by spectroscopic ellipsometry.[14] This refractive index value indicates that the propagating light is confined inside the cavity and that total internal reflection occurs in the region near the circumference of the QD microdisks; substantiating the claim that the fabricated microdisks are, indeed, *whispering gallery mode resonators.*

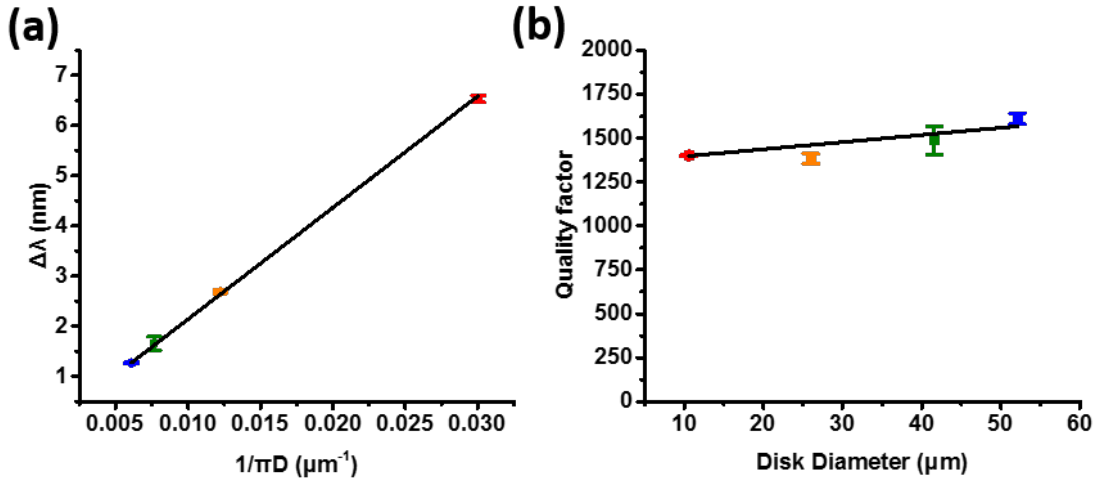

Figure 7.8 (a) Mode spacing of cavity modes as a function of reciprocal optical path length. (b) Microdisk quality factor as a function of disk diameter.

A more accurate effective refractive index of the microdisks (of different diameter) can be estimated using the Fourier transform of the emission spectrum, which contains equally spaced Fourier components with periodicity Δl = nπD (**Figure 7.9**).[29] The path

length (ΔI) of microdisks from small to large diameters are determined to be 60.8 ± 1.3, 147.4 ± 1.3, 262.0 ± 0.1, 325.6 ± 0.1 μm, respectively. These values correspond to n of 1.82 ± 0.04 (10.6 μm), 1.81 ± 0.02 (26.0 μm), 2.00 ± 0.00 (41.6 μm) and 1.99 ± 0.00 (52.1 μm), showing that the larger disks (41.6 μm, 52.1 μm) have higher effective refractive index (~2) than that of the smaller disks (10.6 μm, 26.0 μm around 1.81 and 1.82, respectively). The difference in n indicates better light confinements within the microdisks of larger diameters, which is likely due to less total internal reflection and a relatively steeper incident angle experienced by the resonant wavelength within the smaller microdisks.[24]

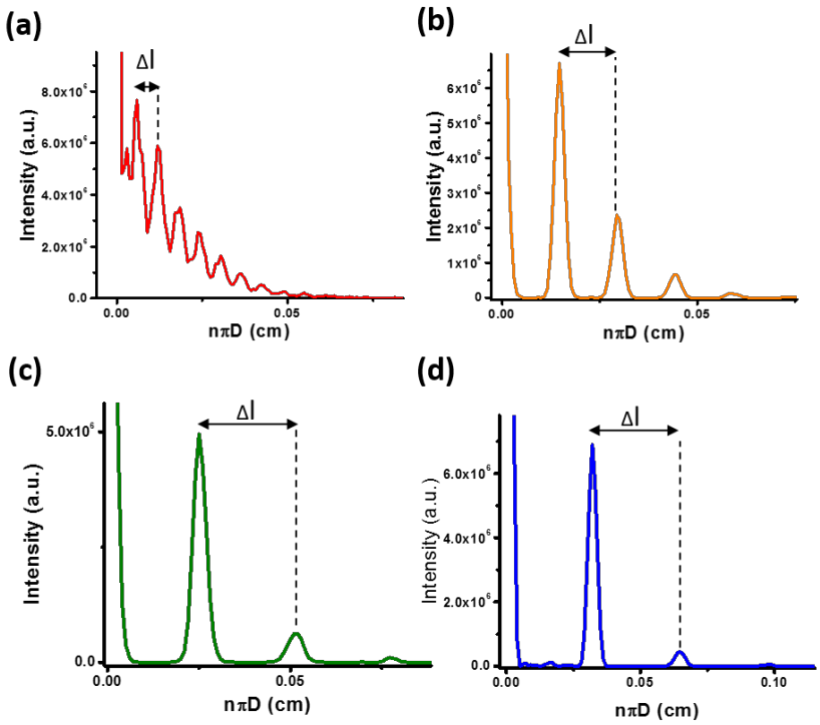

Figure 7.9 Power Fourier transform of lasing spectra from micodisks with diameters of (a) 10.6 μm, (b) 26.0 μm, (c) 41.6 μm, (d) 52.1 μm (*ΔI = nπD).*

Next, the quality factor, which can be deduced from lasing spectra of microdisks, is an important figure of merit that indicates how well energy can be stored.[24] The quality factor is estimated as the ratio λ/δλ, where λ is the peak wavelength of the cavity mode

and δλ is its line width.[24] We observed that the quality factors of the dominant modes are within 1400-1650 for all microdisks with different diameters (**Figure 7.8b**). These values are comparable to those reported for other types of lasing structures using colloidal and solution-processable optically active materials (perovskite, conjugated polymer, and SiN microdisks with QDs).[29, 30, 31] In addition, mode splitting due to scattering centers did not reduce the quality factor of microdisks significantly. Only very modest (5-10%) decrease in quality factor was observed in microdisks with smaller sizes (**Figure C.6**). These results demonstrate the effectiveness of the outlined fabrication approach to provide superior patterning capability while maintaining the high quality factor of robust structures of different sizes. It is worth noting that conventional top-down approaches can yield epitaxially-grown QD doped microdisks that exhibit quality factors exceeding 20000, however, as mentioned these techniques generally require complex protocol and are not scalable.[32] Further improvement on the quality factor of our structures will be important for applications that require very narrow linewidth, such as for ultrasensitive sensors.

Furthermore, we observed a size-dependence of the quality factor, with larger disks displaying higher values. This size dependence can be due to the higher reflectivity in larger disks that leads to better light confinement (energy storage), which is consistently in agreement with the observed trend of higher n in larger disks analyzed by using Fourier transform of emission spectra.[33] Specifically, the quality factor increased by ~20% when the disk size changed from 10.6 μm to 52.1 μm. Since the lasing threshold is typically inversely proportional to the quality factor, this increase yields only a small decrease of lasing threshold and could therefore explain why the lasing thresholds of microdisks of different sizes remained on the same order of magnitude (30-90 μJ/cm^2) (estimated lasing threshold for microdisks ranging from 52.1-10.6 μm).[34] Besides the

disk size, disk thickness can also be another factor that may affect the lasing behavior. In general, mode confinement is stronger as the thickness increases, leading to higher quality factor and lower lasing threshold. On the other hand, the peak position and number of cavity modes, determined by length of disk circumference, do not change with the disk thickness. In our specific case, rim thickness is almost constant and depends on the photoresist thickness while the center thickness grows linearly with the number of depositions. Since the mode volume is heavily concentrated along the circumference, the center thickness should not affect the optical mode confinement significantly.

The size-dependent quality factor and n of our microdisks indeed indicates the curvature of the disk boundary plays an important role in quality factor instead of the center thickness that changes from 150 nm (10.6 μm) to 100nm (25, 40, 50μm). Further optimization of the rim thickness by FDTD can be adopted in the future to improve the lasing performance. In addition, all disks have a higher quality factor at longer wavelengths (**Figures C.7**). This behavior is caused by the optical loss arising from the reabsorption of QD emission (overlap of absorption and emission bands), which is more pronounced on the lower wavelength side of the emission band **(Figure C.1a)**. Overall, the quality factor of all QD microdisks fabricated here remains high, within 1000-2000, for all disks with diameters ranging from 10 to 52 μm. In addition to displaying high quality factors and low lasing thresholds, the amplified spontaneous emission intensity of our crosslinked quantum dot films is quite stable under optical pumping, as demonstrated in our recent study.[14] The combination of stable lasing output with the outlined lasing characteristics of our large-area microdisk arrays suggests that they can indeed support the development of advanced and practical photonic circuits.

7.4 Conclusions

We have demonstrated a viable pattern-assisted assembly process that judiciously combines the facile fabrication and precision of optical lithography for the fabrication of large-area arrays of on-chip QD microdisks with intriguing non-linear optical characteristics. Reliable tuning of the number of cavity modes and their mode spacing was successfully achieved by adjusting the diameter of the fabricated microdisks fabricated as large-area arrays.

7.5 Chapter acknowledgements

Dr. Jaehan Jung and Youngjun Yoon (Prof. Zhiqun Lin's research group, Georgia Institute of Technology): QD synthesis, TEM and ligand exchange. Dr. Evan Lafalce and Qingji Zeng (Prof. Valy Vardeny's research group, University of UTAH): Confocal micro PL measurement. Dr. Sidney Malak and Marcus Smith (Prof. Vladimir Tsukruk's research group, Georgia Institute of Technology): SEM and AFM.

7.6 References (Chapter 7)

1 R. A. Minamisawa, M. J. Süess, R. Spolenak, J. Faist, C. David, J. Gobrecht, K. K. Bourdelle, H. Sigg, *Nat. Commun.* **2012**, 3, 1096.

2 A. C. Scofield, S.-H. Kim, J. N. Shapiro, A. Lin, B. Liang, A. Scherer, D. L. Huffaker, *Nano Lett.* **2011**, 11, 5387.

3 K. H. Li, H. W. Choi, *J. Appl. Phys.* **2011**, 109, 023107.

4 H. Zhu, Y. Fu, F. Meng, X. Wu, Z. Gong, Q. Ding, M. V. Gustafsson, M. T. Trinh, S. Jin, X. Y. Zhu, *Nat. Mater.* **2015**, 14, 636.

5 S. W. Eaton, M. Lai, N. A. Gibson, A. B. Wong, L. Dou, J. Ma, L.-W. Wang, S. R. Leone, P. Yang, *Proc. Natl. Acad. Sci. USA* **2016**, 113, 1993.

6 J. M. Luther, M. Law, Q. Song, C. L. Perkins, M. C. Beard, A. J. Nozik, *ACS Nano* **2008**, 2, 271.

7 C. Jiang, V. V. Tsukruk, *Adv. Mater.* **2006**, 18, 829.

8 G. I. Koleilat, L. Levina, H. Shukla, S. H. Myrskog, S. Hinds, A. G. Pattantyus-Abraham, E. H. Sargent, *ACS Nano* **2008**, 2, 833.

9 L. Feng, Z. J. Wong, R.-M. Ma, Y. Wang, X. Zhang, *Science* **2014**, 346, 972.

10 B. Peng, S. K. Ozdemir, F. Lei, F. Monifi, M. Gianfreda, G. L. Long, S. Fan, F. Nori, C. M. Bender, L. Yang, *Nat. Phys.* **2014**, 10, 394.

11 W. K. Bae, K. Char, H. Hur, S. Lee, *Chem. Mater.* **2008**, 20, 531.

12 Y. Wang, S. Yang, H. Yang, H. Sun, *Adv. Opt. Mater.* **2015**, 3, 652.

13 J. Jung, C. H. Lin, Y. J. Yoon, S. T. Malak, Y. Zhai, E. L. Thomas, V. Vardeny, V. V. Tsukruk, Z. Lin, *Angew. Chem.* **2016**, 128, 5155.

14 C. H. Lin, E. Lafalce, J. Jung, M. J. Smith, S. T. Malak, S. Aryal, Y. J. Yoon, Y. Zhai, Z. Lin, Z. V. Vardeny, V. V. Tsukruk, *ACS Photonics* **2016**, 3, 647.

15 C. A. Mack. *Fundamental principles of optical lithography : the science of microfabrication*; John Wiley & Sons Ltd.: Chichester, West Sussex, England, **2012**.

16 G. Decher, J. B. Schlenoff, *Multilayer thin films: sequential assembly of nanocomposite materials*, Wiley-VCH, Weinheim, **2012**.

17 X. Lan, O. Voznyy, A. Kiani, F. P. García de Arquer, A. S. Abbas, G.-H. Kim, M. Liu, Z. Yang, G. Walters, J. Xu, M. Yuan, Z. Ning, F. Fan, P. Kanjanaboos, I. Kramer, D. Zhitomirsky, P. Lee, A. Perelgut, S. Hoogland, E. H. Sargent, *Adv. Mater.* **2016**, 28, 299.

18 Y. Kim, E. Yassitepe, O. Voznyy, R. Comin, G. Walters, X. Gong, P. Kanjanaboos, A. F. Nogueira, E. H. Sargent, *ACS Appl. Mater. Interfaces* **2015**, 7, 25007.

19 Y. Zhao, K. Zhu, *J. Phys. Chem. Lett.* **2013**, 4, 2880.

20 R. Suntivich, I. Drachuk, R. Calabrese, D. L. Kaplan, V. V. Tsukruk, *Biomacromolecules* **2014**, 15, 1428.

21 P. J. Yunker, T. Still, M. A. Lohr, A. G. Yodh, *Nature* **2011**, 476, 308.

22 Y. Wang, K. E. Fong, S. Yang, Van D. Ta, Y. Gao, Z. Wang, V. Nalla, H. V. Demir, H. Sun, *Laser Photon. Rev.* **2015**, 9, 507.

23 C. Dang, J. Lee, C. Breen, J. S. Steckel, S. Coe-Sullivan, A. Nurmikko, *Nat. Nanotech.* **2012**, 7, 335.

24 S. Yang, Y. Wang, H. Sun, *Adv. Opt. Mater.* **2015**, 3, 1136.

25 Z. Li, Z. Zhang, T. Emery, A. Scherer, D. Psaltis, *Opt. Express* **2006**, 14, 696.

26 G. Agrawal, N. Dutta, *Semiconductor Lasers*, Springer, USA **1993**, pp. 74.

27 L. He, S. K. Ozdemir, J. Zhu, W. Kim, L. Yang, *Nat. Nanotechnol.* **2011**, 6, 428.

28 R. C. Polson, G. Levina, Z. V. Vardeny, *Appl. Phys. Lett.* **2000**, 76, 3858.

29 R. C. Polson, Z. V. Vardeny, D. A. Chinn, *Appl. Phys. Lett.* **2002**, 81, 1561.

30 W. Xie, T. Stöferle, G. Rainò, T. Aubert, S. Bisschop, Y. Zhu, F. Mahrt Rainer, P. Geiregat, E. Brainis, Z. Hens, D. Van Thourhout, *Adv. Mater.* **2017**, 29, 1604866.

31 H. Zhang, Q. Liao, X. Wang, J. Yao, H. Fu, *Adv. Opt. Mater.* **2016**, 4, 1718.

32 Q. Song, W. Fang, B. Liu, S.-T. Ho, G. S. Solomon, H. Cao, *Phys. Rev. A* **2009**, 80, 041807.

33 Y. Zhang, M. Lončar, *Opt. Express* **2008**, 16, 17400.

34 D. J. Gargas, M. C. Moore, A. Ni, S.-W. Chang, Z. Zhang, S.-L. Chuang, P. Yang, *ACS Nano* **2010**, 4, 3270.

CHAPTER 8

LARGE-AREA LASING AND MULTICOLOR PEROVSKITE QUANTUM DOT ARRAYS

8.1 Introduction

Recently, a new class of semiconductor nanocrystals, namely, all-inorganic perovskite $CsPbX_3$ (X=Br, Cl, I) quantum dots (QDs), has attracted great attention due to their intriguing optical, chemical, and lasing properties.[1,2,3,4] Unlike more conventional Cd based QDs, $CsPbX_3$ QDs do not require shell passivation to achieve high quantum yield due to the self-passivation effect of halogen,[5,6] enabling a facile synthesis of highly fluorescent emitters without the need of careful design of core/shell interface.[7,8] In addition, the absorption and emission spectra of QDs can be altered not only by size but also by the facile composition tuning via anion (i.e., X) exchange, thereby providing more freedom to achieve superior optical properties.[9] Moreover, high net optical gain value of 450 cm^{-1} and low pump threshold down to 5 $\mu J/cm^2$ have been reported, demonstrating that these QD can be readily used for light amplification and lasing at very low excitation intensity.[10] These properties have been extensively studied for use in spectrochemical probes, light-emitting diodes, and vertical cavity surface emitting lasers. Clearly, these show that $CsPbX_3$ QDs have potential for a variety of optoelectronic applications.[11,12,13]

In recent years, patterning techniques for single crystal and polycrystalline perovskite materials have been extensively developed including electron beam lithography, controlled crystallization via molding, inkjet printing and template assisted patterning with intriguing photonic properties.[14,15,16,17,18,19] In contrast, nearly all studies of perovskite

nanoparticles such as QDs to date have focused on the synthesis, photophysics and optoelectronic applications while the development of patterning techniques has been comparatively few and limited in scope.[20,21] This approach contrasts sharply to the Cd-based QDs where high-resolution lithographic methods such as electron-beam lithography and photolithography have been adopted widely to integrate Cd-based QDs into micro- and nanoscale devices.[22,23] The difference is essentially understandable, when considering the ionic nature of $CsPbX_3$ QDs, which makes them prone to dissolution in common polar solvents that are required in these high-resolution lithographic methods.[24,25] The chemical instability to polar solvents severely hinders the integration of these QDs into patterned photonic structures. Moreover, unlike counterpart of the bulk perovskite materials that can be patterned by dissolving polymer spheres or templates with non-polar solvent such as toluene[19], the ligand-capped perovskite QDs are unfortunately well dispersed in non-polar solvents. The solvent constraint in both polar and non-polar solvents indeed places the development of $CsPbX_3$ QD patterning for miniaturized optical arrays in a dilemma. Clearly, a novel lithographic method should be proposed to effectively overcome the low material processability of $CsPbX_3$ QDs that originates from the solvent constraint, while preserving the ability to achieve large-area high-resolution patterns.

Herein, we report a novel photolithographical approach that overcomes the processing limitations of perovskite QDs by incorporating a fluorinated polymer resist, which provides orthogonality to these QDs during the lift-off process with the fluorinated solvent processing without affecting QD emission performance. The orthogonality and spatial precision of photolithography enable the facile fabrication of large-area arrays of sophisticated patterns with submicron-sized features. We further demonstrated how this patterning technique can be used in different fabrications including QD microdisk arrays

with lasing properties and multicolor pixels on the same chip. Furthermore, arrays of microdisk laser arrays with high quality factor of optical cavity modes of 500-700 were successfully fabricated. Finally, we demonstrate the versatility of our approach to integrate QDs with different emission properties into large-area arrays of multicolor microscale patterns with high areal density of ~1000 pixels per inch (ppi). Importantly, this novel patterning approach can be potentially applied to other types of QDs with poor environmental stability for the development of QD-based photonic structures.

8.2 Experimental details

***Gain measurements**:* The third harmonic (355 nm) of a Spectra Physics Quanta-Ray INDI-series Pulsed Nd:YAG laser (pulse width of 7 ns, repetition rate of 10 Hz) was used directly as a seed for a GWU-Lasertechnik basiScan Beta-Barium Borate Optical Parametric Oscillator (OPO), producing tunable pulses of 450nm with 10μJ maximum pulse power (pulse width of 7 ns). For the variable stripe length (VSL) gain measurements, the excitation beam was shaped into a stripe of 125 μm width using a cylindrical lens (15 cm focus length), and the stripe length was controlled by a pair of blades mounted on mechanically controlled stages that provided an adjustable slit. Only the central 10 % of the beam was used to minimize pump inhomogeneity due the Gaussian intensity profile. The pump beam intensity, I_p, was varied by means of a pair of polarizers. One end of the stripe excitation was placed on the cleaved edge of the film while the length of the excitation stripe was progressively increased. The emission from the edge was collected with a 1 mm diameter fiber and recorded using a commercial spectrometer (Ocean Optics USB4000; resolution 2 nm). Gain values were extracted by a fit of emission vs. stripe length to data the 1-D amplifier model, as originally proposed by Shaklee and Leheny.[32]

***Fabrication of QD patterns**:* The patterning process used for fabricating QD patterns includes several stages. First, thinning solvent 700 was added to the OSCoR SL 1 resist solution to dilute it to half of the original concentration provided by the company. The diluted resist was spun cast on the silicon substrate to form a 400nm thick film (2000 rpm for 1 min). The cast film was baked at 100℃ for 1 min to remove the residual solvent. Short oxygen plasma etching (5 sec) was performed to improve the wettability of the OSCoR SL 1 film surface for the deposition of the negative photoresist (NR 71-3000 p). Ethyl lactate was added to the negative resist NR71-3000p solution to dilute it to one third of the original concentration provided by the company. The diluted resist was spun cast on top of OSCoR SL 1 film surface (3000 rpm for 1 minute). The cast film was subsequently soft baked at 100℃ for 5 minutes and exposed to 365 nm with a dosage of 123mW. The exposed film was then post-baked at 100℃ for 5 minutes and developed by soaking in RD6 developer for 5 sec.

After the development, the film was rinsed with water and dried by blowing with air.[23] Plasma etching (300W) with fixed gas flow at 45 sccm (O_2) and 5 sccm (Ar) was performed for 60 seconds in order to etch the underlying OSCoR SL 1 resist. $CsPbBr_3$ QD solution was spun cast (1000rpm for 1 minute) on the patterned templates. The sample was subsequently immersed into Orthogonal Stripper 700 for an hour to dissolve the OSCoR SL 1 resist and lift off the photoresist along with the attached $CsPbBr_3$ QD assemblies. To fabricate QD microdisk arrays, a low refractive index layer of CYTOP (n = 1.34, 1.5μm thick) was deposited on the Si wafer (n = 3.44) prior to the deposition of OSCoR SL 1 resist, in order to provide light confinement within the QD cavities.

Confocal PL configuration: The 450-nm output of the OPO was used to pump the samples. A pair of polarizers was used to control the pump fluence, while an iris was used to control the beam spot size. The pump is directed through a 40x (NA = 0.65) microscope objective using a dichroic mirror and focused on the sample. The emission is collected through the same objective, transmitted through the dichroic mirror and focused onto a 0.5-mm diameter optical fiber coupled to a 1/2m spectrometer and CCD array (resolution = 0.29 nm) or collimated and projected onto a camera lens for fluorescence imaging. An additional long pass filter is used to further attenuate the reflected pump beam.

8.3 Results and discussion

8.3.1 Fabrication of $CsPbBr_3$ micropatterns

To fabricate patterns of all-inorganic perovskite quantum dots, we utilized green-emitting $CsPbBr_3$ QDs.[12] **Figure 8.1a** shows the basic optical absorption and emission spectra of synthesized $CsPbBr_3$ QD. Transmission electron microscopy (TEM) was used to examine the overall shape and size of the synthesized $CsPbBr_3$ QDs (**Figure D.1**). The shape of $CsPbBr_3$ QDs is close to cuboids with the average length and width to be 13.1 ± 1.1 nm and 6.5 ± 0.7 nm, respectively. Generally, we do not observe significant difference in their absorption and emission spectra compared to those of QDs with cubic shape because their dimensions are close/above their Bohr diameter (7 nm)[26], indicating that our QDs are in the weak confinement regime with stabilized optical properties.

As known, attempts to purify common perovskite QDs showed that excessive washing steps lead to removal of ligands and insolubility to non-polar solvent, while insufficient washing leads to excessive ligands that are still presented in the final QD solution thus

compromising multi-stage lithographical process.[24] Hence, we have adopted a synthesis method that utilizes only oleic acid as the surface capping agent.[12] This method prevents ligand dynamic binding leading to the facile ligand loss during purification procedures.[12,27] Indeed, as-prepared colloidal solutions show better colloidal stability compared to those synthesized by conventional methods.

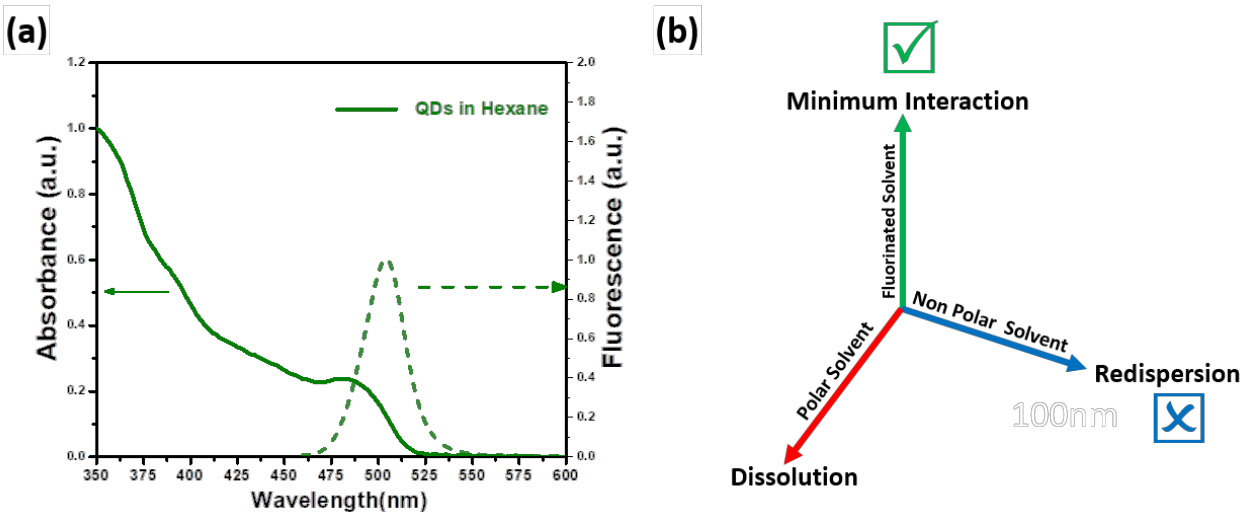

Figure 8.1 (a) Absorbance and fluorescent emission of $CsPbBr_3$ QDs in hexane. (b) Schematic of solvent constraint of $CsPbBr_3$ QDs.

Furthermore, to overcome the solvent constraints, the direct exposure of perovskite QDs to polar and non-polar solvents should be avoided during the lithography process since it causes their dissolution (**Figure 8.1b**). Therefore, we utilize the fluorinated polymer (OSCoR SL 1) as a novel sacrificial layer.[28] This sacrificial layer enables patterning using standard photolithography while providing the orthogonality to $CsPbBr_3$ QDs during lift-off process. Specifically, the fluorinated polymer along with photoresist can be removed by immersing the QDs into the fluorinated stripper which dissolves the underlying fluorinated polymer layer while the $CsPbBr_3$ QD patterns remain intact, because the interaction of the stripper with $CsPbBr_3$ QDs is minimal.

The orthogonal lithography process includes several steps (**Figure 8.2**).[29] First, the fluorinated polymer is spin-cast on a substrate as a sacrificial layer (**Figure 8.2, step 1**). Subsequently, standard photolithography was used to fabricate microscale trenches of predesigned patterns (**Figure 8.2, step 1-4**).

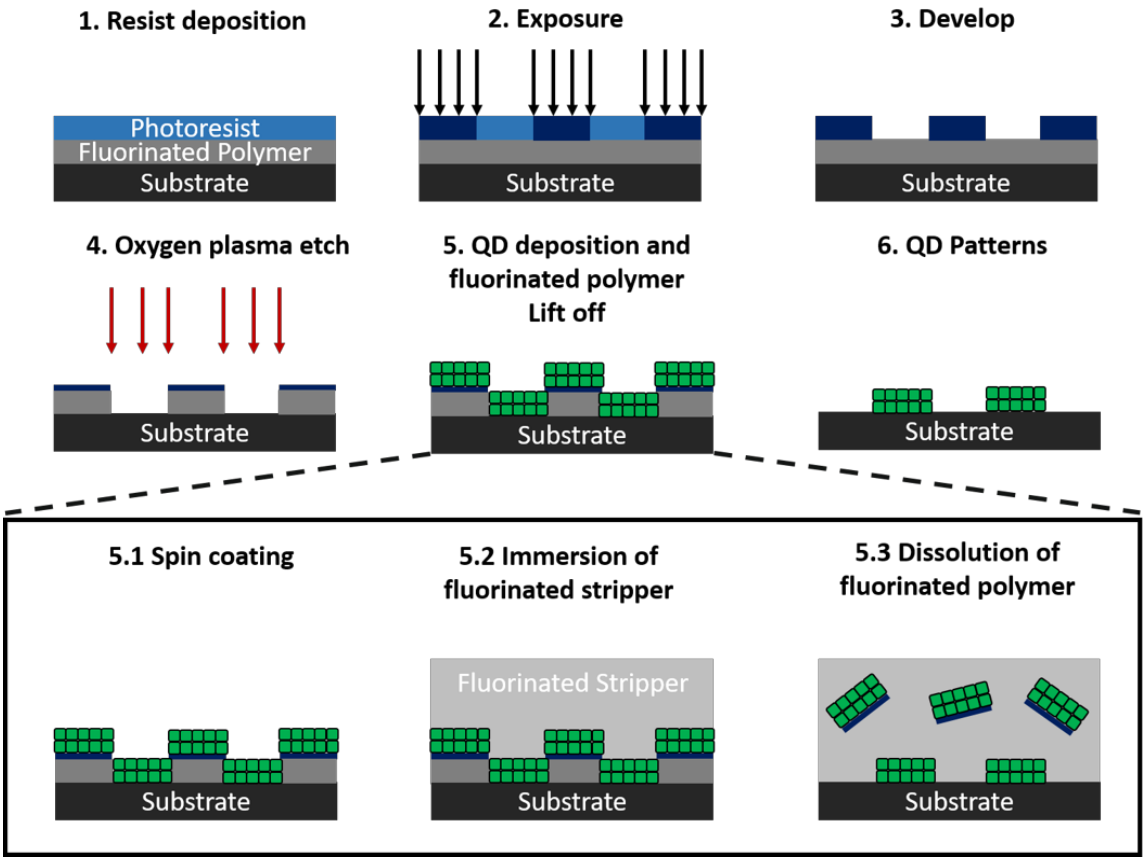

Figure 8.2 Schematic that outlines orthogonal lithography approach for fabricating $CsPbBr_3$ QD patterns via the insertion of fluorinated polymer layer and standard photolithography.

During the patterning process, the photoresist template acted as a mask while an oxygen plasma etch was performed to etch the underlying fluorinated polymer (**Figure 8.2, step 4**). These patterned trenches were subsequently filled with $CsPbBr_3$ QDs via spin-coating (**Figure 8.2, step 5.1**). Finally, the fluorinated polymer was

dissolved by immersing into the fluorinated stripper while CsPbBr3 QDs attached to the photoresist layer were lifted off (**Figure 8.2, step 5.2-5.3**) and remained strongly emissive (**Figure 8.2, step 6**).

With this method, large-area (2 cm x 2 cm) arrays of different patterns can be fabricated (**Figure 8.3a**). Examples of QR codes, circles and square spirals with high emission in green range are shown in **Figure 8.3b, c and D.2**.

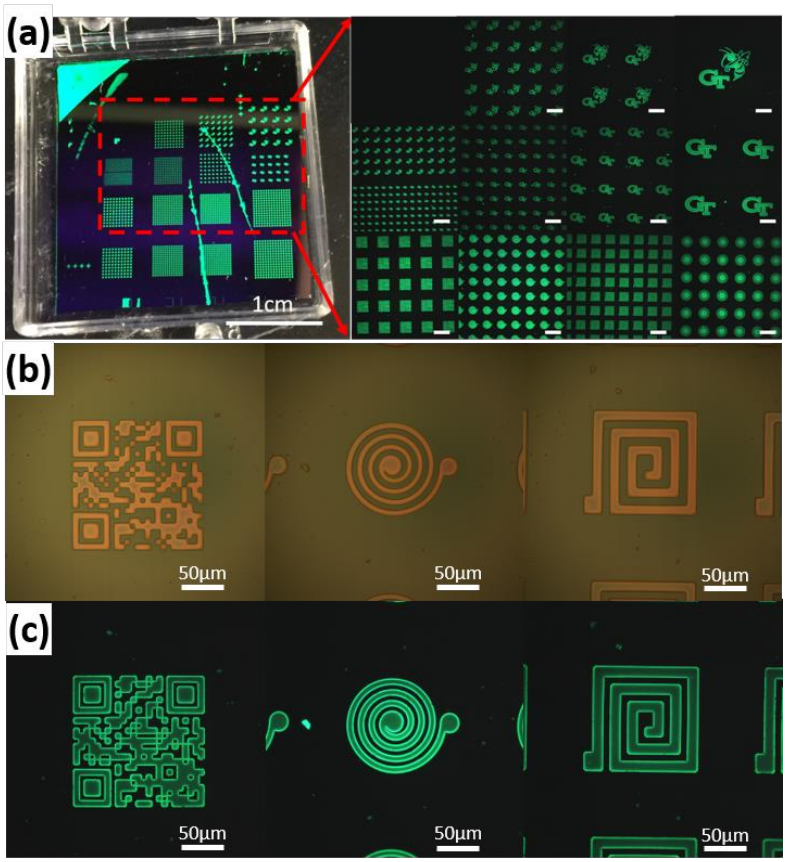

Figure 8.3 (a) Left panel: Optical micrograph of a substrate under UV illumination with arrays of different QD patterns. Right panel: fluorescent images of QD arrays of different patterns at the corresponding positions. All scale bars are 200 µm. Bright field (b) and fluorescent (c) images of different individual elements.

8.3.2 Optical gains of $CsPbBr_3$ QD film

Prior to the investigation of optical mode activity in perovskite microdisks, we conducted measurements to evaluate the lasing properties of assembled uniform $CsPbBr_3$ QD film using a standard configuration of the variable stripe length (VSL) method with a pulse laser excitation.[30] Significant spectral narrowing and an exponential increase of the emission intensity indicate mirrorless laser action (**Figures 8.4a, b, D.3a)**.

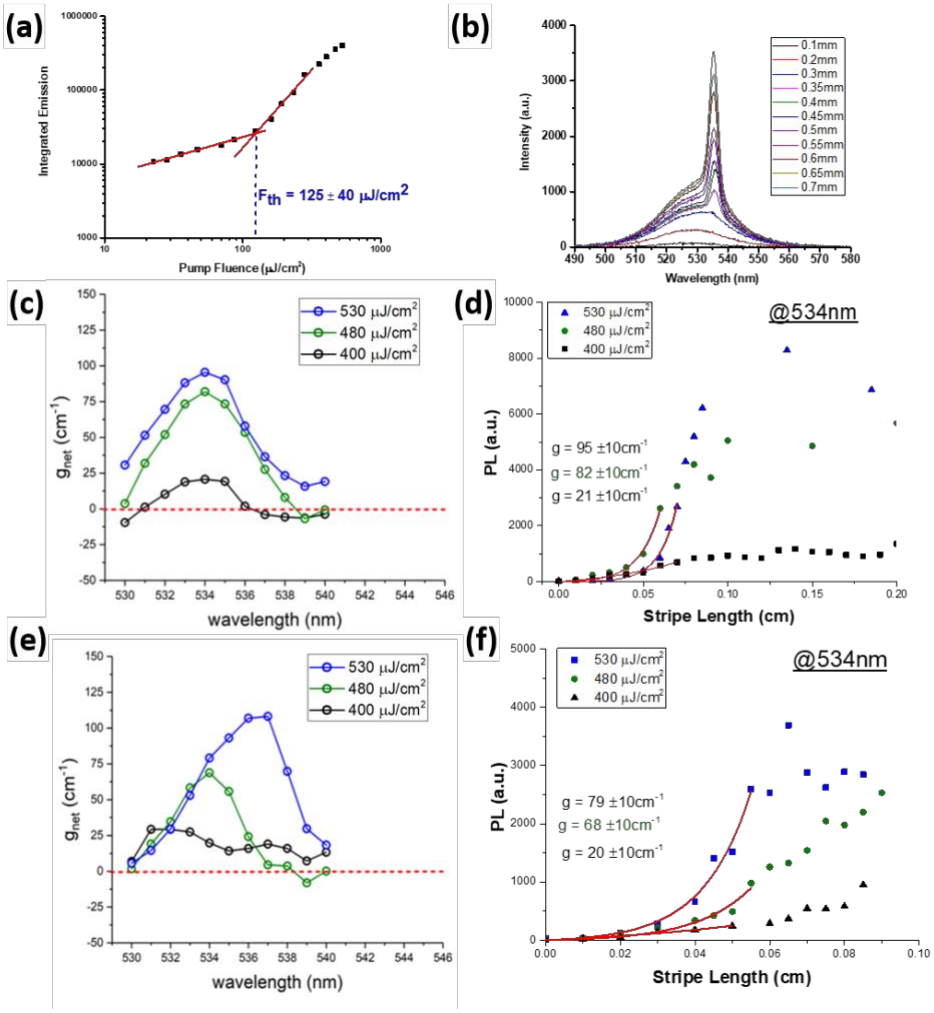

Figure 8.4 (a) Emission intensity vs excitation fluence response of CsPbBr3 QD film with ASE threshold as noted. (b) Emission spectra of QD film at various stripe lengths. (c) The optical gain spectra and (d) fitted optical gain values at 534 nm for as-prepared $CsPbBr_3$ QD film at various pump fluences. (e) The optical gain spectra and (f) optical gain values at 534 nm of $CsPbBr_3$ QD film after immersion into fluorinated stripper for an hour at various fluences.

A characteristic the amplified spontaneous emission (ASE) threshold occurs at 125 ± 40 μJ/cm^2 which is lower than previously reported values and close to those extrapolated for femtosecond lasing.[10,31] Next, net gain values were measured to be as high as 180 ± 25 cm^{-1} in the $CsPbBr_3$ QD films which is higher than that measured for other QD films (**Figures 8.4c, d, D.3b**).[30,32] Furthermore, we have investigated solvent resistance of the $CsPbBr_3$ QD film, since $CsPbBr_3$ QD are known to be extremely sensitive to solvents. In fact, the net gain values remained high after immersion into fluorinated stripper for an hour thus enabling the fabrication of $CsPbBr_3$ QDs patterns (**Figure 8.4e, f**). This is in contrast to fast deterioration of fluorescence after immersion of common photoresists in water for a minute.[33]

8.3.3 Optical properties and lasing behavior of microdisks

To study the optical mode activity of $CsPbBr_3$ QD structures, we have fabricated microdisks with various diameters, *D,* from 11.7 to 52.2 μm (**Figure 8.5**). The QD microdisks were found to possess a nest-like topography, where elevated rims are formed toward the circumference, common for these structures (**Figure 8.5b**).[34,35] The QD microdisks fabricated here display intense localized emission, suggesting strong waveguiding and efficient cavity optical mode generation (**Figure 8.6**). A non-linear behaviour was observed with increasing pump fluence, where the threshold intensity was determined to be ~200 μJ/cm^2 (**Figure 8.6a**), a value similar to threshold values observed for the pristine QD film. In addition, sharp spectral peaks appeared over the broad spontaneous emission band once the pump fluence exceeds the threshold value (**Figure 8.6b**). All of these findings confirm the preservation of optical lasing activity and total internal reflection near the disk circumference. The cavity mode spacing (Δλ) was found to decrease with increasing disk diameter, while the number of resonant

longitudinal cavity modes increases in agreement with theoretical predictions (**Figure 8.6b**).[36,37,38]

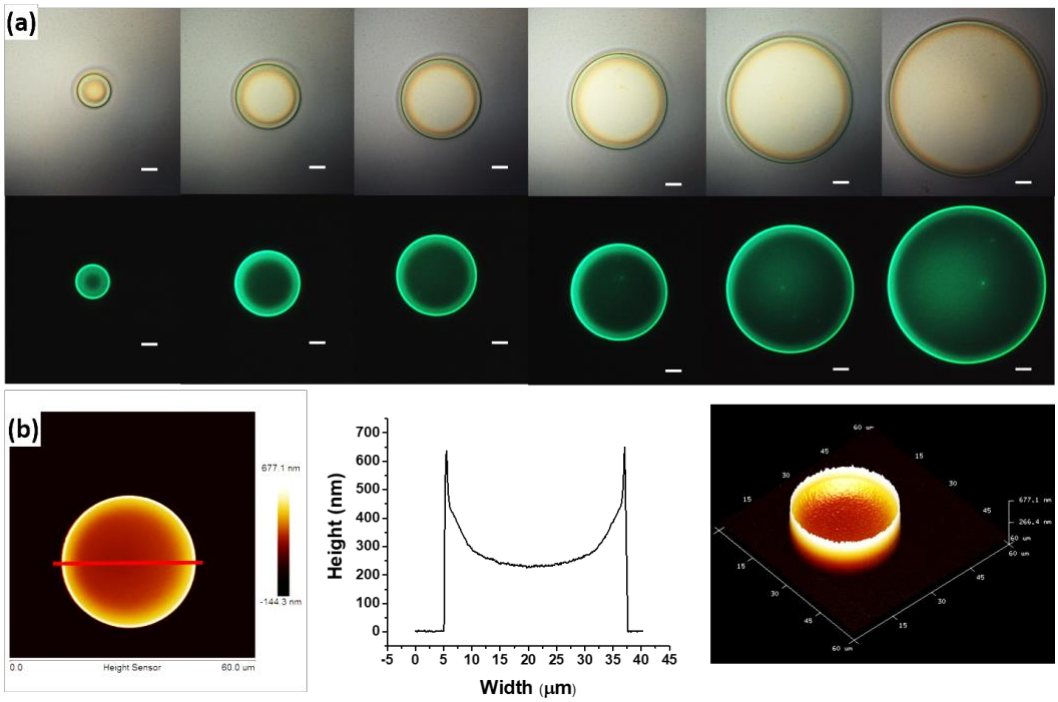

Figure 8.5 (a) Bright field (top) and fluorescent (bottom) images of QD microdisks with diameters of 11.7, 21.8, 26.7, 31.8, 41.6 and 52.2 μm. All scale bars are 5 μm (b) From left to right: AFM topographical image (top-view), height profiles, and 3D image of QD microdisk with diameter of 31.8 μm.

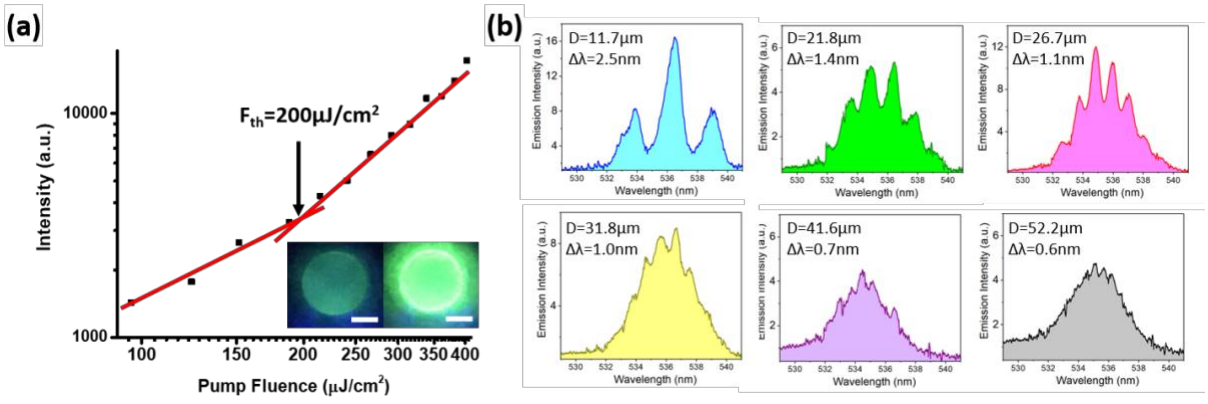

Figure 8.6 (a) Emission intensity vs. excitation fluence measured from a $CsPbBr_3$ QD microdisk. The threshold intensity, F_{th} is determined from the interception of the linear and superlinear responses. Inset: PL images of QDs microdisk (D = 26.7 μm) below (left) and above (right) lasing threshold. The scale bar is 10 μm for both images. (b) Lasing spectra of QD microdisks with D = 11.7 μm, 21.8 μm, 26.7 μm, 31.8 μm, 41.6 μm and 52.2 μm, respectively. Δλ is the average 'mode spacing' of the observed longitudinal cavity modes.

This trend is also confirmed by the linear relationship between the cavity mode spacing ($\Delta\lambda$) and the reciprocal optical path length $1/n\pi D$, according to the relation, $\Delta\lambda = \lambda^2/n\pi D$ which is expected for circular microcavity (**Figure 8.7a**).[36] From this relationship, the group index, n of the $CsPbBr_3$ QDs microdisks was estimated to be 3.2 which is larger than the bulk refractive index of $CsPbBr_3$ (n=2.3).[45] The enhancement in refractive index may be attributed to the exciton-photon coupling that has been discovered in single crystalline perovskites, which should be further investigated in the future.[39,40]

Moreover, the mode number can also be estimated by using lasing spectra of microdisks with different sizes and their corresponding mode spacing. The mode number was estimated to be 3, 6, 7 and 8 for disk size of 11.7 μm, 21.8 μm, 26.7 μm and 31.8 μm. It is noteworthy that the mode number for disk size of 41.6 μm and 52.2 μm can not be exactly estimated since line widths of cavity modes (~0.8-1 nm) are already larger than the mode spacing (0.6-0.7 nm). As expected, the number of modes increases proportionally with the increasing disk size. Therefore, multimode operation with specific set of modes is possible by carefully defining the disk size.[41]

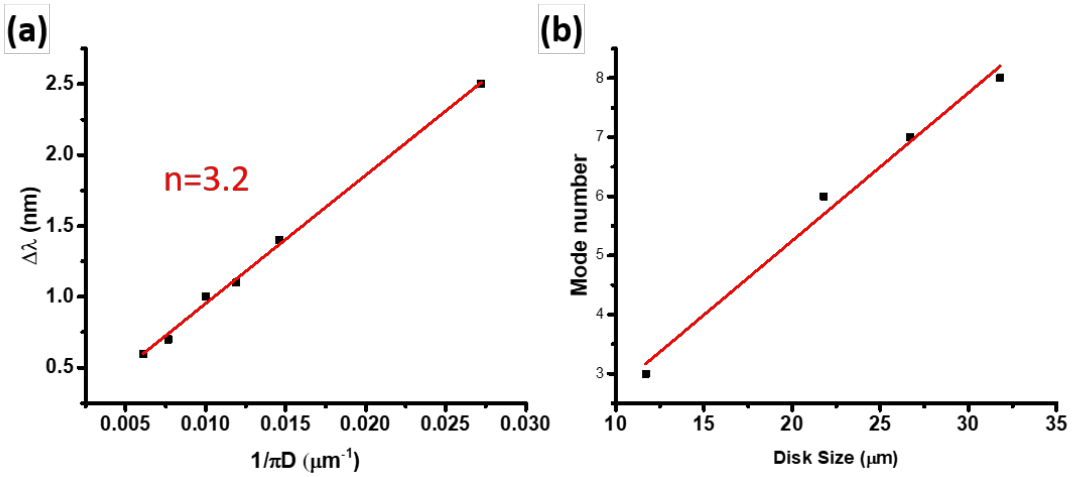

Figure 8.7 (a) The mode spacing, $\Delta\lambda$ of the WG modes in QD micridisk lasers with various diameter, *D* vs. the reciprocal geometrical path length, $1/\pi D$. The group index, n is calculated from the relation: $\Delta\lambda = \lambda^2/n\pi D$. (b) The plot of mode number versus the disk size.

In addition we suggest that a single-mode lasing may be possible by reducing the disk size to a diameter that is small enough to support only one cavity mode or engineering the shape of lasing structures with suppressed secondary modes. Parity-time symmetry is another interesting possibility where coupled lasing structures with balanced gain and loss can achieve the exceptional point with only one specific cavity mode amplified.[42] Furthermore. the quality factor, Q, for microdisks fabricated here can be estimated from the relation $Q = \lambda/\delta\lambda$, where λ is the peak wavelength of the cavity mode and $\delta\lambda$ is its line width.[36] The high quality factor of the dominant modes in QD microdisks with different diameters within the range of 500-700 is comparable to that reported from microcavities of perovskite single crystals.[43,44] However, these single crystal perovskites are grown with random size, geometry and location that excludes fabrication of large-area organized photonic arrays.[45] In contrast, the precise control the spatial organization of QD microstructures at large scale is facilitated by the photo-lithographical approach.

8.3.4 Dual color pixel arrays

In addition to single emission signature microdisk lasers we applied two-stage orthogonal lithography process to fabricate dual color arrays by combining QDs with different emission signature (**Figure 8.8**). The process flow includes the fabrication of first pattern of circular structures (*D*=~11.7 μm) made of green $CsPbBr_3$ QDs (**Figure 8.2**). Next, the second complementary pattern was fabricated from red-emitting $CdSe/Cd_{1-x}Zn_xSe_{1-y}S_y$ QDs by using the same orthogonal lithography process and the mask aligner for positioning microdisks. The standard photolithography was again used to create a secondary photoresist mask on top of the fluorinated polymer with embedded prior fabricated structures (**Figure 8.8, step 1-3**).

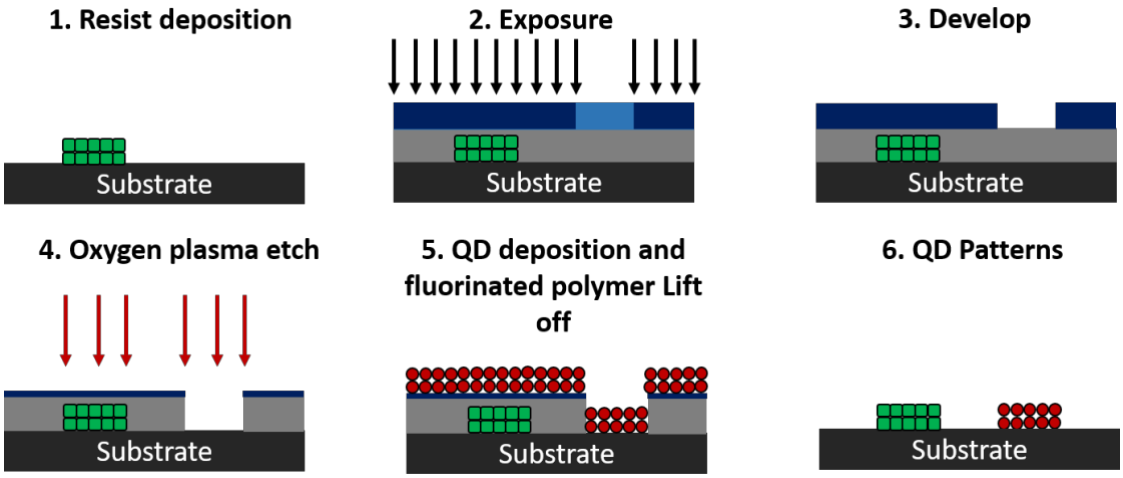

Figure 8.8 Schematic that outlines the orthogonal lithography approach that is used multiple times for fabricating dual-color patterns of QDs.

During the second lithography process, the $CsPbBr_3$ QD patterns were fully protected by the fluorinated polymer and hence maintained their structure integrity. Fluorinated polymer not covered by photoresist was etched by plasma etching, generating local trenches on the substrate (**Figure 8.8, step 4)**. Red-emitting $CdSe/Cd_{1-x}Zn_xSe_{1-y}S_y$ QDs were further deposited via spin-coating and the fluorinated polymer was then dissolved by immersing into the fluorinated stripper (**Figure 8.8, step 5)**. Lastly, the photoresist was lifted off leaving patterns of red $CdSe/Cd_{1-x}Zn_xSe_{1-y}S_y$ QDs on the substrate that are close to the first set of green $CsPbBr_3$ QD structures (**Figure 8.8, step 5-6)**.

The initial fabricated array shows intense green emission from $CsPbBr_3$ QD circular structures (**Figure 8.9a**). After the second stage, the orange color appeared due to the mixed green and red QD emissions, indicating a successful integration of two different QD arrays onto the same chip (**Figure 8.9b**). Indeed, the higher resolution fluorescent image shows microscale pixels that consist of binary pixels of closely packed green and red QD circles (**Figure 8.9c**). Each pixel size is 25 μm x 25μm that corresponds to a density of ~1000 ppi, a value that is higher than the resolution of the current phone

displays which is typically 200-500 ppi (e.g., 264 ppi for Retina Display in iPad display). [46]

Furthermore, optical properties of these circular structures including emission spectrum and spatial distribution of PL intensity within a single pixel were studied using high-resolution hyperspectral system. PL emissions of green and red patterns were centered at 510 nm and 623 nm with full-width half maximum of 22 nm and 40 nm, respectively (**Figure D.4**). Moreover, the spatial distribution of PL intensity for both green and red patterns were found to be nest-like with the PL intensity in the middle region is approximately 30-40% of the maximum PL intensity at the rim (**Figure 8.9d**). These spatial distributions of PL intensity have similar characteristics to the microdisk topography indicating the physical dimension of microscale patterns controls the spatial distribution of PL intensity (**Figure 8.3b**).

Importantly, blue CdSe/$Cd_{1-x}Zn_xSe_{1-y}S_y$ QDs with PL emission centered at 467nm (**Figure D.5**) can also be integrated to form the third set of circle patterns by using our approach repeatedly. **Figure 8.9e** demonstrated the preliminary result of RGB arrays with three sets of QD patterns that emit at blue, green and red region, respectively. Further optimization of our fabrication process can be done in the future to improve the alignment between patterns. This capability can strongly support the realization of high-resolution QD optoelectronic devices with miniaturized pixels including full-color QD light-emitting diodes and photodetectors that require pixels consisting of QD components with precisely controlled emission and absorption properties.[12,47]

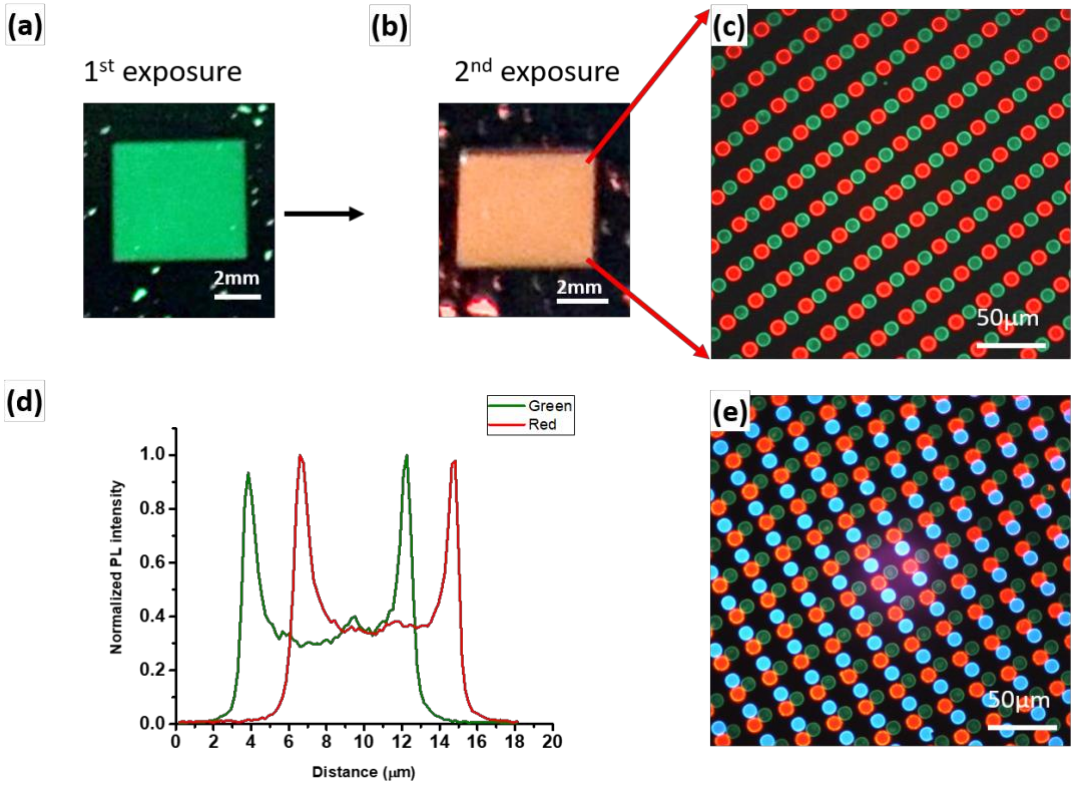

Figure 8.9 (a) Fluorescent image of an array of $CsPbBr_3$ microdisks. (b) Fluorescent image of the binary array of $CsPbBr_3$ QDs (green) and $CdSe/Cd_{1-x}Zn_xSe_{1-y}S_y$ QDs (red) microdisks and corresponding high-resolution fluorescent image (c). (d) Spatial distribution of PL intensity for ~11.7 μm individual green and red QD microdisks. (e) Fluorescent image shows the preliminary result of RGB arrays of red, green and blue QD patterns using our approach.

8.4 Conclusions

In summary, we fabricated high-resolution, large-area patterning of environmentally-sensitive perovskite QDs for efficient lasing structures and multicolor (binary and ternary color) emitting pixel arrays. The utilization of fluorinated photoresist and solvents allows to avoid easy dissolution and damaging of perovskite QDs during the multi-stage lithographical process. This approach preserves the high optical gain performance of QDs film and efficient optical lasing of circular QD microstructures with high quality cavity modes. Furthermore, we have demonstrated the multicolor emission arrays with

paired circular microstructures of green, blue, and red-emitting QDs and high areal density of ~1000 ppi, much higher than common display resolution.

8.5 Chapter acknowledgements

Youngjun Yoon and Yajing Chang (Prof. Zhiqun Lin's research group, Georgia Institute of Technology): QD synthesis, TEM and ligand exchange. Dr. Evan Lafalce and Qingji Zeng (Prof. Valy Vardeny's research group, University of UTAH): Confocal micro PL measurement. Shengtao Yu and Marcus Smith (Prof. Vladimir Tsukruk's research group, Georgia Institute of Technology): AFM, optical characterization.

8.6 References (Chapter 8)

1 N. S. Makarov, S. Guo, O. Isaienko, W. Liu, I. Robel, V. I. Klimov, *Nano Lett.* **2016**, 16, 2349.

2 Y.-S. Park, S. Guo, N. S. Makarov, V. I. Klimov, *ACS Nano* **2015**, 9, 10386.

3 J. Pan, S. P. Sarmah, B. Murali, I. Dursun, W. Peng, M. R. Parida, J. Liu, L. Sinatra, N. Alyami, C. Zhao, E. Alarousu, T. K. Ng, B. S. Ooi, O. M. Bakr, O. F. Mohammed, *J. Phys. Chem. Lett.* **2015**, 6, 5027.

4 J. Pan, L. N. Quan, Y. Zhao, W. Peng, B. Murali, S. P. Sarmah, M. Yuan, L. Sinatra, N. M. Alyami, J. Liu, E. Yassitepe, Z. Yang, O. Voznyy, R. Comin, M. N. Hedhili, O. F. Mohammed, Z. H. Lu, D. H. Kim, E. H. Sargent, O. M. Bakr, *Adv. Mater.* **2016**, 28, 8718.

5 X. Li, Y. Wu, S. Zhang, B. Cai, Y. Gu, J. Song, H. Zeng, Adv. Funct. Mater. 2016, 26, 2435.

6 P. Liu, W. Chen, W. Wang, B. Xu, D. Wu, J. Hao, W. Cao, F. Fang, Y. Li, Y. Zeng, R. Pan, S. Chen, W. Cao, X. W. Sun, K. Wang, Chem. Mater. 2017, 29, 5168.

7 L. Protesescu, S. Yakunin, M. I. Bodnarchuk, F. Krieg, R. Caputo, C. H. Hendon, R. X. Yang, A. Walsh, M. V. Kovalenko, *Nano Lett.* **2015**, 15, 3692.

8 J. Jung, C. H. Lin, Y. J. Yoon, S. T. Malak, Y. Zhai, E. L. Thomas, V. Vardeny, V. V. Tsukruk, Z. Lin, *Angew. Chem.* **2016**, 128, 5155.

9 G. Nedelcu, L. Protesescu, S. Yakunin, M. I. Bodnarchuk, M. J. Grotevent, M. V. Kovalenko, *Nano Lett.* **2015**, 15, 5635.

10 S. Yakunin, L. Protesescu, F. Krieg, M. I. Bodnarchuk, G. Nedelcu, M. Humer, G. De Luca, M. Fiebig, W. Heiss, M. V. Kovalenko, *Nat. Commun.* **2015**, 6, 8056.

11 T. L. Doane, K. L. Ryan, L. Pathade, K. J. Cruz, H. Zang, M. Cotlet, M. M. Maye, *ACS Nano* **2016**, 10, 5864.

12 E. Yassitepe, Z. Yang, O. Voznyy, Y. Kim, G. Walters, J. A. Castañeda, P. Kanjanaboos, M. Yuan, X. Gong, F. Fan, J. Pan, S. Hoogland, R. Comin, O. M. Bakr, L. A. Padilha, A. F. Nogueira, E. H. Sargent, *Adv. Funct. Mater.* **2016**, 26, 8757.

13 C.-Y. Huang, C. Zou, C. Mao, K. L. Corp, Y.-C. Yao, Y.-J. Lee, C. W. Schlenker, A. K. Y. Jen, L. Y. Lin, *ACS Photonics* **2017**, 4, 2281.

14 N. Zhang, W. Sun, S. P. Rodrigues, K. Wang, Z. Gu, S. Wang, W. Cai, S. Xiao, Q. Song, *Adv. Mater.* **2017**, 29, 1606205.

15 X. He, P. Liu, H. Zhang, Q. Liao, J. Yao, H. Fu, *Adv. Mater.* **2017**, 29, 1604510.

16 J. Feng, X. Yan, Y. Zhang, X. Wang, Y. Wu, B. Su, H. Fu, L. Jiang, *Adv. Mater.* **2016**, 28, 3732.

17 P. Liu, X. He, J. Ren, Q. Liao, J. Yao, H. Fu, *ACS Nano* **2017**, 11, 5766.

18 Z. Gu, K. Wang, H. Li, M. Gao, L. Li, M. Kuang, Y. S. Zhao, M. Li, Y. Song, *Small* **2017**, 13, 1603217.

19 S. Schünemann, K. Chen, S. Brittman, E. Garnett, H. Tüysüz, *ACS Appl. Mater. Interfaces* **2016**, 8, 25489.

20 F. Palazon, Q. A. Akkerman, M. Prato, L. Manna, *ACS Nano* **2016**, 10, 1224.

21 J. Chen, Y. Wu, X. Li, F. Cao, Y. Gu, K. Liu, X. Liu, Y. Dong, J. Ji, H. Zeng, *Adv. Mater. Technol.* **2017**, 2, 1700132.

22 T. S. Mentzel, D. D. Wanger, N. Ray, B. J. Walker, D. Strasfeld, M. G. Bawendi, M. A. Kastner, *Nano Lett.* **2012**, 12, 4404.

23 C. H. Lin, Q. Zeng, E. Lafalce, M. J. Smith, S. T. Malak, J. Jung, Y. J. Yoon, Z. Lin, Z. V. Vardeny, V. V. Tsukruk, *Adv. Opt. Mater.* **2017**, 5, 1700011.

24 Y. Kim, E. Yassitepe, O. Voznyy, R. Comin, G. Walters, X. Gong, P. Kanjanaboos, A. F. Nogueira, E. H. Sargent, *ACS Appl. Mater. Interfaces* **2015**, 7, 25007.

25 S. Schünemann, K. Chen, S. Brittman, E. Garnett, H. Tüysüz, *ACS Appl. Mater. Interfaces* **2016**, 8, 25489.

26 J. A. Castañeda, G. Nagamine, E. Yassitepe, L. G. Bonato, O. Voznyy, S. Hoogland, A. F. Nogueira, E. H. Sargent, C. H. B. Cruz, L. A. Padilha, *ACS Nano* **2016**, 10, 8603.

27 J. De Roo, M. Ibáñez, P. Geiregat, G. Nedelcu, W. Walravens, J. Maes, J. C. Martins, I. Van Driessche, M. V. Kovalenko, Z. Hens, *ACS Nano* **2016**, 10, 2071.

28 B. H. Kim, S. Nam, N. Oh, S.-Y. Cho, K. J. Yu, C. H. Lee, J. Zhang, K. Deshpande, P. Trefonas, J.-H. Kim, J. Lee, J. H. Shin, Y. Yu, J. B. Lim, S. M. Won, Y. K. Cho, N. H. Kim, K. J. Seo, H. Lee, T.-i. Kim, M. Shim, J. A. Rogers, *ACS Nano* **2016**, 10, 4920.

29 S. Krotkus, F. Ventsch, D. Kasemann, A. A. Zakhidov, S. Hofmann, K. Leo, M. C. Gather, *Adv. Opt. Mater.* **2014**, 2, 1043.

30 C. H. Lin, E. Lafalce, J. Jung, M. J. Smith, S. T. Malak, S. Aryal, Y. J. Yoon, Y. Zhai, Z. Lin, Z. V. Vardeny, V. V. Tsukruk, *ACS Photonics* **2016**, 3, 647.

31 Y. Wang, X. Li, J. Song, L. Xiao, H. Zeng, H. Sun, *Adv. Mater.* **2015**, 27, 7101.

32 K. L. Shaklee, R. F. Leheny, *Appl. Phys. Lett*. **1971**, 18, 475.

33 A. Loiudice, S. Saris, E. Oveisi, D. T. L. Alexander, R. Buonsanti, *Angew. Chem. Int. Ed.* **2017**, 56, 10696.

34 P. J. Yunker, T. Still, M. A. Lohr, A. G. Yodh, *Nature* **2011**, 476, 308.

35 Y. Wang, K. E. Fong, S. Yang, Van D. Ta, Y. Gao, Z. Wang, V. Nalla, H. V. Demir, H. Sun, *Laser Photon. Rev.* **2015**, 9, 507.

36 S. Yang, Y. Wang, H. Sun, *Adv. Opt. Mater.* **2015**, 3, 1136.

37 R. C. Polson, G. Levina, Z. V. Vardeny, *Appl. Phys. Lett.* **2000**, 76, 3858.

38 R. C. Polson, Z. V. Vardeny, D. A. Chinn, *Appl. Phys. Lett.* **2002**, 81, 1561.

39 K. Park, J. W. Lee, J. D. Kim, N. S. Han, D. M. Jang, S. Jeong, J. Park, J. K. Song, *J. Phys. Chem. Lett.* **2016**, 7, 3703.

40 T. J. S. Evans, A. Schlaus, Y. Fu, X. Zhong, T. L. Atallah, M. S. Spencer, L. E. Brus, S. Jin, X. Y. Zhu, *Adv. Opt. Mater.* **2018**, 6, 1700982.

41 Z. Duan, Y. Wang, G. Li, S. Wang, N. Yi, S. Liu, S. Xiao, Q. Song, *Laser Photon. Rev.* **2018**, 12, 1700234.

42 H. Hodaei, M.-A. Miri, M. Heinrich, D. N. Christodoulides, M. Khajavikhan, *Science* **2014**, 346, 975.

43 J. Xing, X. F. Liu, Q. Zhang, S. T. Ha, Y. W. Yuan, C. Shen, T. C. Sum, Q. Xiong, *Nano Lett.* **2015**, 15, 4571.

44 X. He, P. Liu, H. Zhang, Q. Liao, J. Yao, H. Fu, *Adv. Mater.* **2017**, 29, 1604510.

45 S. W. Eaton, M. Lai, N. A. Gibson, A. B. Wong, L. Dou, J. Ma, L.-W. Wang, S. R. Leone, P. Yang, *Proc. Natl. Acad. Sci. USA* **2016**, 113, 1993.

46 Y. Takubo, Y. Hisatake, T. Lizuka, T. Kawamura, *SID Symposium Digest of Technical Papers* **2012**, 43, 869.

47 M. Kuang, J. Wang, B. Bao, F. Li, L. Wang, L. Jiang, Y. Song, *Adv. Opt. Mater.* **2014**, 2, 34.

CHAPTER 9

SPECTRAL AND DIRECTIONAL PROPERTIES OF NOTCHED AND ELLIPTICAL QUANTUM-DOT MICROLASERS

9.1 Introduction

The miniaturization of lasers represents a significant research effort for the purposes of developing micro-chip scale optical telecommunications networks and micro-sensors. Micro-cavity lasers have the advantages of small modal volume and high Q-factors due to strong light confinement effects, that can help to achieve low thresholds and fine spectral tuning.[1,2] In particular, the class of curved-boundary optical cavities, where confinement is based on total internal reflection such as the sphere[3], disk[4], or toroid[5] configurations have achieved remarkable 'figure of merit' and have been found useful in numerous applications and studies. These devices support 'whispering-gallery modes' (WGMs) that propagate near the circumference of the microdisk and emit isotropically in the circular plane via evanescent leakage, or quantum tunneling in the photon picture.[6] Although such a low loss cavity is beneficial in rendering narrow line-widths and low pump thresholds, the highly valued property of directional emission is lacking. In fact, out-coupling of light in such lasing elements has been traditionally difficult.[7] Therefore, additional efforts have been made to impart directionality to these devices.

The majority of these efforts have involved boundary deformations of microdisk cavities.[8,9,10,11,12] These efforts have been fruitful in obtaining more directional emission

patterns, and, in parallel have shown interesting spectral behavior due to the occurrence of chaotic ray dynamics.[12] Consequently, these curved structures have simultaneously provided for explorations in interesting quantum phenomenon such as studies of quantum chaos via classical correspondence.[2,12] While it can be shown analytically that notched and elliptical cavities will not produce chaotic dynamics[13], the implications for the spectral and directional properties of these structures should be interesting as well. For example, tuning the deformation in liquid droplet WGM lasers enabled the observation of an exceptional point in the Non-Hermitian optical Hamiltonian of the system.[14] Such Non-Hermitian systems have become of dramatically increasing interest due an intriguing new avenue in optics based on Parity-Time (PT) symmetric systems, a field that itself has relied heavily on WGM resonators.[15,16,17,18]

Furthermore, detection and sensing are some of the more promising applications for WGM micro-cavity lasers. In this case, the adhesion of particles or a change in environmental parameters will result in a noticeable change in spectral properties of the laser due to its strong sensitivity to the cavity surface.[19,20] This essentially represents the other side of the interest in boundary deformation, where instead of intentionally disturbing the boundary to achieve a desired property, the change in laser properties can be used to register and characterize an environmentally related event. Therefore, both endeavors will benefit from an increased understanding of the way such deformations from circular boundaries effect the spectral and directional characteristics of the microlasers.

Here we investigate the emissive properties of notched and elliptical microcavity lasers based on CdSe/$Cd_{1-x}Zn_xSe_{1-y}S_y$ core/alloyed-shell quantum dots (QDs). Fabrication of micro-resonators from solution-processable semiconductors such as QDs is particularly

advantageous due to their high optical gain and ease of fabrication, as well as compatibility with many substrates for on-chip integration. Furthermore, the emission wavelength can be controlled by the size of the QDs to allow for flexibility in the working spectral range.

9.2 Experimental details

Confocal micro PL configuration: The fabricated samples were characterized using a home-built micro-photoluminescence setup. Optical pumping to achieve laser action was carried out using a ps-laser at 532 nm that was focused on the sample through a 40x (NA = 0.65) microscope objective using a dichroic mirror. Emission was collected using the same objective, and transmitted via an optical fiber to a ½ met. monochromator spectrometer. Alternatively, emission images were recorded using a camera. The intensity of the pump was controlled using a pair of polarizers. The angular dependence of the laser emission from the microdisks was collected using a 125 μm diameter bare optical fiber mounted on a rotational stage and rotated in the horizontal plane. The fiber was held at ~1.5 mm from the rotation axis during the measurement, giving a full-width angular resolution of about 5°.

FDTD modeling: FDTD (finite difference time domain) simulations of the EM field propagation different shaped cavities were performed using the Lumerical software package.

9.3 Results and discussion

9.3.1 Spectral properties of notched microdisk lasers

Figure 9.1a shows the emission spectrum of a circular microdisk laser of diameter D=25 μm. We see a single set of modes with the expected free-spectral range, Δλ, given approximately by the relation $\Delta\lambda = \lambda^2/(n_{eff}\pi D)$, where n_{eff} is the effective mode index of refraction. The emission image shows a uniform distribution of light intensity along the circumference. In contrast Fig. 3b shows a more typical result, where two sets of modes are observed. In this case we can identify bright spots in the emission image. These bright spots are unintended defects that act as asymmetric scatterers. The presence of defects breaks the degeneracy of clockwise and counter-clockwise WGM, which, in turn leads to the mode splitting in the emission spectrum (Figure 9.1b).

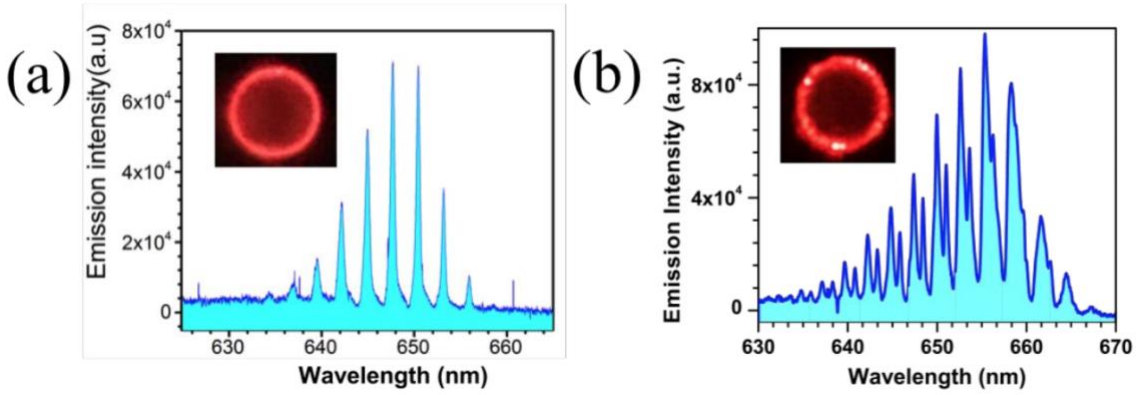

Figure 9.1 Emission spectrum from a microdisk laser with uniform circumferential edge (a) and one with unintended defects that result from the fabrication process (b). The inset in each figure shows the florescent image obtained at the same intensity at which the spectrum was measured.

To further characterize these effects, we next studied similar microdisk cavities having symmetric 'notch' defects that have been intentionally engineered by design. **Figure 9.2**

shows the results associated with these microdisk cavities. In **Figure 9.2a**, we see a similar behavior as in **Figure 9.1b**, when the notch dimensions are small. In this case the circumferential width, w = 0.5μm and the radial depth of the 'notch' is 2μm. When the defect size becomes large, however as in the case when w = 2μm (shown in **Figure 9.3b**), no mode splitting occurs and the expected Δλ value is observed. We have confirmed by studying many sizes of notch that the larger notch the less mode splitting occurs in the emission spectrum.

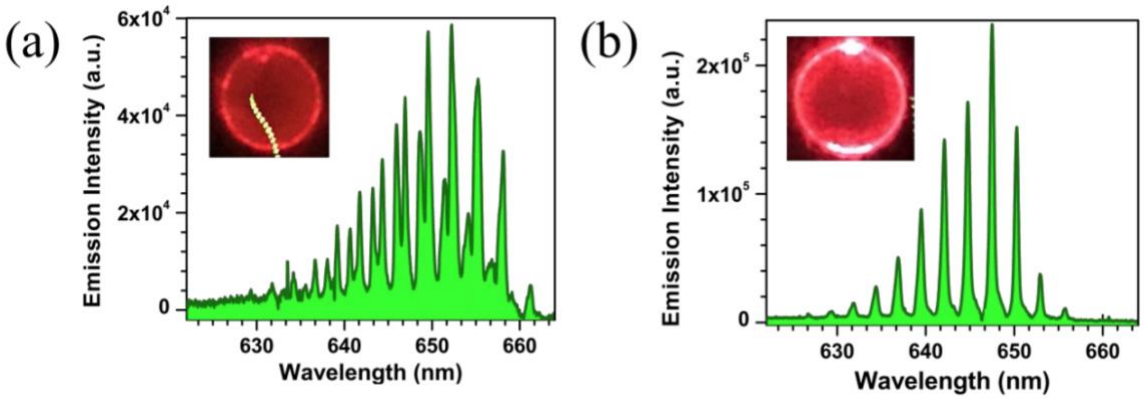

Figure 9.2 Emission spectrum from a microdisk laser with an intentional 'notch' defect of circumferential width, w = 0.5μm and radial depth, d = 2μm (a), and another one with dimensions of w = 2μm and d = 2μm (b). The inset in each figure shows the florescent image obtained at the same intensity at which the spectrum was measured.

In addition to the effect on the spectral properties of these microdisk lasers, we have also observed that the defects control the angular distribution of emission in the azimuthal plane of the microdisk. The PL image shown in Figure 9.3 inset shows a uniform and bright circumference. Since the light is well confined inside the cavity through total internal reflection, the emission originates from 'photon tunneling' through an optical barrier. This occurs uniformly in the plane of the disk, as verified by the isotropic angular dependence of the emission displayed in **Figure 9.3a**. While in

Figure 9.3b, we see that the disk with unintended and randomly distributed defects shows a highly anisotropic profile. The reason for this is most clearly observed in the case of a large 'notch' defect as shown in **Figure 9.3c**. Here it can be seen that the anisotropy occurs diametrically across from the defect, due to light rays scattering at the defect site. Intriguingly, we observe that long-wavelength modes are those that are predominantly scattered, by measuring the spectrum at characteristic azimuthal angles, namely in front of and diametrically across from the 'notch' defect, as displayed in **Figure 9.3d**.

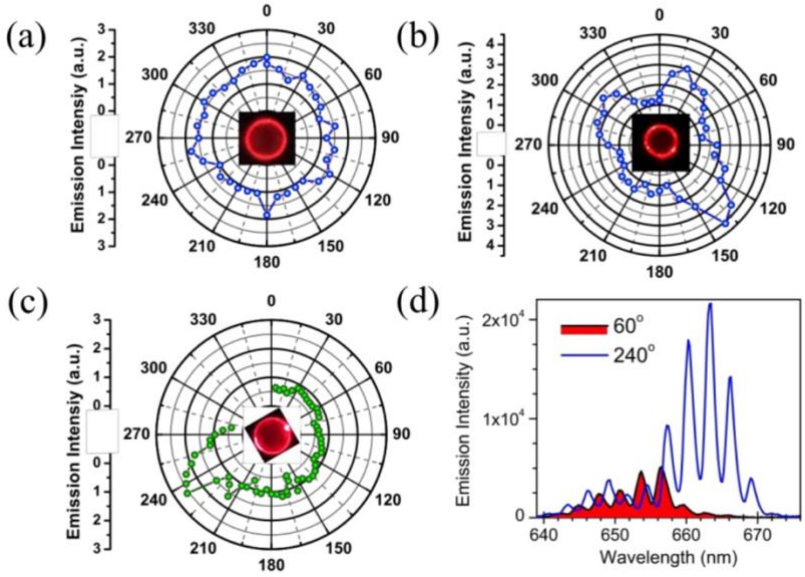

Figure 9.3 Total emissive power measured as a function of the azimuthal angle for the microdisk of Fig. 3a (a), for the microdisk of Fig 3b (b), and for that of Fig 4b (c). (d) Spectra recorded from microdisk shown in (c) at the angular positions of 60° and 240° as indicated

9.3.2 Spectral properties of elliptical microdisk lasers

We next explore deviations from circular symmetric resonators by examining elliptical structures of varying aspect ratio. The structures investigated here all possess a long axis of 25μm and have variable length short axis. We characterized samples of ρ =0.68,

0.72, 0.80, 0.88, and 0.92. In **Figure 9.4a** we present the emission spectrum of an elliptical microdisk with ρ=0.68. In contrast to the circular disk shown in **Figure 9.1a**, here we observe two overlapping sets of peaks. We extract the mode splitting of different peaks and plot it in **Figure 9.4b**. The trend is nearly linear with the splitting decreasing at longer wavelengths. This suggest the possibility that the emission spectrum results from two sets of modes with slightly different Δλ's.

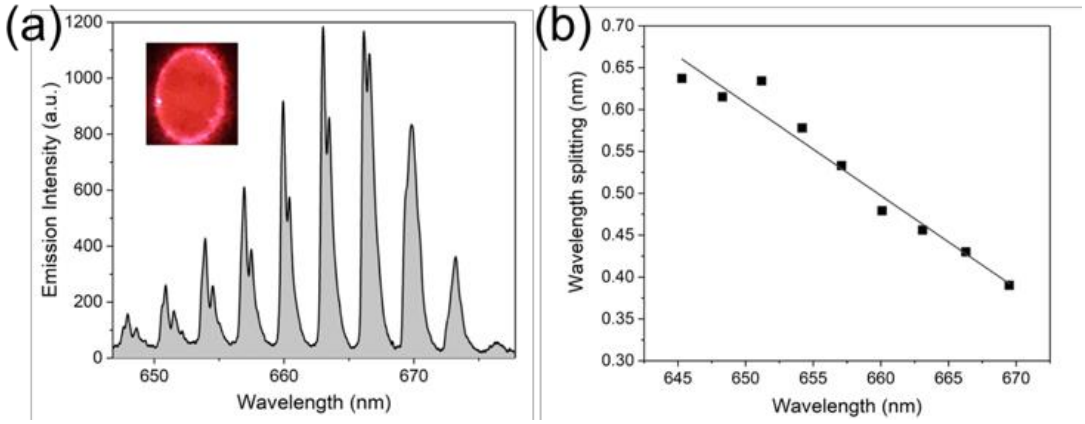

Figure 9.4 (a) Spectral of ellipse microdisk with aspect ratio of 0.68. (b) The mode splitting wavelength of each peaks.

The spectrum shown in **Figure 9.5a** below is typical for the ratio ρ=0.8, characterized by a very large splitting of the primary WGM mode progression, such that the splitting approaches half the natural Δλ of the resonator. A useful means of quantifying this behavior is to perform a Fast Fourier Transform (FFT) of the spectrum, as displayed in **Figure 9.5b**. By first converting the spectrum to units of μm^{-1}, the FFT gives peaks at harmonics of the primary optical path of the lasing modes. Comparing the FFT of a uniform spectrum from a ρ=1 sample (red) to that of the ρ=0.8 sample in **Figure 9.5a** (blue), we see that the ratio of the first to the second harmonic is drastically altered, as the splitting pushes the periodicity towards half of the FSR and adds spectral weight to

the second harmonic. We note that the first harmonic for the cavity of ρ=0.8 is significantly broader compared to that of a circular cavity. This may suggest the presence of distinct optical path lengths separated by a small length difference. Unfortunately, the numerical precision is not enough to more clearly resolve this effect.

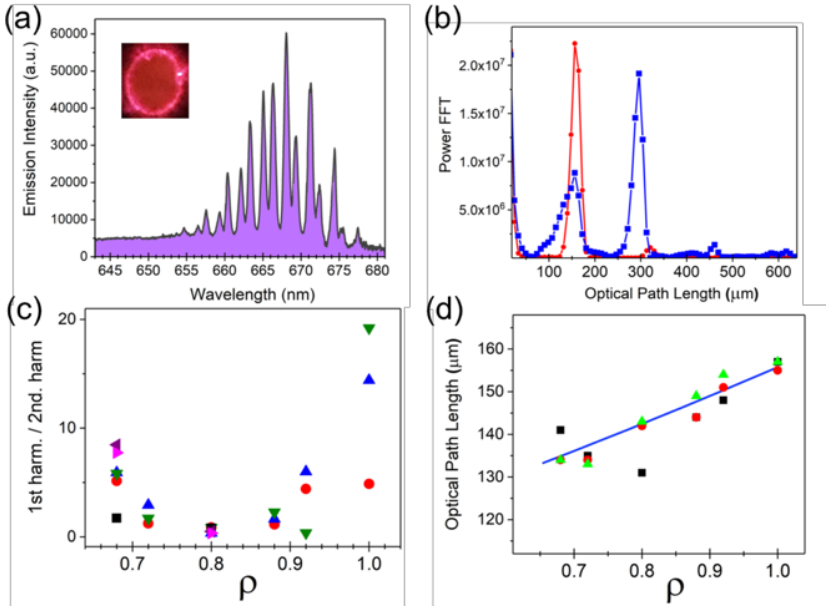

Figure 9.5 (a) Laser emission spectrum from an elliptical micro-cavity with the ratio of short axis to long axis, ρ=0.8. The inset shows the fluorescent image of the laser measured above threshold. (b) Power Fast Fourier Transform (FFT) of a resonator with ρ = 1 (red) compared to that of the spectrum shown in (a) (blue). (c) The ratio of the first to the second harmonic of the FFT for different elliptical microcavities with different values of ρ. (d) The extracted primary optical path length from resonators of different ρ. The various symbols represent different microcavities measured for each value of ρ. The line through the data points is the expected path length based on the perimeter of each ellipse taking a constant n_{eff} = 2.

In **Figure 9.5c** we show the ratio of 1st and 2nd harmonics of the FFT for a number of samples with different ρ. There is a clear and stable minimum at ρ=0.8 showing that the largest splitting occurs at this ratio within the range of samples measured. Before considering the mechanism behind the different degrees of mode splitting that occurs in

different shaped resonators, we point out that by using the position of the first harmonic of the FFT we can reliably extract the primary path length and thus Δλ. In **Figure 9.5d** we plot these values for various resonators having different values of ρ. The line through the data points shows the expected relation using the perimeter of the ellipses to replace the circumference of the disk (n_{eff} πD) with the previously determined index, n_{eff} = 2. The close agreement here shows that the modes are of elliptical WGM nature, that is, Δλ is still controlled by the optical path length at the perimeter, which, in turn depends on the ratio ρ.

We next turn to FTDT (finite difference time domain) simulations of the electromagnetic (EM) field amplitudes of WGMs in these structures. **Figure 9.6a** is the simulation of an ellipse with ρ=0.8. It indicates that the resonator supports WGMs with different radial mode index. The outer and inner circles respectively correspond to the two sets of WGM in the spectrum. These two sets of modes have considerable spatial overlap with each other which leads to coupling between them. Such a coupling produces mode-splitting in the observed emission spectrum consistent with the data. Since the mode-splitting is proportional to the coupling strength, the strong mutual interaction between these two mode sets explains the large splitting observed.

The variation of ρ will deform the WGM and subsequently control the intra-cavity interaction between these modes. In **Figure 9.6b**, we see that the simulation of ellipse with ρ=0.68 shows the deformation of WGM modes are very large due to low aspect ratio, which causes small and non-uniform spatial overlap and thus low coupling strength. Hence, the spectrum contains two sets of modes with distinct Δλ due to the difference in optical paths as shown in Fig. 2. For the ellipse with ρ=0.92 (**Figure 9.6c**) the deformation of the cavity is not large enough to separate radial mode index.

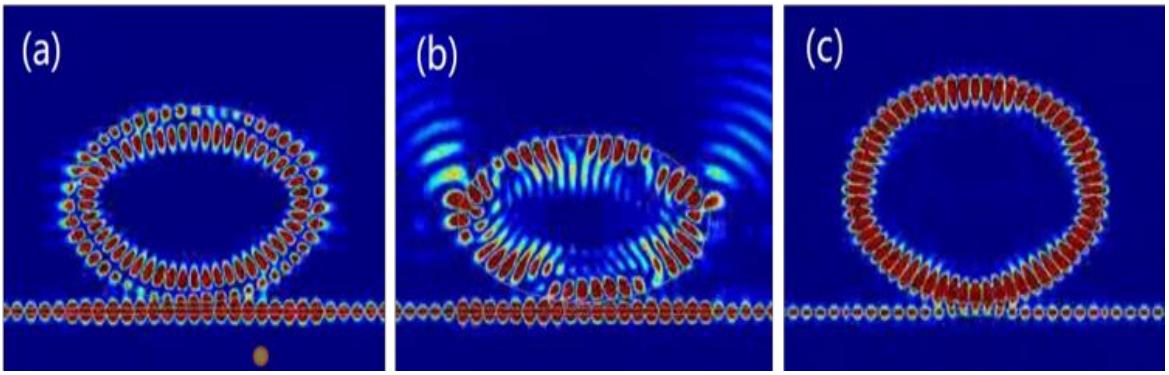

Figure 9.6 (a) Simulation of the EM field in several elliptical micro-cavities with (a) ρ=0.80, (b) ρ=0.68, and (c) ρ=0.92.

9.3.3 Directional emission of elliptical microdisk lasers

The directionality of the laser emission is also influenced by the microcavity shape. As shown in **Figure 9.7**, the emission pattern evolves from the isotropic pattern in circular structures (**Figure 9.3a**) to a dipolar pattern with decreasing ρ. In **Figure 9.7a and b** we show the angular dependence of the emission for elliptical cavities with ρ=0.8 and ρ=0.68, respectively.

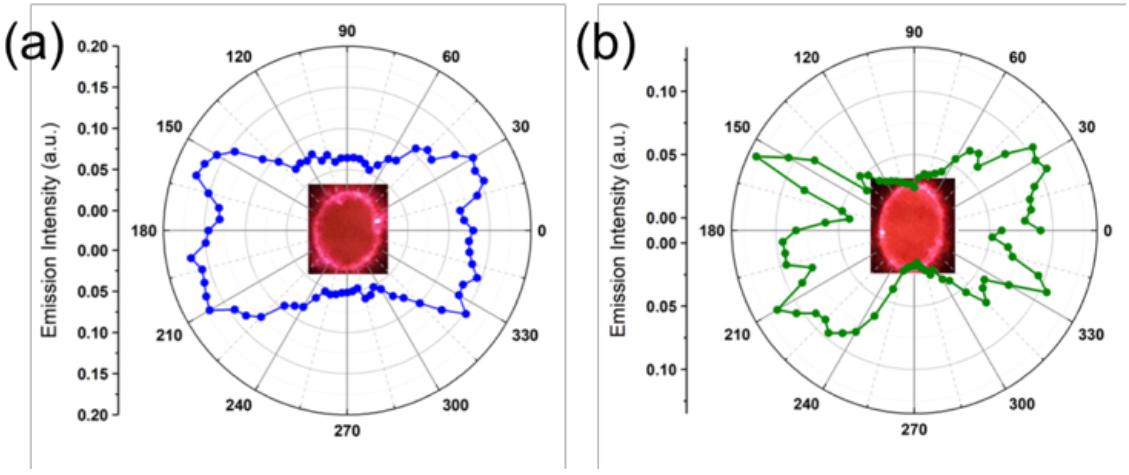

Figure 9.7 (a) Collection-angle dependence of the laser emission with fluorescent image at the center for an elliptical cavity with (a) ρ=0.8 and (b) ρ=0.68.

It is clear that the emission is preferentially emitted perpendicular to the long axis of the ellipse, and increasingly so as the boundary deviates further from circular symmetry.

This is also evident from the FDTD simulations of **Figure 9.6b**, where the leakage from the structure occurs much more strongly near the points of the highest curvature. As discussed in the introduction, one of the significant draw backs of WGM lasers is that strong light confinement limits the output to the quantum tunneling effect and inhibits directionality. The results here suggest a simple means to overcome these limitations.

Finally, we also studied a series of coupled elliptical micro-cavity pairs as shown in **Figure 9.8a and b**. In analogy to molecular dipole interactions, we refer to the case when the coupling axis is perpendicular to the long axis of the ellipses as 'H-type' coupling (as in **Figure 9.8a**), whereas when the coupling axis is along the long axis we refer to this as 'J-type' coupling (see **Figure 9.8b**). When two elliptical cavities joint together, the directional emissive property is enhanced. Figure 6a shows the emission image and angular dependence emission of an H-type ellipse pair both having aspect-ratio of 0.68. Since each single disk has directional emission along the short-axis, one disk acts as a lens to amplify the out-coupling of the other one in this direction. Consequently, compared to single ellipse, the directional emissive property is enhanced. Fig. 6b shows the situation when two disks are J-type coupled. It is seen that this type of structure gives a very interesting cross-pattern. The point of intersection of the two ellipses act as scattering element, leading to narrow cones of light in specific directions. This demonstrates yet another way to control the directionality of laser emission in WGM resonators.

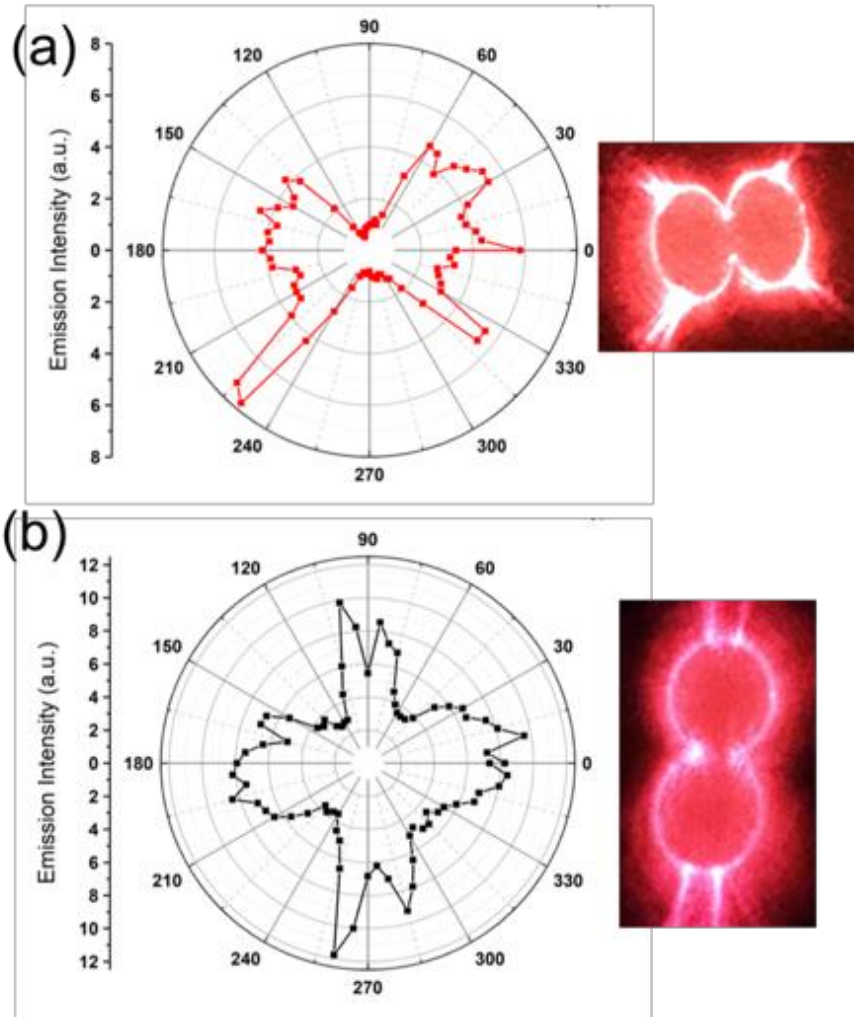

Figure 9.8 (a) Collection-angle dependence of the laser emission from a pair of elliptical cavities (ρ=0.68) with H-type coupling and fluorescent image to the right. (b) Same as in (a) but the two ellipses have J-type coupling.

9.4 Conclusions

We have studied the laser emission spectral and directional properties from notched and elliptical QD microdisk lasers with notch and ellipse of various aspect ratios. We found that the larger the notch the less mode splitting occurs in the emission spectrum. In addition, the placement of notch to the microdisk laser leads to the directional emission towards a particular direction, beneficial for the design of photonic structures that require

enhanced coupling in the specific location. On the other hand, we also found that the ellipse microcavity generates two sets of modes. When the aspect ratio is ~0.8, the coupling between these two sets of modes reach maximum, and consequently the emission spectrum shows maximum splitting. Reducing the ratio even more, reduces the mutual interaction between these mode sets and reduces the splitting. We also show that the aspect ratio of the elliptical cavities leads to directional emission, and this property can be further enhanced and tailored by coupling the microcavities together. These properties hold promise for improving the functionality of such lasers by providing simple means to obtain desired directionality.

9.5 Chapter acknowledgements

Youngjun Yoon and Dr. Jaehan Jung (Prof. Zhiqun Lin's research group, Georgia Institute of Technology): QD synthesis, TEM and ligand exchange. Dr. Evan Lafalce and Qingji Zeng (Prof. Valy Vardeny's research group, University of UTAH): Confocal micro PL measurement. Dr. Sidney Malak and Marcus Smith (Prof. Vladimir Tsukruk's research group, Georgia Institute of Technology): AFM, optical characterization.

9.6 References (Chapter 9)

1 K. J. Vahala, *Nature* **2003**, 424, 839.

2 H. Cao, J. Wiersig, *Rev. Mod. Phys.* **2015**, 87, 61.

3 T. J. Kippenberg, S. M. Spillane, K. J. Vahala, *Opt. Lett.* **2002**, 27, 1669.

4 S. L. McCall, A. F. J. Levi, R. E. Slusher, S. J. Pearton, R. A. Logan, *Appl. Phys. Lett.* **1992**, 60, 289.

5 D. K. Armani, T. J. Kippenberg, S. M. Spillane, K. J. Vahala, *Nature* **2003**, 421, 925.

6 L. He, K. Özdemir Şahin, L. Yang, *Laser Photonics Rev.* **2012**, 7, 60.

7 S. M. Spillane, T. J. Kippenberg, O. J. Painter, K. J. Vahala, *Phys. Rev. Lett.* **2003**, 91, 043902.

8 R. C. Polson, Z. V. Vardeny, *Appl. Phys. Lett.* **2004**, 85, 1892.

9 V. M. Apalkov, M. E. Raikh, *Phys. Rev. B* **2004**, 70, 195317.

10 Q. J. Wang, C. Yan, N. Yu, J. Unterhinninghofen, J. Wiersig, C. Pflügl, L. Diehl, T. Edamura, M. Yamanishi, H. Kan, F. Capasso, *Proc. Natl. Acad. Sci. USA* **2010**, 107, 22407.

11 Q. H. Song, L. Ge, J. Wiersig, J. B. Shim, J. Unterhinninghofen, A. Eberspächer, W. Fang, G. S. Solomon, H. Cao, *Phys. Rev. A* **2011**, 84, 063843.

12 C. Gmachl, F. Capasso, E. E. Narimanov, J. U. Nöckel, A. D. Stone, J. Faist, D. L. Sivco, A. Y. Cho, *Science* **1998**, 280, 1556.

13 M. V. Berry, *Eur. J. Phys.* **1981**, 2, 91.

14 S.-B. Lee, J. Yang, S. Moon, S.-Y. Lee, J.-B. Shim, S. W. Kim, J.-H. Lee, K. An, *Phys. Rev. Lett.* **2009**, 103, 134101.

15 B. Peng, Ş. K. Özdemir, F. Lei, F. Monifi, M. Gianfreda, G. L. Long, S. Fan, F. Nori, C. M. Bender, L. Yang, *Nat. Phys.* **2014**, 10, 394.

16 L. Chang, X. Jiang, S. Hua, C. Yang, J. Wen, L. Jiang, G. Li, G. Wang, M. Xiao, *Nat. Photonics* **2014**, 8, 524.

17H. Hodaei, M.-A. Miri, M. Heinrich, D. N. Christodoulides, M. Khajavikhan, *Science* **2014**, 346, 975.

18 L. Feng, Z. J. Wong, R.-M. Ma, Y. Wang, X. Zhang, *Science* **2014**, 346, 972.

19 A. M. Armani, R. P. Kulkarni, S. E. Fraser, R. C. Flagan, K. J. Vahala, *Science* **2007**, 317, 783.

20 J. Zhu, S. K. Ozdemir, Y.-F. Xiao, L. Li, L. He, D.-R. Chen, L. Yang, *Nat. Photonics* **2009**, 4, 46.

CHAPTER 10

COALESCENCE OF CAVITY MODES AT AN EXCEPTIONAL POINT IN COUPLED MICRODISK LASERS

10.1 Introduction

Non—Hermitian Hamiltonians obeying *Parity-Time* (*PT*) symmetry can have the unusual property of guaranteed real eigenvalues within a finite parameter space.[1,2] Furthermore, these physical systems may contain spontaneous *PT*-symmetry breaking transitions at which real eigenvalues coalesce and become complex conjugate pairs. Such transitions occur at exceptional points (EPs) of the Hamiltonian and therefore the study of exceptional point behavior in both *PT*-symmetric and other complex Hamiltonians has become a subject of significant investigation.[3,4,5,6,7,8,9,10,11] More than a scientific curiosity, these systems have found fruitful realization in classical optics where *PT*-symmetry is impressed upon the Helmholtz wave-equation by appropriate preparation of the imaginary part of the complex index of refraction, i.e. by spatially balancing gain and loss.[8,9,10,12,13,14] Studies of the *PT*-symmetric phase and its spontaneous breaking in waveguides and resonators have been conducted and revealed associated behavior such as loss-induced transparency[8], power oscillations[9], unidirectional invisibility and non-reciprocal light propagation[10,12,13,14] and mode-manipulation in lasers.[15,16]

Semiconductor micro-cavity lasers are characterized by low-thresholds and high Q-values owing to small modal volumes and strong light-confinement effects. These attributes make this laser design promising for many applications, including notable examples in PT-symmetric optics.[15,16,17] A particularly suitable design for sensors is the circular microcavites such as disk, ring, toroid, and sphere configurations.[17,18] In this configuration, light is confined by total internal reflection at the semiconductor air/interface supporting the propagation of so called whispering gallery modes (WGM). High-Q values allow for sensitive detection of a change in environment causing either a shift frequency or splitting of resonance frequencies.[19, 20, 21] In the active laser configuration, these interactions are readily discerned by observing the emission spectrum. However, these applications have so far relied on a precise material systems to achieve the desired performance. Expanding the flexibility of these material requirements is a necessary step to obtain more general platforms for sensing or utilizing the phase-change-behavior of PT-symmetric optics.

Colloidal quantum dots (CQD) are nanoscale semiconductor particles that possess large stimulated emission and absorption cross-sections. These optical properties allow for the achievement of high optical gain by reasonably low intensity optical pumping while the refractive indices are large enough to sustain large critical angles for total internal reflection.[25] More importantly, the emission of CQDs can be tuned to cover a wide range from ultra-violet to infrared region by simply changing their size or composition, providing flexibility to the design of advanced photonic systems that requires lasing emission at specific wavelength.[22] In addition, carefully designed core/alloyed-shell CQDs have also been proven to be highly photostable under intensive optical pumping.[23] These properties make CQDs a promising photonic component to be studied and developed for

future lasing applications. Meanwhile, the ease-of-fabrication can be utilized to create micro-cavities made of solution-processable CQDs by using standard lithographic techniques and a wide variety of substrates. This shows processing advantages over more commercially mature technology based on inorganic semiconductor alloys and multiple quantum wells that are grown via high-vacuum film processing and strict requirements of lattice-matching.[24]

Here, we investigate whispering gallery modes from microdisk cavities formed from robust crosslinked assemblies of CdSe/$Cd_{1-x}Zn_xSe_{1-y}S_y$ core/alloyed-shell CQDs. The majority of the disks studied exhibit mode-splitting associated with local defects on the disk circumference. We then demonstrate the emergence of delocalized interaction modes in near-field coupled pairs of such disks. By a careful study of the emission spectra from closely spaced micro-disk pairs, we observe that actively pumped interacting lasers produce spectra more robust against the appearance of parasitic modes. By spatial variation of gain and loss in the coupled pairs, we show that the suppression of the localized parasitic modes is the result of an exceptional point of the non-Hermitian optical system. In particular, we show that the intra-cavity parasitic modes can be driven into coalescence through gain/loss variation in the presence of inter-cavity coupling to a mode of another active cavity. This phenomenon may therefore be used to circumvent some of the inherent obstacles in using solution-based semiconductor materials for lasing and improve the quality of laser emission.

10.2 Experimental details

Fabrication and characterization of microdisk lasers: To fabricate CQD microdisk lasers, we have adopted a facile one-pot method to synthesize high quality compositional gradient core/alloyed-shell QDs with an average size of 7.5 ± 0.8 nm (**Figure E.1**). The gradient shell help suppress Auger recombination significantly, which is the main obstacle to achieve lasing in CQD films in the past. We then utilized a hybrid top-down and bottom-up approach we previously developed to fabricate these microdisk laser arrays (details described in Chpater 3).[25] In brief, this approach combines standard photolithography and layer-by-layer deposition to integrate tiny CQDs into photoresist templated trenches. Photolithography provides up-scalability and precise control of spatial distribution to these CQD assemblies while the layer-by-layer deposition along with the crosslinking of QDs enhance the mechanical integrity against sonication during photoresist lift-off process.

Atomic force microscopy was used to investigate the formation of possible defects during fabrication (**Figure E.2**). There are generally two types of defects in our microdisk that can induce the mode splitting. The first type is the small QD aggregates that formed near disk circumference. These aggregates may originate from the imperfections that exist in QD solutions which act as seeds to affect the drying process and cause the formation of these small aggregates. The second type is difference in circumference height due to inhomogeneous drying. Both type of defects can introduce localized perturbation of effective refractive indices and light confinement to the disk circumference, lifting the degeneracy between CW and CCW modes.

***Optical characterization*:** The samples were placed on a three-dimensional stage under a home-built confocal micro-photoluminescence set-up. The excitation source was provided by a the second harmonic (532nm) of a solid-state pulsed laser based on Nd:YAG delivering 7ps pulses at a repetition rate of 200Hz. The beam was focused through a 40x (NA=0.65) microscope objective onto the sample using a dichroic mirror (550nm long-pass). The emission from the sample was collected through the same objective transmitted through the dichroic mirror as well as an additional 550nm long-pass filter, focused onto a multimode optical fiber and recorded using a 1/2m spectrometer and CCD array. The spectral revolution of the setup was 0.2nm. Alternatively, a camera was placed in the emission path to collect PL images of the disks. The beam size was set to with an iris a 50μm in diameter.

10.3 Results and discussion

10.3.1 Lasing properties of single disks

Figure 10.1a shows the spectral evolution with increasing pump intensity (Ip). At low intensity only broad photoluminescence band (FWHM ~ 25nm) is observed (black), displaying a peak near 635nm. Above the threshold intensity $I_P = I_{TH} = 29\mu J/cm^2$, narrow modes emerge from the PL spectrum. The free-spectral range is $\Delta\lambda \approx 2.6nm$, increasing slightly with increasing wavelength as described by the formula for WGM's, $\Delta\lambda = \lambda^2/n_{eff}(\pi D)$ where n_{eff} is the effective mode index and D is the disk diameter (D = 25 ± 1 μm). By converting the spectral units to μm^{-1} and taking the Fourier transform, we extract a series of harmonics of the optical path length $n_{eff}(\pi D)$ (inset), giving the effective index n_{eff} = 1.85 ± 0.05 which is in agreement to the CdSe CQD film value determined by ellipsometry.[23,26] In **Figure 10.1b**, we show the angular dependence of

emission in the plane of the disk, which is isotropic signaling a homogenous intensity distribution along the circumference of the disk. Additionally, the fluorescent image of the disk under the lasing condition shows the field amplitude is predominantly located along the perimeter. Thus, the observed emission modes are attributed to WGMs of the CQD micro disk resonator.

In **Figure 10.1c** we present the model emission spectrum from another disk of the same size. In this case, we are able to resolve two sets of modes with **Δ**λ = 2.6nm. The additional set of modes is observed to be split-off from the other WGM modes by ~0.8nm.

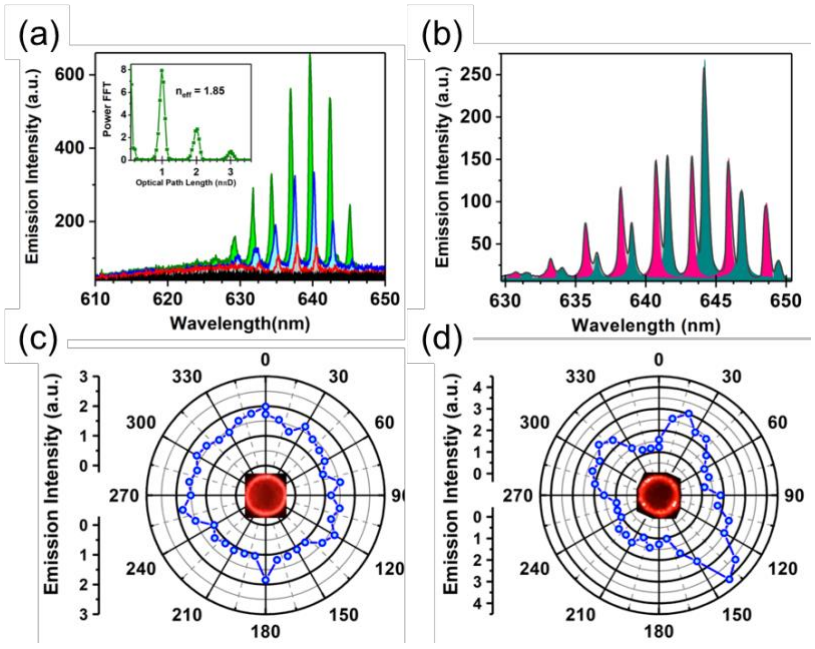

Figure 10.1 (a) Emission from a microdisk pumped at various intensities: 16μJ/cm^2 (black), 29μJ/cm^2 (red), 66μJ/cm^2 (blue), 116μJ/cm^2 (green). Inset shows the FFT of the 116μJ/cm^2 ploted vs. the optical path length $n_{eff}\pi D$ where n_{eff}=1.85 is the effective mode index and $D = 25\mu m$. (b) Collection-angle dependence of the spectrally integrated emissive power in the plane of the disk with fluorescent image at the center. (c) Emission spectrum from a different microdisk of the same diameter pumped at 116μJ/cm^2. The shaded regions indicate Lorentzian fits to the data. (d) Collection-angle dependence of the spectrally integrated emissive power in the plane of the disk in with fluorescent image at the center. The peaks in the data are positioned diametrically from the visible bright spots seen image.

We note that the linewidths of all modes are comparable (~ 0.5nm) and the splitting does not vary much with increasing pump fluence. In the flourescent image of **Figure 10.1d** it is seen that a particularly bright spot has now appeared on the circumference of the disk. Furthermore, bright-field microscopic image of the disk reveals a defect can now be observed at the same positions as the bright spots in the FL image (**Figure E.4**). These latter two observations reveal that the defects are in fact points where material inhomogeneity and structural imperfections occur. These defects then act as asymmetric scattering centers that increase out-coupling in the vertical direction giving them their bright appearance. The occurrence of such defects and the observation of parasitic modes (splitting) is quite common; it has been observed in ~87% of the samples examined.

10.3.2 Lasing properties of coupled-disk pairs

We now turn to the investigation of coupled-microdisk-pairs where two disks are spaced 396 ± 20nm apart (**Figure E.3**). This is less than the wavelength of emission and should provide adequate evanescent coupling between the modes of the two disks. In **Figure 10.2a-c**, we show the emission spectrum obtained when the pair is placed at the center of the beam spot and both individual disks are pumped evenly (**Figure 10.2a-c**), and when the left or right disks are pumped exclusively (**Figure 10.2a-c**). The latter configuration resembles a so-called PT-symmetric laser system, since one disk has gain while the other has loss, although they may not be exactly balanced. The emission spectra in the unbalanced cases are similar to the isolated single disk of **Figure 10.1c**, where two sets of modes with the common $\Delta\lambda$ are observed. It is therefore surprising, that the emission spectrum of the evenly-pumped pair shows no trace of the mode splitting observed when each individual disk is pumped (**Figure 10.2b**). In contrast, to

the majority of isolated disk investigated, we here see a spectrum devoid of parasitic modes, i.e. described by a single WGM progression.

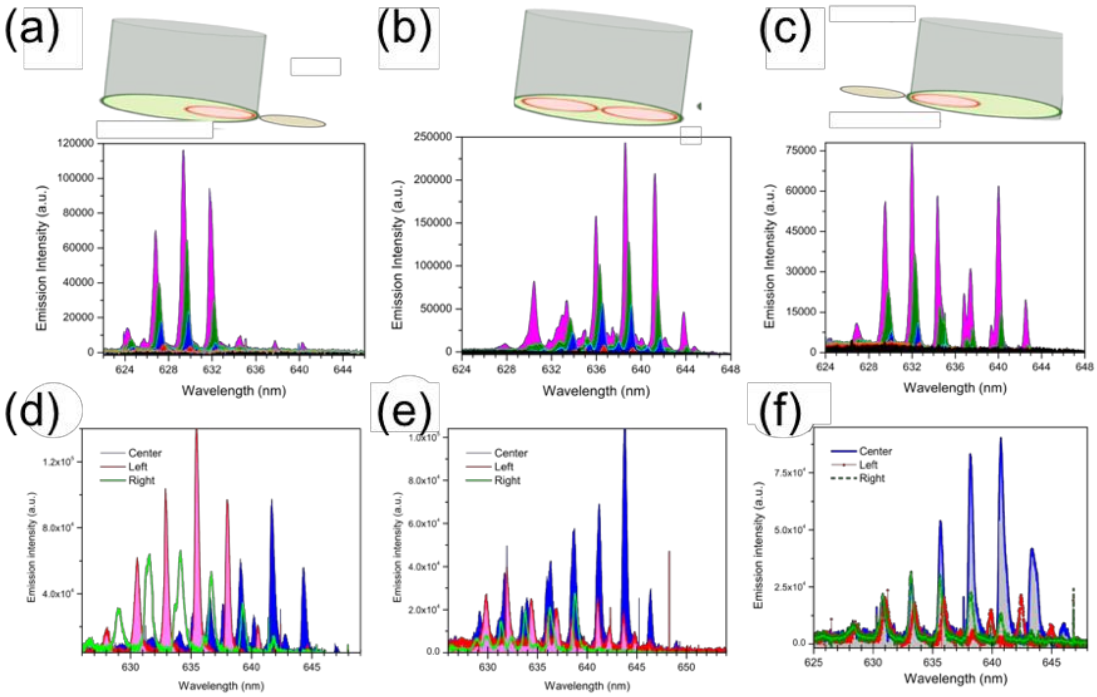

Figure 10.2 (a-c) Emission from a coupled microdisk pair pumped at various intensities where the pair is placed at different locations in the pump beam spot, such that only the left or right disk is pumped (a,c) or the pair is pumped evenly (b), as illustrated schematically. (d-f) Emission spectra from three different microdisk pairs at 116μJ/cm^2. In each figure the spectrum from the left (red), right (green) and center (blue) pump configurations is shown.

As seen in **Figure 10.2a-c**, the spectral shape is independent I_P for all three cases. Similarly, for the pumped pair, the single mode set is observed the entire time. We also point out that the threshold in the three cases is the same, although the emission intensity is stronger when both disks are pumped. The slight but persistent blue-shift with increasing I_P that we attribute to thermal modulation of the effective index n_{eff}. However, when the three spectra at the same pump intensity are overlayed as in

Figure 10.2d-f it is noticeable that the pair spectrum is red-shifted with respect to spectrum when either disk is pumped individually. These figures also confirm that the phenomenon is robust. It is observed in numerous samples and over a wide range of pump intensities. The difference between the evenly pumped and unbalanced cases is most apparent when the spectra from the isolated disks are weak, found at shorter wavelengths displaying mode splitting. In other words, the change is most dramatic when the disks have defects.

That the emission spectrum from the pair is qualitatively different from either of the constituent disks indicates the effect of evanescent coupling between the cavity modes. In the presence of coupling, we can no longer consider modes as belonging to a single disk but instead must consider the modal distribution of the coupled pair as expressed in the following set of coupled differential equations:

Equation 10.1 Equation of coupled differential equations considering the modal distribution of the coupled pair.

$$\frac{dA}{dt} = -i\omega A + g_A A + \kappa B$$

$$\frac{dB}{dt} = -i\omega B + g_B B + \kappa A$$

where A, B are the field amplitudes, $g_{A,B}$ are net modal gain (gain minus loss) and κ is the coupling between modes in Disk A and Disk B. (Solutions of the form $\psi_A = Ae^{-i\omega t}$ are assumed.) These equations yield the eigenvalues

Equation 10.2 Equation of eigenvalues that are derived from Equation 10.1.

$$\omega_{1,2} = \omega_0 + i\left(\frac{g_A + g_B}{2}\right) \pm \sqrt{\kappa^2 - (\Delta g_{AB}/2)^2}$$

where $\Delta g_{AB} = g_A - g_B$, and it is assumed that the frequencies in the absence of coupling are $\omega_A = \omega_B = \omega_0$. According to this theory, inter-cavity mode-splitting will be observed when two disks are pumped evenly, since the gain differential Δg_{AB} = 0 and the effect of the coupling strength is maximized. When one disk is pumped Δg_{AB} will localize these supermodes; their frequencies will coalesce while the linewidths bifurcate, as one experiences loss while the other gain. This has been used to implement single mode emission from multimode resonators similar to those studied in this work. We additionally remark that the *intra-cavity* mode splitting due to defects on a single, isolated disk can also be described by the same formalism, whereby κ is the coupling between clockwise and counter-clockwise propagating modes induced by scattering at the defect site.[20]

In our case, the absence of splitting when both modes are pumped equally here may be explained by a weaker apparent coupling resulting from the larger pair separation in this work such that the splitting due to the inter-disk coupling is not resolvable. However, this level of theory neglects multi-mode interactions which should be important here. Our previous characterizations revealed transient net optical gains greater than 500cm^{-1} in this system.[23] This suggests a very high gain/loss differential such that many modes will lase in PT- broken phase.[27] Still, the question remains, why is the mode splitting of the individual disks not apparent when the pair is evenly pumped? As we show below, the

presence of an exceptional point in the Hamiltonian of the system allows for intra-cavity mode splitting to be modulated through the inter-cavity coupling.

10.3.3 Spatial gain variation

A more detailed look at this behavior is provided by a spatial gain variation. In these measurements, the disk pair is swept through the beam spot in increments of $2.5\mu m$ as shown schematically on the left side of **Figure 10.3a**. The emission spectrum is then plotted versus the offset between the pump spot and the pair center. This experimental parameter, which we call ΔD_P, then becomes a proxy for the gain/loss variation between the two disks, Δg_{AB}. The evolution of the spectrum as ΔD_P goes from -$25\mu m$ to $0\mu m$ is striking. There is an abrupt change when both disks are nearly uniformly pumped. It can be seen that the long wavelength modes increase in intensity and become maximum at the center. Meanwhile, the short wavelength modes of *Disk A* decrease, *as a result of the increase in net gain of Disk B*. Continuing in the same direction we see the short wavelength modes of *Disk B* 'turn-on' not at $\Delta D_P = 0$ but emerge later as the gain in *Disk B* begins to decrease as it is moved outside the beam spot. The fluorescent images depict the emission light distribution as the sample sweeps through the pump beam. To appreciate the significance of this observation, it is important to note that as the transition is approached from either side, the disk with high gain is still entirely covered by the pump beam. Therefore, aside from some slight variations in pump homogeneity, the gain in this resonator does not change. The modes are thus seen to "turn-off'" as a consequence of the increasing gain in the latent resonator.

The “turn-off” behavior at short wavelength is reminiscent of previous work involving exceptional points in coupled lasers.[28,29] Importantly, it was theoretically predicted that observation of this behavior depends on the position of the mode in question with respect to the position of the semiconductor gain distribution. In this case, the presence of a large defect on *disk B* forces the localized modes to short wavelength, as it adds substantial loss to the long wavelength modes. However, the long wavelength modes of *Disk A* are able to cross threshold once the loss of *Disk B* is sufficiently compensated by the application of the pump. We also considered the role of a spatial variation of gain on the single disks (**Figure E.5**) and found the behavior is largely different due to absence of coupling to another disk. The results of this control experiment also suggest spatial pump inhomogeneity does not significantly alter the spectra.

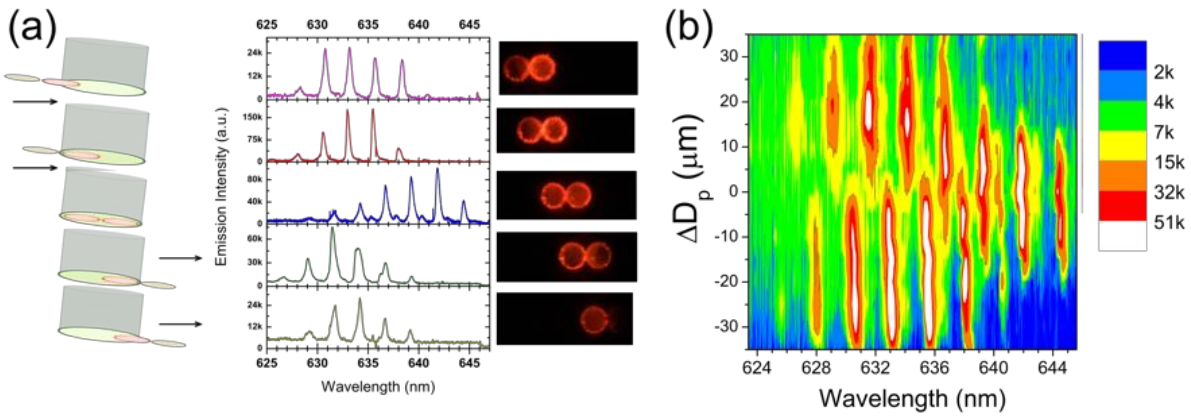

Figure 10.3 (a) Emission spectra from a coupled microdisk pair as the pair is shifted through different locations relative to the pump beam spot, as illustrated schematically to the left of each spectrum. The corresponding fluorescent images are shown to the right of each spectrum. (b) False-color contour plot of the emission intensity vs emission wavelength and the relative distance between the center of the pair to the center of the beam spot, ΔD_p.

10.3.4 Intra-cavity mode coalescence

An even more fascinating scenario arises when the neither disk has a large enough defect to force suppress the long wavelength modes. Such an example is provided in **Figure 10.4**. In this case we find that there is parasitic splitting of the modes of disk A. As ΔD_P is varied and gain is added to disk B, we find that the parasitic localized modes gradually move closer in frequency and eventually coalesce near ΔD_P = -5μm. This indeed is very surprising behavior, as the localized modes are not directly tailored by the application of gain or loss as in the previous studies of a single mode contributed from two resonators. Here, variation of gain/loss in a disk modulates the splitting between the parasitic defect modes via the evanescent coupling.

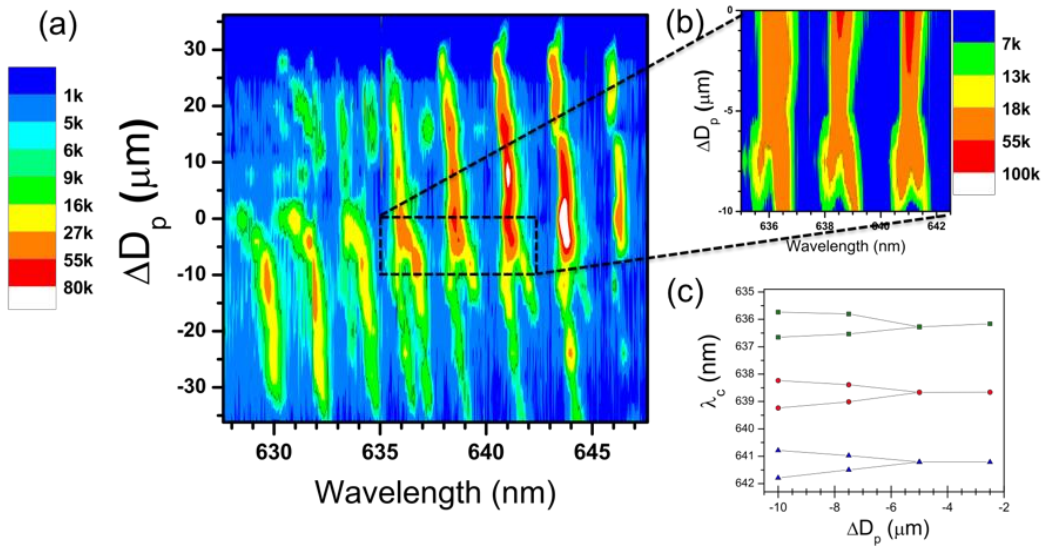

Figure 10.4 (a) E False-color contour plot of the emission intensity vs emission wavelength and ΔD_p. (b) Magnified view of the region inside the box in (a). (c) Peak positions, λ_c, vs ΔD_p for the region in (b), showing the mode coalescence.

To understand this behavior more formally, we consider solutions to the eigenvalue problem described by the following Hamiltonian:

Equation 10.3 Equation of Hamiltonian that describes the eigenvalue problem

$$\widehat{H} = \begin{pmatrix} \boldsymbol{\omega_1^{(A)} + i g_1^{(A)}} & \boldsymbol{\kappa} & \boldsymbol{\gamma_{13}} \\ \boldsymbol{\kappa} & \boldsymbol{\omega_2^{(A)} + i g_2^{(A)}} & \boldsymbol{\gamma_{23}} \\ \boldsymbol{\gamma_{13}} & \boldsymbol{\gamma_{23}} & \boldsymbol{\omega_3^{(B)} + i g_3^{(B)}} \end{pmatrix}$$

Where $\omega_{i=1,2,3}$ are the real parts and $g_{i=1,2,3}$ are the imaginary parts of the eigenfrequencies in the absence of coupling. κ is used to represent the intra-disk coupling between CW and CCW modes in the Disk A (modes 1 and 2), while γ_{ij} describes inter-disk coupling of *i*th mode of Disk A to the mode of Disk B (j=3). This is a generalization of the 2x2 Hamiltonians often considered in Non-Hermitian systems when an interaction exists between one mode from each resonator. In our case the defect-induced mode splitting produces a scenario in which three modes interact, and the resulting Hamiltonian is 3x3. Superscripts indicate in which disk the respective mode will be found in the localized case. In order to consider parameter values consistent with experiment we set $\omega_1 = \omega_2 = \omega_3 = 2.95 \times 10^{15} s^{-1}$ (640nm) and set $\kappa = 2.95 \times 10^{15} s^{-1}$ to reproduce the 0.8nm splitting observed when ΔD_P = -25μm. We simulate the portion of the experiment in which ΔD_P increases to zero by keeping $g_1 = g_2 = g$. (Disk A is entirely covered by the pump) while sweeping g_3 from $-g$ to g. As shown in **Figure 10.5a**, the experimentally observed phenomenon of intra-cavity mode coalescence can be reproduced when a large coupling anisotropy exists between mode 3 and modes 1 and 2 such that $\gamma_{23} \gg \gamma_{13}$.

More generally, we analyzed the Hamiltonian in detail to extract the characteristic behavior of eigenvalues. Shown in **Figure 10.5b**, we see that when the absolute value

of the gain differential $|\Delta g_{AB}|$ is large, the modes are localized in respective disks and the splitting is determined by the intra-cavity coupling factor of Disk A taking a value of 2κ. As $|\Delta g_{AB}|$ decreases, the splitting is reduced, showing square-root dependence on Δg_{AB} that is the signature of exceptional point behavior. At the particular value $\Delta g_{AB} = [\kappa + (\gamma_{23})^2/2\kappa]$ the eigenvalue splitting collapses to γ_{13}. Thus, when $\gamma_{13} = 0$, the eigenvalues coalesce. Note the remarkable implications of this result, as also shown in the experiment, that *the observed splitting of intra-cavity modes of Disk A depends on the gain applied to Disk B*. As $|\Delta g_{AB}|$ decreases further, another transition occurs when $\Delta g_{AB} = 2\gamma_{23}$. At this point ω_1 and ω_3 are repelled by the inter-cavity interaction and split by $2\gamma_{23}$. This transition, which is similar to the typical transition between PT-symmetric and PT-broken phases studied in other systems, is not observed in the experiment as previously noted.

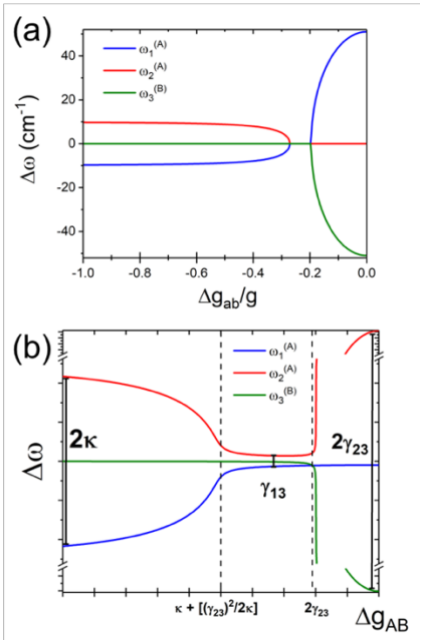

Figure 10.5 Calculated difference in eigenvalues from their uncoupled values of modes 1,2, of disk A and mode 3 of disk B vs. the gain differential between disk A and B Δg_{AB} for parameters comparable to the experiment and (b) for general values of the intradisk mode coupling κ, and inter-disk coupling γ_{13} and γ_{13}, in the limit $\gamma_{13} \ll \gamma_{23}$.

The origin the necessary asymmetry between γ_{23} and γ_{13} is not currently understood. It may result from the rapidly increasing distance between the disks for points displaced from the common equatorial axis. On the other hand, phase restrictions may prevent one mode from delocalizing across the disk pair. Considering that the results here indicate a strong potential to "heal" parasitic modes of individual disks when evanescently coupled, as well as providing a system for ultra-high sensitivity sensing based on the square-root branch topology of exceptional points [30, 31], rigorous understanding and control of such processes provide inspiration for further investigation.

10.4 Conclusions

In summary, we have studied the effect of gain/loss modulation in evanescently coupled CQD microdisks. The parasitic intra-cavity modes that result from material inhomogeneity were driven into coalescence by sweeping the system through an exceptional point. This provides a new perspective on multi-mode management in non-Hermitian optical systems and suggest a mechanism by which unwanted parasitic cavity modes can be removed from the emission output of the coupled cavity system.

10.5 Chapter acknowledgements

Youngjun Yoon and Dr. Jaehan Jung (Prof. Zhiqun Lin's research group, Georgia Institute of Technology): QD synthesis, TEM and ligand exchange. Dr. Evan Lafalce and Qingji Zeng (Prof. Valy Vardeny's research group, University of UTAH): Confocal micro PL measurement. Dr. Sidney Malak and Marcus Smith (Prof. Vladimir Tsukruk's research group, Georgia Institute of Technology): AFM and SEM.

10.6 References (Chapter 10)

1 C. M. Bender, S. Boettcher, *Phys. Rev. Lett.* **1998**, 80, 5243.

2 C. M. Bender, *Rep. Prog. Phys.* **2007**, 70, 947.

3 M. V. Berry, Quantal phase factors accompanying adiabatic changes, Proceedings of the Royal Society of London. Series A. Mathematical and Physical Sciences, **1984**.

4 W. D. Heiss, A. L. Sannino, *J. Phys. A: Math. Gen.* **1990**, 23, 1167.

5 C. Dembowski, H. D. Gräf, H. L. Harney, A. Heine, W. D. Heiss, H. Rehfeld, A. Richter, *Phys. Rev. Lett.* **2001**, 86, 787.

6 C. Dembowski, B. Dietz, H. D. Gräf, H. L. Harney, A. Heine, W. D. Heiss, A. Richter, *Phys. Rev. E* **2004**, 69, 056216.

7 S.-B. Lee, J. Yang, S. Moon, S.-Y. Lee, J.-B. Shim, S. W. Kim, J.-H. Lee, K. An, *Phys. Rev. Lett.* **2009**, 103, 134101.

8 A. Guo, G. J. Salamo, D. Duchesne, R. Morandotti, M. Volatier-Ravat, V. Aimez, G. A. Siviloglou, D. N. Christodoulides, *Phys. Rev. Lett.* **2009**, 103, 093902.

9 C. E. Rüter, K. G. Makris, R. El-Ganainy, D. N. Christodoulides, M. Segev, D. Kip, *Nat. Phys.* **2010**, 6, 192.

10 A. Regensburger, C. Bersch, M.-A. Miri, G. Onishchukov, D. N. Christodoulides, U. Peschel, *Nature* **2012**, 488, 167.

11 T. Gao, E. Estrecho, K. Y. Bliokh, T. C. H. Liew, M. D. Fraser, S. Brodbeck, M. Kamp, C. Schneider, S. Höfling, Y. Yamamoto, F. Nori, Y. S. Kivshar, A. G. Truscott, R. G. Dall, E. A. Ostrovskaya, *Nature* **2015**, 526, 554.

12 L. Feng, Y.-L. Xu, W. S. Fegadolli, M.-H. Lu, J. E. B. Oliveira, V. R. Almeida, Y.-F. Chen, A. Scherer, *Nat. Mater.* **2012**, 12, 108.

13 B. Peng, Ş. K. Özdemir, F. Lei, F. Monifi, M. Gianfreda, G. L. Long, S. Fan, F. Nori, C. M. Bender, L. Yang, *Nat. Phys.* **2014**, 10, 394.

14 L. Chang, X. Jiang, S. Hua, C. Yang, J. Wen, L. Jiang, G. Li, G. Wang, M. Xiao, *Nat. Photonics* **2014**, 8, 524.

15 H. Hodaei, M.-A. Miri, M. Heinrich, D. N. Christodoulides, M. Khajavikhan, *Science* **2014**, 346, 975.

16 L. Feng, Z. J. Wong, R.-M. Ma, Y. Wang, X. Zhang, *Science* **2014**, 346, 972.

17 H. Cao, J. Wiersig, *Rev. Mod. Phys.* **2015**, 87, 61.

18 K. J. Vahala, *Nature* **2003**, 424, 839.

19 A. M. Armani, R. P. Kulkarni, S. E. Fraser, R. C. Flagan, K. J. Vahala, *Science* **2007**, 317, 783.

20 A. Mazzei, S. Götzinger, L. de S. Menezes, G. Zumofen, O. Benson, V. Sandoghdar, *Phys. Rev. Lett.* **2007**, 99, 173603.

21 J. Zhu, S. K. Ozdemir, Y.-F. Xiao, L. Li, L. He, D.-R. Chen, L. Yang, *Nat. Photonics* **2009**, 4, 46.

22 Gaponik, N.; Hickey, S. G.; Dorfs, D.; Rogach, A. L.; Eychmüller, *Small* **2010,** *6*, 1364.

23 C. H. Lin, E. Lafalce, J. Jung, M. J. Smith, S. T. Malak, S. Aryal, Y. J. Yoon, Y. Zhai, Z. Lin, Z. V. Vardeny, V. V. Tsukruk, *ACS Photonics* **2016**, 3, 647.

24 Y. Wang, S. Yang, H. Yang, H. Sun, *Adv. Opt. Mater.* **2015**, 3, 652.

25 C. H. Lin, Q. Zeng, E. Lafalce, M. J. Smith, S. T. Malak, J. Jung, Y. J. Yoon, Z. Lin, Z. V. Vardeny, V. V. Tsukruk, *Adv. Opt. Mater.* **2017**, 5, 1700011.

26 S. T. Malak, E. Lafalce, J. Jung, C. H. Lin, M. J. Smith, Y. J. Yoon, Z. Lin, Z. V. Vardeny, V. V. Tsukruk, *J. Mater. Chem. C* **2016**, 4, 10069.

27 H. Hodaei, M. A. Miri, A. U. Hassan, W. E. Hayenga, M. Heinrich, D. N. Christodoulides, M. Khajavikhan, *Opt. Lett.* **2015**, 40, 4955.

28 M. Liertzer, L. Ge, A. Cerjan, A. D. Stone, H. E. Türeci, S. Rotter, *Phys. Rev. Lett.* **2012**, 108, 173901.

29 M. Brandstetter, M. Liertzer, C. Deutsch, P. Klang, J. Schöberl, H. E. Türeci, G. Strasser, K. Unterrainer, S. Rotter, *Nat. Comm.* **2014**, 5, 4034.

30 H. Hodaei, A. U. Hassan, S. Wittek, H. Garcia-Gracia, R. El-Ganainy, D. N. Christodoulides, M. Khajavikhan, *Nature* **2017**, 548, 187.

31 W. Chen, Ş. Kaya Özdemir, G. Zhao, J. Wiersig, L. Yang, *Nature* **2017**, 548, 192.

CHAPTER 11

GENERAL CONCLUSIONS AND BROADER IMPACT

11.1 General conclusions and discussion

Overall, the research work in this dissertation focused on understanding the fundamental light-matter interactions occurring at each level of QD photonic sources: individual and assembled nanostructures, individual and coupled optical cavities. Specifically, we focus on how the architecture and large-scale arrangement influence the optical characteristics of individual and assembled nanostructures were stressed. In addition, how the physical dimension and gain/loss modulation of optically active cavities affect the resonance and propagation characteristics were also investigated

This research work provides a scientific framework which demonstrats a comprehensive solution when designing the photonic system that requires the control of light-matter interactions including emission, gain and optical mode characteristics. Major themes present in this work include:

1. Examine, measure and investigate the quantum confinement of exciton in individual nanostructures and the coupling behavior within assembled nanostructures (large scale arrangement), aiming to precisely control the optical and lasing properties of these nanostructures;

2. Develop microfabrication methods to control spatial distribution of QD based photonic cavities to control light-matter interactions in these microscale structures, aiming to utilize these controlled interactions to design novel photonic systems;

3. Develop approaches to tailor the deformation of boundary and gain/loss contrast of cavities to alter the scattering condition and energy transfer within optical cavities, aiming to discover new optical phenomena for designing novel photonic systems.

Specific issues and challenges addressed in this study are:

(1) Identify the synthesis route of individual photonic nanostructures with specific core/shell/shell engineering that provides flexibility to tune emission, absorption and lasing properties.

(2) Examine how the large-scale arrangement of QDs can affect film properties including QD loading, refractive index, optical amplification and attenuation process.

(3) Examine how the molecular characteristic of organic ligands including ligand size, functional group and thermodynamic property can affect the chemical, mechanical, optical and lasing properties of QD films.

(4) Develop different photolithography based methods that enable the fabrication of microscale photonic structures with definable physical dimensions and geometries, leading to controllable light-matter interactions including light propagation, mode number and mode spacing.

(5) Finally, utilize optical modulation to control light-matter interactions including near-field coupling and coalescence of defect modes by altering the gain/loss values in localized regions.

Specifically, optical properties of individual QDs with different architectures generated from synthetic chemistry were measured and monitored in this study. The synthetic

chemistry to craft composition gradient shells on CdSe core surface developed by Prof. Lin's group was demonstrated to provide **suppressed re-absorption, reduced Auger recombination, and tunable Stokes shift and emission**. The first absorption peak of these QDs with the emission in visible region was suppressed due to the passivation by larger bandgap of ZnS shell with an absorption onset of 400 nm. The marked red-shift of emission peak in CdSe/$Cd_{1-x}Zn_xSe_{1-y}S_y$/ZnS QDs with the increase of shell thickness was indicative of the delocalization of electron wave function over the entire QD due to the incorporation of graded $Cd_{1-x}Zn_xSe_{1-y}S_y$ shell, leading to the continuous energy level change from CdSe to ZnS. Importantly, these QDs not only showed the tunable emission and suppressed re-absorption but also revealed the suppressed Auger recombination that is important for development of high performance lasing materials.

Next, we examined how the large-scale arrangement of QDs can be explored for dramatic enhancement of the optical properties of QD films, particularly, optical gain. **The replacement of traditional QD organic ligands with shortest ligand yields a dense QD-packing that results in a two-fold increase in optical gain.** Overall, the highly packed QD films exhibited very large net gain values (~500 cm^{-1}) which greatly exceed typical Cd-based QD films with traditional ligands. In addition, thresholds for ASE down to 50 $\mu J/cm^2$ were observed, which is exceptionally low for ns-pulse pumped QD systems. Our results confirmed a new route for obtaining high optical gain using QDs, and outlined a strategy for modifying the optical gain characteristics by ligand exchange without needing to modify the QD selection.

We then further examined how the optimization of molecular dimensions and chemical functionality of the organic ligands of QDs can be selected to improve the material processability while maintaining high optical gain. The short-chain bifunctional

crosslinker selected to tether the neighboring QDs not only significantly improved the net optical gain by allowing for a nearly 2-fold increase in QD loading but also **provided stable passivation of the QDs which imparts mechanical robustness and stability under harsh chemical environments.** The gain achieved here is up to 3-fold higher than that typically reported for traditional drop-cast QD films.

Two different photolithography based methods were developed to integrate these tiny QDs into microscale photonic cavities. The first method combined the **hybrid top-down/bottom-up approach via a pattern-assisted LbL assembly process**. During the LbL deposition, the bifunctional crosslinker was utilized to enhance the structure integrity of microdisks by tethering the neighboring Cd-based QDs. Specifically, microdisk lasers with high quality factors (within 1000–2000) were fabricated with predefined size and shape (as controlled by master templates). In addition, **the number of longitudinal cavity modes in the microdisk laser can be precisely controlled by varying the disk diameter, allowing for either near-single mode or multimode operation while preserving high quality factors.**

The second method was developed to address the chemical instability of all inorganic perovskite QDs to polar solvents, which can not be solved by using standard photolithography. Specifically, this approach involved a combination of a fluorinated polymer and solvent to provide orthogonality to the $CsPbX_3$ QD during the lift-off process. As such, it **overcame the issue of solvent constraints due to chemical instability to polar solvents while preserving the spatial precision**, thus enabling the fabrication of large-area arrays of complex patterns. Importantly, **negligible effect of this approach on the optical gain performance of $CsPbBr_3$ QD films was observed**, demonstrating their lasing properties are not compromised during processing. The optical cavity mode

activity of $CsPbBr_3$ QD microdisk lasers was readily controlled by tuning the disk size, where the mode spacing decreases while the number of modes increases with increasing disk diameter. We also demonstrated in the end the **versatility of our approach to integrate QDs with different emission signatures and composition on the same chip**.

Finally, the developed microfabrication technique was utilized to fabricate QD microdisk lasers with deformed boundary including engineered notch and ellipse. By changing the aspect ratio of these notches and ellipses, the light propagation and cavity resonance were influenced significantly, showing another useful method to **control light-matter interactions within photonic cavities by the slight arrangement of cavity boundary.** Furthermore, optical modulation was utilized to alter the gain/loss values of coupled microdisks. **The intra-cavity mode activity can be controlled by simply altering the gain/loss contrast between cavities to achieve the exceptional point** where the gain/loss contrast was modulated to meet the coupling strength between cavities.

11.2 Significance and broader impact

The scientific significance of this research work is to provide a comprehensive solution for the development in different hierarchical levels of QD photonic systems from individual nanostructures to assembled nanostructures, and to individual and coupled photonic cavities. Generally, scientific and technological approaches were utilized to provide the understanding of how the light-matter interactions can be controlled by using synthetic chemistry, large-scale arrangement, ligand functionality, cavity geometry and gain/loss modulation.

The study of the architecture of individual nanostructures revealed an effective and significant method that provides flexibility to tune the optical properties and to improve the lasing properties of QDs. Although common giant CdSe/CdS QDs also possess less reabsorption and suppressed Auger recombination, **the emission of giant CdSe/CdS QDs is limited to the red region due to the large bandgap of CdS shell. In our work, the tunable emission from blue to red region was demonstrated which is resulted from the careful design of $Cd_{1-x}Zn_xSe_{1-y}S_y$/ZnS shell structure with tunable bandgap.** This also contrasts sharply to the constant emission peak independent of ZnS thickness seen in conventional CdSe/ZnS QDs. As such, these QDs with graded architecture may offer an effective means of tailoring Stokes shift of QDs with engineered properties for applications in lasers, LEDs, solar concentrators and parity-time symmetry materials and devices.

Next, **while most of the studies in the field worked on the design of QD architecture to improve the optical gain performance, the ligand-gain relationship of QD film was rarely studied.** Thus, we reported **the first systematic study that**

demonstrated how ligand size can affect the film properties including QD loading, refractive index and optical gain and loss values significantly. The result showed a clear trend between the ligand size and optical gain/loss values where the shortest ligand can lead to one of the highest gain value (~500 cm^{-1}) in comparison to common ligand capped QD films, demonstrating the optical gain performance can be improved significantly by shortening the inter-particle distance (2-fold increase in QD packing. Overall, our finding can be an important reference for researchers in the field to design advanced photonic systems that require specific value of refractive index and the modulation of optical gain/loss values such as PT photonic systems.

Furthermore, we also studied how the selection of ligand in terms of its molecular functionality and thermodynamic properties can improve the material processability of QD films. Specifically, the short chain bifunctional crosslinker was utilized to **impart the chemical stability and mechanical robustness of QD film via the tethering of neighboring QDs, enabling the film transfer onto another substrate that can not be done for common ligand capped QD film.** In addition, the amine-functionalized ligand capped QDs showed more stable ASE intensity compared with the waxy and bulky oleic acid capped QDs. Moreover, the higher melting point and boiling point of bifunctional crosslinker in comparison to butylamine improve the long term photostability of QDs by providing a more thermally stable passivation to the QD surface, **revealing the molecular functionality can be a key factor to affect the radiative pathways of QDs**.

Importantly, we envision that **this post-synthesis modification can be applied to generally all relevant types of nanocrystal systems** such as CdSe nanoplatelets and $CsPbX_3$ perovskite QDs that are typically capped with long ligands (i.e. oleic acid) due to the common synthetic routine. As the challenges of physical and PL instabilities of QD

materials will be resolved by introduction of short functional highly bound ligands, large increases of net gain and enhanced stability can be expected. Furthermore, the robust crosslinking exploited in our work can also be used to fabricate stable freestanding optical elements with well-defined dimensions that exhibit excellent chemical resistance.

Two different photolithography based methods were presented to resolve the critical material processing issue of different type of QDs. The first method combined the optical precision of the photolithography (top-down) and the LbL deposition process (bottom-up) to fabricate large-area and robust Cd-based QD microdisk lasers. Importantly, this method mitigates limitations on the selection of active inorganic materials arising from lattice mismatch between conventional epitaxially-grown semiconducting layers. **Furthermore, it overcame issues associated with predefined size, shape, and location that commonly plague the synthesis of conventional colloidal cavities grown using traditional bottom-up approaches.** The combined advantages of bottom-up and top-down approaches allows for the effective production of large-scale arrays of QD microdisk lasers with controllable dimensions and locations, **a feat that would be otherwise difficult to achieve using either approach separately**.

Controllable cavity resonance including mode spacing and number of modes was achieved by adjusting the diameter of the fabricated mcirodisks. Such tuning **allowed for readily accessible multimode and near-single mode operation which can be useful for many researchers that are working on applications such as optical communication, particle detection, and PT symmetry studies.**[1,2,3] Moreover, the high quality factors (1000-2000) of these robust disk arrays are comparable to reported values of microdisks made of other materials, demonstrating the capability of the outlined method to tune the size of the cavity while preserving a high quality factor.[4,5,6]

In addition, **chemical crosslinking of the QDs via the bifunctional crosslinker imparts unique properties not achievable by other approaches, including mechanical robustness and chemical resistance.** These properties are essential to maintain the integrity of the structures under the harsh conditions (e.g., sonication) experienced during common patterning steps (the lift-off process) and solvent exposures. We envision that the method discussed here could be potentially applied to other types of colloidal nanocrystals such as CdSe/CdS nanorods and nanoplatelets, which, unlike QDs, possess highly polarized lasing emission.[7,8] The optical anisotropy of these nanocrystals could lead to the fabrication of interesting on-chip structures with polarized lasing output that can be advantageous for many applications.[8]

The second method we presented here aimed at overcoming the solvent constraints of all inorganic perovskite QDs in terms of the material processability. The chemical instability to polar solvents has hindered the development of lithography based methods to pattern these all inorganic perovskite QD materials into high-resolution microscale photonic structures. Since the first synthesis method reported in 2015,[9] nearly all studies have focused on the synthesis, photophysics and optoelectronic applications of $CsPbX_3$ QDs[10] while the development of patterning techniques has been comparatively few and limited in scope.[11,12] In our work, we reported **the first photolithography based method in the field** to fabricate various complicated patterns with smallest feature size down to several μm. Furthermore, the cavity resonance of fabricated microdisk lasers was readily controlled by changing the disk dimension, demonstrating the ability of this approach to pattern these photonic cavities without deteriorating their optical gain performance.

In addition, we have demonstrated the versatility of our approach to integrate QDs with different emission and composition on the same chip. Binary emission arrays with circular patterns of green-emitting $CsPbBr_3$ QD and red-emitting $CdSe/Cd_{1-x}Zn_xSe_{1-y}S_y$ QD were fabricated on the same substrate by performing our method multiple times. **The resulting pattern reaches a resolution of ~1000 ppi, a value that is higher than the resolution of the current phone displays which is typically 200-500 ppi.**[13] The level of resolution that we have achieved together with the scalable fabrication of our method may open up **new avenues in the future development of QDs based optoelectronic devices that require high-resolution micro- and nanoscale arrays with different optical and electrical functions.**

The developed lithography based method was first utilized to control light-matter interactions within photonic cavities of deformed boundary including engineered notches and ellipses. The cavity resonance was readily controlled by the aspect ratio of notches and ellipses where the **larger notches were found to suppress the defect induced modes while the coupling between cavities can be altered by the aspect ratio of ellipse significantly.** In addition, these notched and elliptical microdisk lasers were also found to possess highly directional emission output which is due to the enhanced scattering of the deformed boundary. Specifically, **different aspect ratio and arrangement of these deformed microdisks can alter the angular dependence of emission intensity significantly**. These results demonstrate the capability to control light-matter interactions effectively by slightly rearrange the cavity boundary. Importantly, our work may serve as an important example for **future development of photonic systems that require strong coupling between optical elements where the highly directional emission output can help extend the evanescent field boundary and thus enhance the coupling between cavities in specific directions.**

Finally, we studied how to control light-matter interactions in coupled microcavities by the modulation of gain/loss values in localized regions. By spatially modulate the location of the pump beam across the evanescently coupled mcirodisks, the gain/loss contrast between microdisks was significantly altered**, leading to the coalescence of doublet intra-cavity modes that result from material inhomogeneity.** This unusual behavior is rationalized via a Hamiltonian incorporating both intra-cavity coupling between CW and CCW modes as well as anisotropic inter-cavity coupling between these modes and one originating in the coupled disk.

The abovementioned Hamiltonian verifies the reason for **the observed coalesce is the presence of an exceptional point** in the system that simultaneously involves three modes and suggest a mechanism by which doublet intra-cavity modes can be suppressed from the emission output of the coupled cavity system. Importantly, this work represents **a novel approach** to adjust intra-cavity modes simply by optically modulating the gain/loss contrast of evanescently coupled microcavites. Furthermore, our research work can be an important reference for the future **development of reliable photonic systems that are more robust against the doublet intra-cavity modes which can be induced by defects generated during the fabrication process.**

11.3 General acknowledgements

Primary financial support of this work is acknowledged from the Air Force Office of Scientific Research FA9550-14-1-0037 (Synthetic Photonics Multidisciplinary University Research Initiative). QD synthesis was conducted by Prof. Lin's group with primary financial support from Air Force Office of Scientific Research FA9550-14-1-0037. Optical gain/loss measurement and confocal micro PL measurement were conducted by Prof. Vardeny's group with support from the primary funding of Air Force Office of Scientific Research FA9550-14-1-0037.

11.4 Dissemination of work

This research work has resulted in 12 scientific publications, 1 oral presentation, 5 poster presentations.

11.4.1 Publications

First author

1. **Lin, C. H.**; Smith, M. J.; Yu, S.; Tsukruk, V. V., QD Composite Materials: Synthesis, Functionalization and Microfabrication for Light Management Application. *Adv. Opt. Mater. Invited paper, In preparation*.

2. **Lin, C. H.**; Zeng, Q.; Lafalce, E.; Smith, M. J.; Yu, S.; Yoon, Y.; Chang, Y.; Jiang, Y.; Lin, Z.; Vardeny, Z. V.; Tsukruk, V. V., Large-Area Lasing and Multicolor Perovskite Quantum Dot Patterns. *Adv. Opt. Mater.* **2018***, In print.*

3. **Lin, C. H.**; Zeng, Q.; Lafalce, E.; Smith, M. J.; Malak, S. T.; Jung, J.; Yoon, Y. J.; Lin, Z.; Vardeny, Z. V.; Tsukruk, V. V., Large-Scale Robust Quantum Dot Microdisk Lasers with Controlled High Quality Cavity Modes. *Adv. Opt. Mater.* **2017**, *5*, 1700011.

4. **Lin, C. H.**; Lafalce, E.; Jung, J.; Smith, M. J.; Malak, S. T.; Aryal, S.; Yoon, Y. J.; Zhai, Y.; Lin, Z.; Vardeny, Z. V.; Tsukruk, V. V., Core/Alloyed-Shell Quantum Dot Robust Solid Films with High Optical Gains. *ACS Photonics* **2016,** *3*, 647.

Co-author

5. Zeng, Q.; Lafalce, E.; **Lin, C. H.**; Smith, M. J.; Malak, S. T.; Jung, J.; Yoon, Y.; Lin, Z.; Tsukruk, V. V.; Vardeny, Z. V., Spectral and Directional Properties of Elliptical Quantum Dot Microlasers. *Journal of Photonics for Energy,* **2018***, in print.*

6. Malak, S. T.; Yoon, Y. J.; Smith, M. J.; **Lin, C. H.**; Jung, J.; Lin, Z.; Tsukruk, V. V., Decay-to-Recovery Behavior and on–off Recovery of Photoluminescence Intensity from Core/Shell Quantum Dots. *ACS Photonics* **2017,** *4*, 1691.

7. Malak, S. T.; Liang, G.; Thevamaran, R.; Yoon, Y. J.; Smith, M. J.; Jung, J.; **Lin, C. H.**; Lin, Z.; Thomas, E. L.; Tsukruk, V. V., High-Resolution Quantum Dot Photopatterning via Interference Lithography Assisted Microstamping. *J. Phys. Chem. C* **2017,** *121*, 13370.

8. Smith, M. J.; Malak, S. T.; Jung, J.; Yoon, Y. J.; **Lin, C. H.**; Kim, S.; Lee, K. M.; Ma, R.; White, T. J.; Bunning, T. J.; Lin, Z.; Tsukruk, V. V., Robust, Uniform, and Highly Emissive Quantum Dot–Polymer Films and Patterns Using Thiol–Ene Chemistry. *ACS Appl. Mater. Interfaces* **2017,** *9*, 17435.

9. Malak, S. T.; Smith, M. J.; Yoon, Y. J.; **Lin, C. H.**; Jung, J.; Lin, Z.; Tsukruk, V. V., Programmed Emission Transformations: Negative-to-Positive Patterning Using the Decay-to-Recovery Behavior of Quantum Dots. *Adv. Opt. Mater.* **2017**, *5*, 1600509.

10. Malak, S.; Lafalce, E.; Jung, J.; **Lin, C. H.**; Smith, M. J.; Yoon, Y. J.; Lin, Z.; Tsukruk, V. V.; Vardeny, Z., Enhancement of Optical Gain Characteristics of Quantum Dot films by Optimization of Organic Ligands. *J. Mater. Chem. C* **2016**, *4*, 10069.

11. Malak, S. T.; Jung, J.; Yoon, Y. J.; Smith, M. J.; **Lin, C. H.**; Lin, Z.; Tsukruk, V. V., Large-Area Multicolor Emissive Patterns of Quantum Dot–Polymer Films via Targeted Recovery of Emission Signature. *Adv. Opt. Mater.* **2016,** *4*, 608.

12. Jung, J.; **Lin, C. H.**; Yoon, Y. J.; Malak, S. T.; Zhai, Y.; Thomas, E. L.; Vardeny, V.; Tsukruk, V. V.; Lin, Z., Crafting Core/Graded Shell–Shell Quantum Dots with Suppressed Re-absorption and Tunable Stokes Shift as High Optical Gain Materials. *Angew. Chem.* **2016,** *128*, 5155.

11.4.2 Presentations

Oral

1. **Lin, C. H.**; Zeng, Q.; Lafalce, E.; Smith, M. J.; Yu, S.; Yoon, Y. J.; Chang, Y.; Lin, Z.; Vardeny, Z. V.; Tsukruk, V. V., Large-Area Inorganic Perovskite Quantum Dot Microdisk Microlasers Enabled by Orthogonal Photolithography, *American Physical Society Spring Meeting* **2018**, *Los Angeles, California*.

Posters

1. **Lin, C. H.**; Zeng, Q.; Lafalce, E.; Smith, M. J.; Malak, S. T.; Jung, J.; Yoon, Y. J.; Lin, Z.; Vardeny, Z. V.; Tsukruk, V. V., Large-Scale Robust Quantum Dot Microdisk Lasers with Controlled Cavity Modes, *American Physical Society Spring Meeting* **2018**, *Los Angeles, California*.

2. **Lin, C.H.**; Zeng Q.; Lafalce, E.; Jung, J.; Smith, M.J.; Malak, S.T.; Aryal, S.; Yoon, Y.J.; Zhai, Y.; Lin, Z.; Vardeny, Z.V.; Tsukruk, V.V. Large-Area Robust Core/Alloyed-Shell Quantum Dot Microdisk Lasers with High Optical Gains, *Georgia Tech, Materials Science & Engineering Competition* **2017**.

3. **Lin, C.H.**; Lafalce, E.; Jung, J.; Smith, M.J.; Malak, S.T.; Aryal, S.; Yoon, Y.J.; Zhai, Y.; Lin, Z.; Vardeny, Z.V.; Tsukruk, V.V., Stable Cd-based Colloidal Quantum Dot Films with High Optical Gain in The Quasi-Continuous Wave Region. *Materials Research Society Conference* **Spring 2016**, *Phoenix, Arizona*.

4. **Lin, C.H.**; Lafalce, E.; Jung, J.; Smith, M.J.; Malak, S.T.; Aryal, S.; Yoon, Y.J.; Zhai, Y.; Lin, Z.; Vardeny, Z.V.; Tsukruk, V.V. Robust Core/Alloyed-Shell Quantum Dot Solids with High Optical Gains, *Georgia Tech, Materials Science & Engineering Competition* **2016**.

5. **Lin, C.H.**; Malak, S.T.; Ledin, P.; Jung, J.; Lin, Z.; Tsukruk, V.V. Optical Properties of Quantum Dot-Polymer Composite Films, *Georgia Tech, Materials Science & Engineering Competition* **2014**.

11.5 Reference (Chapter 11)

1 G. Agrawal, N. Dutta, *Semiconductor Lasers*, Springer, USA **1993**, pp. 74.

2 L. He, S. K. Ozdemir, J. Zhu, W. Kim, L. Yang, *Nat. Nanotechnol.* **2011**, 6, 428.

3 H. Hodaei, M.-A. Miri, M. Heinrich, D. N. Christodoulides, M. Khajavikhan, *Science* **2014**, 346, 975.

4 R. C. Polson, Z. V. Vardeny, D. A. Chinn, *Appl. Phys. Lett.* **2002**, 81, 1561.

5 W. Xie, T. Stöferle, G. Rainò, T. Aubert, S. Bisschop, Y. Zhu, F. Mahrt Rainer, P. Geiregat, E. Brainis, Z. Hens, D. Van Thourhout, *Adv. Mater.* **2017**, 29, 1604866.

6 H. Zhang, Q. Liao, X. Wang, J. Yao, H. Fu, *Adv. Opt. Mater.* **2016**, 4, 1718.

7 Y. Gao, V. D. Ta, X. Zhao, Y. Wang, R. Chen, E. Mutlugun, K. E. Fong, S. T. Tan, C. Dang, X. W. Sun, H. Sun, H. V. Demir, *Nanoscale* **2015**, 7, 6481.

8 M. Li, M. Zhi, H. Zhu, W.-Y. Wu, Q.-H. Xu, M. H. Jhon, Y. Chan, *Nat. Commun*. **2015**, 6, 8513.

9 L. Protesescu, S. Yakunin, M. I. Bodnarchuk, F. Krieg, R. Caputo, C. H. Hendon, R. X. Yang, A. Walsh, M. V. Kovalenko, *Nano Lett.* **2015**, 15, 3692.

10 E. Yassitepe, Z. Yang, O. Voznyy, Y. Kim, G. Walters, J. A. Castañeda, P. Kanjanaboos, M. Yuan, X. Gong, F. Fan, J. Pan, S. Hoogland, R. Comin, O. M. Bakr, L. A. Padilha, A. F. Nogueira, E. H. Sargent, *Adv. Funct. Mater.* **2016**, 26, 8757.

11 F. Palazon, Q. A. Akkerman, M. Prato, L. Manna, *ACS Nano* **2016**, 10, 1224.

12 J. Chen, Y. Wu, X. Li, F. Cao, Y. Gu, K. Liu, X. Liu, Y. Dong, J. Ji, H. Zeng, *Advanced Materials Technologies* **2017**, 2, 1700132.

13 Y. Takubo, Y. Hisatake, T. Lizuka, T. Kawamura, *SID Symposium Digest of Technical Papers* **2012**, 43, 869.

Appendix A

Chapter 5 supporting data

(ENHANCEMENT OF OPTICAL GAIN CHARACTERISTICS OF QUANTUM DOT FILMS BY ORGANIC LIGAND SHELL)

Table A.1: Table of the optical properties of the QDs before and after the ligand exchange process. A reduction in quantum yield typically occurs after ligand exchange. The reduction in QY is likely due to a decrease in the passivation of surface bonds that can occur when oleic acid is removed and replaced with the amine ligands. The absorbance and emission profiles are similar before and after the ligand exchange procedure.

	Oleic-acid	Hexadecylamine	Octylamine	Butylamine
QY (%)	50	50	20	29
ABS_{1s} (nm)	614	614	617	617
Emission Position (nm)	624	624	624	623
FWHM (nm)	32	34	31	30

Table A.2: Table of the predicted stimulated emission lifetime of the ligand-QD films based on the measured refractive index and optical gain values of the QD films. The predicated stimulated emission lifetime was calculated using Eq. A2.

QD-ligand	Predicted Stimulated Build-Up Time (ps)
Oleic acid	94
Hexadecylamine	26
Octadecylamine	12
Butylamine	12

Table A.3: Table of the QD-loading (%) of the QD films, the QD volume fraction (%) of the QD solutions (determined by ellipsometry and TGA, respectively), and the thermodynamic properties of each ligand.[1]

QD-ligand	Film QD-loading (%)	Solution QD-loading (%)	Solution-Film Difference (%)	Vapor Pressure, 25C (mmHg)	Boiling Point (°C)
Oleic acid	29	27	2	0	360
HDA	34	31	3	0	330
OctA	45	30	15	0.9	175
BA	49	33	16	82	78

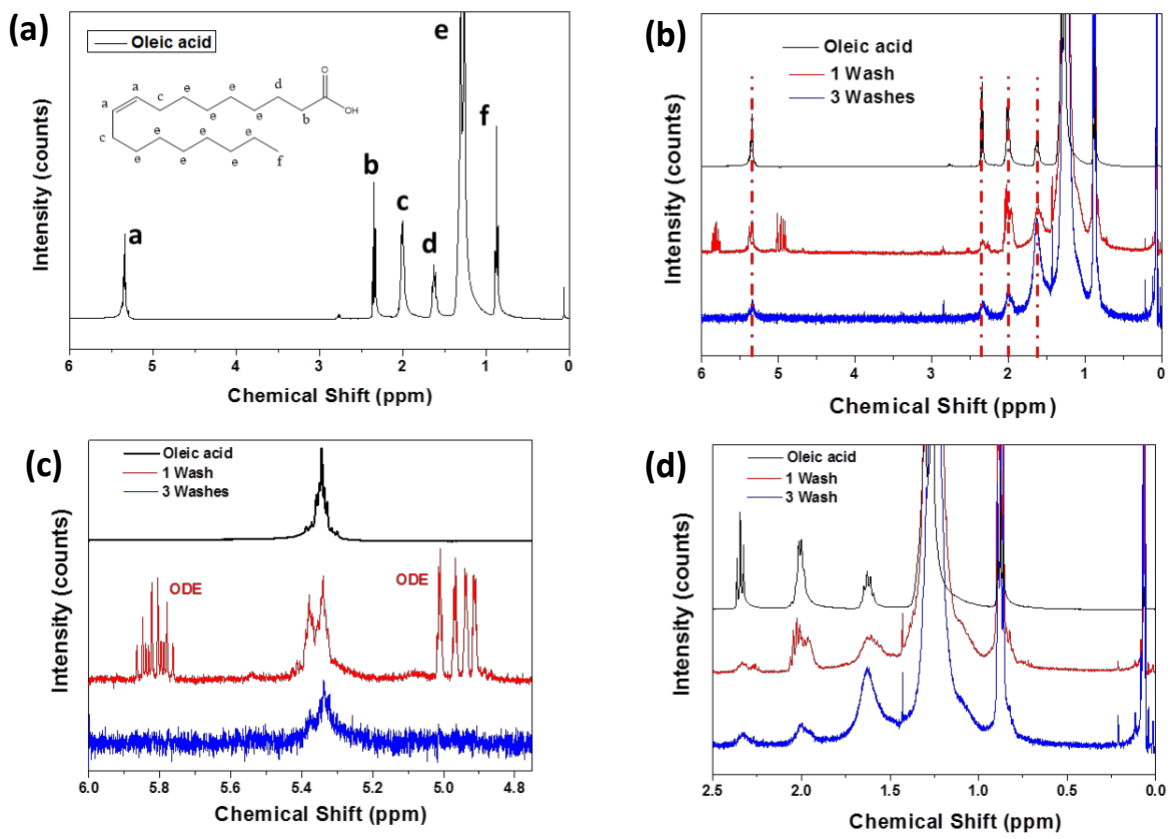

Figure A.1: NMR was used to evaluate the effect of washing the ODE/oleic acid capped QDs before the ligand exchange. (a) NMR of oleic acid. (b) NMR of oleic acid capped QDs at different points during the washing process. Examination of the 4.7-6 ppm regions shows (c) that the ODE peaks disappear and that the peak near 5.35 ppm assigned to vinylic hydrogens broadens, indicating removal of excess free oleic acid. (d) Close-up of the 2.5-0 ppm region shows broadening of the 1.6, 2.0, and 2.3 ppm peaks after successive washing.

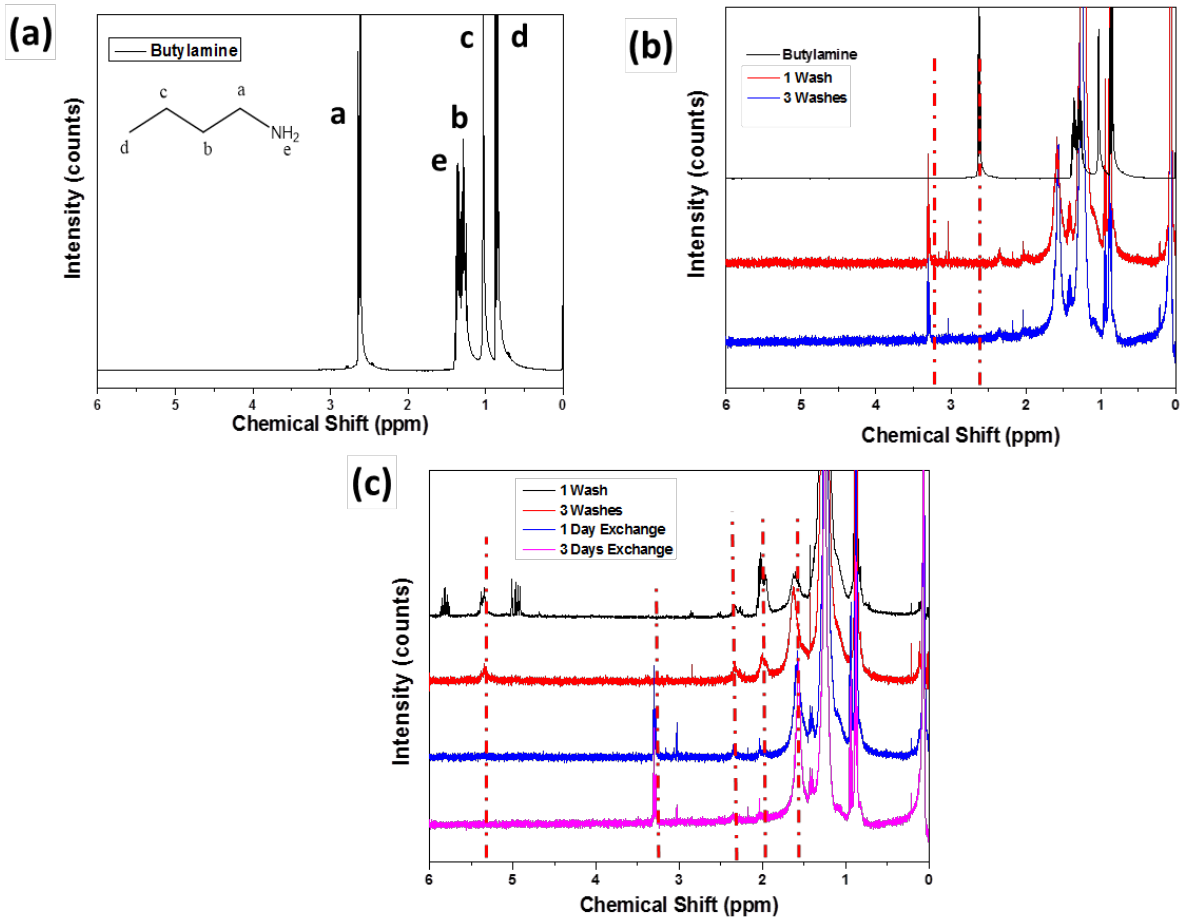

Figure A.2: NMR was used to evaluate the efficiency of the ligand exchange. (a) NMR of butylamine (the ligand that will be displacing oleic acid on the QD surface). (b) NMR of butylamine and of QDs that underwent a ligand exchange from oleic acid to butylamine. The BA peak at 2.8 ppm (hydrogen peak) shifts to 3.2 ppm which is likely due to interaction with QD surface. (c) Comparison of NMR from different points in the washing process and ligand exchange process.

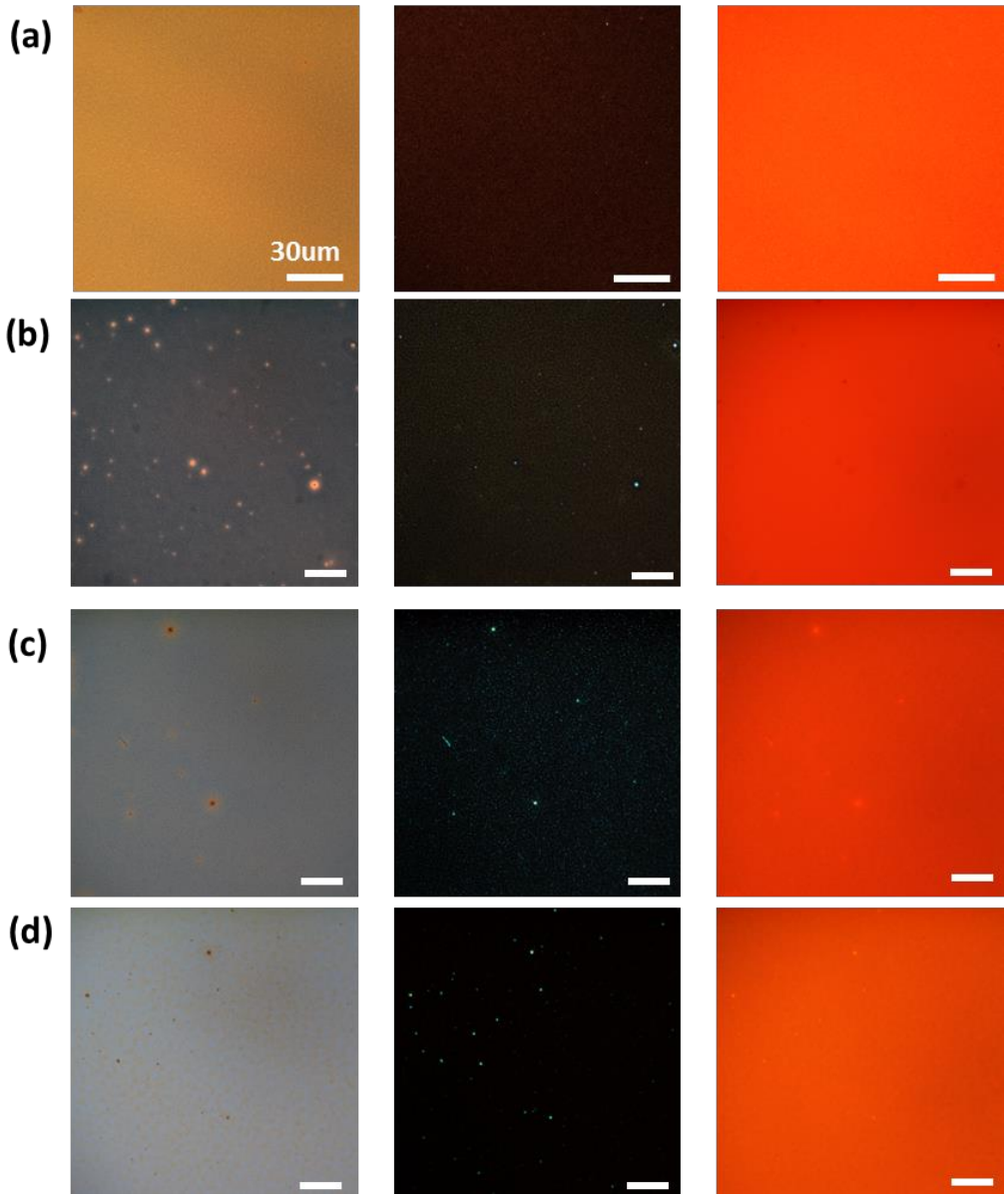

Figure A.3: Bright field (column 1), dark field (column 2), and fluorescence (column 3) images of (a) oleic acid, (b) hexadecylamine, (c) octylamine, and (d) butylamine capped QD films. Imaging shows that the films exhibit similar uniform morphology and fluorescence emission as well as some scattering due to surface defects. All scale bars are 30 um.

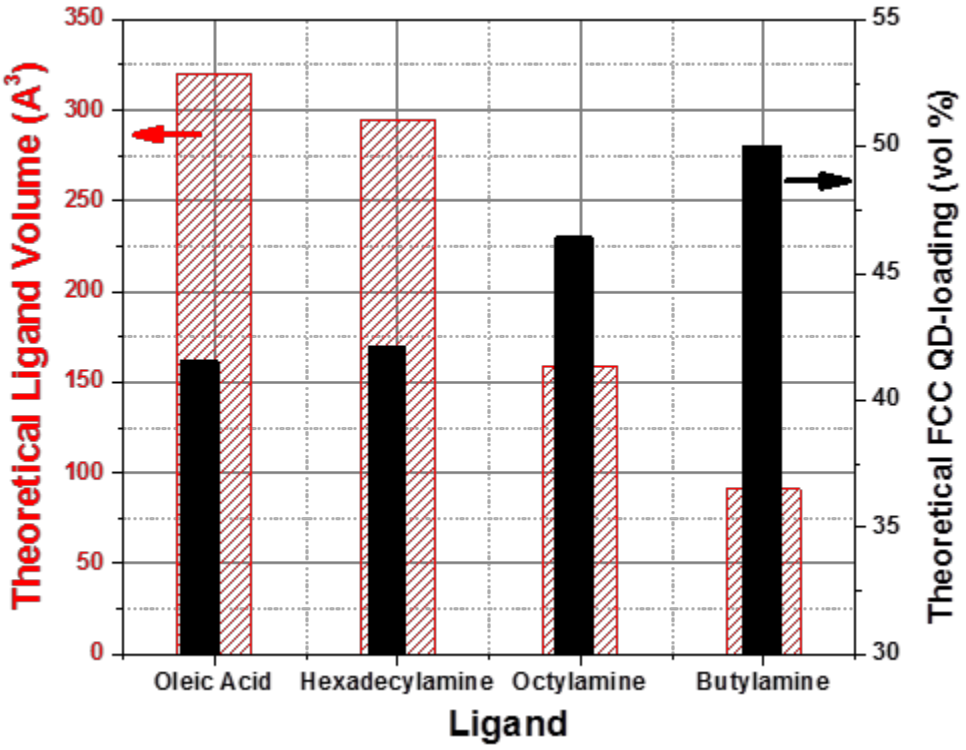

Figure A.4: Plot of the predicted free volume of each QD ligand and the corresponding maximum theoretical FCC QD-packing density (assuming diameter of 8 nm). Reducing the size of the ligand leads to a larger maximum FCC packing for the QDs in the film (and vice versa).

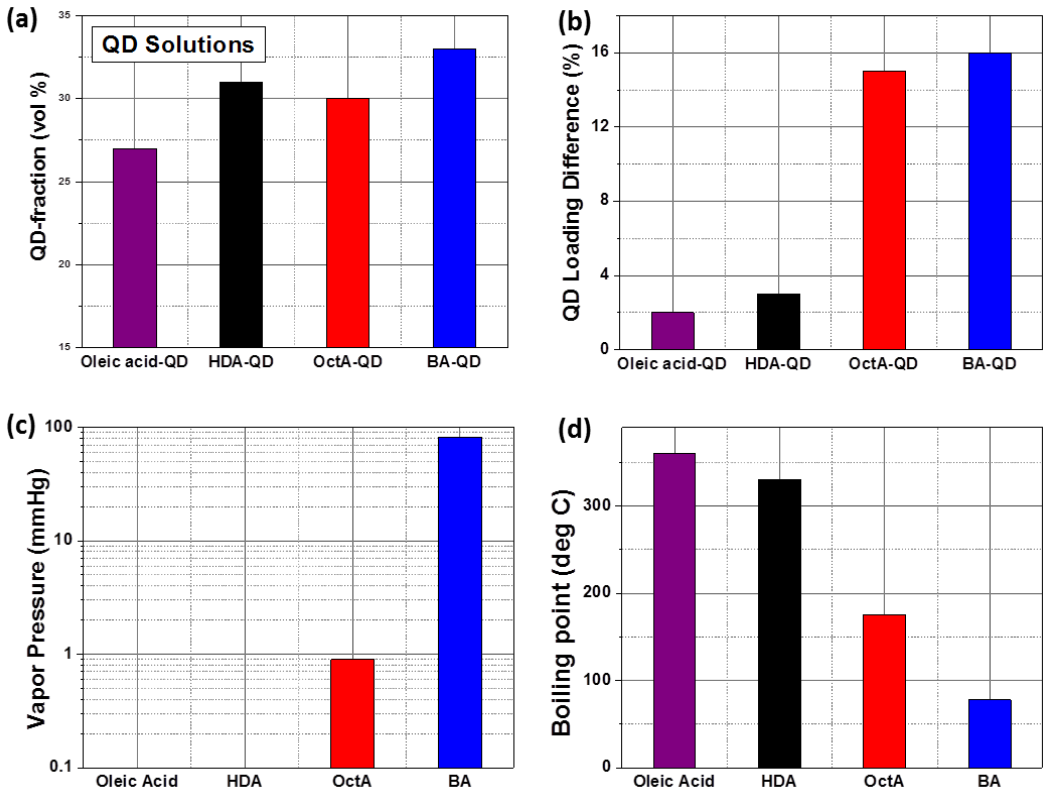

Figure A.5: Examination of the QD fraction in solutions and how it compares to QD films. (a) Thermogravimetric analysis (TGA) of QD solutions. (b) The difference in QD volume fraction between QD films and the QD solutions. The (c) vapor pressure and (d) boiling point of each ligand. Note, the vapor pressure of oleic acid and hexadecylamine area very low at room temperature (< 1 mmHg) and therefore were approximated to have a zero value.

There appears to be a difference of QD volume fraction between the QD films and QD solutions. The magnitude of this difference correlates with the volatility of the specific ligand. For example, butylamine-QDs, which display the largest difference between the film state (49 ±6%) and solution state (33%) also is the most volatile ligand (highest vapor pressure, lowest boiling point). Note, value ranges are one standard deviation in the film state (29 ±6%) and solution state (27%) is the least volatile (lowest vapor pressure (V_p), highest boiling point). This trend occurs for all ligands examined (**Table A.3)**.

The volatility of the ligand is an important factor affecting the formation of the film during spin-casting and storage. The volatility of the QD ligand has been shown to strongly impact ligand desorption, with a highly volatile ligand (pyridine, V_p = 20 mmHg at 25°C) showing large desorption (≈70%) under ambient conditions while a low volatility ligand (trioctylphosphine oxide, V_p ≈ 0 mmHg at 25°C) shows nearly no desorption.[1,2,3] Therefore, the high volatility of butylamine and octylamine leads to some degree of desorption from the film during storage. Even more importantly, the volatile ligands will experience strong desorption from the film surface during spin-casting (unbound ligands in particular) due to the highly turbulent atmosphere above the film. These two factors thus increase the QD volume fraction and lead to a large difference between the QD volume fraction measured in the film state and solution state.

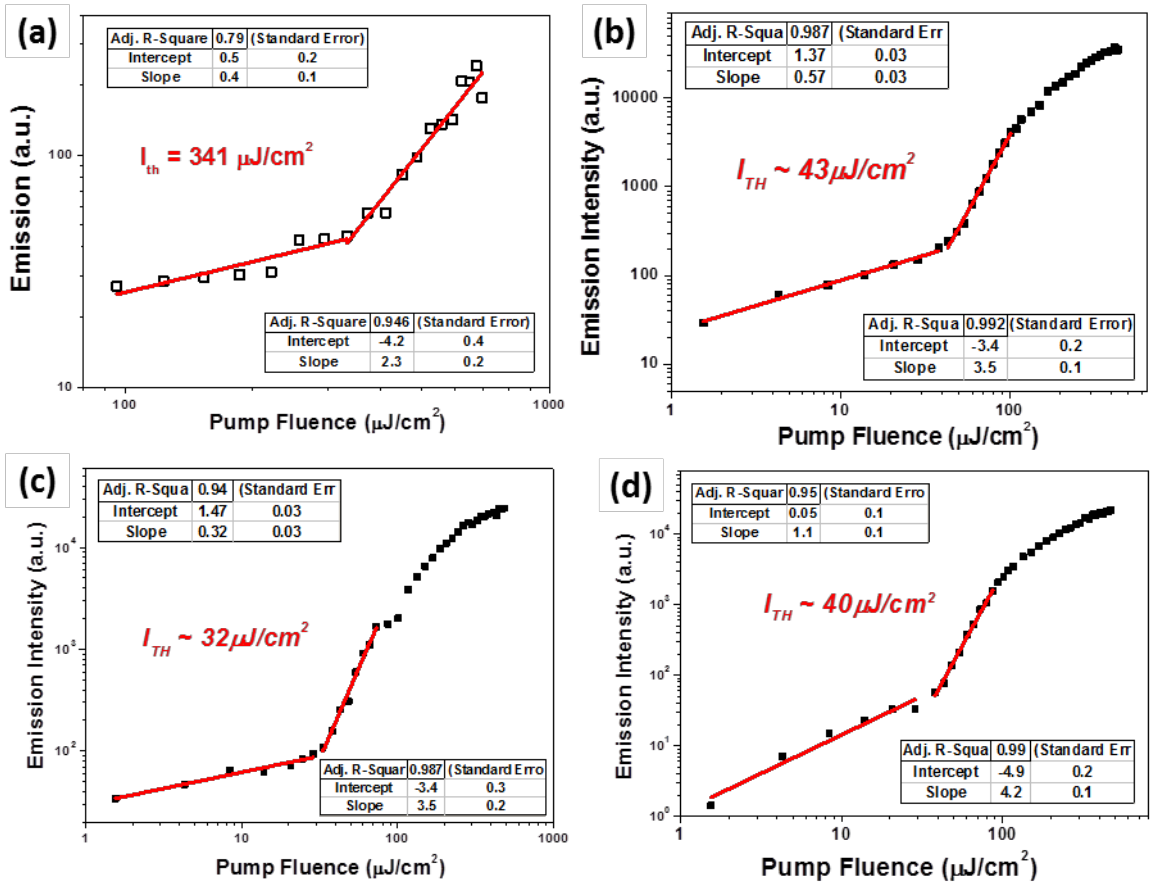

Figure A.6: ASE threshold plots and fitting for different QD-ligand combinations. The threshold value of the QD film is determined by linear fitting of the shallow and steep pump fluence versus emission curve. The pump fluence value at the intersection of the linear fit from the two regions is the threshold fluence. Examples of threshold determination are shown for (a) oleic acid-QD, (b) HDA-QD, (c) OctA-QD, and (d) BA-QD films.

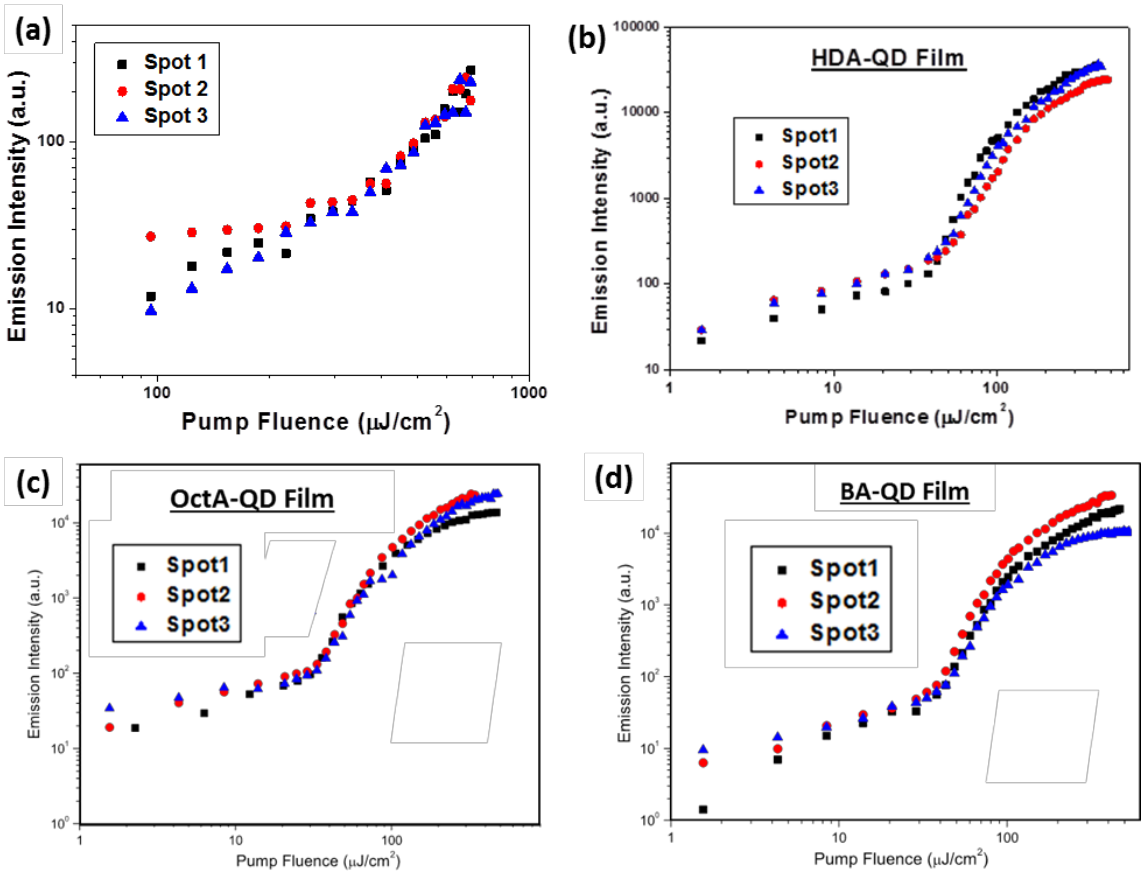

Figure A.7: ASE threshold plots for different QD-ligand combinations from multiple spots. The threshold behavior of the QD films was determined by examining how the pump fluence affects the emission intensity. A transition from a shallow slope to a steep slope indicates an ASE threshold. The threshold behavior for each type of QD film was verified over multiple trials. Examples of threshold examination are shown for (a) oleic acid-QD, (b) HDA-QD, (c) OctA-QD, and (d) BA-QD films.

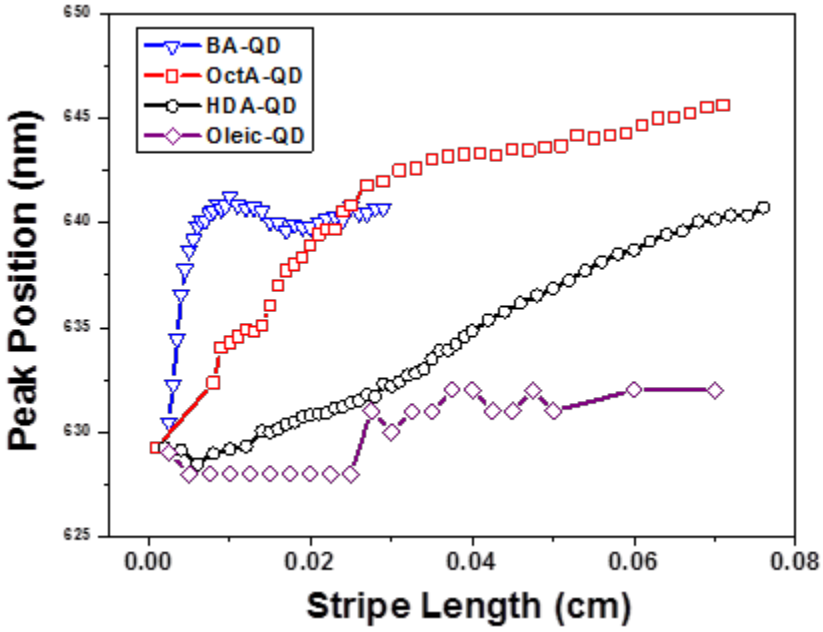

Figure A.8: Peak position of the maximum emission peak versus pump strip length. The presence of ASE is supported by examining a number of parameters including a shift of the ASE peak with respect to the PL peak. Typically the ASE peak red-shifts compared to the PL peak due to reabsorption of the emitted light by the film.[4] All the QD films with amine functionalization in this study exhibited a red-shift of approximately 10-15 nm compared to the PL peak, while the oleic-QD film show a red-shift of only 4 nm, indicating a smaller amount of reabsorption during light propagation.

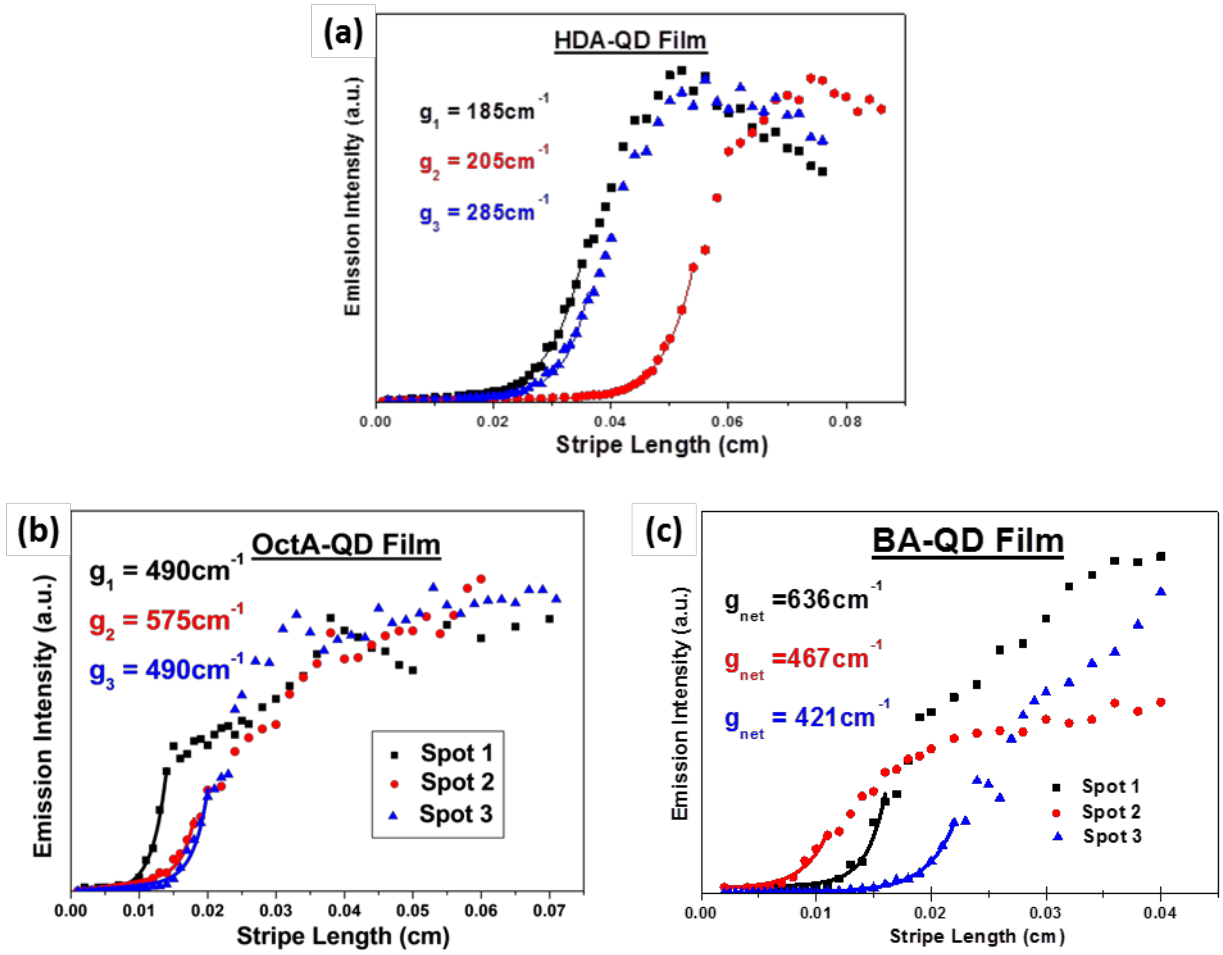

Figure A.9: Data of the emission intensity versus pump strip length from the variable stripe length (VSL) method for various QD-ligand combinations. The optical gain of the QD films was determined by fitting data from the VSL method with an exponential function. The gain value for each type of QD film was determined by averaging over multiple trials. Examples of VSL data and fitting are shown for (a) HDA-QD, (b) OctA-QD, and (c) BA-QD films.

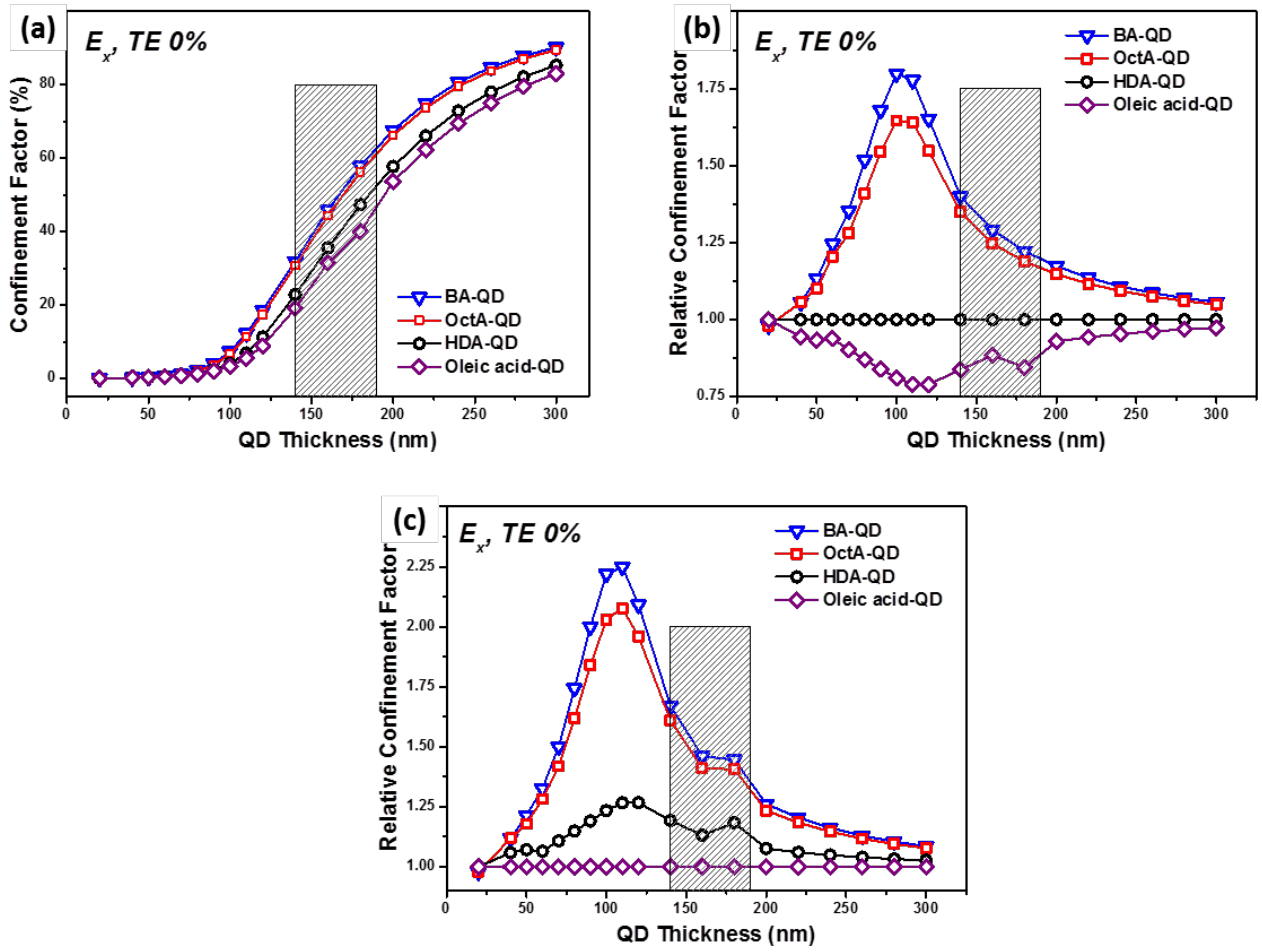

Figure A.10: (a) Plot of the confinement factor (Ex, TE 0% mode) at 635 nm for films of different thickness and different refractive index. The relative confinement factor of each film compared to (b) the HDA-QD film and compared to (c) the oleic-QD film. The confinement factor is higher (for a given film thickness) for films with a higher refractive index. The grey shaded areas represent typical QD film thicknesses in this study.

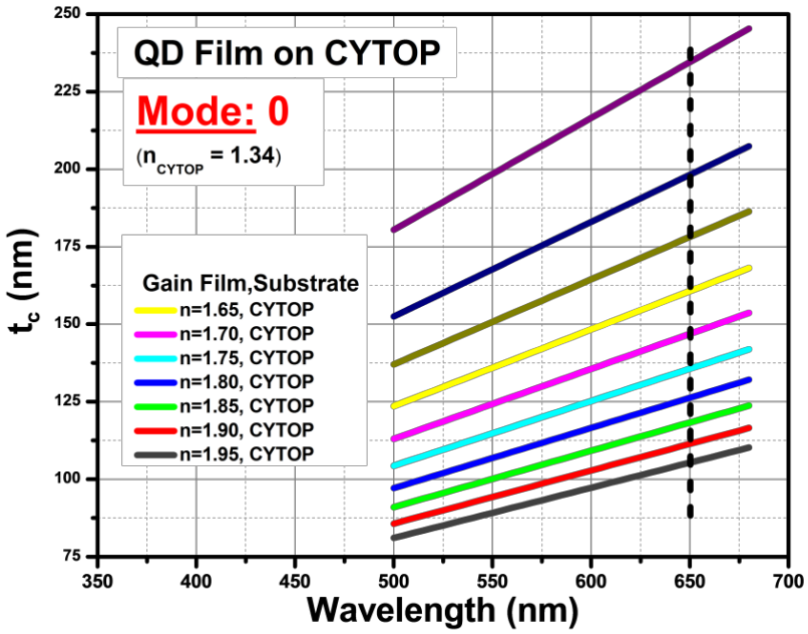

Figure A.11: Plot of the critical thickness for the primary waveguiding mode for QD films with different refractive index on a CYTOP film (refractive index of 1.34). The critical thickness indicates the minimum thickness a film requires in order to support at least one waveguide mode. The function used to calculate the critical film thickness (t_c) assumes that the top layer is air.[5] Each film has a thickness that allows for only one waveguide mode.

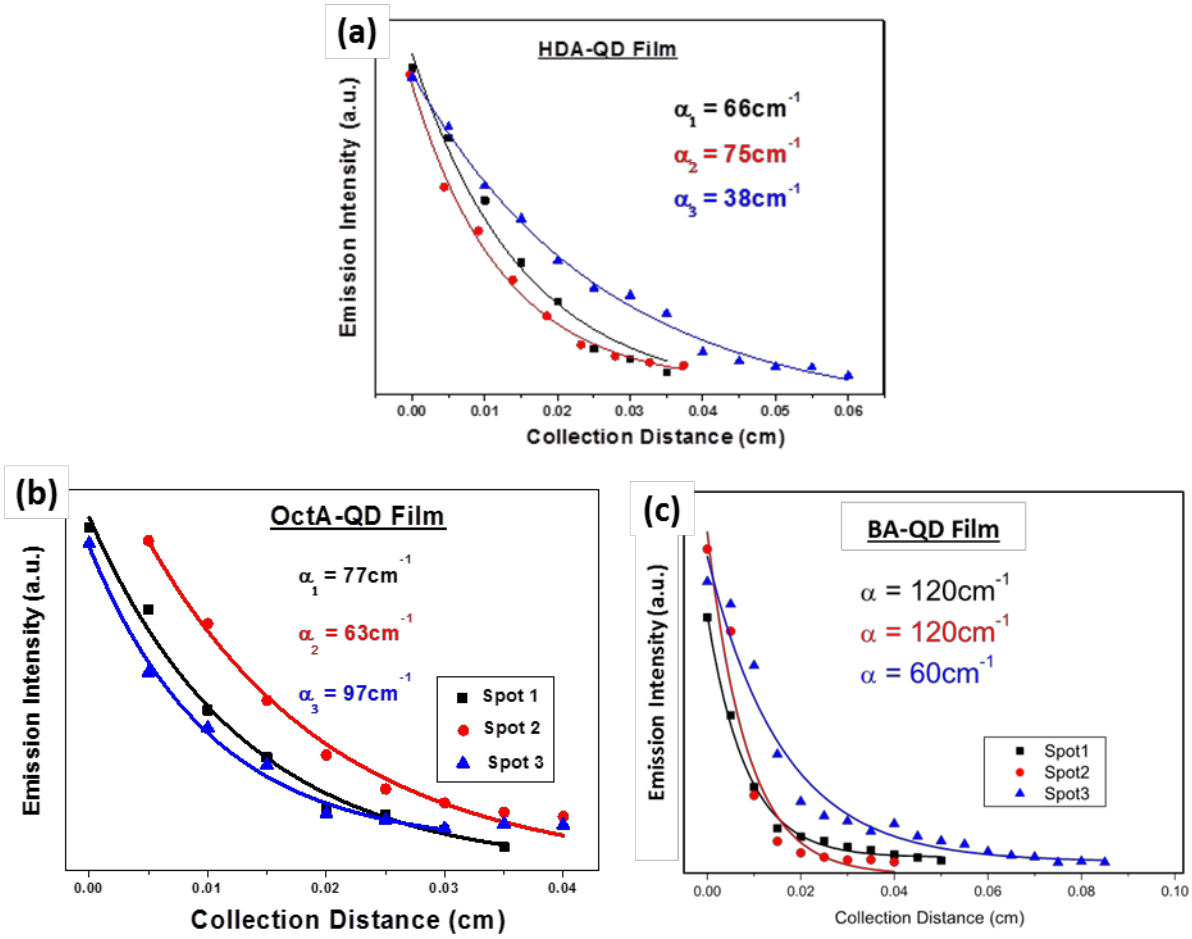

Figure A.12: Plots of optical loss data and fitting for various QD-ligand combinations. The optical loss of the QD films was examined by altering the distance the emission travels through the QD film before reaching the edge of the film. The optical loss value is determined by fitting the data with an exponential decay function. The loss value for each type of QD film was determined by averaging over multiple trials. Examples of loss data and fitting are shown for (a) oleic acid-QD, (b) HDA-QD, (c) OctA-QD, and (d) BA-QD films.

Eq. A.1: Equation outlining the various factors that influence the optical gain magnitude in QD films.[6]

$$G = \frac{\sigma_g \xi}{V_{dot}}$$

Where,
G = gain value
σ_g = gain cross-section
ξ = packing fraction
V_{dot} = volume of QD

Eq. A.2: Equation outlining the various factors that influences the stimulated emission lifetime in QD films.[6]

$$\tau_{SE} = \frac{n_r V_{dot}}{c \sigma_g \xi}$$

Where,
τ_{SE} = Stimulated emission build up time
c = speed of light
G = gain value
n_r = effective refractive index
V_{dot} = volume of QD
ξ = packing fraction
σ_g = gain cross-section

References

1 Sigma-Aldrich, ChemSpider, and Chemicalize for measured and theoretical thermodynamic data and geometry data for butylamine, octylamine, hexadecylamine, oleic acid, trioctylphosphane oxide, and pyridine.

2 B.S. Kim, L. Avila, L.E. Brus, I.P. Herman, *Appl. Phys. Lett.* 2000, **76,** 3715-3717.

3 D.I. Kim, M.A. Islam, L. Avila, I.P. Herman, *J. Phys. Chem. B* 2003, **107,** 6318-6323.

4 S. Yakunin, L. Protesescu, F. Krieg, M.I. Bodnarchuk, G. Nedelcu, M. Humer, G. De Luca, M. Fiebig, W. Heiss, M.V. Kovalenko, *Nat. Comm.* 2015, **6,** 8056-8056.

5 Robert G. Hunsperger, "Integrated Optics, Theory and Technology" (DOI 10.1007/b98730). Springer New York, **2009.** Chapter 2 .Optical Waveguide Modes.

6 S. Hoogland, Optical gain and lasing in colloidal quantum dots, Colloidal Quantum Dot Optoelectronics and Photovoltaics. *Cambridge University Press:* **2013.**

Appendix B

Chapter 6 supporting data

(CORE/ALLOYED-SHELL QUANTUM DOT ROBUST SOLID FILMS WITH HIGH OPTICAL GAINS)

Table B.1 Thermodynamic properties and refractive index of ligands used in this study. Large differences in thermodynamic properties between BA and DIAH leads to a plausible different behavior when they are capped on the QD surface. BA has a free-state melting point (-49 ℃) significantly lower than room temperature, likely causing BA to be in a fluid-like state at room temperature even when bound on the QD surface. Furthermore, BA has a high vapor pressure (68 mmHg at 20℃) which indicates that BA experiences desorption upon exposure to air. On the other hand, DIAH has a much higher melting point (26-29℃) and lower vapor pressure (<1 mmHg at 25℃) than BA, yielding a more solid, physically stable QD film under ambient conditions.

Capping Agent	M_p (°C)	B_p (°C) (760mmHg)	V_p (mmHg) (25°C)	n (at 589.3nm, 20°C)
1,7-Diaminoheptane (DIAH)	28	224	<1	1.461
Butylamine (BA)	-49	78	68 (20°C)	1.401
Oleic acid (OA)	14	360	<1	1.459

Table B.2 The refractive indices of QD films. The QD-loading was calculated using the effective medium Bruggeman model.[1]

QD film	n	Calculated QD Loading
DIAH-tethered QD	1.90	49%
BA-capped QD	1.91	53%
OA-capped QD	1.69	27%

Table B.3 The FTIR results showing the ratios of peak areas for different vibrational modes. Both ratios of asymmetric and symmetric (CH_3/CH_2) peak areas decreased dramatically during the crosslinking process, indicating that a substantial amount of butylamine was replaced with 1,7 diaminoheptane.

QD film	**$(CH_3/CH_2)_{as}$**	**$(CH_3/CH_2)_s$**
BA-QD	0.334	0.739
OA-QD	0.072	0.243

Table B.4 The optical properties of the OA and BA capped QDs that are dispersed in chloroform.

QD solution	absorption peak (nm)	Emission peak (nm)	Stoke shift (nm)	FWHM (nm)	Quantum yield (%)
OA-QD	610	620	10	34	49.6
BA-QD	610	621	11	35	52.3

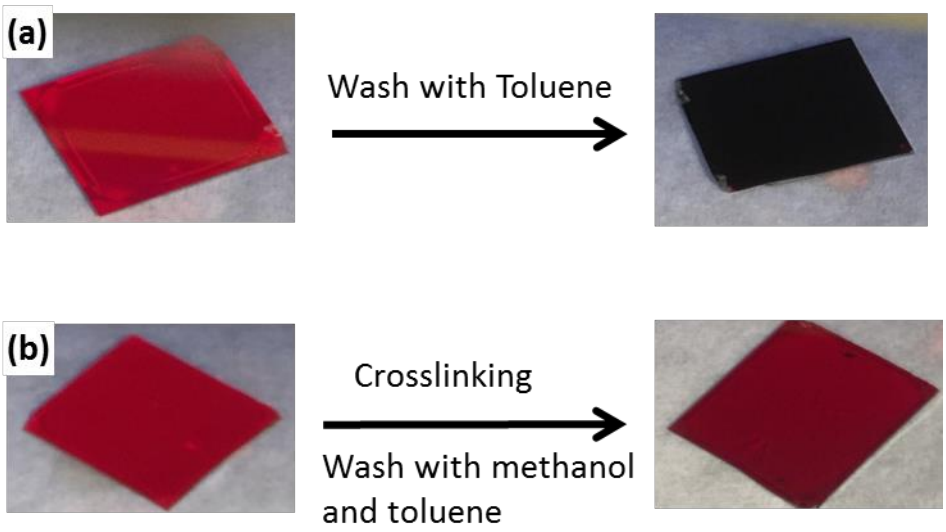

Figure B.1 The crosslinking process provides chemical resistance to both polar (methanol) and nonpolar solvent (toluene/heptane). (a) QD films capped with commonly used ligands such as oleic acid and butylamine would be dissolved after washing with toluene three times (a). The sample shown here is the QD film capped with oleic acid. (b) Crosslinked QD films maintain their photoluminescence after multiple washes with toluene and methanol.

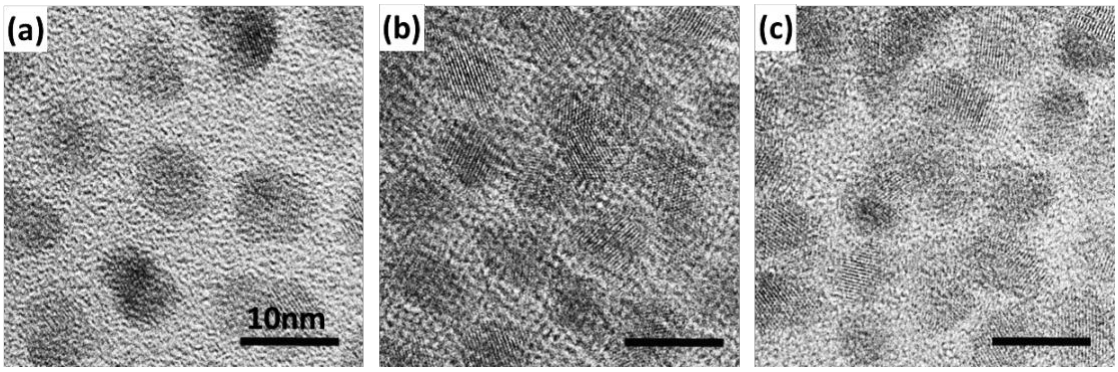

Figure B.2 High-resolution transmission electron microscopy (HR-TEM) images of QDs that are capped with (a) oleic acid, (b) butylamine, and (c) 1,7 diaminoheptane. All scale bars are 10 nm.

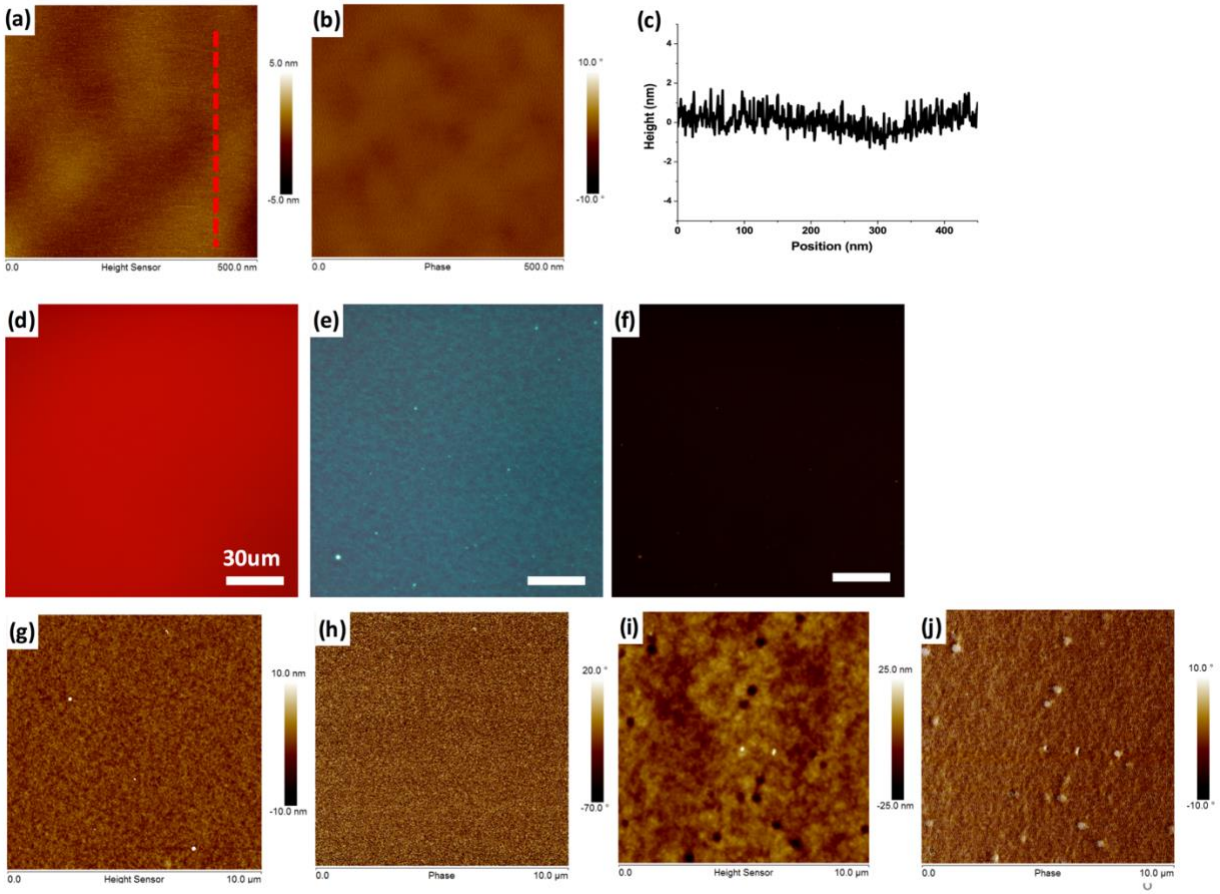

Figure B.3 AFM and optical microscopy images (500nm x 500nm) of the BA-capped QD film: AFM scans of (a) height, (b) phase, and (c) height cross-section for the BA-capped capped QD film. Fluorescence imaging shows uniform emission of large areas (d), while bright field (e) and dark field (f) optical micrographs show uniform morphology with minimal physical defects. All scale bars are 30µm. Large area AFM images (10µm x 10µm) of the DIAH-tethered and BA-capped QD film: AFM scans of (g) height, (h) phase for the DIAH-tethered QD film and (i) height, (j) phase for the BA-capped QD film.

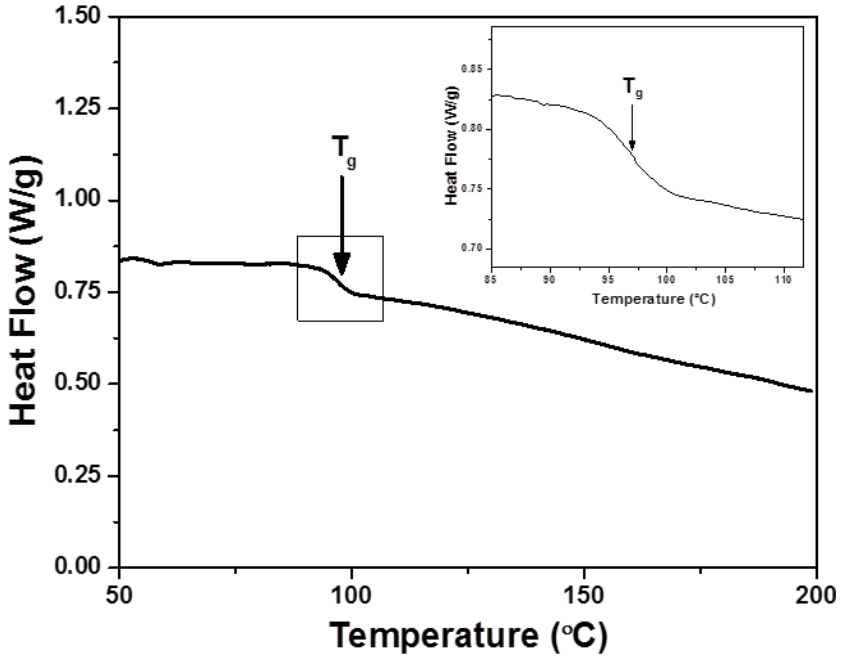

Figure B.4 DSC of the DIAH crosslinked QD films with a glass transition near 97°C (inset).

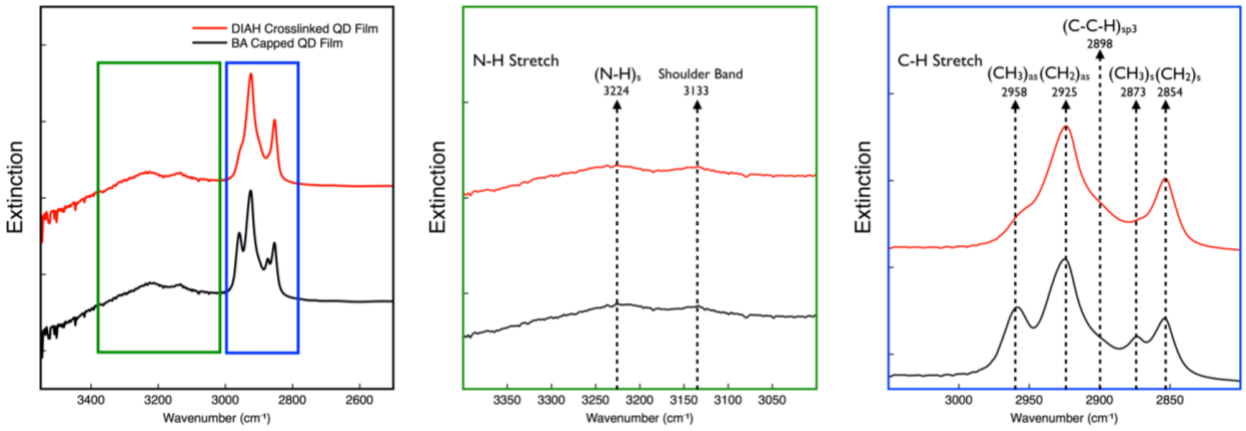

Figure B.5 (a) FTIR spectra from 2500 cm^{-1} to 3500 cm^{-1} for crosslinked DIAH QD film (red line) and BA capped QD film (black line). The C-H stretching band (blue frame) shows the decreased CH_3 asymmetric and symmetric stretching peaks during the solid-exchange ligand exchange process while the N-H stretching band (green frame) remains similar. (b) Magnification of the N-H stretching band region. The assigned peaks are symmetric N-H stretching at 3324 cm^{-1} and shoulder band at 3133 cm^{-1}, respectively. (c) Magnification of the C-H stretching band. The assigned peaks are asymmetric and symmetric CH_3 stretching peaks at 2958 cm^{-1} and 2873 cm^{-1}, asymmetric and symmetric CH_2 stretching peaks at 2925 cm^{-1} and 2854 cm^{-1} and C-C-H peak at 2898 cm^{-1}, respectively. [2,3]

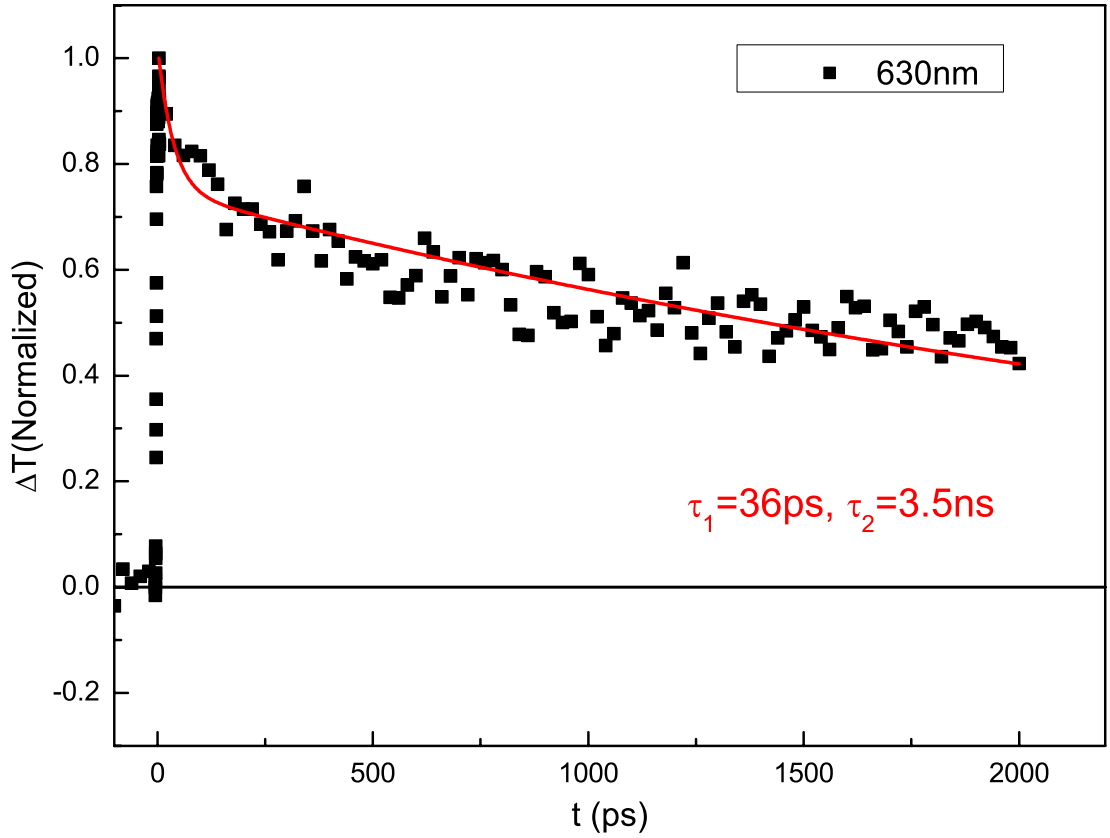

Figure B.6 Transient absorption dynamic at 630 nm for a CdSe/Cd1-xZnxSe1-ySy QD film. The positive sign of the signal indicates that this feature is due to photo-bleaching (PB) of the ground state absorption. The dynamics are adequately described by a bi-exponential fitting, with two distinct lifetimes of 36 ps and 3.5 ns. The amplitudes associated with these decay times are 0.2 and 0.8 respectively. The complex decay mechanisms possibly include surface trapping, Auger recombination, and radiative recombination as well as possible overlap with the PB due to biexcitons.[4] The data indicates that a substantial fraction of the exciton population survives on the time scale of several ns. For QD's of this size, 36 ps is much shorter than expected for Auger decay and is possibly related to other processes.

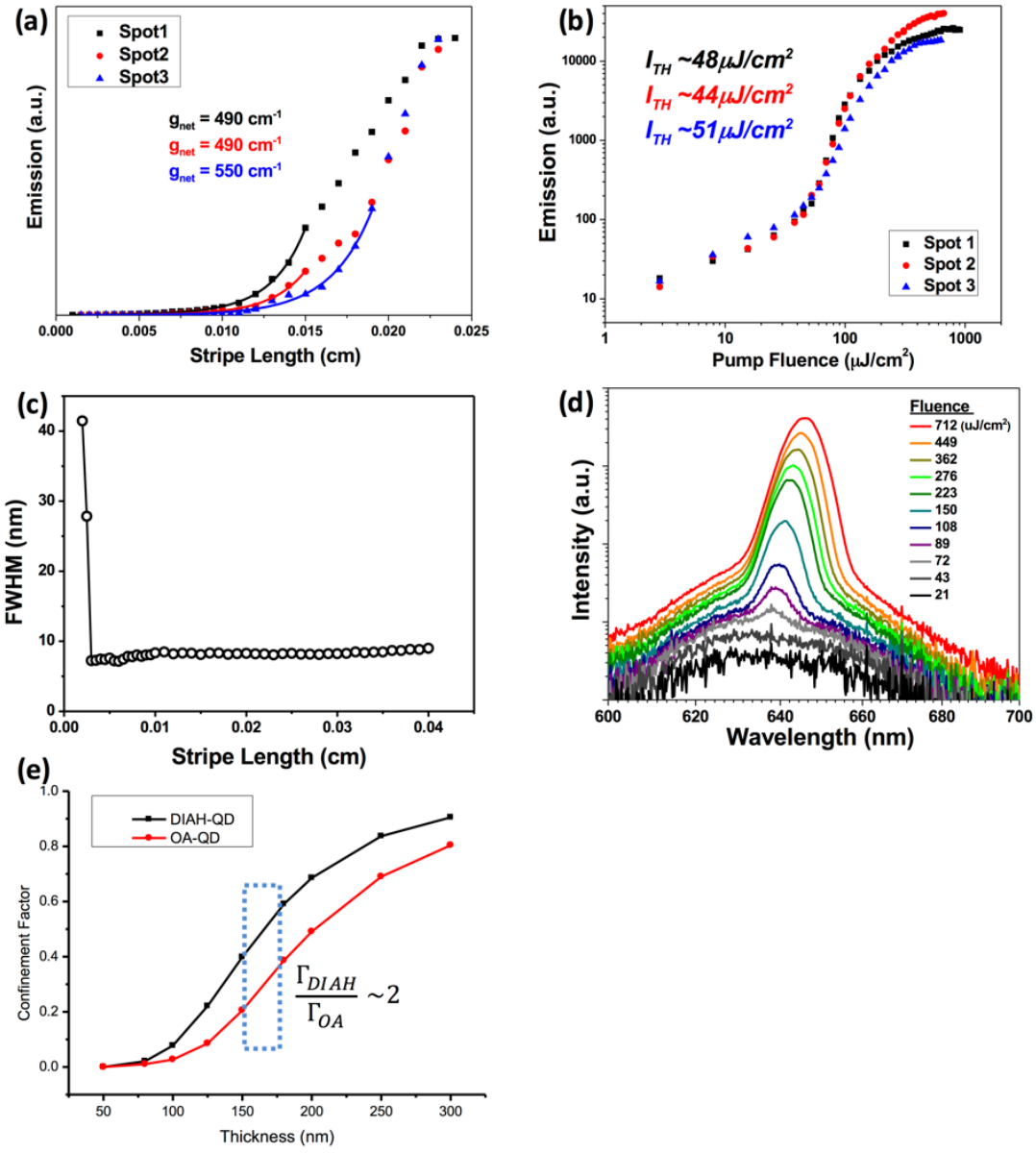

Figure B.7 Optical gain measurements of the crosslinked QD films from the VSL method. An average gain value for the DIAH crosslinked QD films was obtained by examining multiple spots over multiple substrates. Typically, these values exhibited similar net gain values (a). The presence of optical gain was also confirmed from observing threshold behavior in input power-output power plots. These data were also collected from multiple spots over multiple substrates, and also exhibited consistent values (b). Spectral narrowing of the VSL data is a further indication of optical gain (c) The PL spectra of figure 2a that show the transition from spontaneous emission to ASE with increasing pumping fluence. The PL intensity is presented in log scale (d). Thickness dependent confinement factor at 640nm of DIAH- and OA- QD films calculated by using lumerical mode solutions (e).

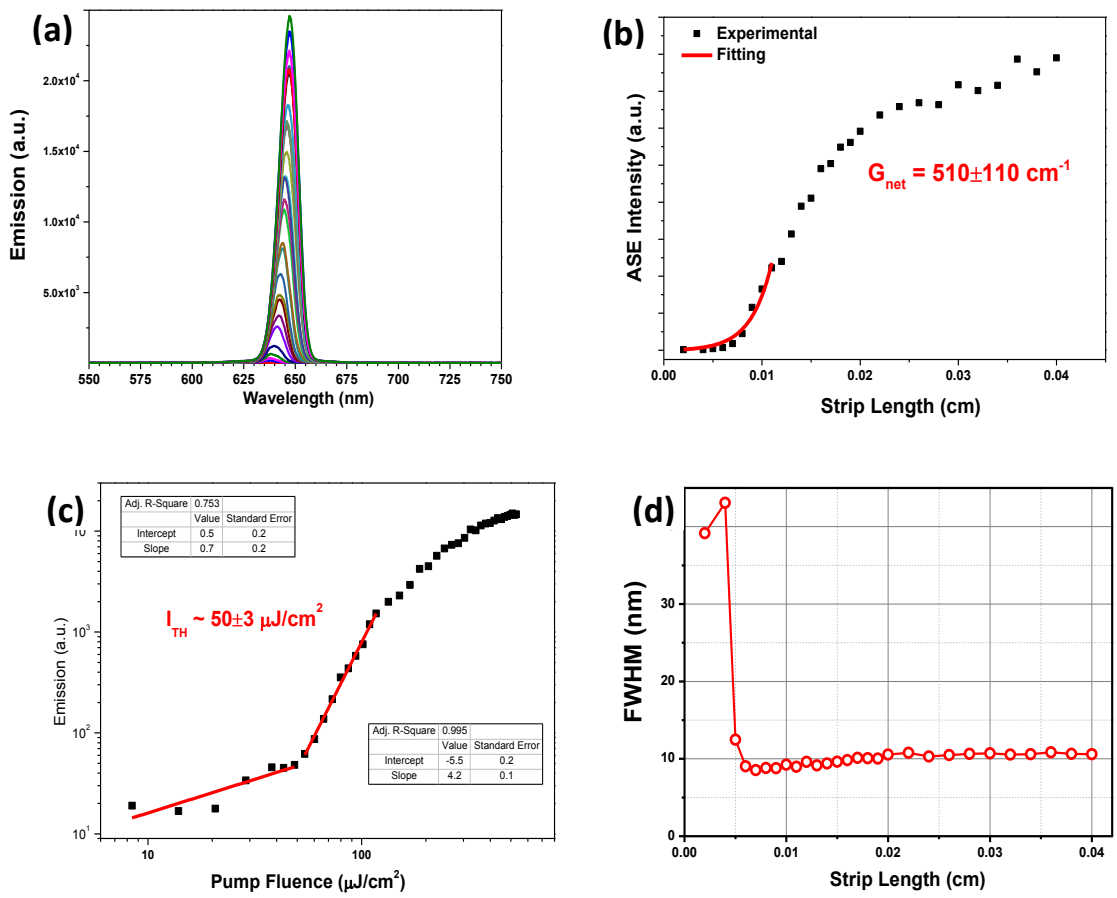

Figure B.8 Emission spectra of BA capped QD films under different excitation strip lengths (a). All spectra are pumped at 440 nm with 5-ns pulse (pumped under 500 μJ/cm^2). The ASE intensity exhibits an exponential increase with longer excitation strip lengths for certain lengths, which indicates the presence of optical gain. The net gain values are fitted with an average net gain of 510±110 cm^{-1} for the BA-capped QD films (b). The presence of optical gain is also supported by threshold behavior in input power-output power plots (average of 50 ±3 μJ/cm^2) (c) spectral narrowing of the emission peak as the pump strip length is increased (d).

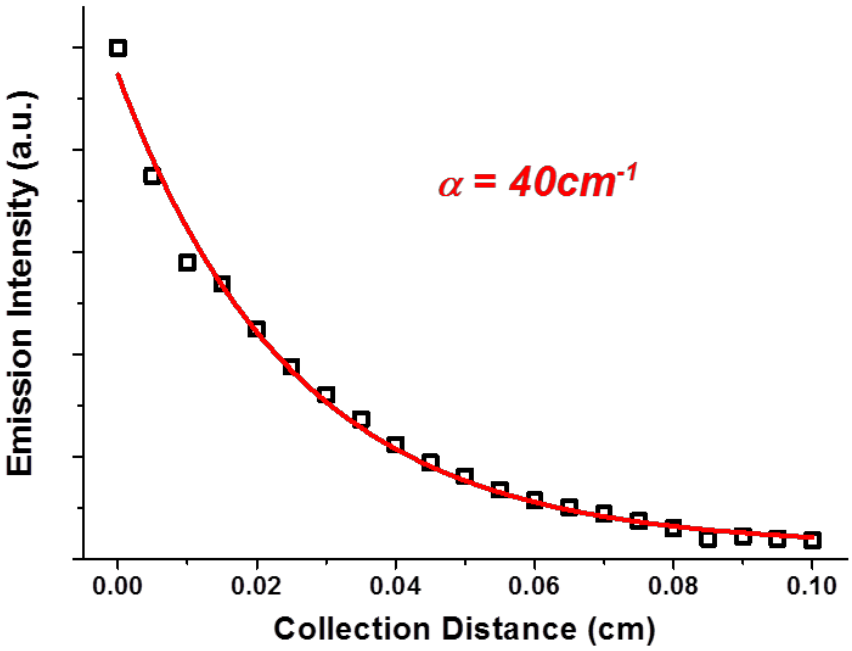

Figure B.9 An example of the experimental data and the fitting from an optical loss measurement for the low loss DIAH-tethered QD films.

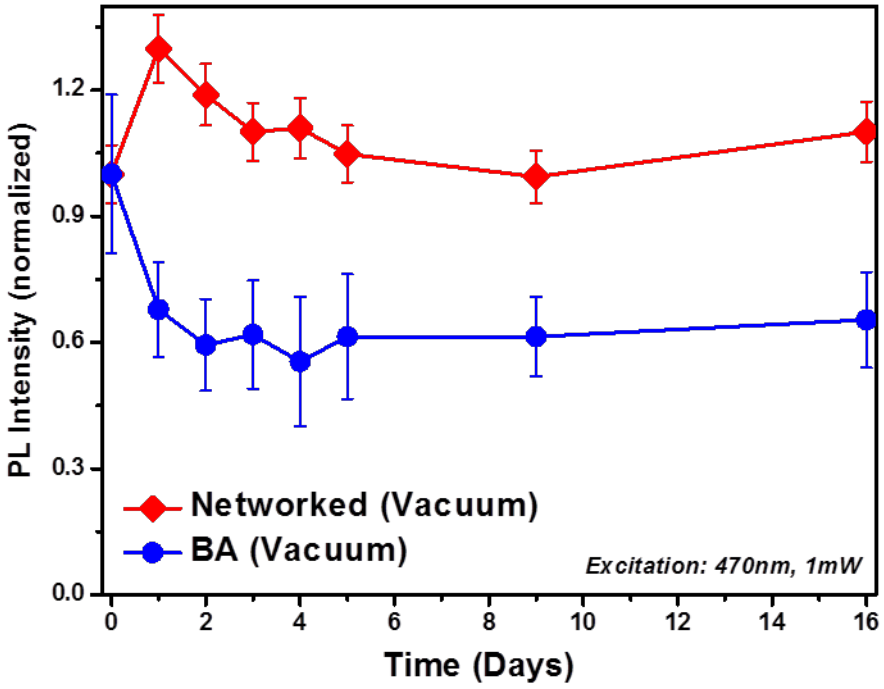

Figure B.10 PL stability tests of DIAH-crosslinked and BA-capped QD films stored in a desiccator under vacuum. The PL intensity of the DIAH-tethered QD film (black) remains stable over 16 days while that of the BA-capped QD film (red) decreased to 60%.

References

1 I. Suárez, H. Gordillo, R. Abargues, S. Albert, J. Martínez-Pastor, *Nanotechnology* **2011**, 22, 435202.

2 G. Socrates, John Wiley & Sons, Ltd.: Chichester, *Infrared and Raman Characteristic Group Frequencies: Tables and Charts*. **2001**; ISBN 0- 471-85298-8.

3 C. P. Marshall, E. J. Javaux, A. H. Knoll, M. R. Walter, *Precambrian Research* **2005**, 138, 208.

4 S. L. Sewall, R. R. Cooney, E. A. Dias, P. Tyagi, P. Kambhampati, *Phys. Rev. B* **2011**, 84, 235304.

Appendix C

Chapter 7 supporting data

(LARGE-SCALE ROBUST QUANTUM DOT MICRODISK LASERS WITH CONTROLLED CAVITY MODES)

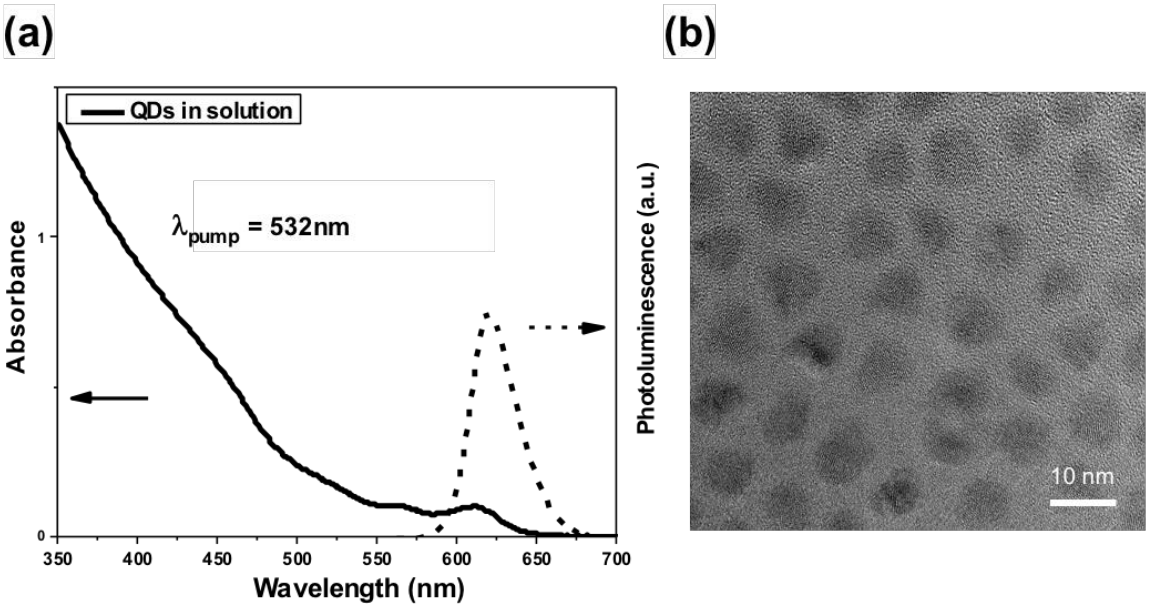

Figure C.1 (a) Optical absorbance (solid) and photoluminescence (dashed) spectra of the oleic acid capped QDs in solution. (b) TEM micrograph of oleic acid-capped core/graded-shell CdSe/$Cd_{1-x}Zn_xSe_{1-y}S_y$ QDs.

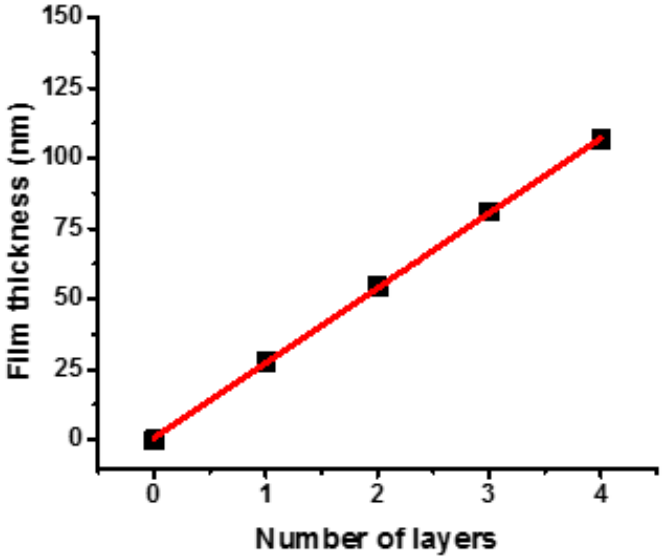

Figure C.2 Film thickness as a function of the number of deposited QD layers during the LbL assembly.

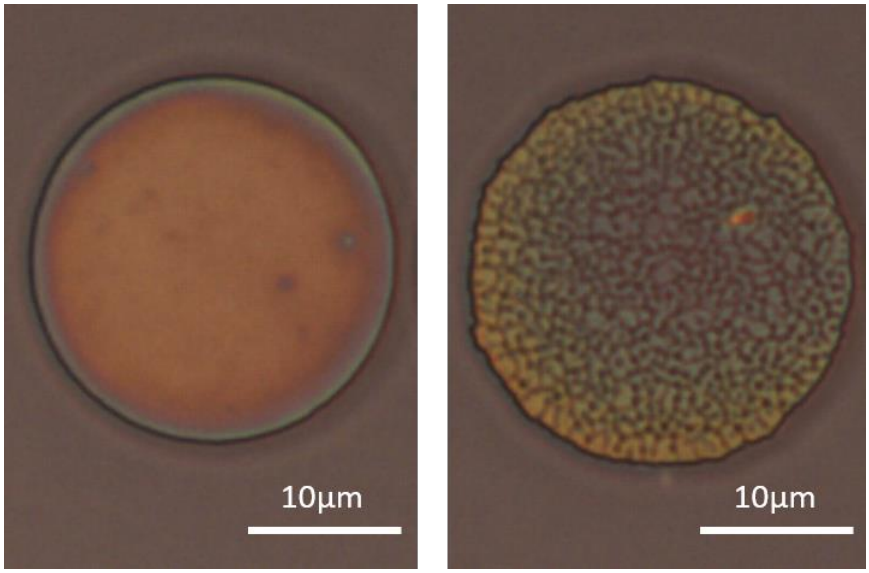

Figure C.3 Bright field optical images of fabricated QD microdisks (diameter of ~25 µm) using the same batch of butylamine capped QDs with (left) and without (right) the crosslinking process. Cracks and non-circular circumference form during sonication in the non-crosslinking case (right).

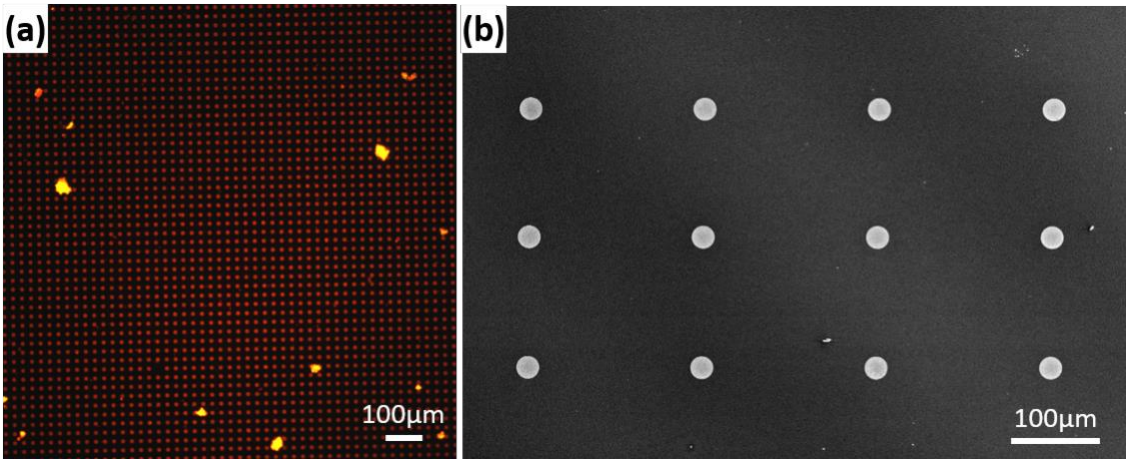

Figure C.4 (a) PL image of an array of microdisks with diameter of 10.6 µm (b) SEM image of an array of microdisks with diameter of 26.0 µm.

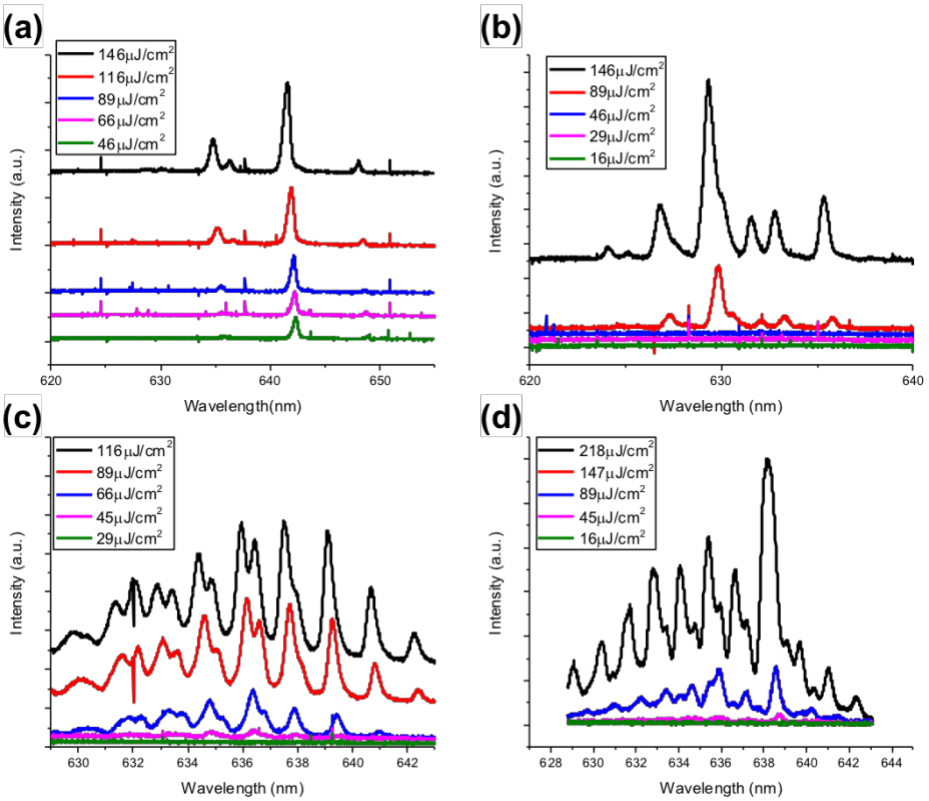

Figure C.5 Lasing spectra with mode splitting in microdisk with diameter of (a) 10.6 μm, (b) 26.0 μm, (c) 41.6 μm, and (d) 52.1 μm.

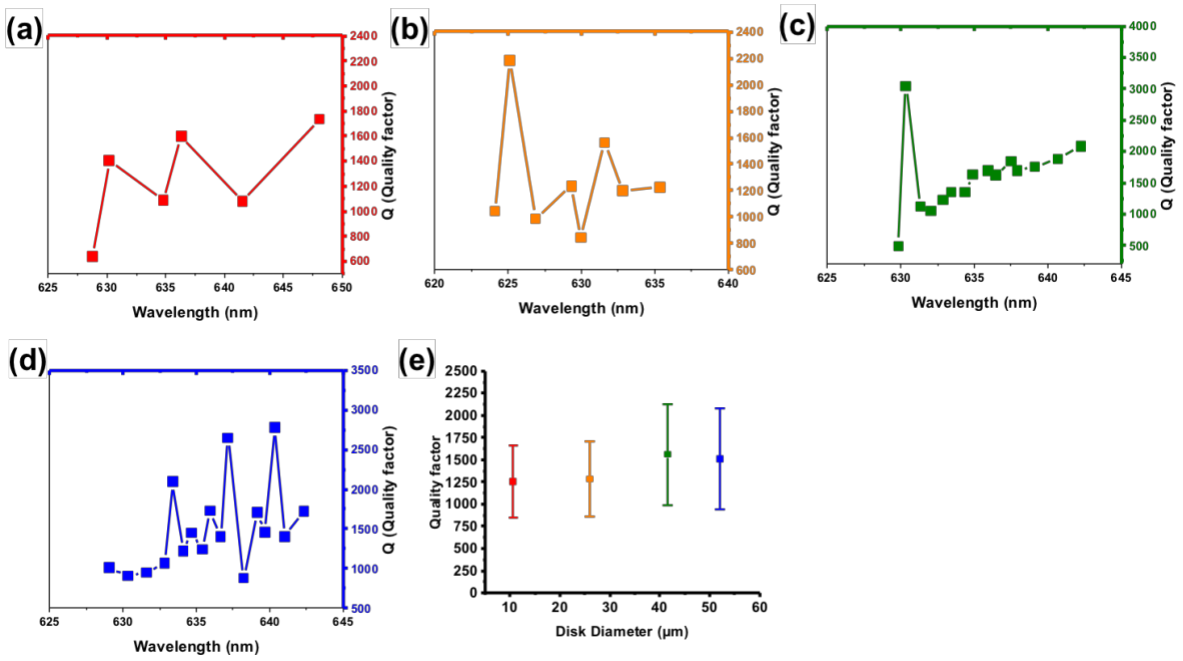

Figure C.6 Quality factor of the longitudinal cavity modes from lasing spectra (mode splitting) of microdisks with diameter of (a) 10.6 μm, (b) 26.0 μm, (c) 41.6 μm, and (d) 52.1 μm. (e) quality factor of lasing spectra with mode splitting as a function of disk diameter.

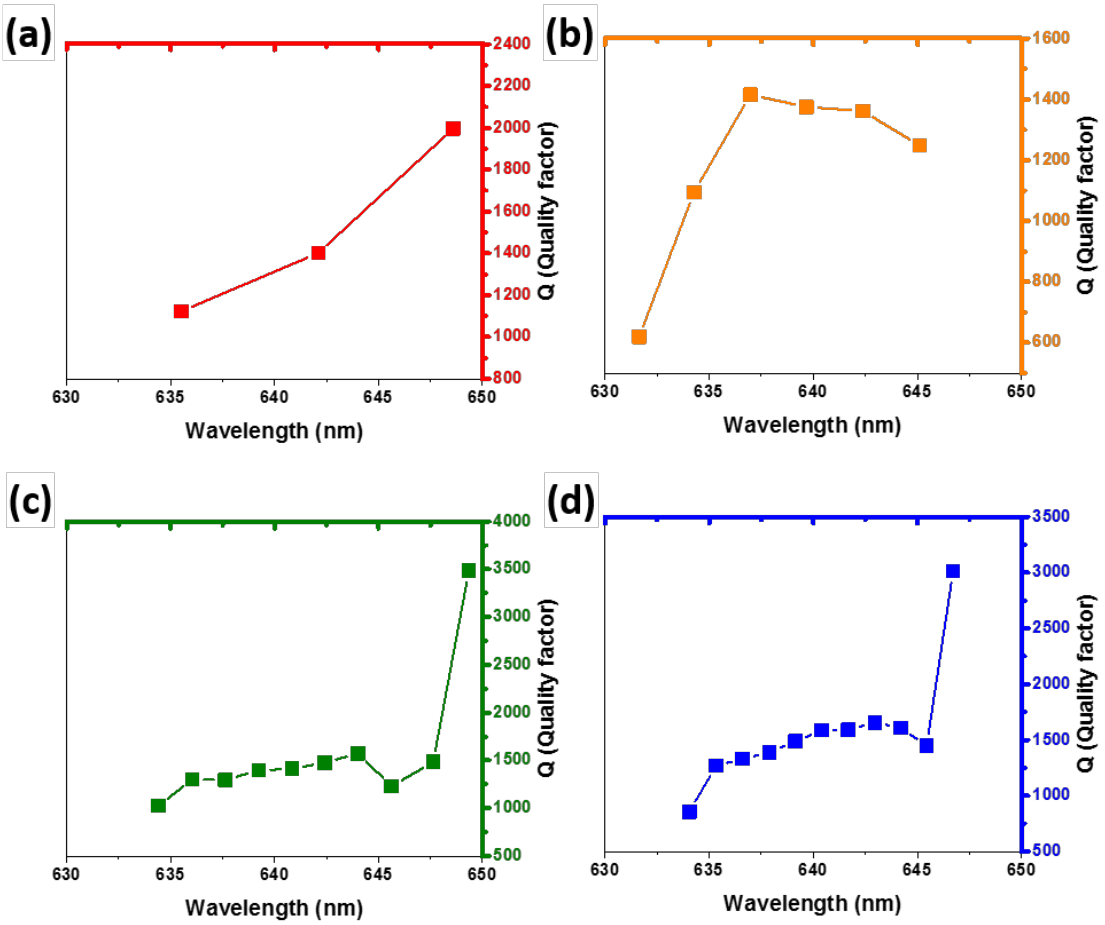

Figure C.7 Quality factor of the longitudinal cavity modes from microdisks with diameter of (a) 10.6 μm, (b) 26.0 μm, (c) 41.6 μm, and (d) 52.1 μm.

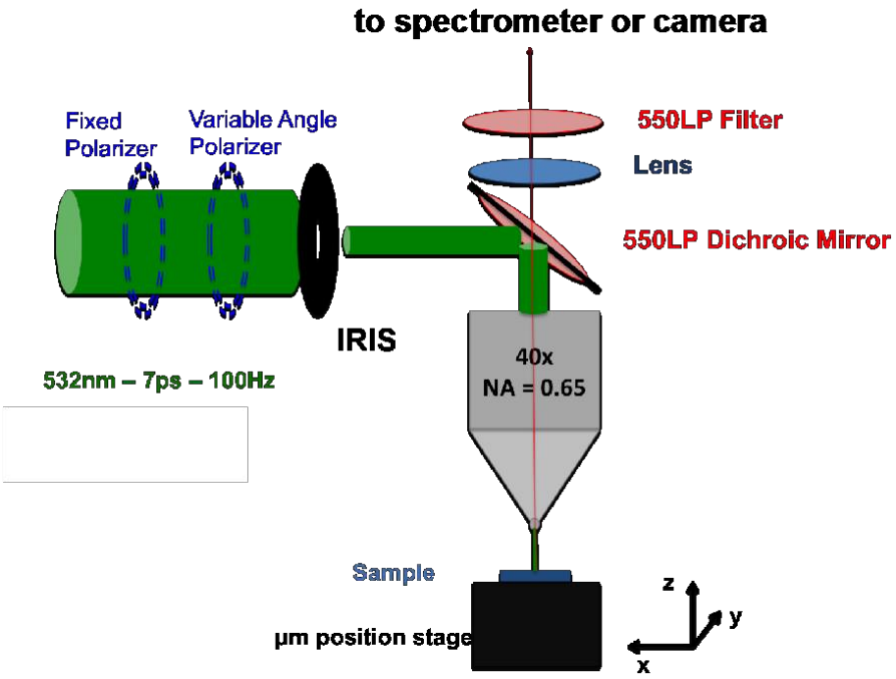

Figure C.8 Schematic of the confocal photoluminescence measurement apparatus.

Appendix D

Chapter 8 supporting data

(LARGE-AREA LASING AND MULTICOLOR PEROVSKITE QUANTUM DOT ARRAYS)

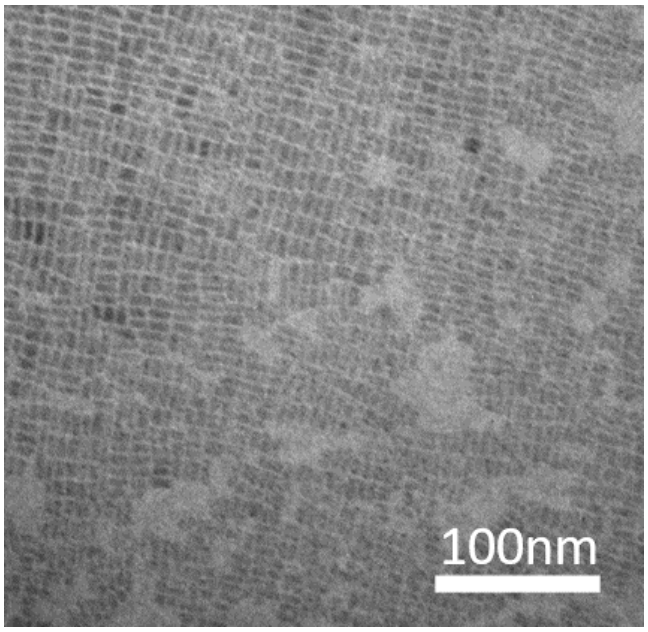

Figure D.1 TEM micrograph of oleic acid-capped $CsPbBr_3$ QDs.

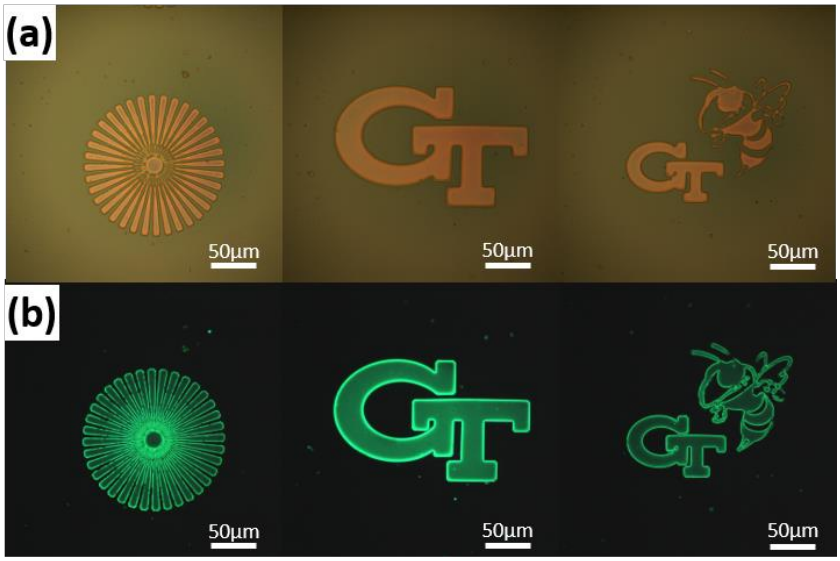

Figure D.2 Bright field (b) and fluorescence (c) images of different individual patterns.

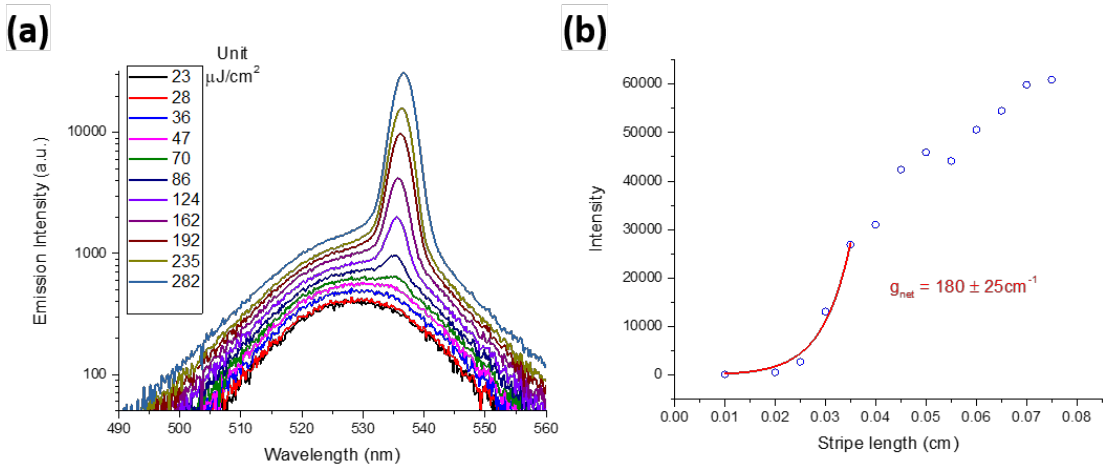

Figure D.3 (a) Emission spectra of $CsPbBr_3$ QD film under different pump fluences showing ASE and spectral narrowing. (b) Optical gain value of $CsPbBr_3$ QD film fitted by using variable stripe length method.

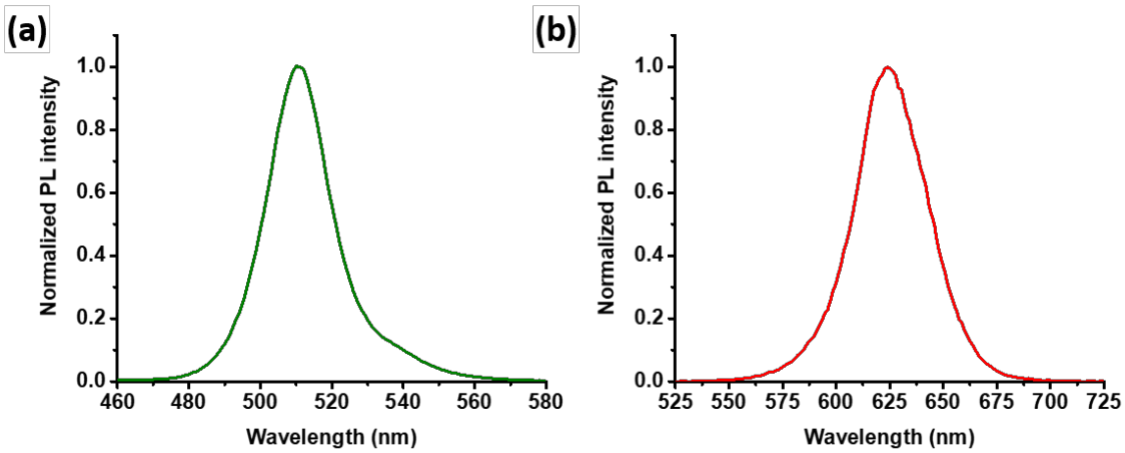

Figure D.4 Emission spectra of (a) $CsPbBr_3$ QD disk pattern; (b) $CdSe/Cd_{1-x}Zn_xSe_{1-y}S_y$ QD disk pattern by integrating the PL emission of an 2 μmx2 μm region within green and red microdisks using hyperspectral system.

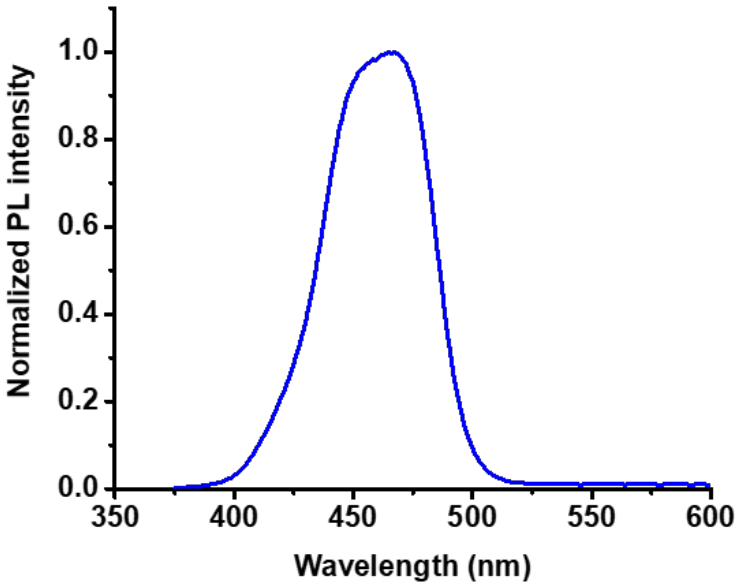

Figure D.5 Emission spectrum of blue CdSe/$Cd_{1-x}Zn_xSe_{1-y}S_y$ QDs dispersed in hexane.

Appendix E

Chapter 10 supporting data

(COALESCENCE OF PARASITIC MODES AT AN EXCEPTIONAL POINT IN COUPLED MICRODISK LASERS)

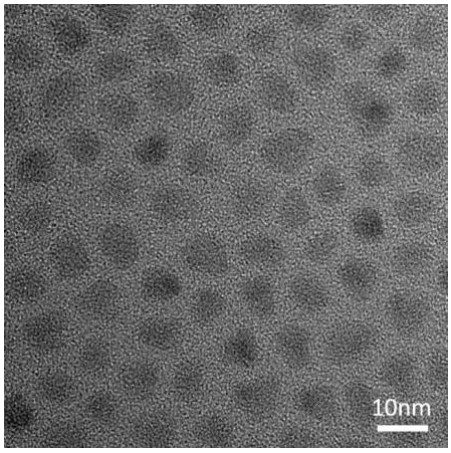

Figure E.1 TEM micrograph of oleic acid-capped CdSe/$Cd_{1-x}Zn_xSe_{1-y}S_y$ QDs.

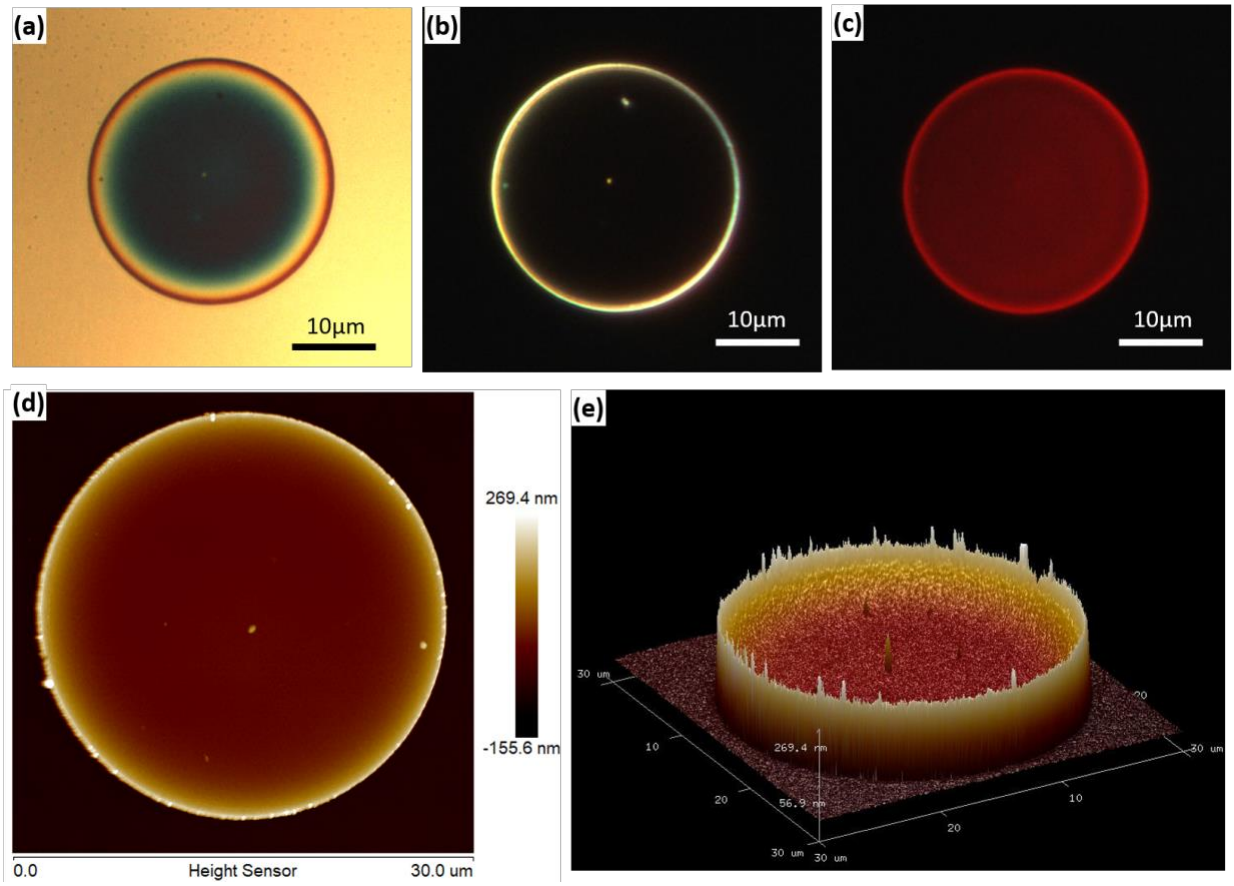

Figure E.2 (a) bright field (b) dark field and (c) photoluminescence microscopic imaging of microdisk with diameter of 25 µm. (d) AFM topographical image (top-view) and (e) 3D projection of microdisk with defects formed near circumference.

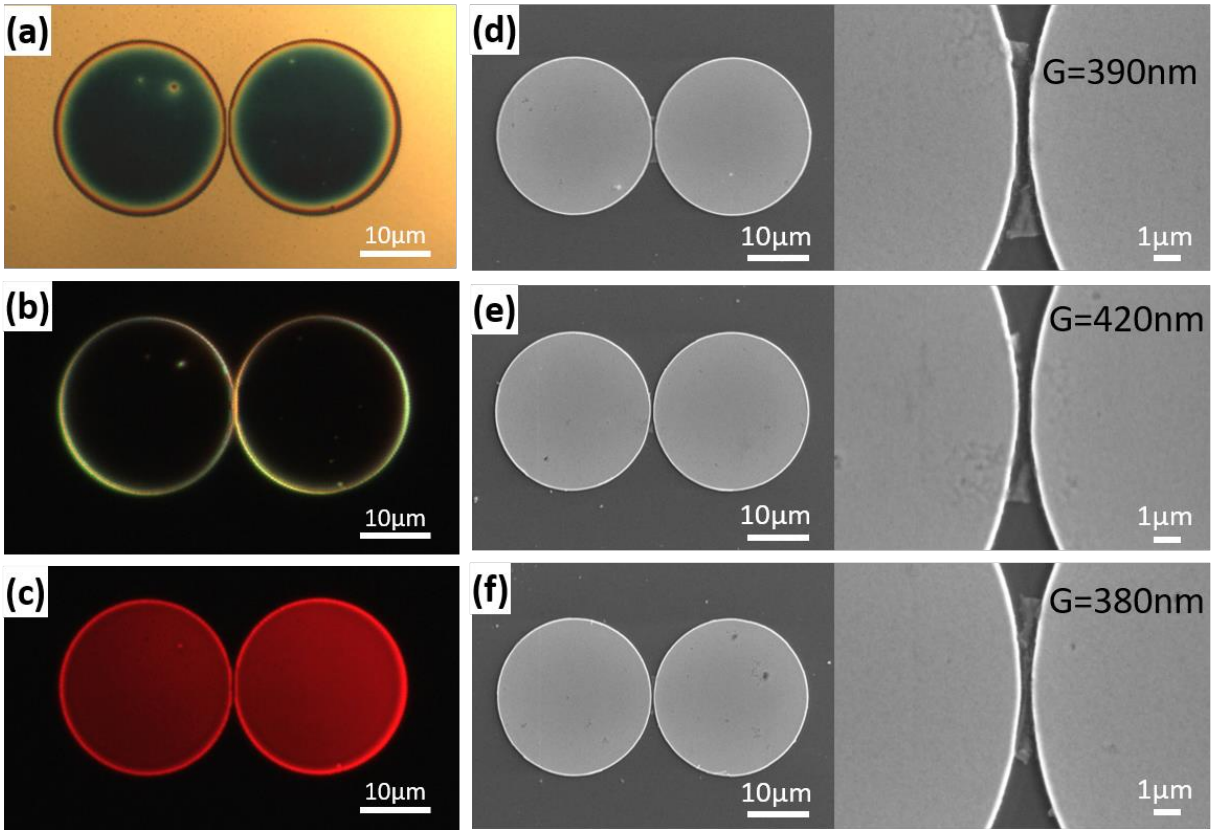

Figure E.3 (a) bright field (b) dark field and (c) photoluminescence microscopic imaging of coupled microdisk with disk diameter of 25 μm. (d), (e), (f) SEM images of 3 sets of coupled microdisks.

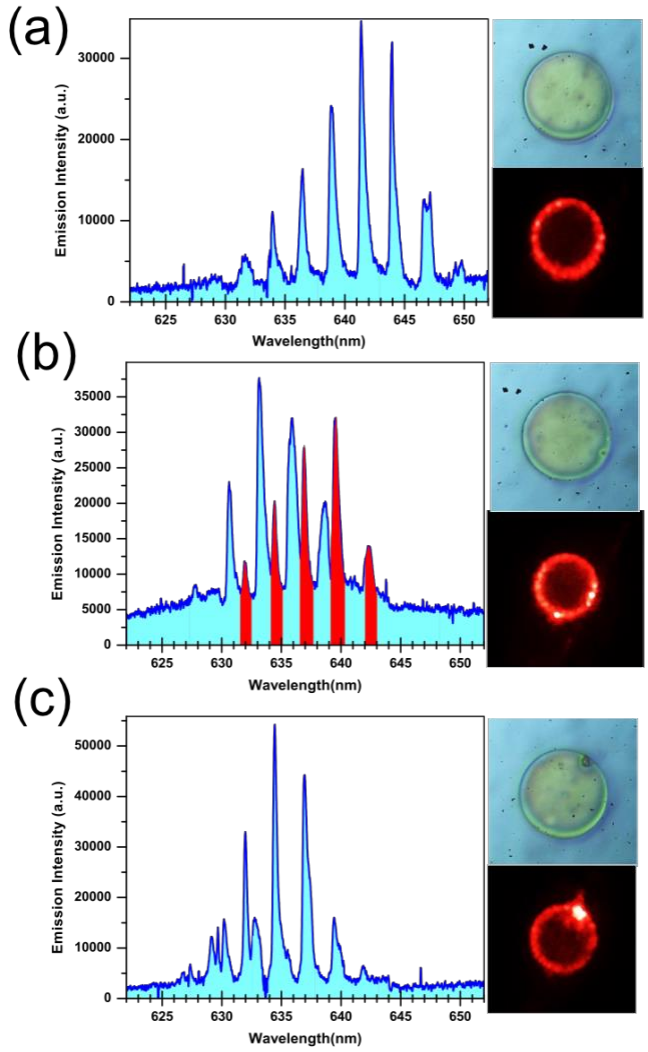

Figure E.4 shows three representative examples of the behaviors of individual microdisks. In (a) the spectrum shows a single mode progression, while the fluorescent and bright field microscope images show a relatively uniform circumference. In (b) and (c) mode splitting is observed in the spectrum and the fluorescent and bright field microscope images show defects along circumference. Not the relative blue shift of the mode envelope between (a), and (b) and (c).

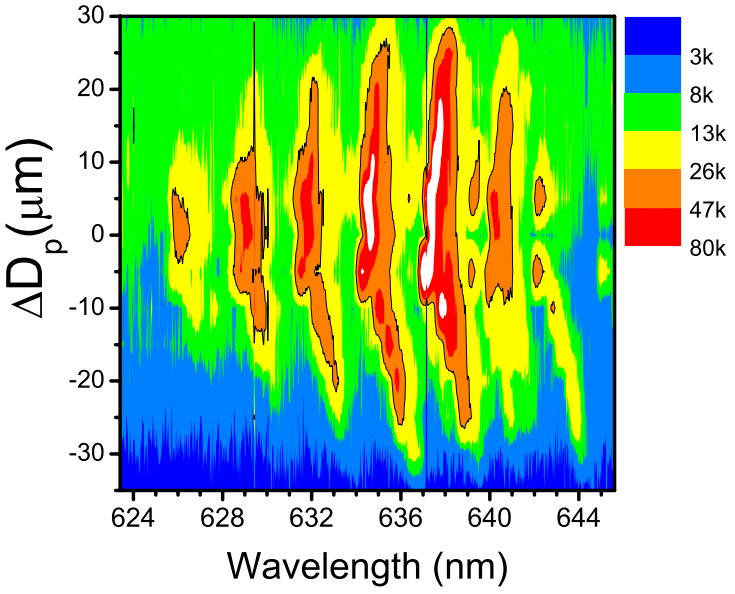

Figure E.5 As an important control experiment, we perform the spatial gain variation measurement on an isolated 25μm diameter disk. Here the behavior is largely different from that of the disk pair due to absence of coupling to another disk. As the disk enters the beam spot, threshold is achieved first at the longest wavelength modes. Then, as it moves completely into the beam spot the shorter wavelength modes are observed and grow more quickly in intensity than the long wavelength modes. This behavior is expected because of the large material loss at shorter wavelength. Thus, when the disk is only partially pumped, the unexcited region contributes much more loss at short wavelength than at long wavelength. There is then a 25μm plateau in emission intensity as the disk moves through the spot but is entirely pumped. The negligible variation in the measured spectrum in this region is a testament to the negligible effects of pump inhomogeneity with the beam spot. We can thus safely conclude that the onset of the long wavelength modes as well as the self-termination of short wavelength modes from the evenly pumped pair are entirely due to the mutual coupling between them and influence of gain/loss contrast between them, and not a property of isolated disks or due to experimental error.

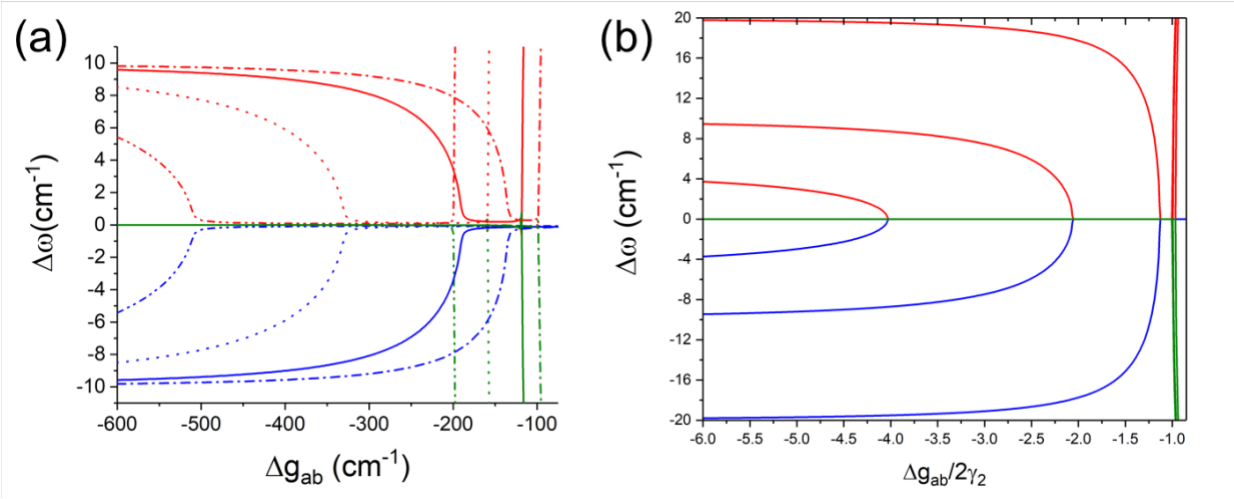

Figure E.6: (a) shows the eigenfrequencies $\omega_1^{(A)}$ (blue), $\omega_2^{(A)}$ (red), and $\omega_3^{(B)}$ (green), vs. the gain differential Δg_{AB} for different values of γ_{23} with κ fixed. As γ_{23} increases the point of coalescence of intra-cavity modes $\omega_1^{(A)}$ and $\omega_2^{(A)}$ moves to larger (negative) values of Δg_{AB}. In (b) a similar behavior occurs for varying values of κ with γ_{23} fixed, however, the coalescence point moves to lower magnitude of Δg_{AB} as κ increases. Empirically, we find that this coalescence occurs at the point $\Delta g_{AB} = (\gamma_{23})^2/2\kappa$. This signals the cross-over from the strong intra-cavity coupling regime to the intermediate coupling regime. In (a), the subsequent bifurcation of inter-cavity modes $\omega_1^{(A)}$ and $\omega_3^{(B)}$ occurs closer to $\Delta g_{AB} = 0$. The bifurcation point scales with γ_{23} as $\Delta g_{AB} = 2\gamma_{23}$. Meanwhile, in (b) we see the bifurcation point is seen to be insensitive to κ. Hence, in this region the inter-cavity coupling dominates and effectively reduces the problem to that of two coupled modes

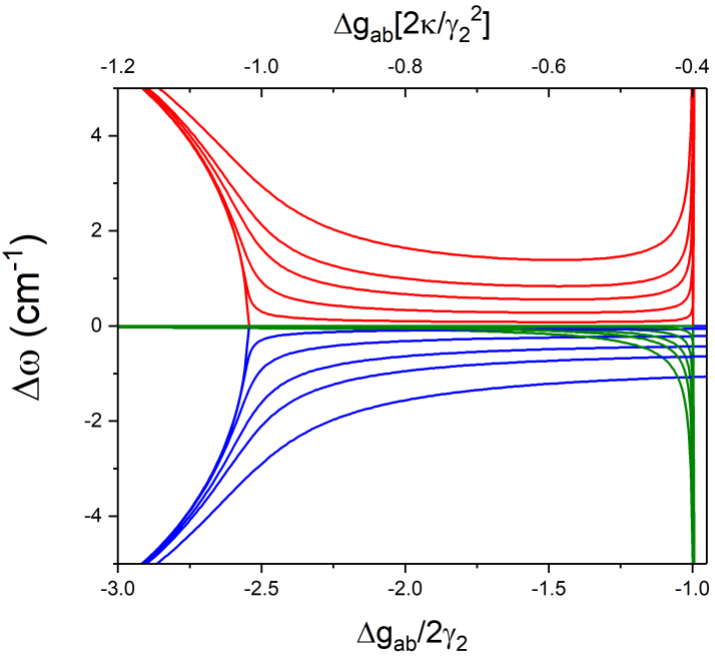

Figure E.7 both γ_{23} and κ are held constant while the value of γ_{12} is increased from zero. It is clear that as γ_{12} increases the coalescence is transformed into and avoided crossing. In the high γ_{23} limit the minimum splitting $\Delta\omega$ that is achieved is $\approx \gamma_{12}$. Thus when $\gamma_{12} = 0$ a true exceptional point is obtained. It is also clear from this figure that the points of coalescence and bifurication are independent of γ_{12}.

VITA

CHUN HAO LIN

Chun Hao Lin was born in Changhua, Taiwan in June 1988 to Pei-Lin Kuo and Chein-Chih Lin. He lived with his family in Xiushui, Changhua where he attended elementary school. After finishing elementary school, he attended Mingdao Junior and Senior High School. He earned his BS in Materials Science and Engineering from National Tsing-Hua University (Hsinchu, Taiwan) in 2010. Following this he pursued his MS in Materials Science and Engineering in University of Florida from 2011 to 2013. After finishing his MS degree, he continued to pursue his PhD at the Georgia Institute of Technology where he was guided by Professor Vladimir V. Tsukruk. After finishing his PhD in summer 2018 he plans to pursue a career in industry pertaining to research and technology development.